

Tracing protein native radicals under  
*in vitro* and *in vivo* conditions via EPR

–

*E. coli* class Ia ribonucleotide reductase  
as a paradigm

Dissertation

for the degree of  
"Doctor rerum naturalium"

TU Dortmund University  
Faculty of Chemistry and Chemical Biology

Submitted by  
Shari Lorraine Meichsner  
from Hamm, Germany  
Dortmund, November 2022



This Doctoral Thesis has been elaborated from November 2018 till November 2022 and has been examined by a committee of the Faculty of Chemistry and Chemical Biology as follows:

**Principal advisor:** **Prof. Dr. Müge Kasanmascheff**  
Faculty of Chemistry and Chemical Biology,  
TU Dortmund University

**Coexaminer:** **Prof. Dr. Daniel Summerer**  
Faculty of Chemistry and Chemical Biology,  
TU Dortmund University

**Submission date:** 15.11.2022

# Conference contributions

## Oral presentation

- 2019 Feb. Tag der Chemie, TU Dortmund (GE)  
2020 Feb. Tag der Chemie, TU Dortmund (GE)  
(received the prize for the best presentation)  
May JEOL Prize Talk at RSC ESR, online  
Nov. Virtual Ruhr EPR seminar, MPI Mülheim (GE)  
July EUROMAR, online  
2022 June JEOL Prize Talk at RSC ESR, St. Andrews (GB)  
Sept. GDCh FGMR Annual Discussion Meeting, Karlsruhe (GE)  
(invited as winner of the Ernst Award)

## Poster presentation

- 2019 Nov. 8<sup>th</sup> EFEPR school, Brno (CZ)  
2021 June Message from the cell, online  
Sept. RESOLV Klausurtagung, Harsewinkel (GE)

# Publications

- I. In-Cell Characterization of the Stable Tyrosyl Radical in *E. coli* Ribonucleotide Reductase Using Advanced EPR Spectroscopy  
Meichsner, S. L., Kutin, Y., Kasanmascheff, M. *Angew. Chem. Int. Ed.* **60**, 19155 – 19161 (2021).
- II. Long-Lived C<sub>60</sub> Radical Anion Stabilized Inside an Electron-Deficient Coordination Cage  
Hasegawa, S., Meichsner, S. L., Holstein, J. J., Baksi, A., Kasanmascheff, M., Clever, G. H., *J. Am. Chem. Soc.* **143**(26), 9718 – 9723 (2021).
- III. Mismetallation or regulation? Role of manganese ions in tuning the radical generation in ribonucleotide reductase  
Meichsner, S. L., Kasanmascheff, M., in preparation.

# Abstract

Although more than a hundred thousand protein structures are registered in the Protein Data Bank (PDB), there are still more open questions than answers. One of these proteins that have captivated researchers for decades is ribonucleotide reductase, short RNR. This enzyme is solely responsible for synthesizing DNA building blocks, the deoxynucleotides, in every living organism. Due to its central role, RNR has been the focus of research on several occasions, but many questions remain unanswered despite numerous studies. Moreover, information about RNR structure in its natural environment, namely living cells, is entirely lacking.

A method that can be used for protein structure elucidation is electron paramagnetic resonance, shortly EPR. EPR is also widely used for RNR studies since the enzyme has a native radical that is used for catalysis by means of a complex proton-coupled electron transfer. For many years, *E. coli* class Ia RNR has been regarded as a paradigm for class Ia enzymes, which is the analog of human RNR.

In this work, state-of-the-art EPR spectroscopy was used to address some of the open questions related to RNR. Advanced EPR techniques were used to determine the structure of the stable tyrosyl radical  $Y_{122}\bullet$  in *E. coli* class Ia RNR in living whole *E. coli* cells at high resolution. It was demonstrated that the structure and electrostatic environment of this essential radical are conserved under *in vitro* and *in vivo* conditions. Surprisingly, the radical distribution in living cells was found to behave differently than assumed by previous *in vitro* experiments. Mismetallation within the cells was identified as a possible influencing factor. In the course of these studies, it was shown that mismetallation with manganese does not lead to irreversible inactivation of protein activity but that the activity can be restored.

In addition to in-cell EPR, three other applications of magnetic resonance spectroscopy are highlighted in this work. First, insights into the development process of a new spin label are given, using RNR as a model system. Through these studies, azidophenylalanine was identified as a suitable candidate that could contribute to the ongoing development in the field of spin labeling for protein structure elucidation. Second, a high-pressure apparatus was used to study the effect of pressure on *E. coli* RNRs structure by EPR. Among other results, these studies revealed the presence of an indeterminate radical formed under the influence of pressure. Finally, independently of RNR, cw-EPR was used to characterize the  $C_{60}$  radical anion generated in a molecular coordination cage. A surprisingly long lifetime of this radical was found, which paves the way for versatile applications.

# Zusammenfassung

Obwohl mehr als hunderttausend Proteinstrukturen in der Protein Datenbank (PDB) registriert sind, existieren häufig immer noch mehr offene Fragen als Antworten. Eines dieser Proteine, was Forscher seit Jahren fesselt, ist die Ribonukleotid Reduktase, kurz RNR. Dieses Enzym ist alleinig in jedem Lebewesen für die Synthese von DNS-Bausteinen zuständig. Durch seine zentrale Rolle ist RNR bereits mehrfach in den Fokus der Forschung gerückt, doch trotz vielerlei Studien bleiben viele Fragen weiterhin unbeantwortet. Was jedoch gänzlich fehlt, sind Informationen über die RNR Struktur in seiner natürlichen Umgebung: in lebenden Zellen.

Eine Methode, die zur Aufklärung von Proteinstrukturen genutzt werden kann, ist Elektronenspinresonanz, kurz ESR. Auch für RNR-Studien wird ESR häufig eingesetzt, da das Enzym ein natives Radikal besitzt, welches mittels einem komplexen Protonengekoppelten Elektronen-Transfers zur Katalyse eingesetzt wird. Dabei wird seit Jahren *E. coli class Ia* RNR als Paradigma für *class Ia* Enzyme verwendet, welches das Analogon zur humanen RNR darstellt.

In dieser Arbeit wurde modernste ESR Spektroskopie genutzt, um einige der offenen Fragen im Zusammenhang mit RNR zu beantworten. Fortgeschrittene ESR Techniken wurden genutzt, um hochauflösend die Struktur des stabilen Tyrosylradikals  $Y_{122}^{\bullet}$  in *E. coli class Ia* RNR in lebenden, ganzen *E. coli* Zellen zu bestimmen. Dabei wurde gezeigt, dass die Struktur und elektrostatische Umgebung dieses essenziellen Radikals unter *in vitro* und *in vivo* Bedingungen konserviert ist. Überraschenderweise verhält sich die Radikal-Verteilung in lebenden Zellen jedoch anders, als durch bisherige *in vitro* Experimente angenommen. Mismetallierung innerhalb der Zellen konnte als ein möglicher beeinflussender Faktor identifiziert werden. Im Verlauf dieser Studien zeigte sich, dass eine Mismetallierung mit Mangan nicht zu einer irreversiblen Inaktivierung der Proteinaktivität führt, sondern dass diese wiederhergestellt werden kann.

Weiterhin werden nebst *in-cell* ESR drei weitere Anwendungsbereiche der Magnetresonanzspektroskopie betrachtet. Zum einen werden Einblicke in den Entwicklungsprozess eines neuen *Spin labels* gegeben, bei welchem RNR als Modellsystem genutzt wurde. Durch diese Studien wurde Azidophenylalanin als ein geeigneter Kandidat identifiziert, welcher zur fortwährenden Weiterentwicklung im Feld der Spin-Markierung zur Proteinstruktur-Aufklärung beitragen könnte. Weiterhin wurde eine Hochdruck-apparatur genutzt, um den Einfluss von Druck auf die Struktur von *E. coli* RNR mittels ESR zu untersuchen. Dabei offenbarte sich unter anderem die Präsenz eines undefinierten Radikals, generiert durch den Einfluss von Druck. Schließlich wurde unabhängig von RNR cw-ESR zur Charakterisierung des  $C_{60}$ -Radikalsanions verwendet, welches in einem molekularen Koordinationskäfig generiert wurde. Eine ungewöhnlich lange Lebenszeit dieses Radikals wurde hierbei festgestellt, welches den Weg für vielseitige Anwendungsmöglichkeiten eröffnet.

# Contents

Conference contributions	
Oral presentation .....	IV
Poster presentation .....	IV
Publications .....	IV
Abstract .....	V
Zusammenfassung.....	VI
Contents .....	VII

## Introduction and aim of this work

<b>1. Ribonucleotide reductase</b>	
1.1. Introduction to ribonucleotide reductase.....	1
1.2. Different classes of ribonucleotide reductases .....	2
1.3. Class Ia ribonucleotide reductase.....	4
1.3.1. Tertiary and quaternary structure of <i>E. coli</i> class Ia RNR.....	4
1.3.2. The puzzle of the radical transfer pathway .....	6
1.3.3. Unnatural amino acids help unravel the PCET mechanism .....	7
1.3.4. EPR measurements prove an $\alpha\beta\beta$ complex assembly.....	10
1.4. Incorporation procedure of unnatural amino acids .....	14
1.5. Radical distribution and half-sites reactivity in <i>E. coli</i> RNR.....	16
1.6. The diiron cofactor assembly .....	18
1.7. Class Ia ribonucleotide reductase <i>in vivo</i> .....	19
Motivation.....	21
Problem .....	21
Objective .....	21
Chapter overview .....	21
<b>2. Theoretical background</b>	
2.1. EPR theory .....	23
2.2. The spin Hamiltonian .....	25
2.2.1. Electron Zeeman interaction.....	26
2.2.2. Nuclear Zeeman interaction .....	26
2.2.3. Hyperfine coupling .....	27
2.2.4. Weak electron-electron interactions .....	28
2.2.5. Nuclear spin quadrupole interaction .....	29
2.2.6. Zero-field splitting .....	31

2.3.	Cw-EPR .....	31
2.4.	Pulse EPR .....	32
2.4.1.	The Hahn echo experiment .....	33
2.4.2.	Relaxation .....	34
2.4.3.	Double electron-electron resonance spectroscopy .....	35
2.4.4.	Electron-nuclear double resonance spectroscopy .....	37
2.5.	Spin labeling in EPR .....	40
2.5.1	Nitroxide spin labels .....	41
2.5.2	Metal-based spin labels.....	41
2.5.3	Trityl spin labels .....	42
2.5.4.	Light-activated spin labels .....	42

## Results and discussion

<b>3.</b>	<b>In-cell characterization of the stable tyrosyl radical in <i>E. coli</i> RNR by EPR spectroscopy</b>	
3.1.	Introduction .....	47
3.1.1.	The problem .....	47
3.1.2.	The solution.....	48
3.2.	Materials and methods.....	49
3.2.1.	Wild-type $\beta 2$ protein expression for in-cell experiments .....	49
3.2.2.	2,3,5-F <sub>3</sub> Y <sub>122</sub> - $\beta 2$ protein expression for in-cell experiments .....	49
3.2.3.	EPR sample preparation .....	50
3.2.4.	Cell counting experiments.....	50
3.2.5.	Details of the EPR experiments .....	50
3.2.6.	Analysis of orientation-selective DEER measurements .....	51
3.3.	Results and discussion .....	53
3.3.1.	Detection and identification of a radical species in <i>E. coli</i> cells.....	53
3.3.2.	Estimation of the intracellular spin concentration.....	57
3.3.3.	Probing the H-bonding environment of Y <sub>122</sub> • in the cells via <sup>1</sup> H ENDOR .....	58
3.3.4.	In-cell distance distribution of Y <sub>122</sub> •-Y <sub>122</sub> • obtained via orientation-averaged DEER measurements .....	59
3.3.5.	Analysis of orientation-selective DEER measurements via PeldorFit .....	61
3.3.6.	Detection and evidence of Mn <sup>II</sup> in the cellular environment.....	64
3.3.7.	Investigating the in-cell radical distribution via DEER spectroscopy .....	66
3.3.8.	The effect of chloroform on radical yield and cell viability .....	68
3.3.9.	Detection of F <sub>3</sub> Y <sub>122</sub> • and F <sub>3</sub> Y <sub>122</sub> •-F <sub>3</sub> Y <sub>122</sub> • pairs within the cells.....	71
3.3.10.	Optimization of F <sub>3</sub> Y <sub>122</sub> • expression conditions.....	75
3.4.	Conclusion and outlook .....	77

<b>4.</b>	<b>Role of manganese ions in tuning the radical generation in ribonucleotide reductase</b>	
4.1.	Introduction.....	79
4.2.	Materials and methods .....	80
4.2.1.	In-cell sample preparation .....	80
4.2.2.	Monitoring of cell density, tyrosyl radical, and manganese content in the cells.....	81
4.2.3.	<i>In vitro</i> sample preparation .....	81
4.2.4.	UV-Vis measurements.....	81
4.2.5.	Size exclusion chromatography for $\beta 2$ dimer and monomer identification .....	82
4.2.6.	Dephosphorylation of azido-CTP .....	82
4.2.7.	$N_3$ CDP-based activity assay.....	83
4.2.8.	Size exclusion chromatography to probe $\alpha 2\beta 2$ complex assembly ....	83
4.2.9.	Detail of the EPR experiments.....	84
4.3.	Results and discussion .....	85
4.3.1.	Relation between cellular metal concentration and $Y_{122}\bullet$ radical yield .....	85
4.3.2.	Metal ion availability influencing the $Y_{122}\bullet$ radical distribution in the cells.....	86
4.3.3.	$Y_{122}\bullet$ radical distribution <i>in vitro</i> as a function of manganese concentration.....	87
4.3.4.	An asymmetric cofactor assembly and radical generation in <i>E. coli</i> RNR verified via <i>in vitro</i> DEER measurements.....	91
4.3.5.	Elucidating the time-dependent <i>in vitro</i> radical generation process ..	95
4.3.6.	Relative binding affinities of manganese and iron.....	99
4.3.7.	Time-dependent DEER experiments allow summarizing the regulatory mechanism of mismetallation .....	101
4.3.8.	$\beta 2$ remains a rigid dimer during recovery from mismetallation.....	103
4.3.9.	Testing the activity of mismetallated RNR using the $N_3$ CDP assay .	104
4.3.10.	Active $\alpha 2\beta 2$ complex formation in mismetallated RNR .....	106
4.4.	Conclusion and outlook.....	108
<b>5.</b>	<b>Development of a new rigid spin label</b>	
5.1.	Introduction.....	110
5.1.1.	The problem .....	110
5.1.2.	The solution approach .....	111
5.2.	Materials and methods .....	113
5.2.1.	Sample preparation and photolysis.....	113
5.2.2.	Details of the EPR experiments .....	113
5.2.3.	Incorporation of azF in $\beta 2$ class Ia <i>E. coli</i> RNR.....	114

5.3.	Results and discussion .....	114
5.3.1.	Amino acid photolysis investigated via 9 GHz cw-EPR measurements .....	114
5.3.2.	AzF-β2 RNR investigated via 34 GHz pulse EPR measurements ....	117
5.4.	Conclusion and outlook .....	120
<b>6.</b>	<b>Investigating <i>E. coli</i> ribonucleotide reductase with high-pressure EPR</b>	
6.1.	Introduction .....	122
6.1.1.	Pressure affecting protein structures .....	122
6.1.2.	Excited states in ribonucleotide reductase .....	124
6.1.3.	High-pressure EPR .....	125
6.2.	Materials and methods .....	125
6.2.1.	Sample preparation .....	125
6.2.2.	Sample pressurization .....	125
6.2.3.	Details of the EPR experiments .....	126
6.3.	Results and discussion .....	127
6.3.1.	The effect of glycerol on <i>E. coli</i> RNR protein structure .....	127
6.3.2.	<i>E. coli</i> RNR under different pressures .....	132
6.3.3.	Pressure-dependent DEER measurements .....	138
6.4.	Conclusion and outlook .....	140
<b>7.</b>	<b>Long-lived C<sub>60</sub> radical anion stabilized inside a molecular coordination cage</b>	
7.1.	Introduction .....	141
7.1.1.	Fullerenes and their functionalization .....	141
7.1.2.	Encapsulated fullerenes .....	142
7.1.3.	The fullerene radical anion .....	143
7.2.	Materials and methods .....	144
7.2.1.	Sample preparation for EPR measurements .....	144
7.2.2.	Details of the EPR experiments .....	144
7.3.	Results and discussion .....	144
7.3.1.	Generation of the C <sub>60</sub> • <sup>-</sup> radical .....	144
7.3.2.	Saturation behavior of the radical signals .....	148
7.3.3.	Half-lifetime determination of C <sub>60</sub> • <sup>-</sup> .....	149
7.4.	Conclusion and outlook .....	153
<b>8.</b>	<b>Materials and methods</b>	
8.1.	Materials .....	154
8.1.1.	Hosts and vectors .....	154
8.1.2.	Instruments .....	155
8.1.3.	Buffers, reagents, and kits .....	156

8.1.4. Software and online tools.....	159
8.2. Methods .....	160
8.2.1. Transformation of competent <i>E. coli</i> cells .....	160
8.2.2. Plasmid isolation from bacterial strains.....	160
8.2.3. Expression and purification of <i>E. coli</i> class Ia RNR (His) <sub>6</sub> - $\alpha$ 2 .....	160
8.2.4. Expression and purification of <i>E. coli</i> class Ia RNR apo- $\beta$ 2.....	161
8.2.5. Reconstitution of apo- $\beta$ 2 to form the diferric-Y• cofactor .....	162
8.2.6. Expression and purification of tyrosine phenol lyase (TPL).....	162
8.2.7. SDS polyacrylamide gel electrophoresis.....	163
8.2.8. Enzymatic synthesis and purification of fluorotyrosines .....	163
8.2.9. Echo-detected EPR (ESE).....	164
8.2.10. Microwave nutation .....	164
8.2.11. Phase memory time.....	164
8.2.12. Davies ENDOR .....	164
8.2.13. DEER .....	165

## Appendix

### A. Supporting information to Chapter 3

Details of <i>in vitro</i> and in-cell DEER measurements .....	166
Analysis of orientation-selective <i>in vitro</i> DEER data by PeldorFit .....	168
Analysis of orientation-selective in-cell DEER data by PeldorFit.....	170
Comparison of transversal relaxation times .....	171
In-cell samples compared to <i>in vitro</i> mimics.....	172
The effect of chloroform investigated by 34 GHz EPR measurements.....	173
Subtraction of the Mn <sup>II</sup> spectral features .....	174
Details of the F <sub>3</sub> Y <sub>122</sub> • DEER measurements and analysis .....	175

### B. Supporting information to Chapter 4

TLC plate to monitor dephosphorylation of N <sub>3</sub> CTP.....	177
Detail of the in-cell DEER measurements .....	178
Y-Mn distance in the crystal structure of manganese-bound RNR $\beta$ 2.....	179
DEER measurements on manganese-bound RNR.....	180
Details of UV-Vis measurements .....	181
DEER experiments with different amounts of iron .....	181
DEER measurements with iron and manganese added at the same time..	182
Excluding concentration-dependent effects on radical recovery.....	183
Time-dependent radical recovery monitored by DEER measurements .....	184

### C. Supporting information to Chapter 5

Photolysis investigated by 34 GHz measurements.....	185
---	-----

<b>D.</b>	<b>Supporting information to Chapter 8</b>	
	NMR spectra of 2,3,5-F <sub>3</sub> Y .....	186
	Abbreviations.....	187
	List of figures .....	189
	List of tables .....	194
	Acknowledgments .....	195
	References .....	197
	Eidesstattliche Versicherung (Affidavit).....	233

INTRODUCTION

AND AIM OF THIS WORK



# 1.

## Ribonucleotide reductase

---

Ribonucleotide reductase (RNR) was the first protein discovered carrying a free radical and since has become a prime example of radical involvement in biological transformations.<sup>1</sup> Even after decades of research, still many questions about the structure and function of this complex protein arise. Answering these questions is of general interest because RNR is an important drug target.

### 1.1. Introduction to ribonucleotide reductase

Ribonucleotide reductase is an essential enzyme in every living organism since it converts nucleotides (NDP or NTP) into the corresponding deoxynucleotides (dNDP or dNTP) through the reduction of the C2'-OH bond (**Figure 1.1**).<sup>2-4</sup> So far, this protein is the only known source responsible for *de novo* biosynthesis of dNTP and hence substantially controls the nucleotide/deoxynucleotide pool in a cell. Due to this central catalytic function, RNRs are one of the most-regulated enzymes.<sup>5-7</sup> Increased RNR activities are found in malignant transformation and tumor cells and thus have been a target for various anticancer drugs.<sup>8,9</sup> In addition, RNR inhibitors are used as antiviral drugs, e.g., against herpes viruses or as antibiotics.<sup>10-12</sup>

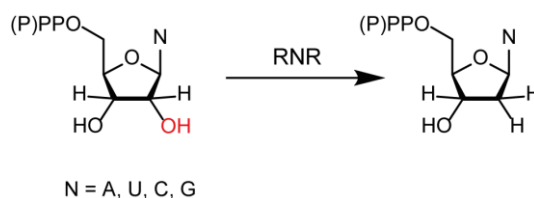


**Figure 1.1: Reaction catalyzed by ribonucleotide reductases.** RNR catalyzes the conversion of adenine (A), uracil (U), cytosine (C), and guanine (G) nucleotides to deoxynucleotides.

---

## 1.2. Different classes of ribonucleotide reductases

All RNRs are characterized by a structurally homologous active site for nucleotide reduction located in the large  $\alpha$  subunit. Catalysis requires the formation of a thiyl radical species ( $\text{Cys}\bullet$ ). Depending on the metal-ion-driven thiyl radical generation mechanism of different RNRs, they are divided into different classes (I, II, and III), with class I divided into five subclasses a-e (Figure 1.2).<sup>13-15</sup> Class I enzymes require a dimetallocofactor, whereas class II utilizes an adenosylcobalamin cofactor. Class III uses a glyceryl radical, which is, in turn, formed by a 4Fe4S iron-sulfur cluster coupled to S-adenosylmethionine (SAM).

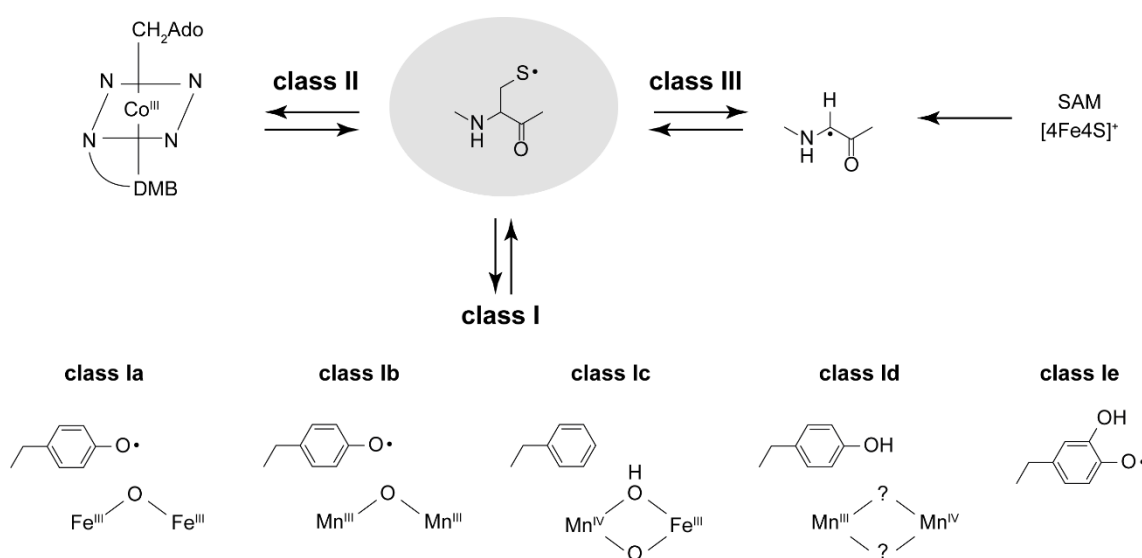


**Figure 1.2: Different classes of RNR based on the required metallocofactor for  $\text{Cys}\bullet$  formation.** Cofactors are shown schematically and simplified.  $\text{Cys}\bullet$  is marked in gray. Ado: adenosyl, SAM: S-adenosylmethionine, DMB: dimethylbenzimidazole.

Furthermore, the classes differ in their oxygen tolerance; class I enzymes are aerobic, whereas class III RNRs are anaerobic and inactivated by the presence of oxygen.<sup>15</sup> In contrast, class II RNRs are indifferent to oxygen, implying they neither require oxygen nor are they inhibited by it.<sup>4</sup> Consequently, the emergence of the various classes varies with different life forms. Class I can be found in all three domains of life, eukaryotes, eubacteria, and a few archaea. Class II proteins occur in both aerobic and anaerobic organisms and are primarily found in eubacteria and archaea. Class III RNRs exist in obligate and facultative anaerobic eubacteria and archaea.

The first class I enzyme that was biochemically characterized requires a binuclear high spin  $\text{Fe}^{\text{III}}$  complex to form an organic radical species, later designated class Ia.<sup>16</sup> Over the years, knowledge has accumulated about five different subclasses distinguished by their number and type of metal ions. It was found that class Ia requires a diiron center ( $\text{Fe}^{\text{III}}\text{Fe}^{\text{III}}$ ) for generating a tyrosyl radical  $\text{Y}\bullet$ . Class Ib binds a dimanganese center

( $\text{Mn}^{\text{III}}\text{Mn}^{\text{III}}$ ) to generate a  $\text{Y}\bullet$ , although this radical can also be generated with a diferric center ( $\text{Fe}^{\text{III}}\text{Fe}^{\text{III}}$ ).<sup>17–19</sup> Class Ic harbors a mixed  $\text{Mn}^{\text{IV}}\text{Fe}^{\text{III}}$  metallocofactor.<sup>20–22</sup> Recently, class Id containing a  $\text{Mn}^{\text{III}}\text{Mn}^{\text{IV}}$  cluster and the metal-free class Ie were discovered.<sup>23–26</sup> Apart from their metals, the subclasses also differ in two other points: the oxidant used to assemble the active cofactor and the involvement of additional proteins such as the flavoprotein NrdI (**Figure 1.3**). After complete cofactor assembly, some of these enzymes form stable tyrosine radicals (class Ia and Ib), further required for  $\text{Cys}\bullet$  formation, whereas others use metal-centered Cys oxidants (class Ic and Id). The metal-free class Ie is an exception, given that it forms a tyrosine radical-derived structure, a dihydroxyphenylalanine radical ( $\text{DOPA}\bullet$ ).

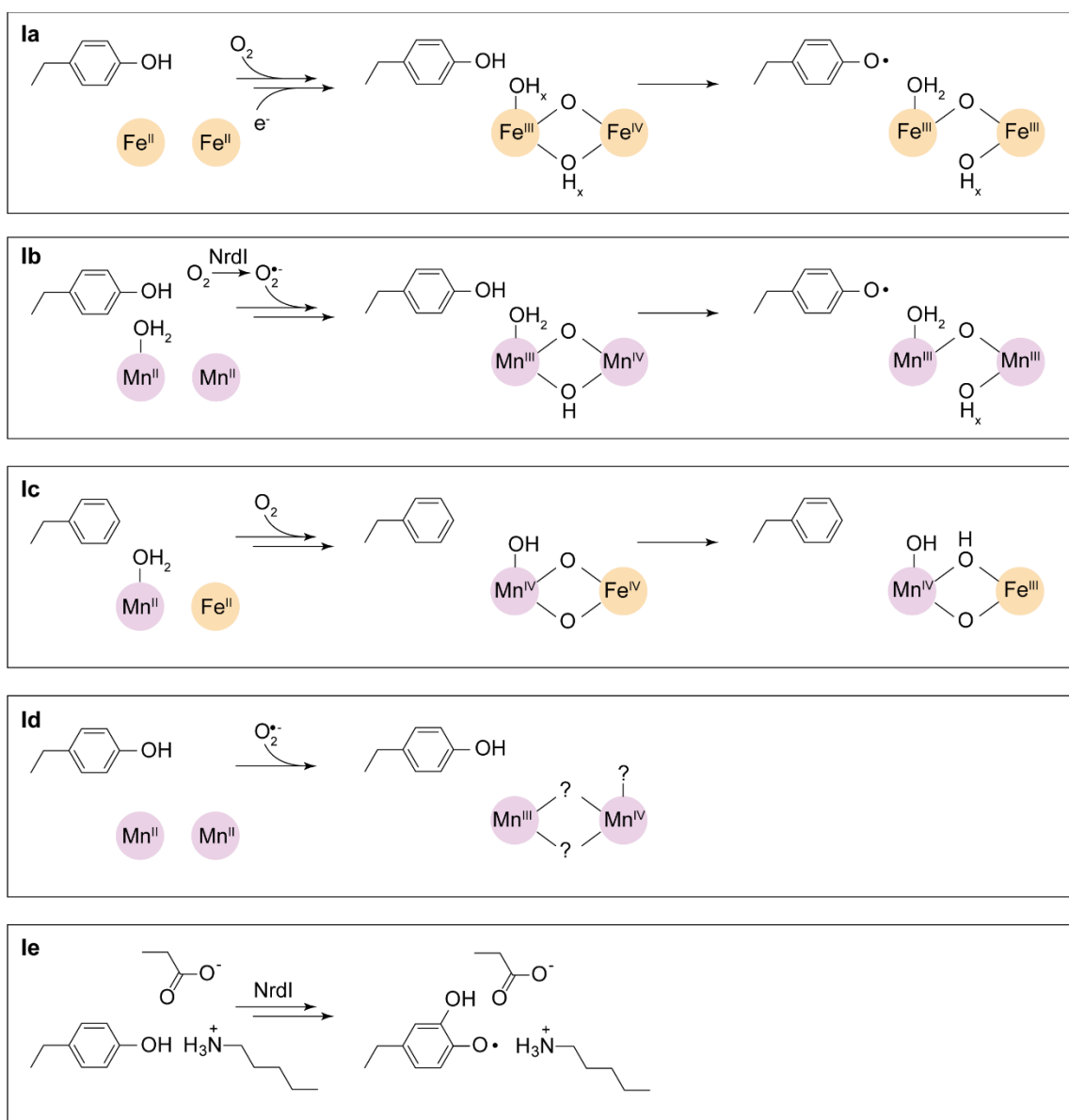


**Figure 1.3: Cofactor assembly mechanisms in different class I RNRs.** Figure adapted from Ruskoski *et al.*<sup>13</sup>

### 1.3. Class Ia ribonucleotide reductase

Class Ia is the most well-studied class of RNRs to date, whereas *Escherichia coli* (*E. coli*) Ia RNR represents a paradigm for class I enzymes and thus has been the focus of numerous studies. Although it has been six decades since the first discovery of ribonucleotide reductase in *E. coli* cell extract,<sup>27</sup> this protein still raises many questions, including structural and mechanistic ones. For this reason, *E. coli* class Ia RNR is the main focus of this work.

#### 1.3.1. Tertiary and quaternary structure of *E. coli* class Ia RNR

In all class Ia RNRs, the catalytic reaction takes place upon intermolecular interactions between two separate subunits, namely a large  $\alpha_2$  subunit (2x86 kDa in *E. coli*, 761 residues) and a smaller  $\beta_2$  subunit (2x44 kDa, 375 residues), which are encoded by the *nrdA* and *nrdB* genes, respectively. The individual subunits have been well characterized via X-ray crystallography, so it is known that the  $\alpha_2$  subunit holds two  $(\beta/\alpha)_{10}$  barrels.<sup>28,29</sup> Surprisingly, both subunits own structurally disordered C-terminal tails, encompassing residues 738 – 761 and 340 – 375 for  $\alpha$  and  $\beta$ , respectively. Nucleotide reduction occurs in the  $\alpha_2$  subunit, containing the catalytically active site and two types of allosteric effector binding sites: a specificity and an activity site (**Figure 1.4A**).<sup>28,30</sup> All four nucleotides, CDP, ADP, GDP, and UDP, can be reduced in the catalytic site. The specificity site, located at the dimer interface, can bind the allosteric effectors dATP, dGTP, dTTP, and ATP, dictating which of the four nucleotides will be converted to the corresponding deoxynucleotide and thus controlling the balance of the nucleotide pool. The activity site, found at the N-terminus of  $\alpha_2$ , is controlled by ATP and dATP binding and is responsible for determining the rate of reduction. While ATP promotes the formation of the active  $\alpha_2\beta_2$  complex, dATP binding leads to the inactive  $\alpha_4\beta_4$  oligomer (**Figure 1.5**).<sup>31</sup>

Once  $\alpha_2\beta_2$  is formed, nucleotide reduction is accomplished, presupposing the formation of the thiyl radical species ( $C_{439}\bullet$  in *E. coli* class Ia RNR).  $C_{439}\bullet$  is generated by a diferric tyrosyl radical cofactor  $Y_{122}\bullet$ , located in the  $\beta_2$  subunit (see **Figure 1.4B**). The resulting  $Y_{122}\bullet$  is an unusually stable radical with  $t_{1/2}$  of about 4 days at 4 °C, compared to 30 min in human or 10 min in mouse class Ia RNRs.<sup>16,32,33</sup> The transient thiyl radical is formed during each catalytic cycle by a long-range proton-coupled electron transfer (PCET) over a distance of  $\sim 32 \text{ \AA}$ <sup>34</sup> from  $\beta_2$  to  $\alpha_2$  and involves the formation of conserved aromatic amino acid radicals (**Figure 1.4C**), further discussed in Section 1.3.2.

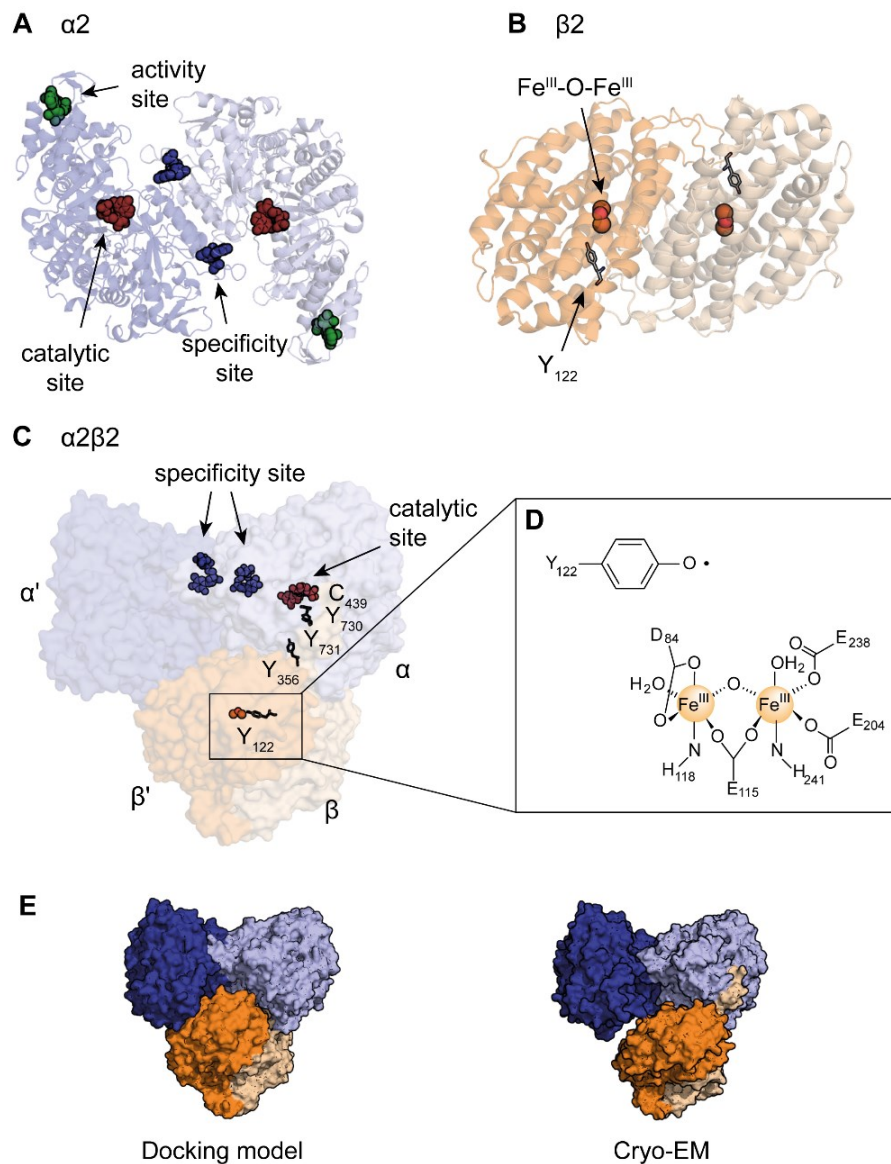


**Figure 1.4: Structure of the *E. coli* class Ia RNR.** (A) Crystal structure of the *E. coli* class Ia  $\alpha 2$  subunit with catalytic, activity, and specificity site highlighted in dark colors. Image was obtained by overlaying PDB structures 4R1R<sup>28</sup> and 3R1R<sup>28</sup>. (B) Crystal structure of the *E. coli*  $\beta 2$  subunit with  $\text{Y}_{122}$  and the diiron cluster highlighted. PDB: 5CI4<sup>35</sup>. (C)  $\alpha 2\beta 2$  complex assembly (PDB: 6W4X<sup>34</sup>) along with catalytically active residues. (D) Schematic representation of the diiron cofactor. (E) Docking model of the  $\alpha 2\beta 2$  complex assembly compared to the cryo-EM structure.

Previous studies on *E. coli* class Ia RNR demonstrated that the two subunits  $\alpha 2$  and  $\beta 2$  cannot be purified as a stable complex, and dissociation rate constants  $k_{\text{dissoc}}$  of 70 – 100  $\text{s}^{-1}$  were established.<sup>36–38</sup> Although  $\alpha 2\beta 2$  is formed transiently upon the catalytic reaction, the complex dissociates after each turnover. Therefore,  $\alpha 2\beta 2$ 's crystal structure remained elusive for a long time, and understanding the reaction mechanism was puzzling. Instead, a docking model of a 260 kDa  $\alpha 2\beta 2$  complex was used, based on shape

complementarity of  $\alpha 2$  and  $\beta 2$  individual crystal structures in agreement with experimental data.<sup>29</sup> 26 years later, a double mutant (F<sub>3</sub>Y<sub>122</sub>/E<sub>52</sub>Q- $\beta 2/\alpha 2$ ) brought the breakthrough, which forms a long-lived  $\alpha 2\beta 2$  complex and thus enabled the acquisition of a cryo-electron microscopy (cryo-EM) structure (see **Figure 1.4C**).<sup>34</sup> Interestingly, this structure indicates an asymmetry of the tetrameric complex, whereas the docking model presented a symmetrical one (**Figure 1.4E**). For the first time, this cryo-EM structure confirmed a long-assumed protein asymmetry that may be related to its half-site reactivity (see Section 1.5). Understanding these structural differences and their mechanistic implications is currently under investigation.

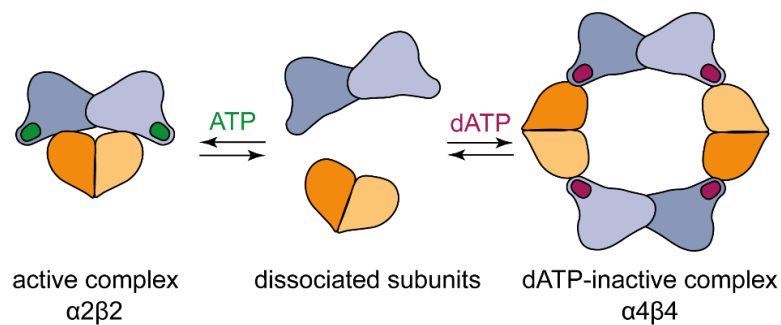


**Figure 1.5: Schematic representation of allosteric regulation of *E. coli* class Ia RNR via ATP and dATP binding.**  $\alpha 2$  is shown in blue and  $\beta 2$  in orange. Figure adapted from Brignole *et al.*<sup>39</sup> and Kang *et al.*<sup>34</sup>

### 1.3.2. The puzzle of the radical transfer pathway

The docking model and cryo-EM structure both propose a long distance of 35 and 32 Å between Y<sub>122</sub> and C<sub>439</sub>, respectively.<sup>29,34</sup> This represents an immense distance for a radical transfer, as most biological systems show a separation of up to 14 Å<sup>40</sup> between redox-active cofactors. Therefore, it was postulated early that other aromatic amino acids, such as tyrosine and tryptophan, must be involved in the transport pathway. Furthermore, it was proven that at physiological pH, Y or W oxidation requires the concerted movement of a proton and an electron, and thus the radical transfer was proposed to be realized via a series of PCET steps.<sup>41,42</sup> However, identifying the amino acid residues involved in this process is complex and has required multiple studies. A closer examination of the docking model led to four conserved amino acids (Y<sub>356</sub> and W<sub>48</sub> in  $\beta 2$ , Y<sub>731</sub> and Y<sub>730</sub> in  $\alpha 2$ ) as possible candidates.<sup>29</sup>

The location of Y<sub>356</sub> on the flexible C-terminal tail, whose structure is unresolved, complicates the determination of its role in the radical transport process. The distance between W<sub>48</sub> and Y<sub>731</sub> is estimated to be around 25 Å based on the docking model, which implies the involvement of the absolute conserved residue Y<sub>356</sub>, positioned between W<sub>48</sub> and Y<sub>731</sub>.<sup>41</sup> Activity assays showed that mutations at Y<sub>356</sub> render the protein inactive.<sup>43,44</sup> Participation of W<sub>48</sub> was suggested because of two observations. First, this residue is a strictly conserved amino acid at the interface. Second, W<sub>48</sub> was found to form an H-bond

network with D<sub>237</sub> and H<sub>118</sub>. W<sub>48</sub> highly resembles W<sub>191</sub> in cytochrome c oxidase, which forms a tryptophan radical intermediate during catalysis.<sup>45</sup> W<sub>48</sub>Y only offers residual activity; however, no direct evidence has been given for the participation of W<sub>48</sub> in the electron transfer of *E. coli* RNR until now.<sup>44</sup> Furthermore, mutation experiments of residues Y<sub>731</sub> and Y<sub>730</sub> to phenylalanine resulted in inactive enzymes but intact interaction of the individual subunits.<sup>46</sup> These studies laid the first foundation for a mechanistic hypothesis and so predicted a radical transfer reaction according to:



However, detection of radical intermediates along the pathway remained challenging, and it is believed that the main reason for the absence of spectroscopic detection in wild-type (wt) RNR is/are rate-limiting protein conformational change(s) upon substrate and allosteric effector binding ( $2 - 10 \text{ s}^{-1}$ ).<sup>47</sup> One strategy that in particular the Stubbe lab extensively used to manipulate these rate-limiting steps was the implementation of unnatural amino acids (UAAs) to study the PCET in RNR.

### 1.3.3. Unnatural amino acids help unravel the PCET mechanism

A standard tool for analyzing protein structure and function is the introduction of mutations into the secondary structure, which allows the identification of amino acid residues involved in catalysis and deciphering their role. However, the 20 canonical amino acids, which offer limited functional chemistries, restrict the pool of variations. Another technique used for around 20 years to circumvent these limitations is the utilization of unnatural amino acids, also called non-canonical amino acids (ncAAs), extending the genetic code and thus providing new physiochemical properties and experimental possibilities.<sup>48-50</sup> Over many years, the Stubbe lab has demonstrated numerous examples on *E. coli* class Ia RNR in which each of the involved pathway residues was site-specifically replaced with unnatural tyrosyl-analogs with altered pK<sub>a</sub>s or reduction potentials. Redox potentials are stated in relation to tyrosine with the reaction  $Y \rightarrow Y \bullet + e^- + H^+$ . A selection of employed UAAs is depicted in **Figure 1.6**. These non-canonical amino acids offer minimal structural changes compared to natural tyrosine, e.g., the van der Waals radius of fluorine atoms is only 0.15 Å larger than that for hydrogens.<sup>35</sup> Below are selected examples where the application of UAAs has led to remarkable progress in elucidating the PCET mechanism in *E. coli* class Ia RNR.

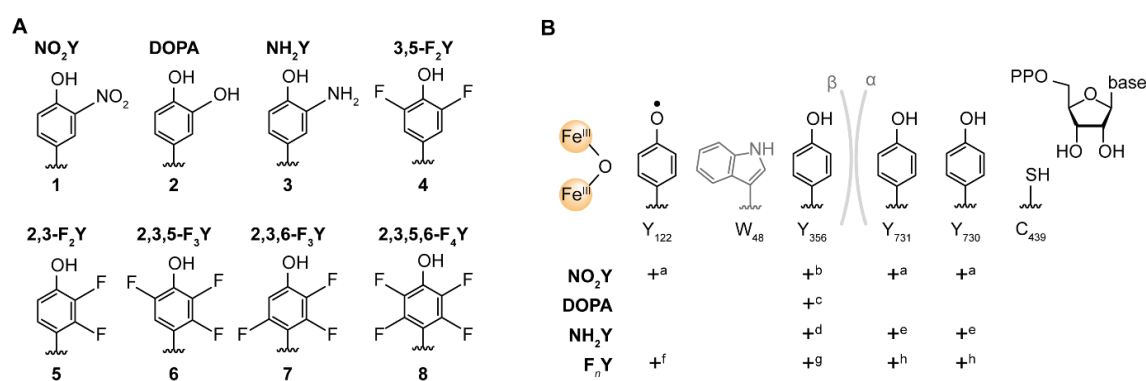


**Figure 1.6: Overview of UAA usage in RNR.** (A) UAAs incorporated into *E. coli* class Ia RNR. (B) Current state of amino acids involved in the PCET reaction, substituted by UAAs. As the role of  $\text{W}_{48}$  is unclear, it is shown in gray. Footnotes a-h specify respective references. Please note that the indicated literature is incomplete as only one example is given per UAA for clarity: a<sup>51</sup>, b<sup>52</sup>, c<sup>53</sup>, d<sup>54</sup>, e<sup>55</sup>, f<sup>56</sup>, g<sup>57</sup>, and h<sup>58</sup>. Figure adapted from Minnihan *et al.*<sup>42</sup>

The first remarkable example of UAA application as a radical trap in RNR concerns the role of  $\text{Y}_{356}$ . Using expressed protein ligation (EPL),  $\text{Y}_{356}$  was replaced with DOPA (**Figure 1.6, UAA 2**), which possesses a peak potential  $E_p$  of 260 mV lower than tyrosine at pH 7 but with comparable  $pK_a$ s.<sup>53</sup> This mutation results in a catalytically inactive protein. The reaction of  $\text{Y}_{356}\text{DOPA-}\beta 2$  with wt- $\alpha 2$  together with substrate and effector was monitored by stopped flow (SF) UV-Vis and electron paramagnetic resonance (EPR) spectroscopy. These experiments revealed a 50% reduction of  $\text{Y}_{122}\bullet$  and subsequent generation of  $\text{DOPA}_{356}\bullet$  in equal amounts.<sup>53</sup> Although these studies proved that  $\text{Y}_{356}$  must play a key role in the PCET, it was not understood at that time why only 50% of the primary  $\text{Y}_{122}\bullet$  was consumed. In the absence of wt- $\alpha 2$  or nucleotides, no  $\text{DOPA}_{356}\bullet$  was observed, implying that nucleotides are required to initiate the radical transfer process. Kinetics of  $\text{DOPA}_{356}\bullet$  formation revealed multiple phases, providing first information about rate constants for conformational changes. In the same year, findings of  $\text{F}_n\text{Y}_{356}$  mutation experiments were published, suggesting the application of these tyrosine analogs to change the rate-determining step from a physical one to the radical propagation step by tuning the reduction potential of  $\text{Y}_{356}\bullet$  via  $\text{F}_n\text{Ys}$ .<sup>59,60</sup> Differential pulsed voltammetry experiments of N-acetyl and C-amide protected  $\text{F}_n\text{Ys}$  unveiled peak potentials ranging from -50 to +270 mV relative to wt-Y in the pH region in which RNR activity can be measured, and  $pK_a$  values varying from 5.6 to 7.8. By increasing the number of fluorine atoms on the phenol ring and modifying its position, the  $pK_a$  and the redox potential can be varied systematically (**Figure 1.7**).

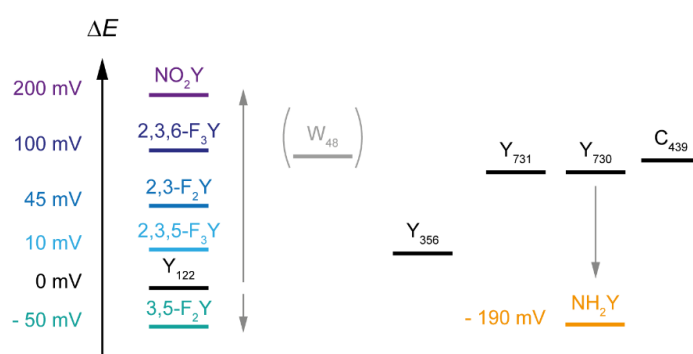


**Figure 1.7: Proposed relative reduction potentials of unnatural amino acids substituting residues on the radical transfer pathway in *E. coli* RNR.** Note that this scheme only estimates relative reduction potentials based on experimental observation. Absolute reduction potentials are not known. Figure adapted from Minnihhan *et al.*<sup>42</sup>

Further attempts were made to stabilize the radical on the pathway by using 3-aminotyrosine (**Figure 1.6**, UAA 3), whose peak potential was proposed to be 190 mV lower than for tyrosine.<sup>61</sup> The  $pK_a$  values of  $NH_2Y$  and  $Y$  are nearly identical.<sup>42</sup> This UAA was incorporated at positions 730 and 731 employing the *in vivo* nonsense suppression method (details in Section 1.4) since the larger size of the  $\alpha$  subunit and the location of the residues within the protein impede EPL.<sup>55,62</sup> Upon the reaction of  $NH_2Y$ - $\alpha 2s$  with wt- $\beta 2$  in the presence of CDP and ATP, a newly emerging EPR signal was assigned to  $NH_2Y\bullet$ . Accordingly,  $NH_2Y$  acts as a conformational probe and allows direct detection of the physical state analogous to DOPA. Surprisingly, the aminotyrosine-mutants retained residual activity, i.e., the ability of dNDP production. It was assumed that the decrease in reduction potential of  $NH_2Y$  relative to  $Y$  is insufficient to shut down the radical transfer entirely.<sup>42,54,55</sup> However, later experiments showed that catalytic activity of  $NH_2Y$ -RNR mutants is quite unlikely as the UAA acts as a deep thermodynamic trap. The residual activity could be attributed to tyrosines mis-incorporated in place of the UAA.<sup>63</sup> X-ray structures of  $Y_{730}NH_2Y$ - $\alpha 2$  and  $Y_{731}NH_2Y$ - $\alpha 2$  indicate only minimal structural changes relative to the wild-type enzyme with unusual stacked conformations of  $Y_{730}$  and  $Y_{731}$ .<sup>54</sup> Interestingly, a flipped conformation of  $Y_{731}$  was seen in  $Y_{730}NH_2Y$ - $\alpha 2s$  structure, which at this time was considered provocative as it assumed a not yet confirmed dynamic flexibility at the  $\alpha 2/\beta 2$  interface.

These examples impressively demonstrated that the non-canonical amino acids used as radical traps have massively contributed to elucidating the radical transport mechanism. Over time, EPR has established itself as a popular analysis method for these long-lived intermediates (e.g.,  $NH_2Y\bullet$ 's own  $t_{1/2s}$  on a minute scale).<sup>42</sup>

### 1.3.4. EPR measurements prove an $\alpha\beta\beta$ complex assembly

The formation of stable radical intermediates in *E. coli* RNR opened the path for in-depth analysis via advanced EPR methods. Because of its 'two or none' radical distribution and half-sites reactivity (explained in Section 1.5), the use of double electron-electron resonance (DEER) (Section 2.4.3), a spectroscopic method for determining distances between two paramagnetic centers, is particularly suitable for investigating *E. coli* class Ia RNR. First experiments of wt- $\beta\beta$  remarkably demonstrated the power of this technique by establishing a distance of  $3.31 \pm 0.2$  nm between the  $Y_{122}\bullet$ - $Y_{122}\bullet$  pair in the  $\beta\beta$  dimer,<sup>64</sup> which became a milestone of all current research. As the generation of  $DOPA_{356}\bullet$ ,  $NH_2Y_{731}\bullet$ , and  $NH_2Y_{730}\bullet$  resulted in 50% residual  $Y_{122}\bullet$ , a diagonal distance between  $Y_{122}\bullet$  and the other residues was measured next.<sup>65</sup> Especially for  $DOPA_{356}$ , these data provided the first structural constraint for  $Y_{356}$  in the active  $\alpha\beta\beta$  complex, whose location has so far remained unpredictable. The diagonal distances measured across the  $\alpha\beta\beta$  interface for  $Y_{122}\bullet$ - $NH_2Y_{731}\bullet$  and  $Y_{122}\bullet$ - $NH_2Y_{730}\bullet$  pairs with  $3.81 \pm 0.12$  and  $3.87 \pm 0.18$  nm, respectively, were in high agreement with those predicted from the docking model (3.85 and 4.01 nm) (**Figure 1.8**). These EPR-based distance measurements supported a long-range radical transfer mechanism.

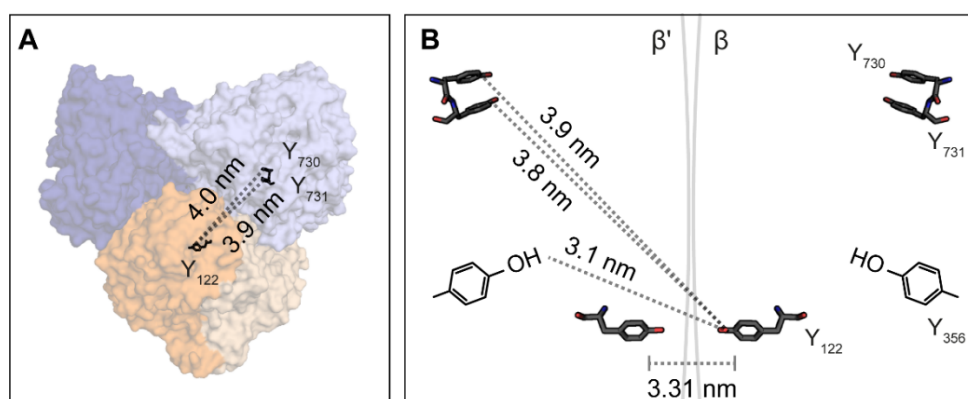


**Figure 1.8: Distances between redox-active amino acids in *E. coli* class Ia RNR.** Diagonal distances between redox-active amino acids in *E. coli* RNR, either predicted by the docking model (A) or obtained by DEER measurements (B) as shown by Seyedsayamdost *et al.*<sup>65</sup> Residues are only labeled in one subunit for clarity. As the position of  $Y_{356}$  is unknown, it is omitted in the docking model (A) and is only schematically visualized in (B). Please note that the illustration on the right is schematic, and distances are not to scale.

Direct evidence of the long distance that needs to be covered for  $C_{439}\bullet$  formation and substrate reduction was later provided by distance measurements using an inhibiting 2'-azido-2'-deoxynucleotide  $N_3NDP$  (shown in **Figure 1.9** as **1b**) that forms a long-lived nitrogen-centered radical  $N\bullet$  (**Figure 1.9** as **7**), covalently bound to  $C_{225}$  and the nucleotide in the active site of  $\alpha\beta$ .<sup>66,67</sup> Due to protein's half-site reactivity, radical transfer initially occurs within a single  $\alpha\beta$  pair, stopped by the inhibitor. The reaction results in one  $N\bullet$  formed per  $\alpha\beta\beta$  and one remaining  $Y_{122}\bullet$ . The employment of  $N_3UDP$  in

combination with DEER and double quantum coherence (DQC) spectroscopy confirmed a diagonal distance of  $4.8 \pm 0.1$  nm between  $Y_{122}\bullet$  and  $N\bullet$ , consistent with the docking model.<sup>68</sup> The absence of an  $N\bullet$ - $N\bullet$  distance highlights the inability of  $\alpha 2\beta 2$  to be catalytically active on both sites simultaneously.

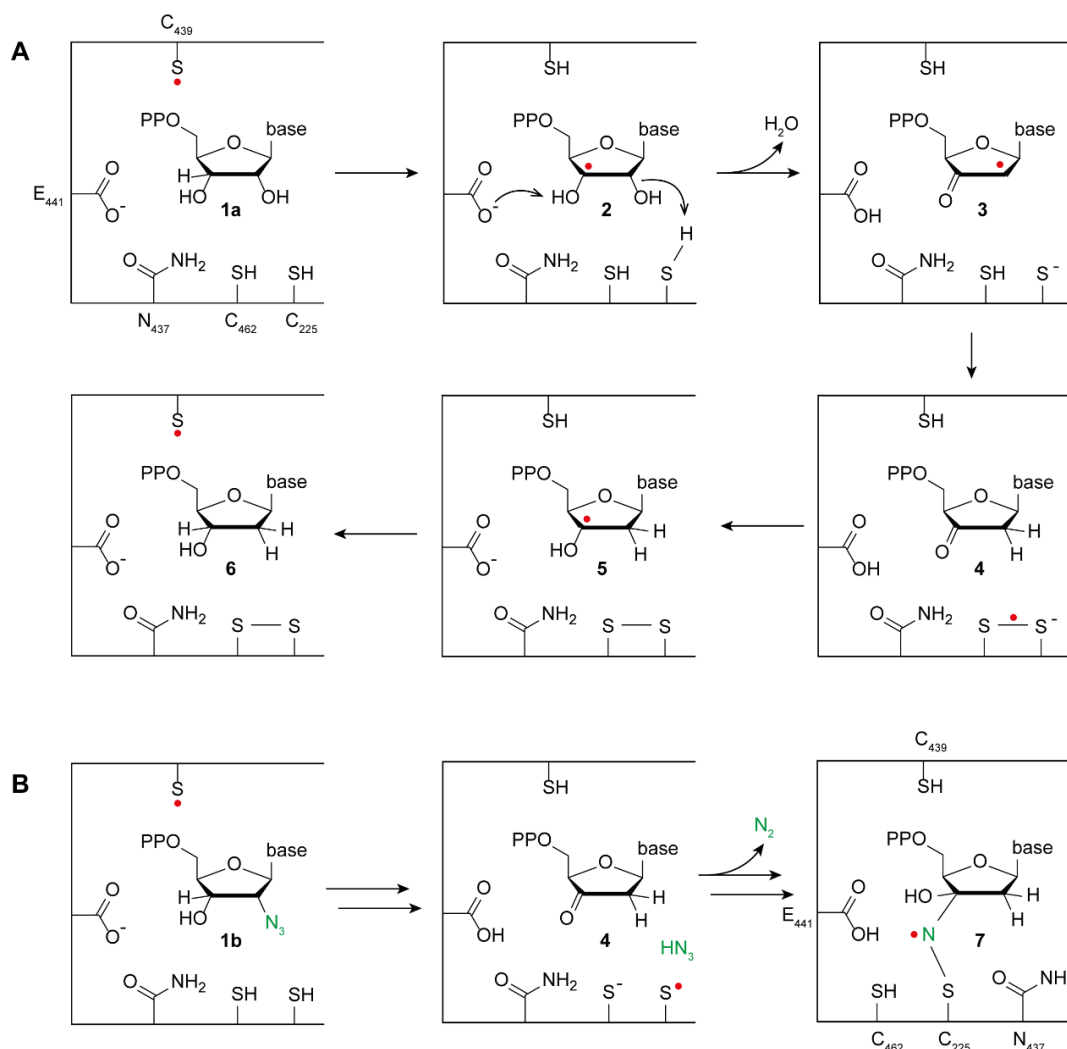


**Figure 1.9: *E. coli* class Ia RNR reaction mechanism.** (A) Schematic representation of the reaction catalyzed by *E. coli* RNR in the active site of  $\alpha 2$  in the presence of nucleotide **1a**. The reaction precedes via intermediates **2-5**, resulting in the deoxynucleotide **6**. (B) Proposed reaction scheme upon binding of 2'-azido-2'-deoxynucleotide **1b**. Nitrogen atoms of **1b** are shown in green. First, the intermediate **4** is formed according to the scheme presented in (A), followed by the formation of **7**, stated  $N\bullet$ . Details of the reaction mechanism were discussed by Fritscher *et al.*<sup>69</sup>

In addition to the fact that all these experiments support the assumption of  $\alpha 2\beta 2$  complex arrangement, they also provided information about the thermodynamic landscape of radical transfer. Potentials of  $Y_{122} < Y_{356} < Y_{731} \approx Y_{730} \leq C_{439}$  increase, driven by the irreversible loss of  $H_2O$  during nucleotide reduction.<sup>42,56,58</sup> With this knowledge at hand, particularly  $F_n Y_s$  with their ability to precisely tune  $pK_a$  values and the redox

potential were implemented to manipulate the rate-limiting steps during the PCET pathway.  $F_nY$ s incorporation thus allowed investigation of otherwise reactive intermediates. Especially the usage of 2,3,5- $F_3Y$  has been demonstrated as a useful radical trap during the PCET pathway.<sup>56,70</sup> If incorporated at position 122, the stable  $F_3Y_{122}\bullet$  is generated with a characteristic EPR lineshape, which is easily differentiable from the wild-type radical. This mutant is catalytically active and performs a single turnover reaction. However, due to its higher relative reduction potential of the UAA compared to  $wt-Y_{122}\bullet$ , the radical is trapped during the reverse radical transfer at position 356 (**Figure 1.10A**). This method of trapping  $Y_{356}\bullet$  allows spectroscopic characterization of the intermediate without the need to introduce specific tyrosine analogs at position 356. Furthermore,  $Y_{356}\bullet$  was generated by the reaction of  $F_3Y_{122}-\beta_2$  with either  $Y_{731}F-\alpha_2$  or  $Y_{730}F-\alpha_2$ . In contrast to  $Y_{356}\bullet$  generated with  $wt-\alpha_2$  during the reverse radical transfer, these mutants allowed  $Y_{356}\bullet$  formation during the forward radical transfer (**Figure 1.10B**).

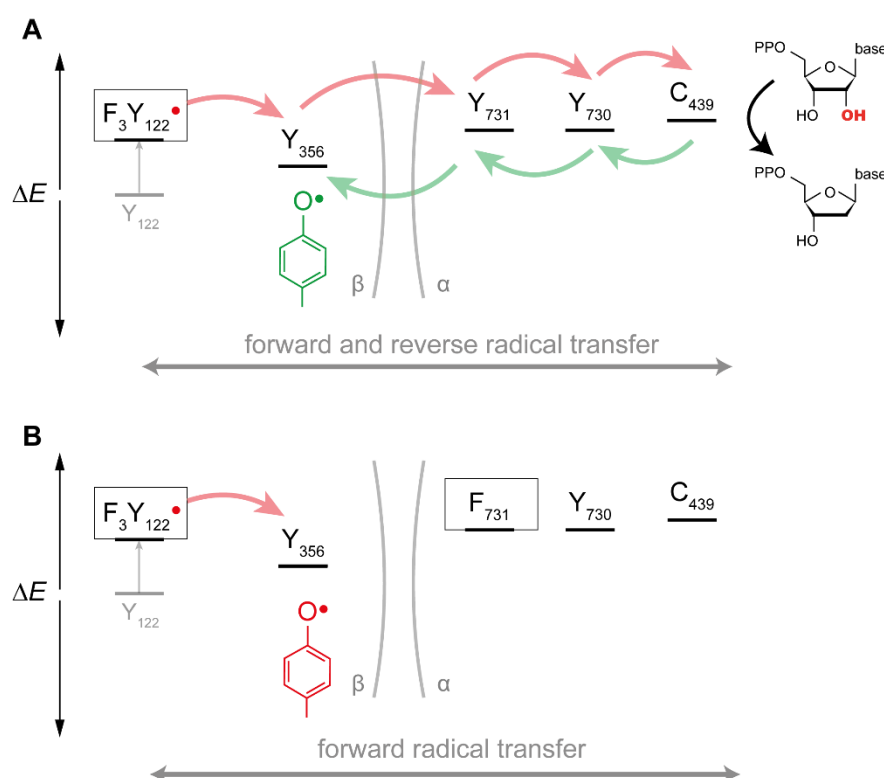


**Figure 1.10: Estimated relative reduction potentials of residues involved in the radical transfer mechanism.** Mutations are highlighted in black boxes. Introduction of  $F_3Y_{122}$  into  $\beta_2$  allows trapping during the reverse radical transfer (A), whereas the additional mutation  $Y_{731}F$  in  $\alpha_2$  blocks the forward radical transfer (B). Both pathways result in the trapping of  $Y_{356}\bullet$ .

Multi-frequency EPR investigations up to 263 GHz allowed accurate resolution of  $g$ - and hyperfine coupling values of  $Y_{356}\bullet$ . All trapped radical intermediates revealed shifted  $g_x$  values with regard to other known  $Y\bullet$  signals. The determined  $g_x$  of 2.00619 was “one of

the lowest  $g_x$  values reported so far<sup>70</sup>. As a comparison,  $Y_{122}\bullet$  has a  $g_x$  of 2.00915 according to the latest 263 GHz EPR experiments.<sup>71</sup> This shift indicates a strong polar environment with strong H-bonds near the phenolic oxygen atom of  $Y_{122}$ . One advanced EPR method often used for probing hydrogen bonds is electron-nuclear double resonance (ENDOR) spectroscopy (explained in Section 2.4.4). ENDOR experiments indicated that  $Y_{356}\bullet$  forms (at least) one moderate H-bond arising from a cluster of water molecules involved in the PCET reaction.<sup>70,72</sup> Furthermore, the radical intermediates generated via different mutants revealed different  $g_x$  values.  $Y_{356}\bullet(\text{wt-}\alpha 2)$  and  $Y_{356}\bullet(Y_{730}\text{F-}\alpha 2)$  both showed the described  $g_x$  value of 2.00619. In contrast,  $Y_{356}\bullet(Y_{731}\text{F-}\alpha 2)$  showed a second resolved  $g_x$  value at 2.00720, indicating the presence of a radical species in a distinct local environment. It was concluded that the presence of the distinct species depends on the ability to communicate between residues  $Y_{356}$  and  $Y_{731}$  via H-bonds across the subunit interface. These studies demonstrated the importance of structured water molecules for the radical transfer mechanism in *E. coli* class Ia RNR.

Another issue that EPR helped to clarify was the flipped conformation of  $Y_{731}$  predicted from the crystal structure. DEER studies on the  $\text{NH}_2Y_{731}/\text{R}_{411}\text{A-}\alpha 2$  double mutant unmasked the first experimental evidence for a  $Y_{731}$  conformer flipped towards the  $\alpha 2/\beta 2$  interface.<sup>73</sup> Two distinct distances of 3.9 and 3.5 nm were detected for the  $Y_{122}\bullet\text{-NH}_2Y_{731}\bullet$  pair, indicating that  $Y_{731}$  can adapt a stacked and a flipped conformation relative to  $Y_{730}$ . However, the shorter distance could only be obtained in the presence of the additional  $\text{R}_{411}\text{A}$  mutation. Orientation-selective  $^{19}\text{F}$  ENDOR measurements performed at  $\alpha/\beta$  pairs of 3,5- $\text{F}_2Y_{731}\text{-}\alpha 2$  with either 2,3,5- $\text{F}_3Y_{122}\text{-}\beta 2$  or  $\text{E}_{52}\text{Q}/\text{F}_3Y_{122}\text{-}\beta 2$  allowed determination of the interspin distance and orientation between  $Y_{356}\bullet$  and the  $^{19}\text{F}$  atoms of  $\text{F}_2Y_{731}$ .<sup>74</sup> In both cases, presence of a flipped  $Y_{731}$  conformation was confirmed, suggesting that the flexibility of this residue might be a crucial element for the communication during PCET. It is currently assumed that the PCET first takes place between  $Y_{356}$  and  $Y_{731}$ , while the following transfer to  $Y_{730}$  requires a conformational change as this transfer occurs in the stacked conformation of  $Y_{731}/Y_{730}$ .<sup>74</sup> The combination of these examples with numerous other studies eventually led to the current model of PCET mechanism in *E. coli* class Ia RNR, as represented in **Figure 1.11**.

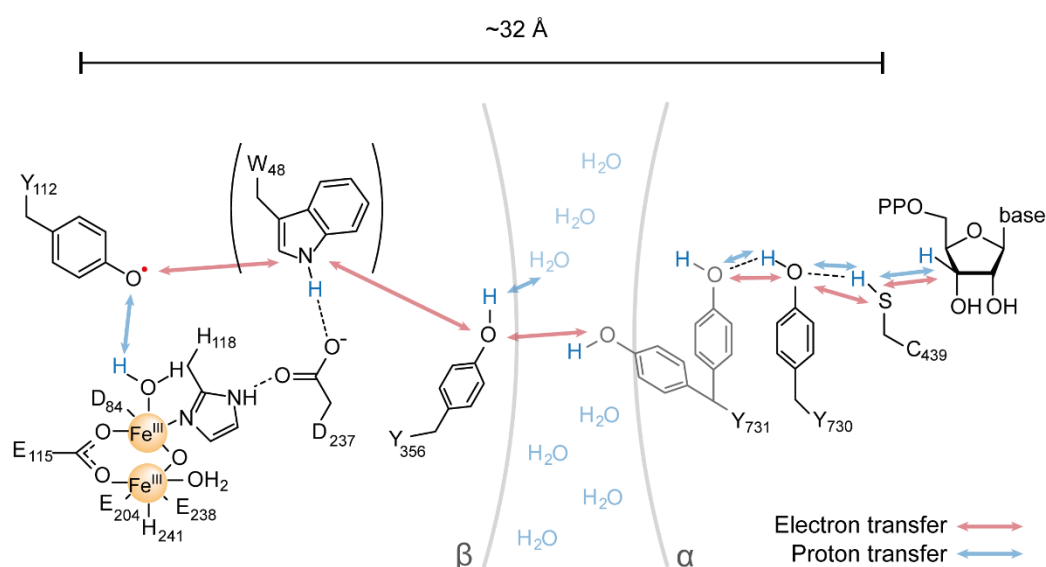


**Figure 1.11: Current model of the radical transfer pathway in *E. coli* class Ia RNR, including redox-active amino acids Y<sub>122</sub>, Y<sub>356</sub>, Y<sub>731</sub>, Y<sub>730</sub>, and C<sub>439</sub>.** W<sub>48</sub> in β2 is believed to donate an electron during the cofactor assembly reaction and is therefore indicated in brackets. Y<sub>731</sub> was shown to adopt two different conformations, depicted in grey each. Y<sub>122</sub>• is separated by about 32 Å from the active site, according to the latest cryo-EM structure.<sup>34</sup>

#### 1.4. Incorporation procedure of unnatural amino acids

More than 200 UAAs with specific characteristics were designed over the years, and many approaches for effective *in vivo* or *in vitro* incorporation were developed.<sup>75,76</sup> The introduction of UAAs can be performed via expressed protein ligation or, more commonly, via the nonsense-codon suppressor tRNA method.<sup>77</sup> EPL is based on intein-mediated self-splicing of the product.<sup>78</sup> The latter method does not require splicing but two key components of the protein synthetic machinery (**Figure 1.12**).<sup>49,50</sup>

First, a codon that is not used by naturally occurring amino acids and can exclusively be employed for the non-canonical amino acid is needed. Therefore, a stop codon is commonly utilized, which is least used in the expression organism. For *E. coli* and yeast, the amber stop codon TAG is the first choice among the three existing ones. Using TAG thus ideally prevents growth perturbation of the host organism. The stop codon usage was expanded lately so that even two different unnatural amino acids can be incorporated at distinct sites in the same protein by a combination of amber and frameshift codons (e.g., TAG and AGGA).<sup>79</sup>

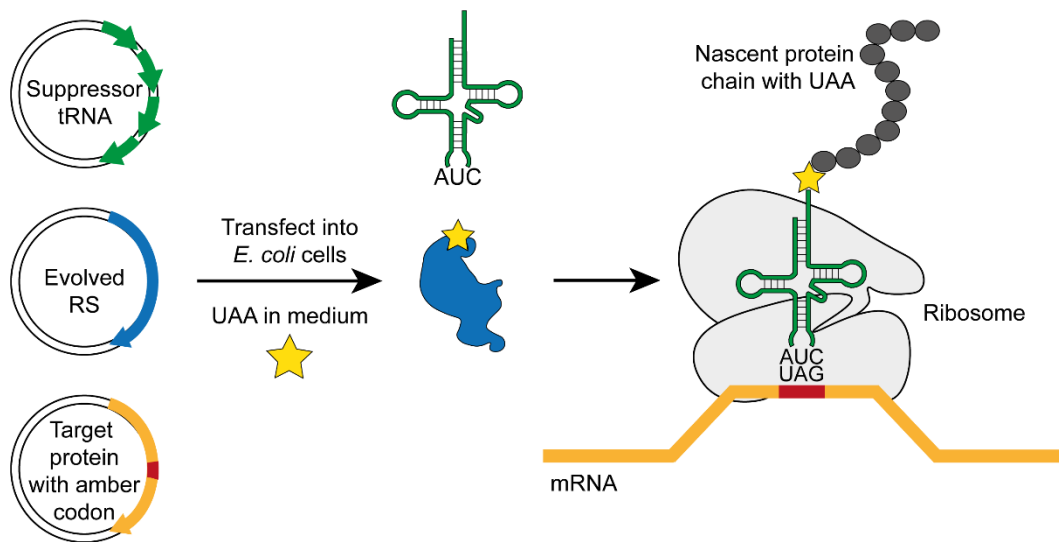


**Figure 1.12: Unnatural amino acid incorporation through *in vivo* nonsense codon suppression method.** Plasmids containing suppressor tRNA (green), an evolved tRNA synthetase (RS) (blue), and the targeted gene (orange), modified with the amber stop codon (red), are transfected into *E. coli* cells. Cells are grown in UAA-containing medium. RS loads the tRNA with the respective UAA (yellow star). The ribosome (grey) recognizes the nonsense codon within the mRNA of the gene of interest and uses the charged tRNA to site-specifically incorporate the unnatural amino acid into the nascent protein chain.

Second, an orthogonal tRNA-aminoacyl/tRNA synthetase pair is required. The tRNA recognizes the stop codon and will be loaded with the amino acid of interest by the tRNA synthetase (RS). This orthogonal tRNA-synthetase can often be derived from a different organism with distinct recognition elements, which therefore do not cross-react with endogenous synthetases. For *E. coli*, the first orthogonal tRNA-synthetase pair was derived from an archaeal tyrosyl-tRNA synthetase pair from *Methanococcus jannaschii*.<sup>49,50</sup> The evolution of this tRNA-synthetase pair has allowed over 20 UAAs to be incorporated via expression in *E. coli*.<sup>80</sup> Further variants of these tRNA pairs were developed and validated by detailed positive and negative selection criteria, leading to altered synthetase specificity.<sup>81</sup> Positive selection turns are conducted in the presence of UAA and synthetase. Therefore, an amber codon is placed in a drug-resistance gene at a nonessential position, allowing the selection of tRNAs/RS pairs by their ability to insert an amino acid in response to the used stop codon. Cells with non-functional tRNA or tRNAs not recognized by RS will be sensitive to the selected antibiotic. Next, in the negative selection, an amber codon is introduced in a toxic gene at a nonessential position and carried out in the absence of UAA and/or synthetase. Often the toxicity of barnase is tested for selection in *E. coli*. When the selected tRNA is aminoacylated by endogenous *E. coli* synthetases, the amber codon is suppressed, and the toxic product barnase leads to cell death. Cell death also results if the tRNA is incorrectly loaded with a naturally occurring amino acid in the absence of UAA. Thus, only cells that do harbor an orthogonal tRNA charged with the desired UAA will survive. On average, three to

six rounds of selection are required to find a tRNA/RS pair that meets the criteria for orthogonality. The evolution theoretically enables the introduction of any unnatural amino acid into a target protein. With the right choice of the two components described, such incorporation is highly efficient. In the event of incorrect or missing incorporation of the UAA, the translation will be aborted, resulting in truncated protein. The modified protein can be easily separated via size exclusion chromatography during protein purification.

### 1.5. Radical distribution and half-sites reactivity in *E. coli* RNR

Through a series of experiments, insights were gained into two mechanistic characteristics of *E. coli* class Ia RNR. The first point concerns the radical distribution of  $Y_{122}\bullet$  in the  $\beta_2$  subunit. The diferric- $Y\bullet$  cofactor can be reconstituted in two different ways. Either, this involves the addition of ferrous ammonium sulfate and sodium ascorbate to the cell-free extract prior to  $\beta_2$  purification. Instead,  $\beta_2$  can also be purified in the apo form, and subsequently, the cofactor can be self-assembled by treatment with ferrous ammonium sulfate and  $O_2$ . In both cases, the optimized process results in  $3.6 Fe^{III}/\beta_2$  and  $1.2 Y\bullet/\beta_2$ . The reason why maximum loading is not reached, namely  $4 Fe^{III}/\beta_2$  and  $2 Y\bullet/\beta_2$ , remains hidden. For  $F_3Y_{122}\text{-}\beta_2$ , apo-purification and subsequent cofactor yielded ca.  $0.8 F_3Y\bullet/\beta_2$ .<sup>82</sup> Monitoring the reaction of  $F_3Y_{122}\text{-}\beta_2$  with wt- $\alpha_2$  by rapid freeze-quench (RFQ) EPR unraveled, that 50% of the initial  $F_3Y\bullet$  was converted to  $Y_{356}\bullet$ , regardless of the radical yield used in the sample. These results provided evidence for a ‘two or none’ radical distribution in the  $\beta_2$  subunit of *E. coli* RNR.<sup>82</sup> This means a sample with a radical yield of  $1.2 Y\bullet/\beta_2$  consists of 60% active  $\beta_2$  dimers and 40% inactive ones. (**Figure 1.13**). Consequently, dimers with only one radical do not exist. For  $F_3Y_{122}$ , 40% active and 60% inactive ones are present reversely.

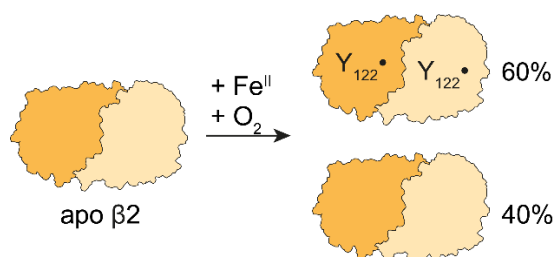


**Figure 1.13: Two or none radical distribution in *E. coli* class Ia RNR.** Accordingly, wt- $\beta_2$  with  $1.2 Y\bullet/\beta_2$  consists of 60% active and 40% inactive dimers.

The second observation concerns RNR's reaction mechanism. All experimental results, such as those obtained by radical traps or  $N_3UDP$ , indicate that only one of the two possible  $Y_{122}\bullet$ s in  $\alpha_2\beta_2$  reacts simultaneously. This observation was denoted as half-site

reactivity of the protein. A model for the reaction mechanisms has manifested, starting with the association of  $\alpha_2$  and  $\beta_2$  pairs to form a symmetric  $\alpha_2\beta_2$  complex. Conformational gating then leads to an asymmetric structure in which only one  $\alpha/\beta$  pair initiates the catalysis, here termed  $\alpha'$  and  $\beta'$  (**Figure 1.14**). After reverse PCET and product release, conformational changes enable the second  $\alpha/\beta$  pair to start the radical transfer and hence the second turnover. Such a process results in  $2 \text{ dNDPs}/\alpha_2$ . While  $\beta_2$  returns to its original state containing two  $\text{Y}_{122}\bullet$ s, the alpha subunit is consumed since residues  $\text{C}_{225}$  and  $\text{C}_{462}$  have been oxidized to form a disulfide bond.<sup>83,84</sup>  $\text{C}_{754}$  and  $\text{C}_{759}$ , located on the C-terminal tail of  $\alpha_2$ , aid in rereduction of the active site disulfide.<sup>47</sup> Afterward, it is suggested that the individual subunits dissociate and reassociate, followed by a third and fourth turnover. In the absence of an endogenous reduction agent, a maximum of 4 dNDPs per  $\alpha_2$  can thus be formed during a complete turnover. A detailed overview of the individual reaction steps and their kinetics is given by Ravichandran *et al.*<sup>37</sup> The occurrence of an asymmetric reaction process in contrast to a symmetrical  $\alpha_2\beta_2$  structure predicted by the docking model appeared conflicting for a long time. However, the recently obtained cryo-EM structure of a trapped active complex directly supports this asymmetric behavior by its asymmetric structure.<sup>34</sup>

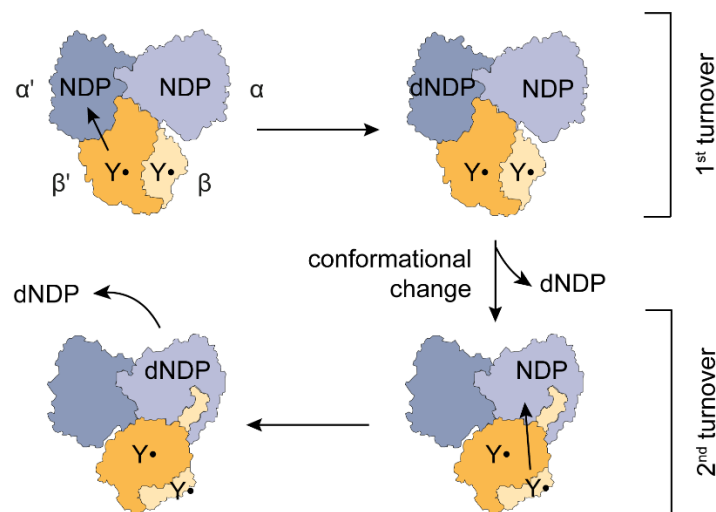


**Figure 1.14: Schematic representation of the half-sites reactivity in *E. coli* RNR.** The radical transfer (and thus catalysis) first occurs within a single  $\alpha/\beta$  pair ( $\alpha'$  and  $\beta'$ ), followed by conformational changes and product release (first turnover). Subsequently, the second  $\alpha/\beta$  pair performs the catalysis (second turnover). Figure adapted from Kang *et al.*<sup>34</sup>

## 1.6. The diiron cofactor assembly

Apart from the regulation maintained by  $\alpha 4\beta 4$  complex formation, a far less understood regulatory machinery is the metallocofactor assembly in ribonucleotide reductase. Correlations between  $Y\bullet$  levels and protein activity were found for *Saccharomyces cerevisiae* (*S. cerevisiae*) and *E. coli* RNR, both class Ia enzymes.<sup>85</sup> In *E. coli*, the essential cofactor can be obtained from the apo enzyme *in vitro* by adding  $Fe^{II}$ . After discovering this option of cofactor reconstitution, three methods were frequently employed to unravel the cofactor assembly *in vitro*: SF UV/Vis, RFQ-EPR, and RFQ Mössbauer spectroscopy. These studies revealed that an extra electron is required for the four-electron reduction of  $O_2$ , along with the three electrons resulting from the oxidation of  $Y_{122}$  and 2  $Fe^{II}$ s.<sup>86–88</sup>



The missing reducing equivalent can be provided by another  $Fe^{II}$  atom, resulting in 3 equivalents of  $Fe^{II}$  needed to yield one mole of  $Y_{122}\bullet$ . In practice, a maximum iron loading efficiency of 3.2 – 3.6  $Fe^{III}/\beta 2$  is reached by this process, and thus the use of 5 equivalents  $Fe^{II}/apo-\beta 2$  has been established for a successful radical formation.<sup>88</sup> The diiron cofactor is coordinated by four carboxylate and two histidine ligands, buried inside the protein, and thus protected from solvent.<sup>89</sup> Yet, an internal hydrophobic cavity and an open coordination site propose possible access for  $O_2$ . The oxygen is rapidly added to the  $Fe^{II}Fe^{II}$  center, resulting in a short-lived  $\mu$ -peroxo- $Fe^{III}Fe^{III}$  intermediate.<sup>90,91</sup> The solvent-accessible tryptophan  $W_{48}$  helps to cleave the peroxide unit by providing an electron, forming a  $W_{48}^+\bullet$  and a  $Fe^{IV}Fe^{III}$  center, entitled intermediate X.<sup>92–94</sup> This transient high-oxidation state intermediate X is formed with a rate constant of  $8 s^{-1}$  and degrades with a rate constant of  $1 s^{-1}$  according to kinetic analysis.<sup>86</sup> The rate constant for the decomposition of X is in the same range as the one for  $Y_{122}\bullet$  formation. While  $W_{48}^+\bullet$  is rapidly reduced by an external reductant ( $Fe^{II}$ , ascorbate, thiols), X is converted to the  $\mu$ -oxo- $Fe^{III}Fe^{III}$  cofactor, oxidizing the adjacent tyrosine to  $Y_{122}\bullet$ .

Free  $Fe^{II}$  is most likely not the additional electron donor inside living cells since  $Fe^{II}$  *in vivo* is highly reactive and would have to be chelated and maintained. Hence, the intracellular cofactor assembly most probably involves a biosynthetic pathway. A ferredoxin encoding gene was found by bioinformatic studies located downstream of *nrdB*.<sup>95</sup> This gene encodes for YfeE in *E. coli* which is supposed to be involved in the metallocofactor biosynthetic or maintenance pathway *in vivo*.

Furthermore, the two iron binding sites within a single  $\beta$  monomer exhibit different binding affinities. The  $Fe_B$  site, which is 8.3 Å away from  $Y_{122}$ , has an approximately 5-fold higher binding affinity for  $Fe^{II}$  than the  $Fe_A$  site, located 5.3 Å away from  $Y_{122}$ .<sup>96,97</sup> However, the  $Fe^{III}Fe^{III}$  center is inaccessible for EPR spectroscopy due to strong antiferromagnetic exchange coupling between the two metal sites.<sup>98</sup> In order to

investigate the cofactor formation via EPR spectroscopy,  $\text{Mn}^{\text{II}}$  was chosen as a paramagnetic substituent for  $\text{Fe}^{\text{II}}$ , which has also been shown to bind to the protein metal binding sites with a similar ligand environment.<sup>99,100</sup> Depending on the experimental conditions, either noncooperative or anticooperative binding behavior was observed. The first case occurred at a high glycerol concentration (20%) in the buffer, whereas metal binding in both  $\text{Fe}_B$  sites of the  $\beta_2$  dimer was observed prior to  $\text{Fe}_A$  loading.<sup>99</sup> In the next step, the  $\text{Fe}_A$  sites become metal-loaded so that binding of 4  $\text{Mn}^{\text{II}}/\beta_2$  is achieved. In the second model, where 5% glycerol was used, one  $\text{Fe}_B$  binding site on one side of the dimer ( $\beta_{\text{I}}$ ) is first occupied by  $\text{Mn}^{\text{II}}$ , followed by the  $\text{Fe}_A$  site in the same dimer half. The other half of the dimer ( $\beta_{\text{II}}$ ) remained metal-free, reaching a maximum of 2  $\text{Mn}^{\text{II}}/\beta_2$ . In both cases, manganese-loaded subunits were unable to form  $\text{Y}_{122}\bullet$ . Based on these findings for anticooperative binding, it was hypothesized that once the protein is able to form intermediate X, it is in such a conformation that favors metal binding in  $\beta_{\text{II}}$ .<sup>90,100</sup> Details of the metal binding mechanism and its mechanistic implications, also with regard to activity regulation, are still uncertain.

### 1.7. Class Ia ribonucleotide reductase *in vivo*

Overall, data concerning *in vivo* experiments on RNR are relatively sparse. A general reason for this could be that endogenous RNR levels are below the detection limit for most spectroscopic methods, so overexpression of the protein inside the host is necessary.<sup>101</sup> First attempts to identify the free radical's nature in *E. coli* RNR were carried out in the *E. coli* strain KK546, allowing overproduction of the target protein with subsequent EPR characterization.<sup>102,103</sup> The use of [ $\beta,\beta$ -<sup>2</sup>H]tyrosine<sup>102</sup> and uniformly labeled <sup>13</sup>C-tyrosine<sup>103</sup> allowed to identify a tyrosine residue located in  $\beta_2$  being responsible for the protein's characteristic EPR spectrum, which provided the first steps toward simulations and interpretations of the radical species.

The class Ia radical is somewhat unstable as it degrades within minutes to days at most, depending on the organism, and can also be scavenged by small molecules such as hydroxyurea. Disappearance of the tyrosyl radical  $\text{Y}_{122}\bullet$  leads to the inactive met- $\beta_2$ , with the diferric cluster being present but  $\text{Y}_{122}$  being reduced. However, it is known that radical concentration and protein activity correlate, raising the question of a maintenance pathway required in the cells. Inspired by this question, radical yields and iron-loading efficiencies were compared in *S. cerevisiae* and *E. coli* cells and crude cell extracts.<sup>85,101</sup> Strikingly, the two organisms showed different characteristics. While for *S. cerevisiae*, the cells owned almost stoichiometric amounts of  $\text{Y}\bullet$  and diiron cluster per  $\beta$  subunit, *E. coli* exhibited substoichiometric radical yields. Even though low levels of  $\text{Y}\bullet$  were observed in *E. coli* (max. 0.25  $\text{Y}\bullet/\beta$ ), the protein was almost completely loaded with iron. Titration of the crude cell extract with reduced YfeE led to a surprisingly high cofactor assembly efficiency, namely 2  $\text{Y}\bullet/\beta_2$  and 4  $\text{Fe}/\beta_2$ . These findings suggest a

regulatory mechanism in *E. coli*, which might reduce  $Y\bullet$  levels and downregulate RNR activity if needed and vice versa. In contrast, results of *S. cerevisiae* indicated that diferric  $Y\bullet$ -cofactor concentrations are not regulated as a function of the cell cycle and thus are not involved in RNR activity regulation in the cell. Although both enzymes belong to the same class, they hold a different cofactor distribution. While in *E. coli*, the active enzyme is formed by the homodimeric  $\beta_2$ , *S. cerevisiae* RNR consists of the heterodimeric  $\beta\beta'$ .<sup>104,105</sup> Compared to  $\beta$ , three of the six amino acids involved in iron binding are mutated in  $\beta'$ , resulting in a maximum of 1  $Y\bullet/\beta\beta'$ .<sup>85,106</sup> Possible connections between these different radical distributions and their effect on activity regulation have not been clarified yet.

## Motivation

### Problem

Its central role in DNA replication and repair and its unusual catalytic mechanism made ribonucleotide reductases an attractive research target for biochemical and medical applications. RNR reflects an outstanding example of a long-range radical transfer mechanism in proteins and, in addition, is a highly regulated enzyme. Although much information and studies are already available, the basic processes, including PCET, cofactor assembly, and its regulation (especially *in vivo*), are still only partially understood. In order to target these processes for drug development, especially in human RNR, the underlying mechanism must be clarified. An excellent prototype model for this purpose is the *E. coli* RNR, which represents a paradigm for class Ia enzymes, including the human one. The *E. coli* protein is by far the best characterized one of the RNR family and is also easily accessible by expression in its original host organism.

### Objective

This work aims to gain further knowledge on the various exciting areas of RNR research, especially with regard to in-cell studies, and seeks to develop strategies to overcome these challenges by using primarily EPR spectroscopy in combination with other methods such as UV-Vis or high pressure. The in-cell EPR studies on a native paramagnetic center will be the first of their kind, delivering unique insight into the structure and regulation of *E. coli* RNR inside living cells.

### Chapter overview

First, the basic theoretical principles and methodologies of EPR spectroscopy are discussed in **Chapter 2**. These principles find their application in the following Chapters.

**Chapter 3** focuses on the in-cell characterization of the stable tyrosyl radical in *E. coli* RNR. To understand mechanistic details in the cells, in-depth characterization of the *in vivo* protein structure is certainly needed first. The intrinsically occurring tyrosine radical at position 122 is the perfect starting point for this type of study as it represents the first step in the PCET mechanism. A few X-band in-cell spectra of  $Y_{122}\bullet$  have been presented earlier,<sup>101–103</sup> yet a detailed spectroscopic EPR characterization is missing. Therefore, multi-frequency EPR and ENDOR spectroscopy are employed in this work to probe the structure and electrostatic environment of  $Y_{122}\bullet$ . Furthermore, orientation-selective DEER distance measurements are utilized to examine  $Y_{122}\bullet$ - $Y_{122}\bullet$  pairs in the cell and to conclude on  $\beta 2$  in-cell structure. Moreover, these studies address the radical distribution in the cells.

Studies on the in-cell radical distribution directly led to the next question concerning the influence of different metal ions (in particular manganese and iron) on the cofactor assembly and regulation of RNR inside the cell. The metallocofactor assembly mechanism has only been studied *in vitro* so far. However, different metals present in the cell might interfere with the correct cofactor assembly. In **Chapter 4**, DEER measurements are used primarily to demonstrate how mismetallation occurs in the protein and whether this process is reversible. These results revealed an unprecedented asymmetric cofactor assembly *in vitro* and *in vivo*, consistent with protein asymmetry and half-sites reactivity.

Conformational changes accompanying processes such as mismetallation or PCET can generally be detected by performing EPR distance measurements in combination with spin labeling. However, the existing spin labels are not optimal for this purpose. Hence, **Chapter 5** outlines the development of a new, rigid spin label suited for in-cell distance measurements. The  $\beta 2$  subunit of *E. coli* RNR is thereby used as a model, although this spin label can be introduced in all other existing proteins. First, the dimeric  $\beta 2$  requires only one labeling site per subunit, and second the expected distance between a Y<sub>122</sub>-Y<sub>122</sub> pair has been thoroughly described in Chapter 3, which makes this protein a suitable candidate as a model system.

In **Chapter 6**, *E. coli* RNR is investigated under high pressures up to 4 kbar by using a home-built high-pressure EPR setup. Pressure can be used to convert native to excited conformational states in protein structures. The aim is thus to artificially induce structural intermediate states in RNR that might play a role during PCET. Since the high-pressure setup is new and RNR has never been examined under pressure, this part of the thesis is intended more as a proof of concept for pressure studies on RNR.

**Chapter 7** is independent of RNR studies and provides insights into a completely different area of chemistry, for which EPR can also serve as an excellent tool. One-electron photoreduction is used to generate a fullerene anion radical C<sub>60</sub>•<sup>-</sup> inside a molecular coordination cage. Subsequently, the formed radical species is analyzed by X-band cw-EPR, and its lifetime is determined. The EPR results are supported by UV-Vis NIR studies.

**Chapter 8** lists all materials and standard methods, such as protein expression and purification and standard EPR pulse sequences. As soon as changes have been made to the standard methods, they are mentioned in the materials and methods section of the respective chapter. Furthermore, methods that were only used for specific tasks in individual chapters are not mentioned in Chapter 8. Their descriptions can also be found in the corresponding section of the specific chapter.

# 2.

## Theoretical background

---

Electron paramagnetic resonance, also called electron spin resonance (ESR) spectroscopy, is an essential and selective tool to investigate systems carrying paramagnetic centers such as radicals or certain transition metal ions. This technique has been widely used for elucidating the structure and function of biomolecules, particularly proteins. In EPR, the resonant absorption of electromagnetic radiation by the paramagnetic center is measured in the presence of an external magnetic field. Different techniques, such as continuous wave (cw) EPR (see Section 2.3) and pulse EPR (Section 2.4), offer distinct experimental conditions and thus provide a variety of information. Furthermore, advanced pulse methods offer various techniques to study electron spin interactions and their environment. For example, long-range interactions such as dipole-dipole coupling between two electron spins are routinely studied via DEER (Section 2.4.3), whereas local interactions of an electron spin with surrounding magnetic nuclei can be probed by ENDOR spectroscopy (Section 2.4.4).

### 2.1. EPR theory

Electrons have an intrinsic angular momentum  $\mathbf{S}$ , also called electron spin, which is a quantum-mechanical entity without a classical analog.\* The angular momentum is linked to a magnetic moment  $\boldsymbol{\mu}_e$  via the electron gyromagnetic ratio  $\gamma_e$

$$\boldsymbol{\mu}_e = \gamma_e \mathbf{S}. \quad (2.1)$$

The gyromagnetic ratio is thus a proportionality factor and can be further expressed by the  $g$ -value of a free electron ( $g_e = 2.002319315$ )<sup>107</sup>, the Bohr magneton  $\mu_B$ , and the reduced Planck constant  $\hbar = h/2\pi$  as

---

\* Vectors and matrices are indicated in bold within this thesis.

$$\gamma_e = -\frac{g_e \mu_B}{\hbar}. \quad (2.2)$$

The spin state of an electron is described by two quantum numbers: the spin quantum number  $S$ , and the magnetic spin quantum number  $m_S$ . For one unpaired electron,  $S$  equals  $1/2$  and  $m_S$  can take the values of  $\pm 1/2$ . If an external magnetic field  $\mathbf{B}_0 = (0, 0, B_0)$  is applied, the electron spin vector is spatially quantized and aligns parallel ( $\alpha$  state) or antiparallel ( $\beta$  state) to the magnetic field. The z-component of the spin vector  $S_z$  can thus be described as

$$S_z = m_S \hbar \quad (2.3)$$

and the magnetic moment takes two discrete values

$$\mu_{e,z} = -\frac{g_e \mu_B}{\hbar} m_S \hbar = \pm \frac{1}{2} g_e \mu_B. \quad (2.4)$$

The energy  $E$  of the spin states is given by

$$E = -\mu_{e,z} B_0 = g_e \mu_B m_S B_0. \quad (2.5)$$

In the absence of a magnetic field, the magnetic moment is randomly oriented and the two energy levels are degenerate, whereas the application of  $B_0$  leads to a splitting of the two states, the so-called electron Zeeman splitting (**Figure 2.1**). The energy levels of these two spin states with the electron spin aligned parallel ( $m_S = +1/2$ ) or antiparallel ( $m_S = -1/2$ ) in respect to the magnetic field, also called spin 'up' and 'down', are described by

$$E_\alpha = +\frac{1}{2} g_e \mu_B B_0 \quad (2.6)$$

$$E_\beta = -\frac{1}{2} g_e \mu_B B_0. \quad (2.7)$$

The Boltzmann distribution describes the ratio of the number of spins  $N$  populating each energy level with  $k_B$  as Boltzmann constant and  $T$  as absolute temperature:

$$\frac{N_\alpha}{N_\beta} = e^{-\frac{\Delta E}{k_B T}} = e^{-\frac{g_e \mu_B B_0}{k_B T}}. \quad (2.8)$$

Transitions between the  $\alpha$  and  $\beta$  states can be induced by electromagnetic radiation in the microwave range, whose oscillating magnetic component  $\mathbf{B}_1$  is oriented perpendicular to  $\mathbf{B}_0$ . Therefore, the energy quantum of the radiation must match the resonance condition

$$\Delta E = h\nu = E_\alpha - E_\beta = g_e\mu_B B_0. \quad (2.9)$$

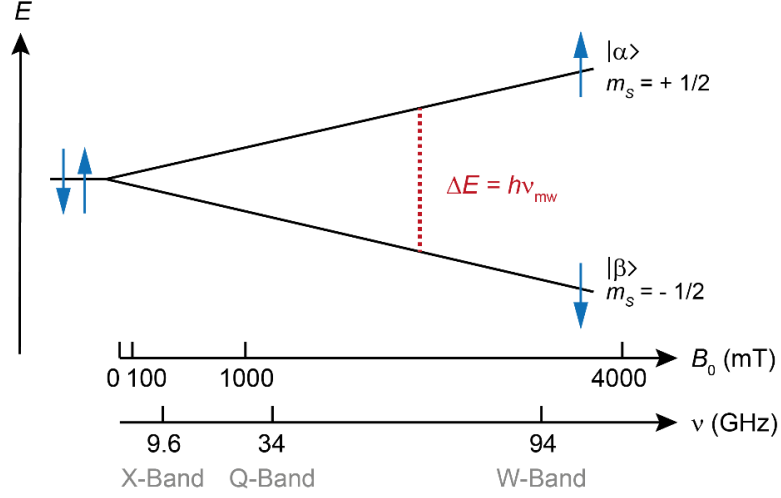


**Figure 2.1: Electron Zeeman splitting of the energy levels of an electron spin with  $S = 1/2$  in the absence and presence of magnetic field  $B_0$ .** Blue arrows indicate the orientation of the electron spin vector. The red line indicates microwave (mw) absorption at resonance condition. Frequency bands commonly used in EPR spectrometers are shown with the corresponding frequency and magnetic field values. Figure adapted from Junk *et al.*<sup>108</sup>

The resulting microwave absorption is detected as an EPR resonant line, with the microwave frequency typically held constant and the magnetic field swept. EPR spectrometers operate at different microwave frequencies. The most common ones, also used in this work, are X- (8 – 10 GHz), Q- (~34 GHz), and W-band (~94 GHz). The range > 90 GHz is generally considered ‘high-frequency’.<sup>109</sup> As demonstrated by equation 2.8, an increasing magnetic field causes an increase in population difference between the two spin states and thus enhances EPR signal intensity. Furthermore, the sensitivity can be enhanced by lowering the temperature.

## 2.2. The spin Hamiltonian

Unpaired electrons in a sample typically cannot be regarded as free electrons because of environmental interactions with nuclear and other electron spins, expressed as separate terms in the spin Hamiltonian  $\hat{\mathcal{H}}_S$  with

$$\hat{\mathcal{H}}_S = \hat{\mathcal{H}}_{EZ} + \hat{\mathcal{H}}_{NZ} + \hat{\mathcal{H}}_{HF} + \hat{\mathcal{H}}_{ex} + \hat{\mathcal{H}}_{DD} + \hat{\mathcal{H}}_{NQ} + \hat{\mathcal{H}}_{ZFS} \quad (2.10)$$

and  $\hat{\mathcal{H}}_{EZ}$  describing the electron Zeeman interaction,  $\hat{\mathcal{H}}_{NZ}$  the nuclear Zeeman interaction,  $\hat{\mathcal{H}}_{HF}$  the hyperfine coupling,  $\hat{\mathcal{H}}_{ex}$  the exchange coupling,  $\hat{\mathcal{H}}_{DD}$  the dipole-dipole coupling,  $\hat{\mathcal{H}}_{NQ}$  the nuclear spin quadrupole interaction, and  $\hat{\mathcal{H}}_{ZFS}$  the zero-field

splitting.<sup>110</sup> The description of these interactions is widely covered in magnetic resonance literature. Therefore, the following sections will provide only a short overview of the different terms and their impact on the present studies.

### 2.2.1. Electron Zeeman interaction

The electron Zeeman interaction describes the interaction of the electron magnetic moment with the applied magnetic field. In the operator form, the interaction of an electron or nuclear spin is, in general, described by

$$\hat{\mathcal{H}} = -\hat{\mathbf{B}}_0^T \hat{\boldsymbol{\mu}} \quad (2.11)$$

using the external magnetic field operator  $\hat{\mathbf{B}}_0$  (the circumflex will be omitted hereafter) and the magnetic moment operator  $\hat{\boldsymbol{\mu}}$ .<sup>111</sup> The superscript T indicates the transposition of a matrix or a vector. Insertion of equations 2.1 and 2.2 results in

$$\hat{\mathcal{H}}_{\text{EZ}} = \frac{\mu_B}{\hbar} \mathbf{B}_0^T \mathbf{g} \hat{\mathbf{S}} \quad (2.12)$$

for the electron Zeeman interaction with  $\mathbf{B}_0 = (B_{0x}, B_{0y}, B_{0z})$ .  $\mathbf{g}$  is the  $g$ -tensor and  $\hat{\mathbf{S}}$  the electron spin operator  $\hat{\mathbf{S}} = (\hat{\mathbf{S}}_x, \hat{\mathbf{S}}_y, \hat{\mathbf{S}}_z)$ . As the unpaired electron can experience spin-orbit coupling between the orbital angular momentum ( $\mathbf{L}$ ) and the spin angular momentum ( $\mathbf{S}$ ), the observed  $g$ -value will deviate from  $g_e$  and becomes anisotropic. The  $g$ -tensor is assumed symmetric and can be described by three principal values  $g_x$ ,  $g_y$ , and  $g_z$ . For isotropic systems, the principal values are equal ( $g_x = g_y = g_z$ ). Axial symmetry is characterized by  $g_x = g_y \neq g_z$ , whereas for rhombic symmetry all three principal values are distinct ( $g_x \neq g_y \neq g_z$ ). If the paramagnetic sample is transferred to a low-viscosity environment, e.g., from frozen into liquid state, fast molecular motion averages out the three  $g$ -values to the isotropic  $g$ -value  $g_{\text{iso}}$

$$g_{\text{iso}} = \frac{1}{3}(g_x + g_y + g_z). \quad (2.13)$$

### 2.2.2. Nuclear Zeeman interaction

The nuclear Zeeman interaction is the analog of the electron Zeeman interaction but, in this case, defines the interaction of the nuclear spin  $\mathbf{I}$  with  $\mathbf{B}_0$ . Similar to equation 2.12, it is described by:

$$\hat{\mathcal{H}}_{\text{NZ}} = -\frac{\mu_n}{\hbar} \mathbf{B}_0^T g_n \hat{\mathbf{I}}, \quad (2.14)$$

where  $\mu_n$  denotes the nuclear magneton and  $g_n$  the nuclear  $g$ -value. The negative sign comes from the opposite electric charge of a nucleus compared to an electron.

### 2.2.3. Hyperfine coupling

Some of the most informative parameters in EPR spectroscopy are hyperfine couplings. This effect is found when the electron spin is in proximity to a nucleus with a nuclear spin number  $I > 0$ . The electron thus experiences the local magnetic field generated by the nucleus in addition to the external magnetic field. The spin Hamiltonian describing this interaction between an electron spin  $\mathbf{S}$  and a nuclear spin  $\mathbf{I}$  is given by

$$\hat{\mathcal{H}}_{\text{HF}} = \hat{\mathbf{S}}^T \mathbf{A} \hat{\mathbf{I}}. \quad (2.15)$$

$\mathbf{A}$  is called the hyperfine coupling (hfc) tensor and provides information on the nature, orientation, and coupling strength of surrounding magnetic nuclei. This tensor is composed of two physical contributions:<sup>112</sup>

$$\mathbf{A} = a_{\text{iso}} \mathbf{1} + \mathbf{T}. \quad (2.16)$$

The element  $\mathbf{1}$  is the unit matrix. The isotropic part  $a_{\text{iso}}$  mainly results from Fermi-contact interaction, which is characterized by the spatial probability density of finding an unpaired electron in an  $s$  orbital at the same position as the nucleus and is non-zero. The  $a_{\text{iso}}$  is given by

$$a_{\text{iso}} = \frac{2\mu_0}{3\hbar} g_e \mu_B g_n \mu_n |\Psi_0(0)|^2 \quad (2.17)$$

with the vacuum permeability  $\mu_0$  and the electron wave function  $\Psi_0(r)$ .  $|\Psi_0(0)|^2$  is the probability density of the electron density located at the nucleus ( $r = 0$ ).<sup>113</sup> As shown for  $g_{\text{iso}}$  in equation 2.13,  $a_{\text{iso}}$  can be obtained accordingly:

$$a_{\text{iso}} = \frac{1}{3} (A_x + A_y + A_z). \quad (2.18)$$

Orientation-dependent electron-nuclear dipole-dipole couplings of electrons residing in  $p$ ,  $d$ , and  $f$  orbitals are considered in the dipolar coupling tensor  $\mathbf{T}$ . For isotropic electron Zeeman interactions  $\mathbf{T}$  is defined by

$$\mathbf{T} = \frac{\mu_0}{4\pi\hbar r^3} g_e \mu_B g_n \mu_n \begin{pmatrix} -1 & & \\ & -1 & \\ & & 2 \end{pmatrix}. \quad (2.19)$$

However, the equation is occasionally used as an approximation for small  $g$  anisotropies.<sup>113</sup> Here,  $r$  is the distance between the magnetic dipoles of the electron and the nucleus.

The presence of nuclear spins with  $I > 0$  leads to a splitting of the detected spectral lines. For  $m$  nuclei with spins  $I_k$  the number of allowed EPR transitions  $N_{\text{EPR}}$  is<sup>114</sup>

$$N_{\text{EPR}} = \prod_{k=1}^m (2I_k + 1). \quad (2.20)$$

Thus, for an exemplary system with  $S = 1/2$  and  $I = 1/2$  (e.g., a proton), two EPR lines will be detected.

#### 2.2.4. Weak electron-electron interactions

Systems with more than one electron undergo further exchange and dipole-dipole interactions. While two electrons with a strong interaction that experience zero-field splitting (Section 2.2.6) are usually treated collectively, weakly coupled spins are usually viewed as individual spins  $S_1$  and  $S_2$ . Then exchange couplings and dipole-dipole couplings need to be considered. The exchange interaction decreases exponentially with increasing distance between two paramagnetic centers. At short distances ( $r < 0.8$  nm), exchange coupling is predominant, whereas at longer distances ( $r > 1.5$  nm), dipole-dipole coupling prevails.<sup>115</sup> Exchange couplings can be observed if the orbitals of the two spins overlap to a significant extent. The Heisenberg exchange coupling is defined by

$$\hat{\mathcal{H}}_{\text{ex}} = -2J\hat{\mathbf{S}}_1\hat{\mathbf{S}}_2 \quad (2.21)$$

with the isotropic exchange interaction  $J$ .<sup>116</sup> It must be noted that various forms of this mathematical description circulate in the literature. In the formalism selected here, negative values for  $J$  correspond to antiferromagnetic coupling, meaning the lowest total spin state is energetically favored. In contrast, positive values indicate that the highest total spin state is energetically favored, hence the coupling is ferromagnetic.

However, dipole-dipole interactions are the focus of this work, which are characterized by the dipole-dipole coupling tensor  $\mathbf{D}$ :<sup>117</sup>

$$\hat{\mathcal{H}}_{\text{DD}} = \hat{\mathbf{S}}_1^T \mathbf{D} \hat{\mathbf{S}}_2 = \frac{1}{r^3} \frac{\mu_0}{4\pi\hbar} g_1 g_2 \mu_B^2 \left[ \hat{\mathbf{S}}_1^T \hat{\mathbf{S}}_2 - \frac{3}{r^2} (\hat{\mathbf{S}}_1^T \mathbf{r})(\hat{\mathbf{S}}_2^T \mathbf{r}) \right]. \quad (2.22)$$

Here,  $\mathbf{r}$  is the inter-spin vector connecting two magnetic dipoles (**Figure 2.2**),  $r$  its distance, and  $g_1$  and  $g_2$  the  $g$ -values of the two spins.  $\hat{\mathcal{H}}_{\text{DD}}$  is often also expressed as follows:

$$\hat{\mathcal{H}}_{\text{DD}} = \frac{1}{r^3} \frac{\mu_0}{4\pi\hbar} g_1 g_2 \mu_{\text{B}}^2 [\hat{A} + \hat{B} + \hat{C} + \hat{D} + \hat{E} + \hat{F}].^{118} \quad (2.23)$$

The operators  $\hat{A} - \hat{F}$  are used to describe the orientation of the molecule with respect to the external magnetic field. Their expression can be found in the literature.<sup>119</sup> If the Zeeman splitting of the electron spin states is large compared to the dipolar coupling between the electron spins and  $g$ -anisotropy is neglected, only  $\hat{A}$  must be considered.<sup>119,120</sup> Then the equation simplifies to:

$$\hat{\mathcal{H}}_{\text{DD}} = \omega_{\text{DD}} (1 - 3 \cos^2 \theta) \hat{\mathbf{S}}_1 \hat{\mathbf{S}}_2 \quad (2.24)$$

with the dipolar coupling constant  $\omega_{\text{DD}}$

$$\omega_{\text{DD}} = \frac{\mu_0 \mu_{\text{B}}^2}{4\pi\hbar} \frac{g_1 g_2}{r^3}. \quad (2.25)$$

The angle between the static magnetic field  $\mathbf{B}_0$  and the interspin vector connecting the coupled electron spins is represented by  $\theta$  (**Figure 2.2**). Since the dipolar coupling frequency is proportional to  $r^{-3}$ , the distance between the coupled spins can be resolved with corresponding spectroscopic methods.<sup>121</sup>

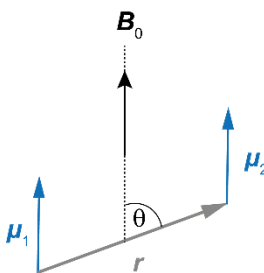


**Figure 2.2: Dipole-dipole interaction.** Interaction between two spins  $S_1$  and  $S_2$ , with their respective magnetic moment  $\mu_1$  and  $\mu_2$ , connected by the interspin distance vector  $\mathbf{r}$ . Dipoles are aligned along the external magnetic field  $\mathbf{B}_0$ . Figure adapted from Borbat *et al.*<sup>122</sup>

### 2.2.5. Nuclear spin quadrupole interaction

Nuclear quadrupole interaction (NQI) is only observed for nuclei with a spin quantum number  $I > 1/2$ . Their non-spherical charge distribution induces an electric quadrupole moment  $Q$ , which interacts with the electric field gradient at the nucleus generated by

the electrons and surrounding nuclei.<sup>116</sup> The Hamiltonian of this interaction can be described using

$$\hat{\mathcal{H}}_{\text{NQ}} = \hat{\mathbf{I}}^T \mathbf{Q} \hat{\mathbf{I}}. \quad (2.26)$$

The nuclear quadrupole tensor  $\mathbf{Q}$  is defined by

$$\mathbf{Q} = \begin{pmatrix} Q_1 & & \\ & Q_2 & \\ & & Q_3 \end{pmatrix} = \frac{e^2 Q q}{4I(2I-1)\hbar} \begin{pmatrix} -(1-\eta) & & \\ & -(1-\eta) & \\ & & 2 \end{pmatrix}, \quad (2.27)$$

where  $e$  is the elemental charge,  $q$  is the charge of the nucleus and  $\eta$  the asymmetry parameter

$$\eta = \frac{Q_1 - Q_2}{Q_3} \quad (2.28)$$

which can take values between 0 and 1 with the ordering convention  $|Q_1| \leq |Q_2| < |Q_3|$ . NQIs are usually not resolved in cw experiments, as all EPR transitions are shifted equally due to first order of perturbation (**Figure 2.3**). Second-order effects such as a shift of resonance lines and the appearance of forbidden transitions are difficult to observe but can be detected experimentally with pulse EPR methods such as ENDOR. Inhomogeneous broadening of the EPR lines often hampers the detection of weak nuclear quadrupole interactions.

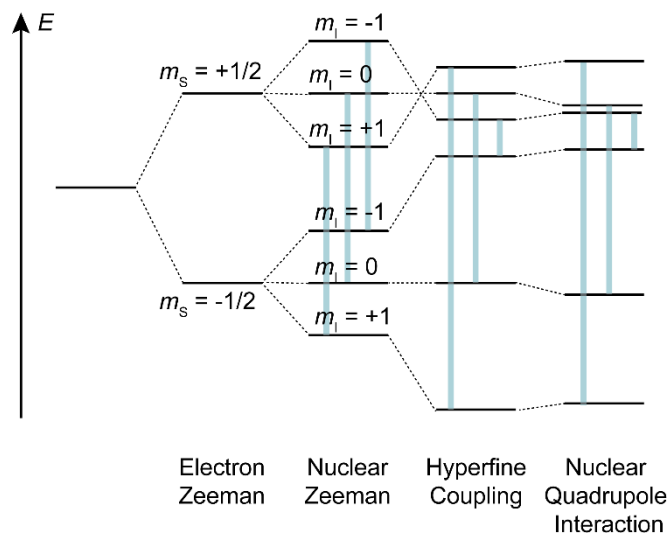


**Figure 2.3: Nuclear quadrupole interaction.** Energy level diagram for a system with  $S = 1/2$  and  $I = 1$  in the strong coupling case ( $|A/2| > |v_1|$ ) with  $Q > 0$  and  $\eta = 0$ . Allowed EPR transitions ( $\Delta m_s = \pm 1$  and  $\Delta m_i = 0$ ) are marked with blue lines. Figure adapted from Goldfarb *et al.* and Colligiani.<sup>116,123</sup>

### 2.2.6. Zero-field splitting

A system with a total electron spin larger than  $1/2$ , in which the electrons experience strong coupling, is described by the anisotropic zero-field splitting (ZFS). Prominent examples are transition metals with unpaired  $d$ -electrons (e.g., high-spin  $\text{Mn}^{\text{II}}$ ) or triplet states in organic molecules. ZFS in transition metals often arises from spin-orbit coupling, whereas dipolar interactions play a major role in organic molecules.<sup>124</sup> As the name implies, zero-field splitting is also present in the absence of an external magnetic field. Its Hamiltonian can be written as

$$\hat{H}_{\text{ZFS}} = \hat{\mathbf{S}}^T \mathbf{D} \hat{\mathbf{S}} \quad (2.29)$$

containing the zero-field splitting tensor  $\mathbf{D}$  with its principal values  $D_x$ ,  $D_y$ , and  $D_z$  where  $|D_z| \geq |D_x|, |D_y|$ . Parameters  $D$  and  $E$  are defined as the axial and transversal components, respectively:

$$D = \frac{3D_z}{2}, \quad (2.30)$$

$$E = \frac{D_x - D_y}{2}. \quad (2.31)$$

The Hamiltonian can be represented in the principal axis system of  $\mathbf{D}$ :

$$\hat{H}_{\text{ZFS}} = D \left( \hat{S}_z^2 - \frac{1}{3} S(S+1) \right) + E (\hat{S}_x^2 - \hat{S}_y^2). \quad (2.32)$$

Note that for axial symmetry along the  $z$ -axis  $D_x$  and  $D_y$  are equal so that  $D \neq 0$  and  $E = 0$ , whereas for rhombic symmetry both  $D \neq 0$  and  $E \neq 0$  are valid.

### 2.3. Cw-EPR

Two mechanistically distinct types of experiments can be performed to record an EPR spectrum: cw- or pulse EPR (described in Section 2.4), with the former usually being the simplest possible experiment. In cw EPR, a sample is continuously irradiated by mw power. Its frequency  $\nu_{\text{mw}}$  is kept constant while the external magnetic field  $\mathbf{B}_0$  is swept. Sweeping the mw frequency is not possible with commercially available EPR spectrometers due to technical constraints.<sup>125</sup> The mw field is built up in a resonator which typically has the form of a rectangular or cylindrical cavity.<sup>126</sup> At the center of a rectangular cavity designed for the  $\text{TE}_{102}$  mode, the amplitude of the magnetic component of the mw field exhibits a maximum, whereas the electric component has a local minimum at this position.<sup>116</sup> The coupling of the cavity can be adjusted by the size of an iris. If this resonator is critically coupled, the incident mw power is entirely absorbed by the resonator. Under the resonance condition, the transition between the

two spin states is induced in the sample by the mw irradiation, which results in additional absorption. Since the coupling is no longer critical, this leads to a reflection of mw power, measured as a function of the applied magnetic field. The recorded spectrum in cw experiments is presented in the form of the first derivative yielded by the sinusoidal amplitude modulation of the magnetic field and the lock-in detection.<sup>116</sup> An appropriate choice of the field modulation amplitude  $B_{\text{mod}}$  needs to be considered.  $B_{\text{mod}}$  may not exceed the peak-to-peak amplitude of the EPR signal  $\Delta B_{\text{pp}}$ , because otherwise, line broadening takes place, and spectral information will get lost. For accurate measurements, choosing  $B_{\text{mod}}$  of at least one third of  $\Delta B_{\text{pp}}$  is recommended.

## 2.4. Pulse EPR

Although cw is a popular spectroscopic method, some information is very difficult or even impossible to obtain by simply using cw-EPR. Some examples are relaxation times, small hyperfine couplings, or intermolecular interactions. Developing new pulse EPR methods is a growing field of interest to overcome these challenges.

Short (ns range) high-power microwave pulses are generally used to induce spin transitions in a pulse EPR experiment. The fundamental aspects of spin dynamics can best be visualized via the motion of the macroscopic magnetization vector  $\mathbf{M}$  within a rotating coordinate system, known as rotating frame. Magnetization is the sum of the individual magnetic moments of the spins normalized to the volume. In the presence of the external magnetic field  $\mathbf{B}_0 = (0, 0, B_0)$ , the magnetic moment is either aligned parallel or antiparallel to  $\mathbf{B}_0$ . According to the Boltzmann distribution, the parallel state of the magnetic moment has lower energy and a higher spin occupancy at thermal equilibrium. Therefore, the net magnetization  $M_z$  is observed parallel to the z-axis. However,  $\mathbf{M}$  precesses along the z-axis of the laboratory frame with the Larmor frequency  $\omega_L$

$$\omega_L = \frac{g\mu_B}{\hbar} B_0 = -\gamma_e B_0. \quad (2.33)$$

The introduction of an mw pulse generates an additional magnetic field component  $\mathbf{B}_1$ , perpendicular to  $\mathbf{B}_0$ , and causes  $\mathbf{M}$  to undergo a supplementary precession, complicating its description. This problem is simplified by introducing the rotating frame formalism, which rotates around the z-axis of the laboratory frame with  $\omega_L$ . When

a suitable microwave pulse is applied, the only precession in the rotating frame is observed along the  $\mathbf{B}_1$ -direction with the Rabi frequency  $\omega_1$

$$\omega_1 = \frac{g\mu_B}{\hbar} B_1. \quad (2.34)$$

The pulse turning angle  $\theta$ , also called flip angle,<sup>127</sup> is described by

$$\theta = \omega_1 t_p. \quad (2.35)$$

This description clearly demonstrates that the flip angle is proportional to the mw pulse length  $t_p$ .

Typically, the transverse magnetization is measured in a pulse EPR experiment.<sup>116</sup> The most straightforward pulsed EPR experiment is based on a single  $\pi/2$  pulse, which, by definition, rotates the magnetization by  $90^\circ$  to the  $-y$ -direction, assuming  $\mathbf{B}_1$  is along the  $x$ -axis. After switching off the mw pulse, the magnetization vector returns to its equilibrium position along the  $z$ -axis due to spin-lattice relaxation described by the  $T_1$  relaxation time (Section 2.4.2). Meanwhile, the magnetization vector will precess around the  $z$ -axis, causing oscillations of the  $M_x$  and  $M_y$  components, which can be monitored as free induction decay (FID). Additionally, to the described spin-lattice relaxation, the transverse magnetization dephases due to spin-spin relaxation, characterized by the  $T_2$  relaxation time (Section 2.4.2). However, recording the FID is often not the best experimental choice due to the dead time of the spectrometer which is around 100 ns.<sup>115</sup> After high-power pulses, the power levels are too high to open the sensitive receiver. Most EPR lines are inhomogeneously broadened, leading to a fast decay of the resulting FID, shorter than the dead time, so that the FID is not observable.<sup>115</sup> This problem can be solved by applying a second pulse, described in the next chapter.

### 2.4.1. The Hahn echo experiment

The Hahn echo sequence is a two-pulse electron spin echo (ESE) experiment where the dephasing of the spin packets can be partially reversed by adding a  $\pi$  pulse after the initial  $\pi/2$  pulse (**Figure 2.4**) and was first described by Erwin Hahn.<sup>128</sup> The time between these two pulses is denoted as  $\tau$ . Thus, an echo is observed after a delay time of  $2\tau$ . After the first  $\pi/2$  pulse, the spin packets dephase during  $\tau$  because of the distribution of their Larmor frequencies. The  $\pi$  pulse causes a rotation of the spin packets by  $180^\circ$  around the  $x$ -axis so that after  $2\tau$ , all spin packets are refocused at the  $y$ -axis, yielding the detectable Hahn echo, also called primary echo. Its amplitude is proportional to the number of excited spins. By plotting the integral of the echo versus the swept field, an EPR spectrum is obtained. This two-pulse experiment provides the basis for many other advanced pulse techniques.

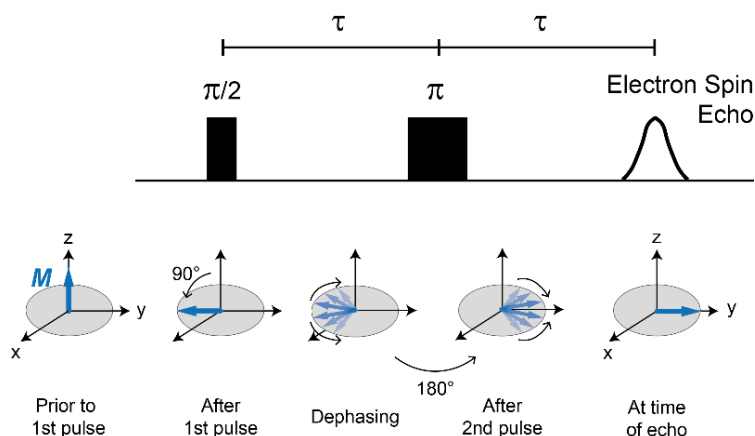


**Figure 2.4: The Hahn echo sequence, consisting of two pulses leading to the electron spin echo (ESE).** Magnetization of the spin ensemble (blue arrow) in the rotating frame is shown at the corresponding time points. Figure adapted from Goldfarb *et al.*<sup>116</sup>

### 2.4.2. Relaxation

Relaxation theories are among the more complex mathematical constructs. Hence, a numerically precise description is not presented in this work but, instead, a phenomenological approach.

After applying a pulse, the spins will start to relax back to thermal equilibrium, driven by longitudinal (spin-lattice) and transversal (spin-spin) relaxation. The first process is characterized by  $T_1$ , and the second via  $T_2$ , while  $T_2$  is usually much shorter than  $T_1$ . During  $T_1$ , the spins disperse their energy into the lattice, i.e., the surroundings, by returning to the z-axis to restore the thermal equilibrium given by the Boltzmann distribution. This parameter is crucial, e.g., for the shot repetition time (srt) of a pulse experiment, which is the time between the two applied pulse sequences, allowing the spins to relax back to thermal equilibrium. The  $T_1$  time can be determined experimentally, e.g., by inversion recovery, where a single  $\pi$  pulse first inverts the magnetization.<sup>129</sup> The magnetization can recover during the time  $T$ , followed by the Hahn echo sequence used for detection. Furthermore, saturation recovery or echo-detected saturation recovery experiments can be implemented to obtain  $T_1$  times.

Dephasing of the spins takes place due to spin-exchange mechanisms, e.g., spin flip-flops (one spin changes from  $\alpha$ - to  $\beta$ -state, while another spin changes from  $\beta$  to  $\alpha$ ).<sup>130</sup> The relaxation time can be measured by a modified Hahn echo experiment in which  $\tau$  is incremented, also known as two pulse electron spin echo envelope modulation (2PESEEM) experiment (**Figure 2.5**). This pulse experiment allows determining the phase memory decay time  $T_m$ , which, in addition to  $T_2$ , includes contributions from  $T_1$  and many other processes, such as instantaneous diffusion and nuclear spin diffusion. The influence of the instantaneous diffusion is, among other things, given by local spin

concentration. High spin concentrations can lead to shorter relaxation times. Moreover, the extent of the nuclear spin diffusion is determined by the magnetic moment of the dipolar coupled nuclear spin. Larger magnetic moments will again shorten the relaxation time. If the  $T_m$  time needs to be extended for an experiment, deuteration of a sample can help since  $^2\text{H}$  has a smaller magnetic moment than  $^1\text{H}$ , which further reduces the dipole-dipole interaction and thus increases  $T_m$ .<sup>116</sup> Deuteration is regularly used in dipolar spectroscopy since the possible length of a DEER trace depends on  $T_2$  relaxation.<sup>131</sup>

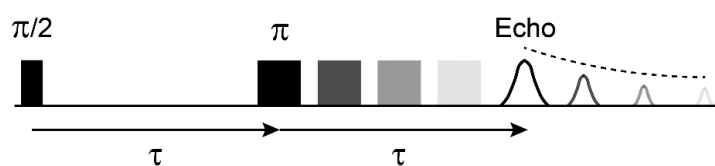


**Figure 2.5: 2PESEEM pulse sequence.** Integrated echo is measured as a function between  $\tau$ .  $T_m$  can be obtained from the echo decay (dotted line).

Furthermore, relaxation times are essential not only for pulse experiments but for cw experiments as well. For instance, cw spin counting needs to be carried out under non-saturating conditions. A saturation factor  $s$  can be calculated from the relaxation times by<sup>116,126</sup>

$$s = \frac{1}{1 + \gamma_e^2 B_1^2 T_1 T_2}. \quad (2.36)$$

For  $s < 1$ , the amplitude of the cw-EPR signal decreases, and signal broadening may appear. Furthermore, the signal lineshape is influenced by relaxation times. The lineshape of an unsaturated cw signal without unresolved hyperfine splitting is represented by a Lorentzian function and its linewidth  $\Delta B_{pp}$  is correlated to  $T_2$  via

$$\Delta B_{pp} = \frac{2}{\sqrt{3} \gamma_e T_2}. \quad (2.37)$$

### 2.4.3. Double electron-electron resonance spectroscopy

A large part of this work is based on Double Electron-Electron Resonance (DEER), also called Pulsed Electron-Electron Double Resonance (PELDOR) spectroscopy. This method is used for distance determination between two paramagnetic centers. The DEER pulse sequence employs two different mw frequencies applied during the experiment. The four-pulse DEER sequence (**Figure 2.6A**) consists of an initial Hahn echo sequence applied at the so-called detect frequency  $\nu_{det}$ , which excites only those spins in resonance with  $\nu_{det}$ , denoted as spins A. During the time  $\tau_2$ , a  $\pi$  pulse at the

second frequency, the pump frequency ( $\nu_{\text{pump}}$ ), is applied at a variable time  $t$  with respect to the primary echo, which likewise excites (or ‘pumps’) spins in resonance with the pump frequency, referred to as spins B. This pulse flips the magnetization of the B spins into the  $-z$ -direction in a time-dependent manner. Thus, the local magnetic field experienced by the A-spin changes the frequency of spin A via the dipole-dipole coupling. After the time  $\tau_2$  following the primary echo, an additional  $\pi$  pulse is applied at the detect frequency to refocus the magnetization. The refocused echo generated in this way appears with a delay of  $\tau_2$  after the last detection pulse. The signal phase is adjusted so that the refocused echo shows a maximum positive amplitude. The echo integral is then recorded against the time  $t$ . If spins A and B experience dipole-dipole coupling, the refocused echo intensity of spin A oscillates with  $\cos(\omega_{\text{AB}}t)$ :<sup>132</sup>

$$\omega_{\text{AB}} = \omega_{\text{DD}}(1 - 3 \cos^2 \theta). \quad (2.38)$$

The recorded signal  $V(t)$  is a product of intra- and intermolecular interactions:<sup>133</sup>

$$V(t) = V(t)_{\text{intra}}V(t)_{\text{inter}}. \quad (2.39)$$

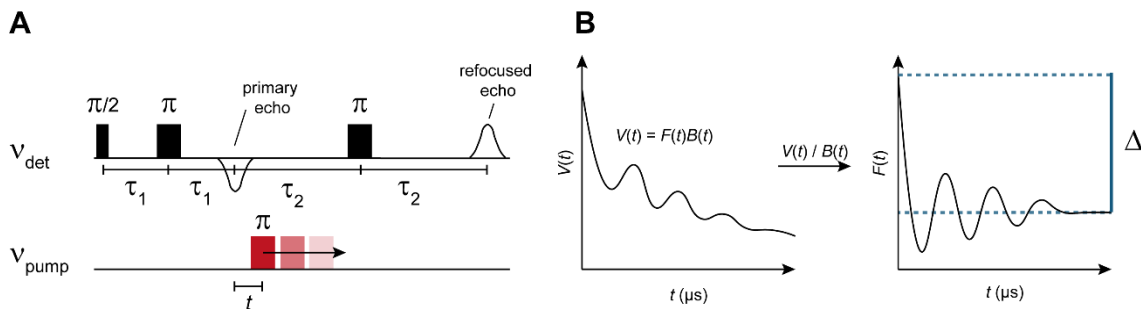


**Figure 2.6: Double electron-electron resonance spectroscopy.** (A) The four-pulse DEER pulse sequence. (B) Schematic DEER time trace before (left) and after (right) background correction. The modulation depth  $\Delta$  parameter is indicated in blue.

Spins coupled within one spin cluster (or molecule) are taken into account by  $V(t)_{\text{intra}}$ , whereas  $V(t)_{\text{inter}}$  describes the contribution to the echo decay from homogeneously distributed spins in the sample. In the case of a random spin distribution  $V(t)_{\text{inter}}$  takes the form:

$$V(t)_{\text{inter}} = V_0 \exp\left(-\frac{2\pi\gamma_A\gamma_B\mu_0}{9\sqrt{3}\hbar} c\lambda_B t\right), \quad (2.40)$$

where  $\gamma$  is the gyromagnetic ratio of the spins,  $\lambda_B$  the fraction of B-spins inverted by the pump pulse, and  $c$  the spin concentration in the sample.<sup>132,134</sup> Note that higher spin

concentration leads to an increased  $V(t)_{\text{inter}}$ . Because of these contributions,  $V(t)$  needs to be background corrected with the function  $B(t)$ , yielding the background-corrected DEER trace  $F(t)$ , or called form factor, with  $V(t) = F(t)B(t)$  (**Figure 2.6B**). The background correction must be performed carefully; otherwise, undiscovered modulations could disappear during this process. Subsequently, Fourier-transformation of  $F(t)$  delivers the distance  $r$  between spin A and B with the help of the previously presented equation 2.25. Contributions from exchange coupling are neglected in this assumption.<sup>132</sup>

The inversion efficiency  $\lambda_B$  depends on excitation bandwidth and flip angle. The experimentally obtained modulation depth  $\Delta$  (see **Figure 2.6**) can be approximated by

$$\Delta = 1 - (1 - \lambda_B)^{(N-1)}, \quad (2.41)$$

where  $N$  is the number of spins in a cluster, assuming all spins of group B are of similar nature. If the coupled spins possess different spectral widths, the respective  $\lambda_B$  values need to be regarded additionally. For a mixture of monomers, dimers, and higher oligomers, the fraction of each oligomer  $x_i$  needs to be considered. Additionally, different transversal relaxation times must be taken into consideration, leading to different contributions to the refocused echo intensity, which is described by the scaling factor  $s_i$ :<sup>132</sup>

$$\Delta = \frac{\sum_i s_i x_i \Delta_i}{\sum_i s_i x_i}. \quad (2.42)$$

This equation clarifies that a monomeric spin, which does not couple to other spins within its cluster and thus exhibits a modulation depth of 0, will decrease the experimentally detected modulation depth in a mixture. For guidelines on experimental details and analyses, the reader is referred to Schiemann *et al.*<sup>134</sup>

#### 2.4.4. Electron-nuclear double resonance spectroscopy

Cw or ESE pulse experiments provide key information on a sample, such as  $g$ -anisotropy or large hyperfine interactions. However, the resolution in these experiments is limited, and many smaller couplings are hidden in the spectral linewidth. Electron-Nuclear Double Resonance (ENDOR) is a common EPR technique to investigate hyperfine couplings in high resolution, combining the advantages of EPR with those of NMR (Nuclear Magnetic Resonance) spectroscopy. The two most frequently used pulse ENDOR sequences are Davies ENDOR, derived from the inversion recovery sequence, and Mims ENDOR, derived from the stimulated echo sequence.<sup>115,135,136</sup> Mims sequence is used for small hyperfine coupling values, whereas for larger ones ( $> 3$  MHz), Davies ENDOR is the method of choice.<sup>137</sup> As only the latter was utilized in this study, this will

be explained in more detail. In Davies ENDOR pulse sequence (**Figure 2.7A**), a selective mw  $\pi$  pulse is applied first, which inverts the spin population of one allowed EPR transition. This process is often referred to as ‘hole burning’ into the EPR line. Then, a radiofrequency (rf)  $\pi$  pulse is applied during the time T, that drives the allowed NMR transitions, followed by a detecting Hahn echo sequence.

The principle of this experiment is best explained by observing the polarization transfer between the different energy levels (**Figure 2.7B**) of an exemplary system with  $S = 1/2$  and  $I = 1/2$ . In the presence of an external magnetic field, this system has four distinct energy levels labeled according to their spin states. Due to the Boltzmann distribution, spin states with  $m_S = -1/2$  hold a higher population (black bar) than  $m_S = +1/2$  (white bar), and the electron spin transitions (blue lines) are stronger polarized than the nuclear spin transitions (orange lines) at thermal equilibrium.

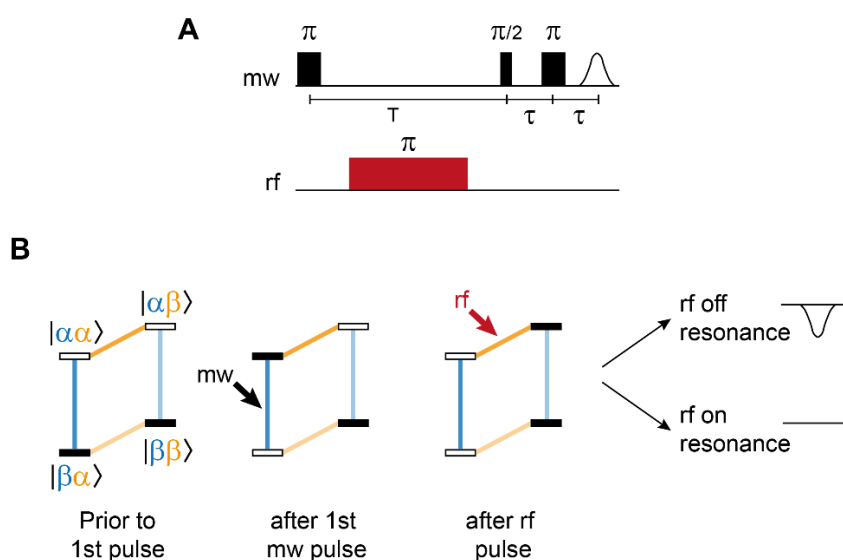


**Figure 2.7: Electron-nuclear resonance spectroscopy.** (A) Davies ENDOR pulse sequence. (B) Polarization transfer during the Davies ENDOR experiment. Energy levels are depicted as black and white bars, with higher populations represented in black. Electron spin transitions are shown in blue, and nuclear spin transitions in orange. Transitions that are driven by the respective pulses are indicated by arrows. Figure adapted from Tyryshkin *et al.*<sup>138</sup>

The first microwave  $\pi$  pulse inverts only one of the two possible electron spin transitions as it is transition-selective; in this case,  $|\beta\alpha\rangle$  to  $|\alpha\alpha\rangle$  (dark blue), whereas the  $|\beta\beta\rangle$  to  $|\alpha\beta\rangle$  transition (pale blue) is not inverted. Now the electron and nuclear spin transitions are polarized with opposite signs each. The following radiofrequency pulse is also transition-selective; in this case, inverting the  $|\alpha\alpha\rangle$  to  $|\alpha\beta\rangle$  transition (dark orange). This leads to a case where no polarization resides on the two electron spin transitions, so no echo can be observed if the rf pulse is on resonance. If the rf pulse is off resonance, an inverted echo is observed by the Hahn echo sequence. Hence, the echo intensity is directly linked to the effective flip angle of the rf pulse. The spectrum is presented as a

function of the echo intensity against the rf pulse frequency, and the detected ENDOR lines correspond to the nuclear spin transition frequencies.

For the exemplary system with  $S = 1/2$  and  $I = 1/2$  the  $g$ -tensor and hyperfine coupling are assumed isotropic ( $A = a_{\text{iso}}$ ). Then its Hamiltonian can be written as

$$\hat{\mathcal{H}} = \frac{g\mu_B}{\hbar} \mathbf{B}_0 \hat{\mathbf{S}} - \frac{g_n \mu_n}{\hbar} \mathbf{B}_0 \hat{\mathbf{I}} + A \hat{\mathbf{S}} \hat{\mathbf{I}}. \quad (2.43)$$

The first term in this sum describes the electron Zeeman interaction, the second describes the nuclear Zeeman interaction, and the third represents the hyperfine interactions. The corresponding energy levels of the individual spin states can be expressed by

$$E(m_S, m_I) = g_e \mu_B m_S B_0 - g_n \mu_n m_I B_0 + A m_S m_I. \quad (2.44)$$

The energy levels are depicted in **Figure 2.8A** with the two resulting electron spin transitions detected by cw-EPR experiments, split by  $A$  (**Figure 2.8B**). As comparison, an exemplary ENDOR spectrum is illustrated with the two detected nuclear spin transitions split by  $A$  and centered around the nuclear Larmor frequency  $\nu_n$  (**Figure 2.8**). Anisotropy of  $\mathbf{A}$  can be resolved by performing several ENDOR experiments at distinct  $g$ -values. These orientation-selective measurements can deliver accurate information about the orientation of coupled nuclei with respect to the paramagnetic center.

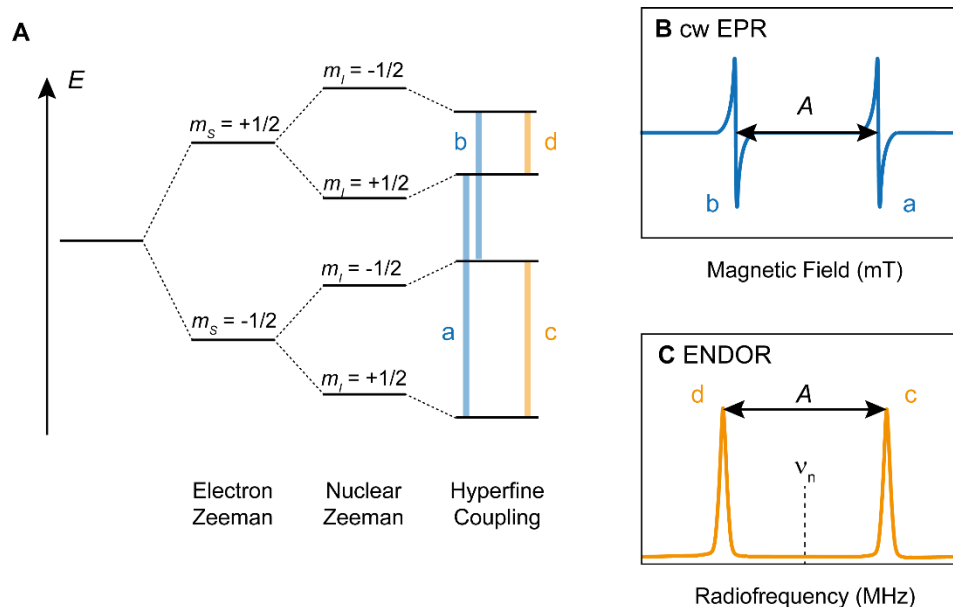


**Figure 2.8: Detected transitions in cw-EPR and ENDOR experiments.** (A) Energy level diagram for a system  $S = 1/2$  and  $I = 1/2$ . Blue lines represent allowed EPR transitions (a and b), and orange lines allowed NMR (or ENDOR) transitions (c and d). Furthermore, the resulting cw-EPR (B) and ENDOR (C) spectra are illustrated schematically. Figure adapted from Cutsail *et al.*<sup>139</sup>

## 2.5. Spin labeling in EPR

In principle, EPR spectroscopy is limited to molecules with intrinsic paramagnetic centers, such as metalloproteins or enzymes containing radicals.<sup>140</sup> However, molecular biology tools have been developed to incorporate stable radicals at user-defined positions into various biological systems, called site-directed spin labeling (SDSL),<sup>141–143</sup> extending the possible application of EPR spectroscopy. SDSL can be performed at almost any sample, ranging from soluble molecules, e.g., proteins and nucleic acids, to more insoluble membrane proteins. Most commonly, a spin label is attached to a cysteine residue via a sulfhydryl-specific nitroxide reagent, whereas other accessible cysteines in the sample that should not be labeled must be mutated, for instance, to alanine or serine.<sup>140,144</sup> The most popular spin label is methanethiosulfonate (MTSSL). Furthermore, the nonsense suppression method or solid-phase peptide synthesis can be used for spin label introduction. As this thesis focuses on EPR spectroscopy on proteins, only protein spin tags will be discussed in the following part, using examples of fundamental SDSL techniques as well as recent developments. This chapter only gives a short overview, and numerous examples can be found in the literature.

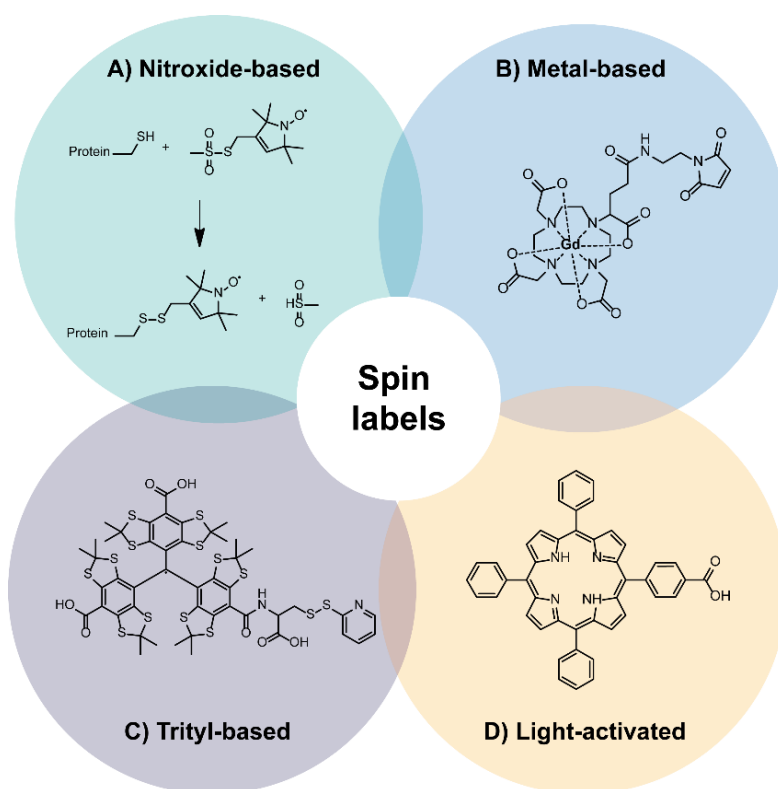


**Figure 2.9: Overview of different spin labels covered in this section.** (A) The attachment of MTSSL to a cysteine residue. (B) Gd-DOTA-maleimide as an example for metal-based spin labels. (C) TAM-reagent, exemplarily shown for Trityl labels. (D) The light-activatable TTP label.

### 2.5.1 Nitroxide spin labels

The first groundbreaking EPR experiments using MTSSL were presented in 1989 by Hubbel *et al.*<sup>141,142</sup> The spin label forms a disulfide bond to the protein via a cysteine residue connected by a linker (**Figure 2.9A**). The linker renders the spin label flexible, thus avoiding disturbances of the protein tertiary structure. The nitroxide EPR spectrum is strongly dependent on its rotational correlation time.<sup>145-147</sup> At room temperature, a solvent-exposed label is dominated by a small linewidth with three hyperfine coupling lines since the mobility of the spin label is only partially restricted. On the other hand, interactions of the nitroxide tag with protein backbones and side chains produce EPR spectra with broader linewidths. Completely immobilized spin label side chains, buried labeling sites, and samples in frozen state show the broadest spectra. Thus SDSL-EPR spectroscopy with nitroxides can be used to monitor disorder-to-order transitions and possible conformational changes in proteins. Nevertheless, the linker group also represents a disadvantage in terms of measurement accuracy. The distance distribution between two MTSSLs often results in broad peaks.<sup>148</sup> Based on the structure of MTSSL different labels have been developed which differ, for example, in the linker groups such as MTS-4-oxyl or maleimide-functionalized compounds.<sup>149</sup> An elegant way to use nitroxide radicals for protein structure analysis was demonstrated recently, combining spin labeling with the advantages of unnatural amino acid incorporation.<sup>150-153</sup> The need for a cysteine residue can thus be avoided by site-specifically attaching the label to a UAA via copper-catalyzed azide-alkyne cycloaddition. However, nitroxide radicals are reduced in the cellular environment, limiting their *in vivo* application, which can be overcome by chemical shielding.<sup>154-159</sup> One reason nitroxide labeling is nevertheless a popular tool for intracellular studies is the possibility of performing the EPR measurements at room temperature.<sup>160-163</sup>

### 2.5.2 Metal-based spin labels

The *in vivo* lifetime limitation of nitroxides led to the development of metal-based spin labels such as Gd<sup>III</sup>, Cu<sup>II</sup>, or Mn<sup>II</sup>. Reduction-stable paramagnetic Gd<sup>III</sup>-complexes were highly useful in EPR distance measurements *in vitro* and inside cells.<sup>164-168</sup> Different complexes exhibit distinct advantages, such as reduced zero-field splitting or increased phase memory time.<sup>169</sup> The exemplarily shown Gd-DOTA-maleimide label (**Figure 2.9B**) is often used due to its biocompatibility and suitability for cysteine labeling.<sup>168</sup> These labels often require a cell-free protein synthesis approach with subsequent microinjection or transfection procedures to transfer the labeled protein back into living cells. In-cell labeling strategies with Gd-DOTA-maleimide were unsuccessful because of Gd<sup>III</sup> release inside the cells.<sup>170</sup> However, azide-functionalized Gd-DOTA labels were used successfully for this purpose.<sup>171</sup>

One example of using copper as a spin label is found in the double-histidine (dHis) binding motif.<sup>172-174</sup> In contrast to the other labels, which often require cysteine residues

for labeling, dHis uses two histidines to chelate  $\text{Cu}^{\text{II}}$  as paramagnetic species. Single histidine residues have only two rotatable bonds, whereas the coordination of  $\text{Cu}^{\text{II}}$  by two histidine residues further restricts the rotational movements, providing narrower distance distributions than those found with MTSSL, for example.<sup>172</sup> The spin label can be assembled intracellularly by adding  $\text{Cu}^{\text{II}}$ -nitrilotriacetic acid ( $\text{Cu}^{\text{II}}$ -NTA),<sup>175</sup> thus avoiding the need for posttranslational modification. However, mutation of two amino acids is required, in contrast to only one residue for the other presented labels, potentially interfering with the protein structure.

### 2.5.3 Trityl spin labels

Triarylmethyl radicals, or short trityl spin labels (**Figure 2.9C**), were developed to overcome the limitations of cellular reduction and to enhance relaxation times at room temperature, compared to nitroxide spin labels.<sup>176</sup> Trityl radicals offer a narrow spectral width, which allows for a better signal-to-noise (S/N) ratio than nitroxides and helps to avoid orientation-selective measurements. In-cell RIDME (Relaxation-Induced Dipolar Modulation Enhancement) experiments have been reported for  $\text{Fe}^{\text{III}}$ -trityl distances in cytochrome P450 CYP101, where  $\text{Fe}^{\text{III}}$  is present as an intrinsic paramagnetic center and the trityl label conjugated via an engineered cysteine residue.<sup>176</sup> Furthermore, trityl-trityl DEER measurements were presented in whole cells at cryogenic temperatures offering high stability and sensitivity inside the cellular environment.<sup>177–179</sup> Trityl-trityl distance measurements using DQC showed high sensitivity, even at 150 K.<sup>180</sup> Further improvement of relaxation times needs to be accomplished, in order to enhance the range of detectable distances and to enable in-cell room temperature measurements.<sup>181</sup>

### 2.5.4 Light-activated spin labels

Light-activated spin labels can theoretically be divided into two groups depending on the activation mechanism. The first group consists of radicals generated by a chemical reaction triggered by light. One example is the PaNDA label (Photoactivatable Nitroxide for inverse-electron-demand Diels-Alder reaction), which has a photoremovable protection group.<sup>182</sup> Irradiation and subsequent oxidation initiate the formation of a nitroxyl radical. This label is currently under development and first experiments indicate that it can be a promising candidate for distance measurements *in vitro* and *in vivo*.<sup>183</sup>

The second group of light-activated spin labels involves the formation of excited triplet states, demonstrating a field currently under development. The resulting EPR signals of triplets are stronger than those of Boltzmann-populated paramagnetic centers, as in this case, a spinpolarized state is formed.<sup>184–186</sup> If the triplet states have a sufficiently long lifetime in a microsecond or millisecond time scale, they can be investigated by pulse EPR coupled to laser excitation.<sup>187</sup> Dipolar couplings can be resolved using recently developed pulse sequences such as light-induced DEER (LiDEER),<sup>188,189</sup> laser-induced

magnetic dipolar (LaserIMD) spectroscopy,<sup>190</sup> or light-induced triplet-triplet electron resonance spectroscopy (LITTER).<sup>191</sup> Whereas the latter is used for distance measurements between two triplets, LiDEER and LaserIMD help to extract distance information between triplet-radical pairs. In this way, orientation-selective distance measurements between porphyrins and nitroxides are feasible.<sup>187–189</sup> In previous studies, a model peptide was labeled with 5-(4-carboxyphenyl)-10,15,20-triphenylporphyrin, short TPP, represented in **Figure 2.9D**. The LiDEER sequence is related to the four-pulse DEER sequence, but in this case, the observed species, meaning the triplet state, is first populated by a laser flash prior to the Hahn echo sequence (**Figure 2.10**).<sup>188</sup> This, in turn, leads to an oscillating DEER trace which is analyzed in the same way a typical DEER experiment. Another approach for extracting distance information from triplet states by light-induced dipolar spectroscopy is LaserIMD (**Figure 2.10**). Instead of changing the dipolar interaction with a microwave pump pulse during the echo sequence as in LiDEER, the dipole-dipole coupling is introduced by triplet excitation via a laser pulse. Temporal overlaps of the laser flash with the microwave pulses or the acquisition trigger are allowed, which permits the acquisition of the primary echo rather than the refocused echo, as used in LiDEER. An advantage of the photoinduced activation of the spin label is the avoidance of reduction in the cellular environment since the paramagnetic species can be formed shortly before its measurement.

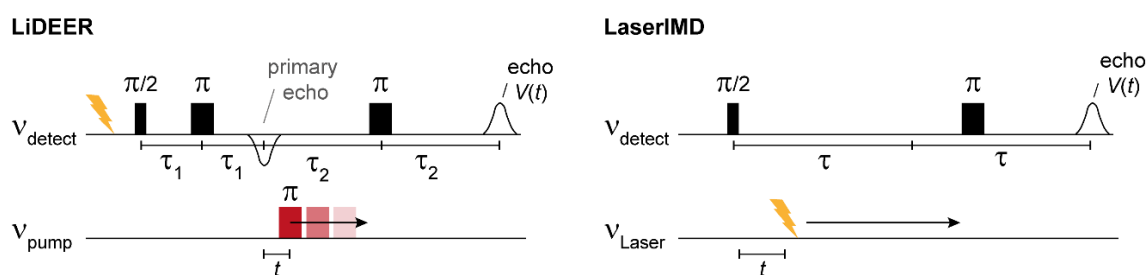


**Figure 2.10: LiDEER and LaserIMD pulse sequence.** The pulse sequence of a four-pulse DEER experiment with an initial laser flash yields the LiDEER sequence. In contrast, LaserIMD is based on the three-pulse DEER sequence with a laser flash instead of a pump pulse. Figure adapted from Hintze *et al.*<sup>190</sup>



RESULTS  
AND DISCUSSION



# 3.

## In-cell characterization of the stable tyrosyl radical in *E. coli* RNR by EPR spectroscopy

---

---

Parts of the results presented in this chapter are published in:

Meichsner, S. L., Kutin, Y., Kasanmascheff, M. In-Cell Characterization of the Stable Tyrosyl Radical in *E. coli* Ribonucleotide Reductase Using Advanced EPR Spectroscopy. *Angew. Chem. Int. Ed.* **60**, 19155 – 19161 (2021).<sup>192</sup>

### 3.1. Introduction

One of the most challenging tasks for structural biology techniques is to achieve high resolution within the native environment of biomolecules, i.e., the cells. Whereas dipolar spectroscopy in combination with spin-labeled biomolecules is an emerging field, only a few examples of in-cell EPR performed at intrinsic paramagnetic centers have been presented up until now, primarily focusing on cw-EPR only.<sup>102,103,193,194</sup> So far, there is very little information about the *in vivo* structure and regulation of ribonucleotide reductase in particular, which is crucial because of its vital role as a cancer drug target. Therefore, the presented work intended to solve this problem and study RNR inside its natural cellular environment using EPR spectroscopic methods.

#### 3.1.1. The problem

A common type of in-cell EPR spectroscopy is the introduction of spin-labeled protein samples into HeLa cells via electroporation. Therefore, our first attempt was to insert the  $\beta$ 2 subunit into HeLa cells by electroporation according to previously published protocols.<sup>167,169</sup> Successful protein uptake was confirmed through fluorescence microscopy using fluorescently labeled protein (**Figure 3.1A**). Despite varying experimental conditions, no Y<sub>122</sub>• was detected by EPR (data not shown).

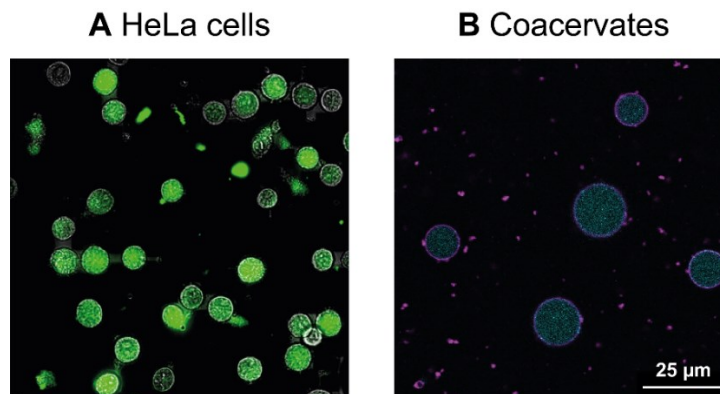


**Figure 3.1: Fluorescence images of the  $\beta 2$  subunit of *E. coli* class Ia RNR in living HeLa cells or in a cell-mimicking system.** RNR wt- $\beta 2$  was labeled with Alexa Fluor 488 C<sub>5</sub> Maleimide Dye. (A) RNR was inserted into human HeLa cells via electroporation. Images were recorded after 6 h incubation after electroporation. Brightfield microscopic image is merged with fluorescence image. (B) Fluorescence image of RNR in coacervates. The terpolymer is labeled with Nile red.

In addition, the usually stable tyrosyl radical was attempted to be studied in coacervates. Coacervates are condensed, liquid-like droplets that are typically formed from oppositely charged polymer molecules.<sup>195</sup> These structures are used, among other things, to mimic cellular crowdedness and can be loaded with various cargos, including proteins, nucleic acids, and metabolites.<sup>196</sup> Shortly, coacervation is achieved by mixing positively and negatively charged amylose. Stabilization is reached via the subsequent addition of a block terpolymer which self-assembles on the surface of the nascent coacervate due to electrostatic interactions. Protein uptake into the coacervate is realized by the molecular charge: highly negatively charged proteins are included in the coacervate phase, whereas positively or neutrally charged proteins remain excluded.<sup>196</sup> Since  $\beta 2$  of *E. coli* RNR is negatively charged, this procedure is suitable for testing the enzyme in such a cell-mimicking system. Again, successful protein uptake was confirmed by fluorescence imaging (**Figure 3.1B**); however, no radical was seen in cw-EPR experiments.

### 3.1.2. The solution

Apparently, the usually relatively stable tyrosyl radical in *E. coli* RNR is susceptible to its environment. The inability to detect the native tyrosyl radical  $Y_{122}^{\bullet}$  of *E. coli* RNR other than in its host organism might presumably be a reason for the current absence of detailed in-cell RNR studies. Therefore, we took the opportunity to study class Ia RNR in its original host organism, *E. coli*, by overexpressing the protein, followed by advanced EPR spectroscopic techniques.

## 3.2. Materials and methods

### 3.2.1. Wild-type β<sub>2</sub> protein expression for in-cell experiments

Expression of wt-β<sub>2</sub> was carried out as described in Section 8.2.4. After 4 h of protein overproduction, the cells were harvested by gentle centrifugation. Although 7000 xg for 20 min centrifugation was performed for *E.coli* whole-cell RNR experiments previously,<sup>101</sup> here the centrifugation is performed at 6000 xg for 15 min at 4 °C in order to keep as many cells intact and alive as possible. A typical 2.5 – 3 g cell paste/L media was obtained. For in-cell sample preparations, the harvested cell pellet was washed several times and resuspended in 50 mM Tris pH 7.6 with 5% glycerol using 3 mL of buffer per g cell paste. 0.13 mM Fe<sup>II</sup>(NH<sub>4</sub>)<sub>2</sub>(SO<sub>4</sub>)<sub>2</sub> (~5 equivalents of Fe<sup>II</sup> with respect to the estimated protein concentration) was added to this buffer. The added Fe concentration was only 13% of the concentration that has been shown to inhibit *E. coli* cell growth.<sup>197</sup> The suspension was kept on ice for 10 min and subsequently saturated with O<sub>2</sub> gas on ice for 1 – 2 min.

### 3.2.2. 2,3,5-F<sub>3</sub>Y<sub>122</sub>-β<sub>2</sub> protein expression for in-cell experiments

*E. coli* BL21(DE3)-Gold cells were co-transformed with pBAD-*nrdB*<sub>122TAG</sub> and pEVOL-F<sub>n</sub>YRS-E3, and plated on LB-agar plates with 100 µg/mL carbenicillin (Carb) and 35 µg/mL chloramphenicol (Cm) at 37 °C. Positive clones were selected, and a starter culture (5 mL) was grown overnight in LB-medium enriched with Carb and Cm at 37 °C until saturation. An intermediate culture (100 mL) was enriched with 1 mL of the starter culture, also grown overnight. The expression culture was grown with a 200-fold dilution of the intermediate culture in 2XYT medium containing Carb and Cm. At OD<sub>600</sub> ~0.3, F<sub>3</sub>Y was added to a final concentration of 0.7 mM. After 30 min, 100 µM 1,10-phenanthroline was added to chelate iron. Protein expression was induced with 0.5% (w/v) L-arabinose after another 30 min. After 4 h protein overproduction, the cells were harvested by gentle centrifugation at 6000 xg for 15 min at 4 °C. For *in vitro* sample preparations, the apo-2,3,5-F<sub>3</sub>Y<sub>122</sub> construct was purified as described for the wild-type protein in Section 8.2.4. Protein concentration was determined via UV-Vis spectroscopy. For in-cell sample preparations, the harvested cell pellet was washed several times and resuspended in 50 mM Tris pH 7.6 with 5% glycerol using 3 mL of buffer per g cell paste. 0.13 mM Fe<sup>II</sup>(NH<sub>4</sub>)<sub>2</sub>(SO<sub>4</sub>)<sub>2</sub> (~5 equivalents of Fe<sup>II</sup> with respect to the estimated protein concentration) was added to this buffer. The BL21 cell suspension was allowed to sit on ice for 5 min and then saturated with O<sub>2</sub> gas on ice for 1 – 2 min.

### 3.2.3. EPR sample preparation

After radical formation, 200  $\mu$ L cell suspension was directly transferred into EPR tubes and frozen gently in an isopropanol rack at  $-80$  °C to secure slow cooling and prevent cell damage. Spin concentrations of the samples were determined via 9.6 GHz cw-EPR measurements (Table 3.1) by comparing them to an RNR standard sample and a Cu<sup>II</sup>-EDTA standard sample.

### 3.2.4. Cell counting experiments

Prior to EPR experiments, cell suspensions from four distinct expression batches were plated on LB-agar plates after protein overproduction to check the viability of the cells. Therefore, a dilution series of the cell suspension was prepared with SOC medium up to a 1:10<sup>12</sup> dilution, followed by plating and incubation at 37 °C overnight. Grown colonies were counted the next day.

### 3.2.5. Details of the EPR experiments

**X-band:** X-band cw-EPR measurements were carried out at  $T = 100$  K using a Bruker EMX-Nano Benchtop spectrometer equipped with a continuous-flow nitrogen cryostat.

**Q-band:** Q-Band pulse EPR measurements were carried out at  $T = 10$  K using a Bruker Eleksys E580 spectrometer equipped with a 150 W TWT amplifier, Bruker ER 5106QT-2 resonator, Bruker SpinJet AWG, Oxford Instruments CF935 continuous-flow helium cryostat and Oxford Instruments MercuryITC temperature controller.

**Orientation-selective DEER experiments** were performed using the 4-pulse DEER pulse sequence with 16-step phase cycling and Gaussian pulses. The frequency separation  $\Delta f = f_{\text{pump}} - f_{\text{det}}$  was 84 MHz, and an overcoupled resonator with  $f_{\text{pump}}$  set to the center of the resonator dip was used. The optimal  $\pi$ -pulse lengths were determined using transient nutation experiments and typically were  $\sim 30$  ns for the pump pulse and  $\sim 70$  ns for the detection. If not stated otherwise, DEER time traces were background-corrected using an empirical second-order polynomial fitting.

**ENDOR experiments** were carried out at 10 K using a Bruker EN 5107D2 resonator and an AR 600 W radiofrequency (RF) amplifier. Orientation-selective <sup>1</sup>H ENDOR spectra were recorded using the Davies ENDOR pulse sequence. Three consecutive measurements at field positions corresponding to  $g = 2.0094$ ,  $2.0059$ , and  $2.0005$  were performed for the in-cell and *in vitro* samples. For the sample of pure *E. coli* cells, the ENDOR measurement was performed at  $g = 2.0094$ , with the microwave power optimized for an  $S = 5/2$  species.

**W-band:** W-band pulse EPR measurements were carried out at  $T = 20$  K using the Bruker E680 spectrometer equipped with a Cryogenic Systems closed-cycle 6T magnet, and a variable temperature insert (VTI) that allowed varying the temperature within the range of 2 – 300 K. Additional LakeShore 335 temperature controller equipped with a Cernox sensor was used to record the sample temperature. Due to relatively high uncertainty in the external magnetic field values, the field axis of the W-band EPR spectra was adjusted so that the  $Y_{122}^{\bullet}$  spectral width matched the spin Hamiltonian parameters used for the X- and Q-band EPR/ENDOR simulations. This was achieved by compressing the x-axis of all field-swept W-band spectra by ~5%.

### 3.2.6. Analysis of orientation-selective DEER measurements

Analysis of the orientation-selective DEER data was performed in two different ways:

**Analysis by DEERAnalysis as shown in Section 3.3.4:** Each orientation-selective primary time trace was first normalized to the same signal intensity at zero time for orientation-averaging. Afterward, these traces were normalized to the signal intensity at the pump position. The summation of the DEER traces leads to the orientation-averaged time trace.

**Analysis by PeldorFit as shown in Section 3.3.5:** DeerAnalysis background-corrected data were used. Subsequently, these data were each analyzed three times with the same settings using PeldorFit. Due to uncertainty in the external magnetic field values, the field position specified in the configuration file was adjusted so that detect and pump position matched the experimental settings. All values were shifted to higher field positions with 10 G, 6 G, and 8 G for positions 1, 2, and 3, respectively.

**Table 3.1: Samples used in Chapter 3.** Y• concentrations were determined via cw-EPR experiments recorded at X-band. Furthermore, added Mn<sup>II</sup> concentrations are listed.

Experiment	Sample	Y• (μM)*	Mn <sup>II</sup> (μM)
ENDOR			
	<i>in vitro</i>	18	0
	in-cell 3	14	-
Orientation-selective DEER			
	<i>in vitro</i>	240	0
	in-cell 3	22	-
W-band EPR			
	<i>in vitro</i>	18	0
	in-cell 1 <sup>†</sup>	22	-
	in-cell 4 <sup>†</sup>	30	-
Calibration curve			
	1	150	0
	0.66	150	100
	0.54	150	200
Y <sub>122</sub> • fractions:	0.36	72	280
	0.18 (mimic 1) <sup>‡</sup>	22	100
	0.18 (mimic 2) <sup>‡</sup>	22	100
	0.12	22	132
	in-cell 1 <sup>†</sup>	22	-
	in-cell 2 <sup>†</sup>	22	-
	in-cell 3 <sup>†</sup>	14	-
Experiments with F <sub>3</sub> Y <sub>122</sub> •			
	<i>in vitro</i>	130	0
	in-cell (BL21)	17	-

\* Radical concentrations are detected via spin quantification experiments at X-band. An inherent error of at most 20% should be considered.

<sup>†</sup> Samples were produced from different cell growths, each starting from new LB-agar plates. All samples were prepared in the same way, except for the harvesting centrifugation step. In-cell 1 was centrifuged at 6000 xg for 15 min at 4 °C, whereas in-cell 2,3 and 4 were centrifuged at 3000 xg for 20 min at 4 °C.

<sup>‡</sup> Samples were produced from different *in vitro* protein purification batches.

### 3.3. Results and discussion

#### 3.3.1. Detection and identification of a radical species in *E. coli* cells

Under normal growth conditions,  $Y_{122}^{\bullet}$  concentrations in *E. coli* cells are below the detection limit for EPR spectroscopy. Hence the protein was overexpressed in *E. coli* cells.<sup>101</sup> To test the cell viability after overexpression, cells were diluted and plated onto LB-agar plates. The concentration of cells in the suspension containing wt- $\beta 2$  overexpression plasmid was  $3 - 60 \cdot 10^{11}$  cells per mL cell suspension, in remarkable agreement with previously reported numbers ( $1 - 3 \cdot 10^{11}$  TOP10 cells per mL cell suspension<sup>101</sup>). Furthermore, cell concentrations for BL21 cells lacking the overexpression plasmid were  $3 - 13 \cdot 10^{11}$  and  $4 \cdot 10^{11}$  cells per mL cell suspension before and after iron addition, respectively. These results prove that the cells used for EPR measurements were intact and alive and show that protein overexpression and radical generation do not significantly impair cell viability.

In addition, the possibility of cell damage and thus high amounts of protein leakage from the cells into the suspension buffer was excluded via polyacrylamide gel electrophoresis (**Figure 3.2A**) and EPR experiments (**Figure 3.2B**) by collecting the supernatant of suspended *E. coli* BL21 cells after wt- $\beta 2$  expression and  $Fe^{II}/O_2$  treatment. This supernatant was loaded onto an SDS-PAGE and subsequently, band intensities were compared to those of purified protein with known concentrations ( $2 \mu M$  and  $5 \mu M$ ) for analysis. Both bands of the purified wt- $\beta 2$  exhibited clearly stronger bands than the supernatant. Thus, the extracellular protein concentration of in-cell samples must be below  $2 \mu M$ , supported by cw-EPR experiments. The cell suspension treated with  $Fe^{II}$  and  $O_2$  reveals a strong EPR signal, yielding a spin concentration of approximately  $22 \mu M$  according to cw spin-counting experiments. The supernatant of this sample showed a signal with negligible intensity. A second supernatant sample from a different expression batch revealed no EPR signal. The small peak detected in this case arises from the resonator background. These results demonstrate that the detected cw-EPR signal must originate from a paramagnetic species inherent in the cells.

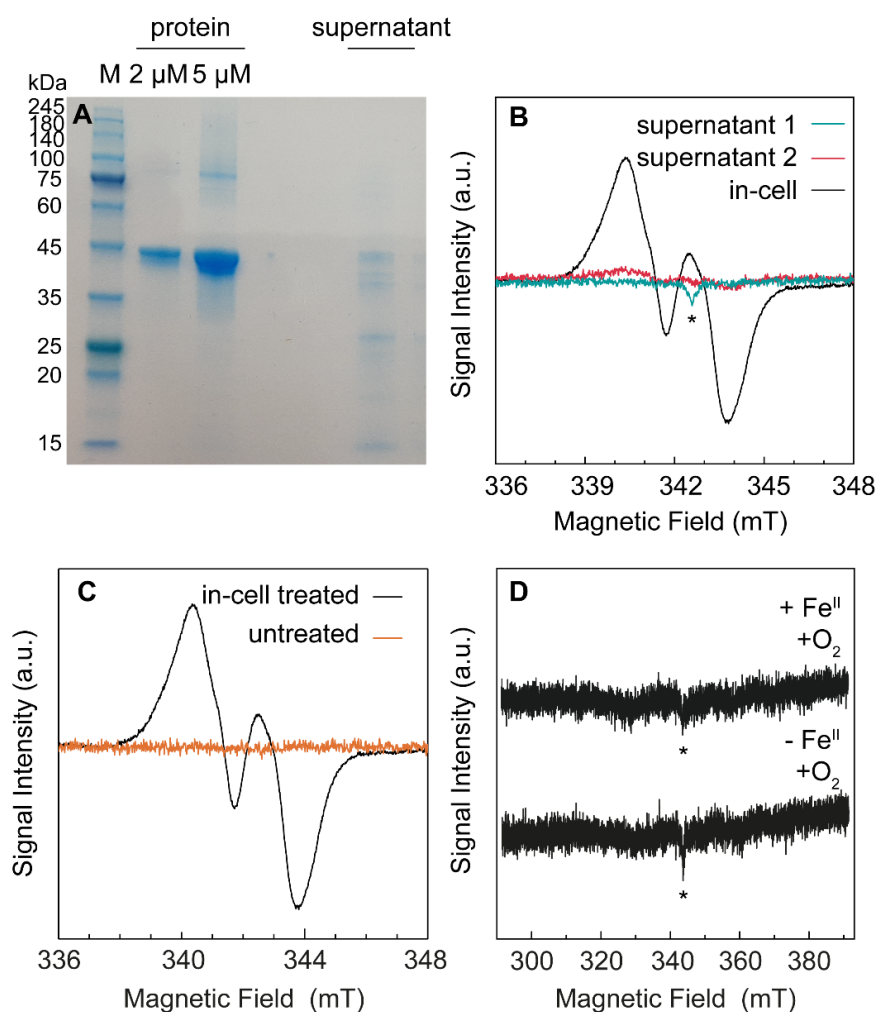


**Figure 3.2: SDS-PAGE and cw-EPR analysis of *E. coli* in-cell samples under different treatment conditions.** (A) Determination of protein leakage outside the cells via SDS-PAGE Lane M: molecular mass standards (5  $\mu\text{L}$ ); Lane protein: 5  $\mu\text{L}$  of 0.9 and 2  $\mu\text{g}$  purified wt- $\beta$ 2 having a molecular mass of 44 kDa per monomer. The concentrations of the loaded wt- $\beta$ 2 protein correspond to 2 and 5  $\mu\text{M}$ , respectively. Lane supernatant: 5  $\mu\text{L}$  supernatant of *E. coli* BL21(DE3)-Gold cell pellet (containing 14  $\mu\text{M}$   $\text{Y}_{122}^{\bullet}$  in total) collected after wt- $\beta$ 2 expression and  $\text{Fe}^{\text{II}}/\text{O}_2$  treatment. (B) Cw-EPR spectra of wt- $\beta$ 2 expressing whole *E. coli* cells (black) compared to the supernatant of two samples, collected after centrifugation for 10 min at 2000  $\times g$  and 4  $^{\circ}\text{C}$  (green and red). Supernatant 1 originates from a 14  $\mu\text{M}$   $\text{Y}^{\bullet}$  in-cell sample. Supernatant 2 was taken from the 22  $\mu\text{M}$   $\text{Y}^{\bullet}$  in-cell sample shown in black. (C) Cw-EPR spectra of wt- $\beta$ 2 expressed in whole *E. coli* cells recorded before (orange) and after (black)  $\text{Fe}^{\text{II}}/\text{O}_2$  treatment. (D) Cw-EPR spectra of *E. coli* cells grown without wt- $\beta$ 2 expression plasmid. Before the EPR experiments, the cells were treated with either  $\text{Fe}^{\text{II}}$  and  $\text{O}_2$  or only  $\text{O}_2$ . Signals arising from the resonator background are marked with an asterisk \*. Experimental conditions: 9.6 GHz, 100 K, 31.6 mW power, 1.5 G modulation amplitude, 100 kHz modulation frequency, 5.12 ms as time constant, and 19.9 ms conversion time. Number of scans: (B) 200 (black), 67 (green), 50 (red); (C) 40 (orange) and 200 (black); (D) 30 scans each.

Subsequently, cw-EPR spectra of in-cell samples overexpressing apo- $\beta$ 2 were recorded before and after treatment with  $\text{Fe}^{\text{II}}$  and  $\text{O}_2$  (Figure 3.2C). Therefore, the cell pellet was suspended in Tris buffer with or without 0.13 mM  $\text{Fe}^{\text{II}}$  salt, followed by  $\text{O}_2$  treatment of both samples. Only the iron-containing sample displayed an EPR signal, whose

signature is similar to that of  $Y_{122}\bullet$  known from *in vitro* measurements. Furthermore, BL21 cells lacking the overexpression plasmid did not reveal any EPR signal after  $O_2$  and  $Fe^{II}/O_2$  treatment (**Figure 3.2D**). These data suggest that the formed organic radical detected in the cells originates from  $Y_{122}\bullet$  in the overexpressed  $\beta_2$  subunit of *E. coli* RNR.

In order to assign and examine the generated radical species, multi-frequency (9.6, 34, and 94 GHz) EPR spectra of iron-treated *E. coli* cells were recorded and further analyzed via spectral simulations (**Figure 3.3A**). The simulation parameters (**Table 3.2**) used for the in-cell dataset were in excellent agreement with previously reported multi-frequency/ENDOR data from *in vitro*  $Y_{122}\bullet$ .<sup>71</sup>

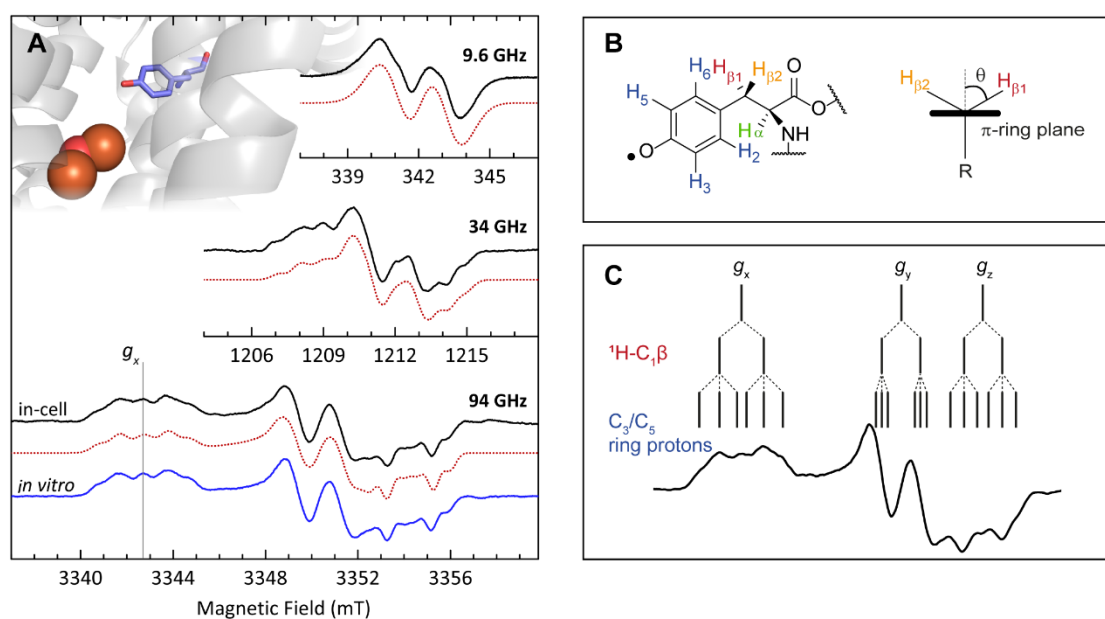


**Figure 3.3: Multi-frequency EPR spectra of  $Y_{122}\bullet$  in whole *E. coli* cells.** (A) Continuous wave EPR (9.6 GHz, top) and first-derivative pulse EPR (34 GHz, middle and 94 GHz, bottom) spectra of  $Y_{122}\bullet$  in whole *E. coli* cells. In-cell data are shown in solid black lines along with the corresponding EasySpin simulations in dotted red lines (**Table 3.2**). The 94 GHz EPR spectrum of *in vitro*  $Y_{122}\bullet$  (solid blue line) is shown for comparison. Position of the  $g_x$  value is displayed with a grey vertical line. Inset: The isolated di-iron center (orange and red spheres) and residue  $Y_{122}$  (blue sticks) are shown within the protein environment. (B) Left: Schematic representation of protons included for the simulation of  $Y_{122}\bullet$  shown in different colors. Ring protons are shown in blue. Hyperfine coupling values for  $C_{\beta}$ -methylene protons (orange and red) are strongly dependent on the angle  $\theta$ , defined by the dihedral angle between the  $C_{\beta}$ -H bond and the  $p_z$  orbital axis of  $C1$ . (C) First-derivative pulse EPR spectrum of an *in vitro* sample recorded at 94 GHz, shown together with its splitting scheme.

**Table 3.2:  $^1\text{H}$  Hyperfine coupling parameters used for spectral simulations of multi-frequency EPR spectra of  $\text{Y}_{122}\bullet$  in whole *E. coli* cells.** The  $g$ -tensor was  $g_{x,y,z} = 2.00915, 2.00460, 2.00225$ , as reported earlier.<sup>71</sup> The Euler angles  $\alpha$ ,  $\beta$ , and  $\gamma$  are defined within the EasySpin  $z,y',z''$  convention and refer to rotation from the  $g$ -tensor into the hyperfine tensor frames. Positive angles are clockwise rotations viewed along the rotation axis.

Proton	$A_x$ (MHz)	$A_y$ (MHz)	$A_z$ (MHz)	$\alpha$	$\beta$	$\gamma$
$\text{C}_{1\beta}\text{-H}$	59.0	55.0	56.0	0	0	0
$\text{C}_{2\beta}\text{-H}$	8.0	-1.0	-1.0	70	4	-7
$\text{C}\alpha\text{-H}$	1.2	-1.0	-4.1	60	-20	0
$\text{C}_3/\text{C}_5$ ring protons	-27.2	-7.9	-19.8	0	0	-25/-155
$\text{C}_2/\text{C}_6$ ring protons	4.9	7.7	1.7	0	0	25/155

Two main components play a decisive role in determining the differences in tyrosyl radicals EPR spectral shape: principal  $g$ -values and hyperfine coupling parameters related to ring- and  $\beta$ -methylene protons.<sup>198</sup> Therefore, these parameters are highly relevant when comparing *in vitro* and *in vivo* datasets, which are most evident in the 94 GHz spectra. At high frequencies, the EPR line shape is dominated by  $g$ - and hyperfine anisotropy. These parameters are both susceptible to the molecular environment of tyrosyl radicals.<sup>70,199,200</sup>

The first factor that enables an assignment to  $\text{Y}_{122}\bullet$  is the  $g_x$  value, which reports on the electrostatic environment of tyrosyl radicals. This value is affected by changes in the local environment, such as the addition or loss of H-bonds.<sup>70,199,201,202</sup> The tyrosyl radical found in *E. coli* class Ia RNR, among other reported values for RNRs from different organisms, has a uniquely high  $g_x$  value of 2.00915.<sup>71</sup> Only the tyrosyl radical formed in class Ib RNR in *Mycobacterium tuberculosis* exhibits a slightly higher  $g_x$  of 2.0092.<sup>203,204</sup> All other reported values are between 2.0076 and 2.0089.<sup>205,206</sup> A decrease in  $g_x$  upon formation of hydrogen bonds could be traced back to lower angular momentum and lower spin-orbit coupling matrix elements between the ground state and the first excited state.<sup>202</sup> In contrast,  $g_y$  is less affected by hydrogen bonds, whereas  $g_z$  remains mainly unaffected. Furthermore, broad distributions of the  $g_x$  value would indicate multiple molecular orientations or radical environments. The observed  $g_x$  value and its distribution, considered by the  $g$ -strain in the simulations, were the same for *in-cell* and *in vitro* (**Figure 3.3A**).

Another essential structural parameter is the strength of the hyperfine couplings of  $\text{C}\beta$ -methylene protons. The  $\text{C}_{1\beta}\text{-H}$  hyperfine couplings decisively influence the EPR lineshape, as depicted in **Figure 3.3C**. Their isotropic part  $a_{\text{iso}}^\beta$  is related to the dihedral angle between  $\text{C}\beta\text{-H}$  bonds and the ring plane according to the McConnell equation

$$a_{\text{iso}}^\beta = \rho_{\text{C}1}(B' + B'' \cos^2 \theta).^{207} \quad (3.1)$$

The angle  $\theta$  is defined as the dihedral angle between the  $C\beta$ -H bond and the  $p_z$  orbital axis of the  $C_1$  atom (**Figure 3.3B**). The strength of the  $C\beta$ -methylene couplings is affected by the spin density  $\rho$  on atom  $C_1$ .  $B'$  and  $B''$  are constants, whereas  $B'$  is generally neglected. According to this correlation, these couplings provide crucial information on the structure of tyrosyl radicals. Changes in the angle  $\theta$  or the spin density would immediately be reflected in the EPR lineshape.<sup>73</sup> However, the detected signals for in-cell and *in vitro* samples are almost identical.

Overall, the EPR data and simulations conclusively show that the radical generated in whole cells can be assigned to *E. coli* RNRs  $Y_{122}\bullet$  as a single radical species with one set of magnetic parameters and a well-defined orientation. Moreover, the structure and environment of  $Y_{122}\bullet$  in the cells are highly similar to those *in vitro*. These results are not unexpected considering the isolated nature of  $Y_{122}\bullet$  inside the protein, approximately 10 Å away from its surface.

### 3.3.2. Estimation of the intracellular spin concentration

In order to get an impression of the in-cell radical yield of the reconstituted apo- $\beta_2$ , cw-EPR experiments of *in vitro* and different in-cell samples were performed. All spectra revealed similar spectral lineshapes. The protein and radical content of the *in vitro* sample were determined as  $200 \pm 50 \mu\text{M}$  and  $1.2 Y\bullet/\beta_2$  via UV-Vis spectroscopy prior to EPR experiments. Consequently, the *in vitro*  $Y_{122}\bullet$  standard sample has a spin concentration of  $240 \pm 60 \mu\text{M}$ . Subsequently, EPR spectral intensities of five in-cell samples, prepared from different growths and/or distinct overexpression levels, were compared to the *in vitro* sample. This comparison demonstrated that the in-cell radical concentration is approximately 18  $\mu\text{M}$  on average, with a maximum variation between batches of  $\pm 6 \mu\text{M}$ . It should be noted that 18  $\mu\text{M}$  is the average bulk concentration in the EPR tube, which contains 200  $\mu\text{L}$  of the in-cell sample.

In order to estimate the spin concentration within the cells, the intracellular aqueous volume  $V_{\text{in}}$  of BL21(DE3) cells in the EPR tube was calculated. Previously,  $V_{\text{in}}$  of 1.9 or 2.5  $\mu\text{L mg}^{-1}$  was determined either by a concentration-dependent or a gravimetric method.<sup>208</sup> As 3 mL of buffer was used to dissolve 1 g of cell pellet, 200  $\mu\text{L}$  contained ca. 67 mg cell mass. Accordingly, out of 200  $\mu\text{L}$  cell suspension, 127  $\mu\text{L}$  or 167  $\mu\text{L}$  are reserved by intracellular volume. As spin-counting experiments revealed a bulk spin concentration of 18  $\mu\text{M}$  and protein leakage was less than 2  $\mu\text{M}$ , 200  $\mu\text{L}$  cell suspension contained ca.  $3.6 \pm 1.2 \text{ nmol } Y_{122}\bullet$ . Divided by  $V_{\text{in}}$ , this yields an average spin concentration within the cells of approximately  $25 \pm 4 \mu\text{M}$ .

### 3.3.3. Probing the H-bonding environment of $Y_{122}^{\bullet}$ in the cells via $^1\text{H}$ ENDOR

While the EPR line shape is mostly dominated by larger hyperfine couplings, smaller couplings can be assessed via ENDOR spectroscopy to characterize the H-bonding environment. Hence, orientation-selective  $^1\text{H}$  Davies ENDOR spectra were recorded at three different field positions within the  $Y_{122}^{\bullet}$  spectrum, corresponding to molecular orientations at  $g_{xy}$ ,  $g_y$ , and  $g_{yz}$  (**Figure 3.4A**). This procedure was performed for in-cell as well as for *in vitro* samples.

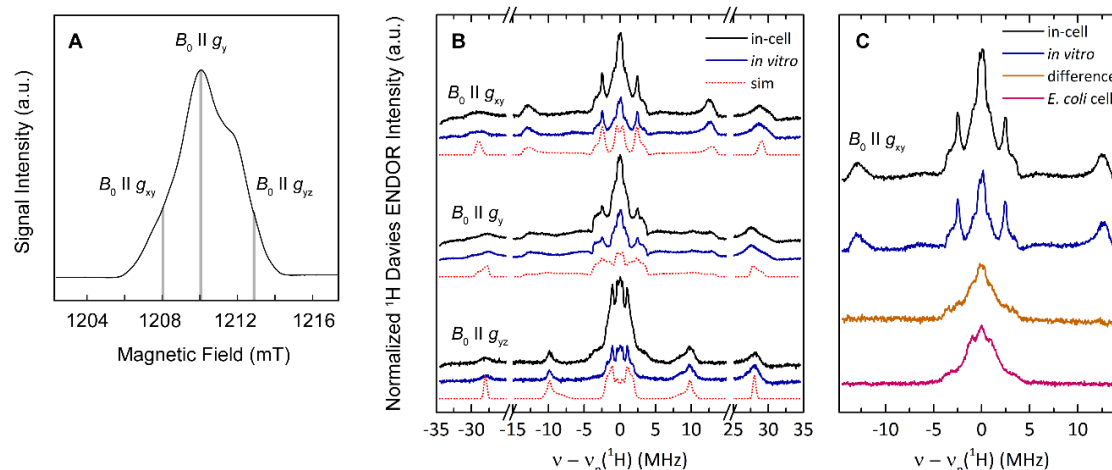


**Figure 3.4: Orientation-selective  $^1\text{H}$  Davies ENDOR of  $Y_{122}^{\bullet}$ .** (A) Field positions chosen for orientation-selective  $^1\text{H}$  Davies ENDOR measurements, exemplarily shown at a 34 GHz *in vitro*  $Y_{122}^{\bullet}$  spectrum corresponding to  $g = 2.0094$  ( $B_0 \parallel g_{xy}$ ), 2.0059 ( $B_0 \parallel g_y$ ) and 2.0005 ( $B_0 \parallel g_{yz}$ ). (B) Orientation-selective  $^1\text{H}$  Davies ENDOR spectra of in-cell (black) and *in vitro* (blue)  $Y_{122}^{\bullet}$ , recorded at 34 GHz at three field positions. Simulations (red dotted lines) were performed using the spin Hamiltonian parameters determined by Tkach *et al.* (**Table 3.2**).<sup>71</sup> (C) ENDOR spectra ( $B_0 \parallel g_{xy}$ ) of in-cell (black) and *in vitro* (blue)  $Y_{122}^{\bullet}$ , the scaled subtraction result (orange), and  $\text{Mn}^{\text{II}}$ -related  $^1\text{H}$  ENDOR features of iron-untreated *E. coli* cells (pink).

EasySpin simulations could reproduce the spectral lines using the same parameters reported in **Table 3.2** for seven internal  $^1\text{H}$  hyperfine couplings (**Figure 3.4B**). However, the  $^1\text{H}$  Davies ENDOR line shape of in-cell  $Y_{122}^{\bullet}$  contained additional spectral features compared to the *in vitro* one. Therefore, the *in vitro* spectrum was subtracted from the in-cell data after normalizing the spectral intensities to the  $\text{C}_1\beta\text{-H}$  ENDOR line, whose couplings are observed at around  $\pm 28$  MHz in **Figure 3.4B**. The resulting spectrum (orange trace in **Figure 3.4C**) is very similar to the  $^1\text{H}$  Davies ENDOR spectrum recorded with *E. coli* cells containing overexpressed apo- $\beta 2$  without  $\text{Fe}^{\text{II}}/\text{O}_2$  treatment (pink trace in **Figure 3.4C**). ESE spectra of this sample revealed  $\text{Mn}^{\text{II}}$  as the only EPR-detectable species. This comparison demonstrates that the additional proton hyperfine couplings observed for the in-cell sample are not related to  $Y_{122}^{\bullet}$  but rather to  $\text{Mn}^{\text{II}}$  in *E. coli*. Indeed, the additional  $^1\text{H}$  ENDOR features detected in the untreated *E. coli* cells closely resemble the in-cell  $\text{Mn}^{\text{II}}$  ENDOR line shape established in the previous literature<sup>209</sup>, with broad shoulders reaching  $\pm 3.8$  MHz around the  $^1\text{H}$  Larmor frequency, indicative of a water-

ligated  $Mn^{II}$  species.<sup>210</sup> The presence of manganese in the cells is not surprising<sup>211</sup> and is a well-known problem in in-cell EPR studies.<sup>168,212</sup> The fact that besides the Mn-dependent proton coupling, no further  $^1H$  hyperfine couplings are observed is in line with the multi-frequency EPR data. No additional H-bonds are detected for  $Y_{122}\bullet$  in the cells compared to *in vitro* conditions, showing that  $Y_{122}\bullet$ 's structure and its H-bonding environment are conserved.

### 3.3.4. In-cell distance distribution of $Y_{122}\bullet$ - $Y_{122}\bullet$ obtained via orientation-averaged DEER measurements

DEER measurements between two  $Y_{122}\bullet$  residing in wt- $\beta 2$  deliver information about tertiary and quaternary protein structures. Since orientation-selectivity is known to be found for the  $Y_{122}\bullet$ - $Y_{122}\bullet$  pair, orientation-selective DEER spectra were measured.<sup>213</sup> To cover the whole EPR line, three DEER traces were recorded at distinct g-tensor orientations (**Figure 3.5A**) for *in vitro* and in-cell samples, and the obtained dipolar traces were summed up, yielding an orientation-averaged DEER trace. Fourier transformation of in-cell and *in vitro* traces led to an almost ideal Pake Pattern. The resulting orientation-averaged form factors and extracted distance distributions evaluated by the software DeerAnalysis are depicted in **Figure 3.5B** and **C**, respectively.

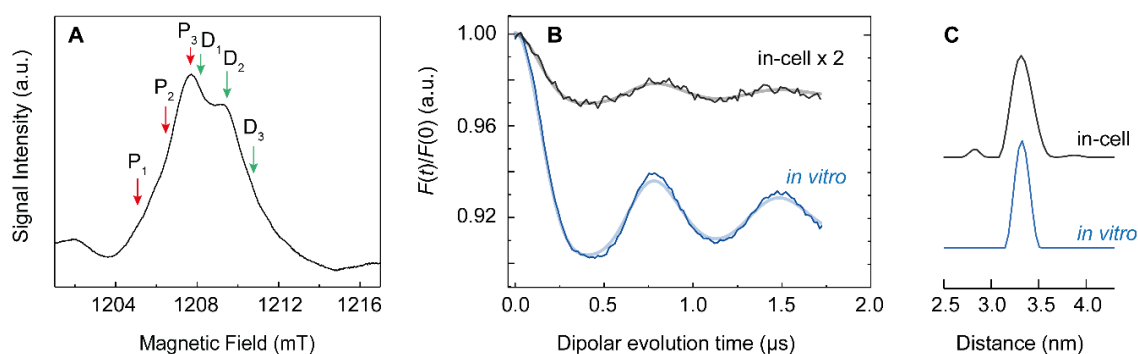


**Figure 3.5: Orientation-averaged time traces for  $Y_{122}\bullet$ - $Y_{122}\bullet$  in *E. coli* RNR for in-cell and *in vitro*.** (A) ESE-detected EPR spectrum of an in-cell sample, recorded at 10 K and 34 GHz. Three consecutive DEER measurements for *in vitro* and in-cell samples were spaced by 14 G. Detect (D1, D2, and D3) and pump (P1, P2, and P3) positions for orientation-selective DEER measurements are indicated with green and red arrows, respectively. Frequency separations between detection and pump positions were 84 MHz. (B) Background- and phase-corrected, normalized, and orientation-averaged 34 GHz in-cell (black) and *in vitro* (blue) DEER traces of the  $\beta 2$  subunit of *E. coli* RNR. Fits are overlaid in a paler shade. (C)  $Y_{122}\bullet$ - $Y_{122}\bullet$  distance distributions obtained by DeerAnalysis. The original in-cell trace is magnified by a factor of two for better visualization. Details of the analysis are shown in the supporting information in **Figure A.1**.

Analysis of the in-cell DEER data revealed a main mean distance at 3.32 nm with a distance distribution of  $\sigma = 0.09$  nm ( $\sigma$  is the standard deviation of the distribution, which is assumed to be Gaussian). This distance can directly be assigned to the  $Y_{122}\bullet$ - $Y_{122}\bullet$  pair, as it is identical to the *in vitro*  $Y_{122}\bullet$ - $Y_{122}\bullet$  distances detected here (3.32 nm with

$\sigma = 0.07$  nm) and previously ( $3.31$  nm<sup>64</sup>). The detected narrow in-cell distance distribution and the presence of orientation-selectivity demonstrate the rigid nature of  $Y_{122}\bullet S$ , as different conformers would lead to a broadened distance distribution. More importantly, these data support a consistent structure of the  $\beta 2$  dimer in cells and *in vitro* since changes in the quaternary structure would again result in a change or broadening of the distance distribution.

The distance distribution of wt- $\beta 2$  in cells shows the presence of an additional distance at around  $2.8$  nm with an extremely small intensity, which is also validated. Three possibilities were evaluated to elucidate the origin of this peak:

### I. A distinct $Y_{122}\bullet$ - $Y_{122}\bullet$ distance

A distinct  $Y_{122}\bullet$  conformer could lead to a smaller distance detected between both residues. However, this may not be the cause of this peak since no changes are observed in the  $94$  GHz EPR spectrum.

### II. A $Mn^{II}$ - $Mn^{II}$ distance

As reported previously,  $Mn^{II}$  can occupy the iron site in wt- $\beta 2$  *in vitro*.<sup>99,100</sup> Considering the high  $Mn^{II}$  content within the cells, a possible  $Mn^{II}$ - $Mn^{II}$  distance was investigated by performing  $Mn^{II}$  DEER experiments with *E. coli* cells that either contain the apo wt- $\beta 2$  protein or completely lack the overexpression plasmid. None of these experiments showed any dipolar modulation and thus did not result in any distance (**Figure 3.6**). These data suggest that a  $Mn^{II}$ - $Mn^{II}$  pair may not cause the occurrence of an additional distance.

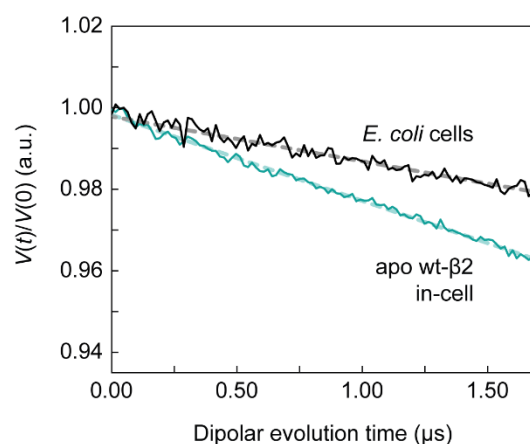


**Figure 3.6:** DEER measurements of *E. coli* cells that contain overexpressed apo wt- $\beta 2$  (blue) or lack it (black) at  $34$  GHz and  $10$  K. The fits shown with dashed lines are based on a homogeneous, three-dimensional background function.

### I. Orientation selection artifact

The observed second distance resembles the one extracted by DeerAnalysis when the distance vector  $r_{Y_{122}^{\bullet}-Y_{122}^{\bullet}}$  is parallel to the magnetic field, with the  $v_{\parallel}$  component dominating the dipolar spectrum. The normalization and summation procedure of the individual orientation-selective DEERs is not ideal for in-cell traces due to the low S/N ratios and huge  $Mn^{II}$  contribution at pump and detect positions. Hence, the distance resulting from the  $v_{\parallel}$  component might be over-pronounced in the orientation-averaged trace leading to the observed second peak.

This evaluation suggests that the additional small peak of the in-cell distance distribution is most likely an artifact caused by the orientation-averaging procedure. Low S/N ratios of the individual in-cell DEER traces and the spectral overlap between  $Y_{122}^{\bullet}$  and  $Mn^{II}$  EPR features complicate the orientation-averaging process, which is further discussed in Section 3.3.6.

#### 3.3.5. Analysis of orientation-selective DEER measurements via PeldorFit

Nowadays, many different softwares are available to assist in the analysis of DEER data. Probably the most widely used one is DeerAnalysis, as also utilized for the analysis in the previous section of this work. However, this analytic tool is not ideally suited for analyzing orientation-selective DEER data. A software that was specifically designed for this purpose is PeldorFit. The underlying principle is to fit the time traces by using a geometric model of the spin system. This model is described by a defined set of parameters consisting of the distance and relative orientation between the electron spin centers. These parameters are then optimized during the fitting process through a genetic algorithm in order to minimize the root-mean-square deviation (RMSD) between experimental and simulated traces. The accuracy of the optimized fitting parameters can subsequently be assessed by error plots, which allows a detailed analysis of the spatial arrangement of the paramagnetic pair. Conformational changes between *in vitro* and *in vivo* samples of RNR  $\beta_2$  could thus be revealed. Therefore, the previously presented orientation-selective DEER data were additionally evaluated with PeldorFit.

For the fitting process, a configuration file must be provided in which, e.g.,  $g$ - and  $A$ -tensors of the system under investigation must be specified. However, the software only allows consideration of two nuclei. Therefore, protons with the strongest coupling ( $C_{1\beta}$ -H and  $C_3$ -H) were chosen. All other couplings must be neglected for the analysis. Furthermore,  $g$ -values given in **Table 3.2** were used. The fitting results of *in vitro* DEER time traces are shown in **Figure 3.7A**. The analysis results in a  $Y_{122}^{\bullet}$ - $Y_{122}^{\bullet}$  distance  $r$  of 3.31 nm (**Table 3.3**), which is in excellent agreement with the previous results obtained by DeerAnalysis.

Furthermore, the geometric arrangement can be assessed by the angles  $\xi$ ,  $\varphi$ ,  $\alpha$ ,  $\beta$ , and  $\gamma$ . The reference coordinate system coincides with the  $g$ -tensor axes of one spin, termed spin A. Orientation of the  $g$ -tensor axes of the second spin, spin B, is given by the three Euler angles  $\alpha$ ,  $\beta$ ,  $\gamma$  with  $z, x', z''$  convention. The vector connecting spin A and B is defined by the polar angle  $\xi$  and the azimuthal angle  $\varphi$ . The calculated angles  $\xi$  and  $\varphi$  agree with the spatial arrangement of both  $Y_{122S}$  in the crystal structure (**Figure 3.7C and D**), showing the model's validity. However, it must be mentioned that the different runs of the optimization process often led to different results for the Euler angles while using the same settings (**Figure A.2 and Table A.1**). It can also be seen from **Figure 3.7** that the orientation of the spin B does not exactly match the crystal structure, due to  $\beta$  being underestimated by the fit. This indicates that the Euler angles and thus the orientation of spin B cannot be determined unambiguously with the available measurement set. Further measurements at additional field positions could solve this problem. **Table 3.3** lists only the fitting results with the highest agreement compared to literature values.<sup>213</sup>

**Table 3.3:  $Y_{122\bullet}$ - $Y_{122\bullet}$  pair distance analysis derived from DEER experiments using PeldorFit.** The value in brackets indicates the error of the respective parameter. The error is determined by the range in which 110% of the minimal RMSD is reached. The first value per column is the mean value of the parameter, while the second value represents the uniform width (or in case of  $r$  the standard deviation) of each parameter. Reference values were transformed from the  $z, y', z''$  into  $z, x', z''$  convention by using Matlab.

Parameter		Value				Denysenkov <i>et al.</i> <sup>213</sup>
		<i>in vitro</i>		in-cell		
$r$ (nm)	$\Delta r$ (nm)	3.31(0.03)	0.03(0.04)	3.32(0.03)	0.10(0.05)	3.31
$\xi$ (°)	$\Delta\xi$ (°)	28(9)	1(32)	19(19)	8(14)	
$\varphi$ (°)	$\Delta\varphi$ (°)	94(13)	20(71)	77(50)	11(84)	
$\alpha$ (°)	$\Delta\alpha$ (°)	172(12) <sup>§</sup>	6(9) <sup>§</sup>	108(21) <sup>§</sup>	4(42) <sup>§</sup>	174
$\beta$ (°)	$\Delta\beta$ (°)	30(6) <sup>§</sup>	66(5) <sup>§</sup>	12(17) <sup>§</sup>	74(46) <sup>§</sup>	118
$\gamma$ (°)	$\Delta\gamma$ (°)	7(5) <sup>§</sup>	77(20) <sup>§</sup>	70(9) <sup>§</sup>	1(98) <sup>§</sup>	6

Additionally, the orientation-selective DEER time traces of the in-cell sample were analyzed in the same way. Details of the analysis can be found in **Figure A.3 and Table A.2**. The determined  $Y_{122\bullet}$ - $Y_{122\bullet}$  distance, as well as the angles  $\xi$  and  $\varphi$  agree within error for *in vitro* and in-cell samples (**Table 3.3**). Moreover, the distance distribution of the in-cell sample is somewhat broader compared to the *in vitro* one, reproducing the analytical results of DeerAnalysis. These results hint at the absence of conformational changes of  $Y_{122\bullet}$  in the cells compared to *in vitro*. However, this statement is only valid with

<sup>§</sup> These values are not reliable. For explanation see main text and supporting information to Chapter 3.

reservations due to the large error of  $\xi$  and  $\varphi$ . The Euler angles do not match the *in vitro* and literature values, which is not surprising considering the enormous variance of the individual fitting procedures. Therefore, no meaningful analysis of the data can be given by PeldorFit.

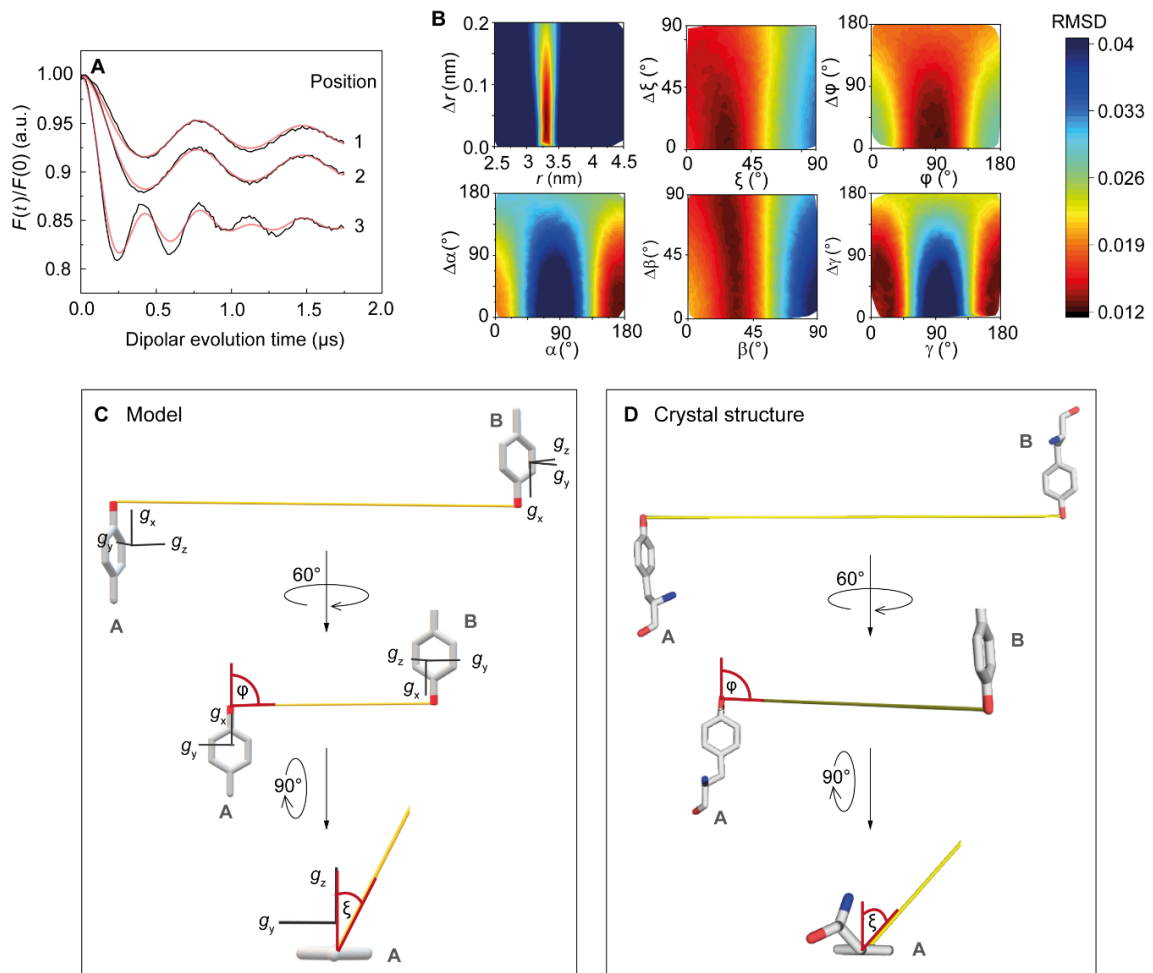


**Figure 3.7: Analysis of 34 GHz orientation-selective DEER data of  $Y_{122}\bullet$ - $Y_{122}\bullet$  in *E. coli* RNR *in vitro*.** (A) Orientation-selective 34 GHz DEER time traces acquired at different positions (1, 2, 3) overlaid with the PeldorFit simulations (red). Traces and positions correspond to the ones presented in **Figure 3.5**. (B) RMSD between experimental and simulated DEER time traces as a function of the geometric parameter of PeldorFit. (C) Geometric arrangement of the  $Y_{122}\bullet$ - $Y_{122}\bullet$  pair as predicted by PeldorFit, visualized by a model consisting of spin A and B. The  $g$ -tensor is shown in black. The directions of its principal axes are collinear with the molecular axes.<sup>214,215</sup> (D) Geometric arrangement of the  $Y_{122}\bullet$ - $Y_{122}\bullet$  pair obtained from the crystal structure, PDB: 5CI4<sup>35</sup>.

So far, PeldorFit has mainly been used for systems containing nitroxide<sup>216–218</sup> or copper<sup>219,220</sup> labels, whereas distances between organic native radicals in a protein have not yet been investigated. This is the first time to be shown that PeldorFit is also a good choice for analyzing orientation-selectivity in intrinsic paramagnetic centers. The

investigation of in-cell DEER data may be complicated by the presence of manganese, making this software of limited use for such more complex systems.

### 3.3.6. Detection and evidence of Mn<sup>II</sup> in the cellular environment

Different metals are present in all living systems, including the paramagnetic metal manganese. To illustrate the contribution of Mn<sup>II</sup> to the in-cell spectra, different Hahn echoes and a refocused echo were recorded with three different samples (**Figure 3.8**):

- I. An in-cell sample with 22  $\mu\text{M}$  bulk Y<sub>122</sub>• concentration.
- II. An *in vitro* sample with 240  $\mu\text{M}$  Y<sub>122</sub>• radical concentration.
- III. *E. coli* cells that lack the wt- $\beta$ 2 overexpression plasmid, consequently having a Y<sub>122</sub>• concentration below the detection limit.

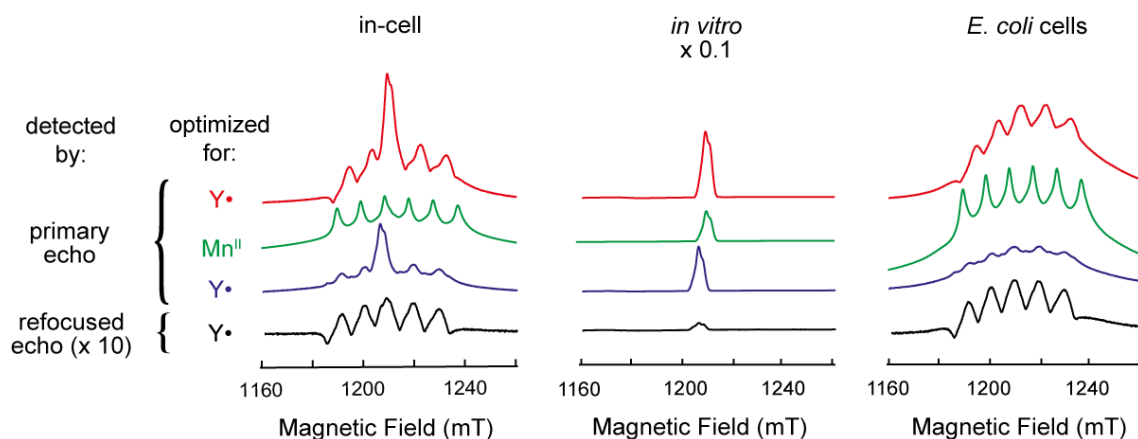


**Figure 3.8: 34 GHz ESE spectra of Y<sub>122</sub>• and Mn<sup>II</sup> in different samples.** Pulse EPR spectra of Y<sub>122</sub>• in cells (left) and *in vitro* (middle) compared to *E. coli* cells without overexpression plasmid (right). The detection is either optimized for Y• (red) or Mn<sup>II</sup> (green). Furthermore, the optimization results for Y• at the detect frequency of the DEER experiments (blue) are shown along with the refocused echo field-swept spectra (black). The EPR spectra were recorded at 10 K and normalized to the same video gain and number of scans. Experimental conditions:  $\pi = 28$  ns for the measurements at the pump frequency and  $\pi = 70$  ns for the detect frequency;  $\tau_1 = 300$  ns (green with 200 ns),  $\tau_2 = 2.1$   $\mu\text{s}$  (refocused echo); srt = 4 ms (green with 2 ms), shots per point = 100, microwave power = 20 mW (green with 3.2 mW).

The Hahn echo spectra were optimized to detect either Y<sub>122</sub>• or Mn<sup>II</sup> at pump or detect frequencies for DEER experiments. Optimization for Mn<sup>II</sup> detection was accomplished by lowering the microwave power and shot repetition time, revealing the characteristic six hyperfine lines of Mn<sup>II</sup> species in both cellular samples. Mn<sup>II</sup> in its 3d<sup>5</sup> configuration has a total electron spin state of  $S = 5/2$ .<sup>221</sup> This results in five possible EPR transitions with  $\Delta m_S = \pm 1$ . Its effective spin Hamiltonian can be expressed as

$$\begin{aligned}\hat{\mathcal{H}}_{\text{eff}} &= \hat{\mathcal{H}}_{\text{EZ}} + \hat{\mathcal{H}}_{\text{HF}} + \hat{\mathcal{H}}_{\text{ZFS}} \\ &= \frac{\mu_B}{\hbar} \mathbf{B}_0^T \mathbf{g} \hat{\mathbf{S}} + \hat{\mathbf{S}}^T \mathbf{A} \hat{\mathbf{I}} + D \left( \hat{S}_z^2 - \frac{1}{3} \hat{S}^2 \right) + E (\hat{S}_x^2 - \hat{S}_y^2).\end{aligned}^{222}$$

The Hamiltonian demonstrates that hyperfine interactions of the nuclear spin  $I = 5/2$  further split the EPR transitions into six lines. Additionally,  $\text{Mn}^{\text{II}}$  experiences zero-field splitting, which further splits the energy levels of the different  $m_S$  spin states. In  $\text{Mn}^{\text{II}}$  EPR spectra, usually the hyperfine lines of the central transition ( $m_S = -1/2 \leftrightarrow +1/2$ ) are resolved, while the so-called outer transitions ( $m_S = \pm 3/2 \leftrightarrow \pm 1/2$  and  $m_S = \pm 5/2 \leftrightarrow \pm 3/2$ ) are unresolved and appear as broad spectral wings.<sup>223</sup> The anisotropy of the Zeeman interactions is usually quite small, leading to signals centered around  $g = 2$ .<sup>222</sup> Upon increasing the mw power to optimize for  $Y^\bullet$  detection, forbidden transitions with  $\Delta m_S = \pm 1$  and  $\Delta m_I = \pm 1$  become predominant, leading to broad signals located between the central transitions as seen earlier.<sup>224</sup>

Especially in the refocused echo, manganese is the predominant species due to its longer transverse relaxation time (supporting information **Figure A.4**). Furthermore, significant changes in the detected  $\text{Mn}^{\text{II}}$  lineshape are observed upon switching the  $\pi$  pump pulse optimized for an  $S = 1/2$  species on or off (**Figure 3.9**). The spectrum shown on the right-hand side was obtained by integrating the refocused echo with a pump pulse applied at zero dipolar time. Adding the pump pulse leads to an accentuation of the allowed EPR transitions of the  $\text{Mn}^{\text{II}}$  species. As a result, the absorption maximum of  $Y_{122}^\bullet$  falls into a local absorption minimum of the  $\text{Mn}^{\text{II}}$  spectrum and thus contributes with a higher relative influence on the total spectral intensity as compared to the spectrum without the pump pulse applied. Pump pulses influencing the refocused echo have been reported for  $\text{Gd}^{\text{III}}$  echo signals in previous literature.<sup>225–227</sup>

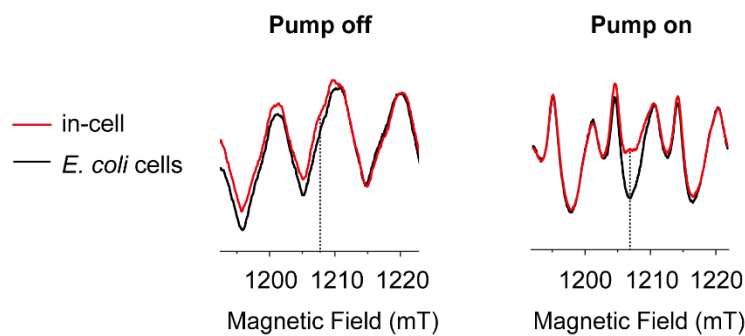


**Figure 3.9: Refocused spin echo field sweep experiments with pump pulse on or off.** Spectra were recorded with an in-cell sample (red) or *E. coli* cells (black) with the pump pulse off (left) or applied at the primary echo position (right). Spectra are normalized to the  $\text{Mn}^{\text{II}}$  intensity. The observer position of the DEER experiments is marked with a dashed line. Experimental conditions:  $\pi_{\text{det}} = 70$  ns,  $\pi_{\text{pump}} = 28$  ns,  $\text{srt} = 4$  ms;  $\text{spp} = 100$ ,  $\tau_1 = 300$  ns,  $\tau_2 = 2.1$   $\mu\text{s}$ , microwave power = 20 mW.

### 3.3.7. Investigating the in-cell radical distribution via DEER spectroscopy

Being able to detect a  $Y_{122}\bullet$ - $Y_{122}\bullet$  distance in the cells is not self-evident because *in vivo* radical distribution in  $\beta 2$  subunits is unknown. The radical distribution within the cells, which was suggested to play a key role in RNR regulation and activity,<sup>7,101</sup> can be assessed via the modulation depth parameter of DEER experiments. As  $\Delta$  depends on the fraction of spin pairs in a sample, monomers and the presence of other paramagnetic species will suppress the observed modulation depth. A comparison of the orientation-averaged DEER traces of **Figure 3.5** already indicated a severe reduction in modulation for the in-cell traces compared to *in vitro*, which is not surprising considering the substantial contribution from  $Mn^{II}$ . To clarify whether  $Mn^{II}$  solely accounts for the reduction of  $\Delta$  in the cells, its effect on  $\Delta$  was quantified by adding various amounts of  $Mn^{II}$  to *in vitro* RNR samples (**Figure 3.10**). DEER measurements were performed at position 1 as indicated in **Figure 3.5A**. Subsequently, the modulation depth was plotted against the fraction of  $Y_{122}\bullet$  monitored in the refocused echo with the pump pulse applied. The  $Y_{122}\bullet$  fraction was calculated via:

$$Y_{122}\bullet \text{ fraction} = I(Y_{122}\bullet) / [I(Mn^{II}) + I(Y_{122}\bullet)] \quad (3.2)$$

measured at the detect position (dashed line in **Figure 3.10A**). This plot resulted in a calibration curve with a positive linear relationship, as shown in **Figure 3.10D** (black data points). As expected, a substantial reduction in  $\Delta$  with increasing  $Mn^{II}$  fraction is observed. The modulation depth of *in vitro* wt- $\beta 2$  samples without additional  $Mn^{II}$  neither depends on the protein nor the spin concentration,<sup>213</sup> according to the ‘two or none’ model. Hence,  $Mn^{II}$  is the only reason for a reduced  $\Delta$  in the *in vitro* samples. The metal ions are homogeneously distributed and thus do not contribute to the detected distances and distributions, as shown in **Figure 3.6**.

The same procedure was followed with three different in-cell samples from different expression batches (see **Table 3.1**). In all cases, the detected modulation depth falls below the *in vitro* calibration curve (red data points in **Figure 3.10D**). Details of the measurements can be found in **Figure A.5**. The variance in modulation depth within the different cellular samples is to be expected, as it is a living, dynamic system, and furthermore, expression conditions can never be fully reproduced despite all efforts. The reduction of in-cell  $\Delta$  becomes particularly evident in the direct comparison with a sample prepared to mimic the cellular conditions, shown in yellow in **Figure 3.10**. Duplicates of this mimic were prepared as shown in **Figure A.5**, but for simplicity, only one of them is shown here. Both *in vitro* mimics showed very similar  $Y_{122}\bullet$  fractions compared to the in-cell samples. However, the detected modulation depth for in-cell samples is consistently lower than for the mimics. This result shows that the presence of manganese alone cannot explain the reduction of  $\Delta$  in the cells. As  $Y_{122}\bullet$  and  $Mn^{II}$  are the only paramagnetic species detected within the cells, an additional monomeric species must be present in the cell. Either some of the  $\beta 2$  dimers must contain only one  $Y_{122}\bullet$ , or

$Y_{122}^\bullet$ -carrying  $\beta$ -monomers do exist, both possibilities leading to further reduction of  $\Delta$  values. *In vivo* presence of 1  $Y^\bullet$  per  $\beta_2$  would be consistent with the asymmetric  $\alpha\beta_2$  complex structure. Either way, these data suggest a distinct radical distribution being present in *E. coli* cells compared to the *in vitro* 'two or none' hypothesis. Such a distinct radical distribution has never been observed in *E. coli* RNR before and strongly supports a model in which protein activity is regulated via modulation of  $Y^\bullet$  concentrations in the cells.

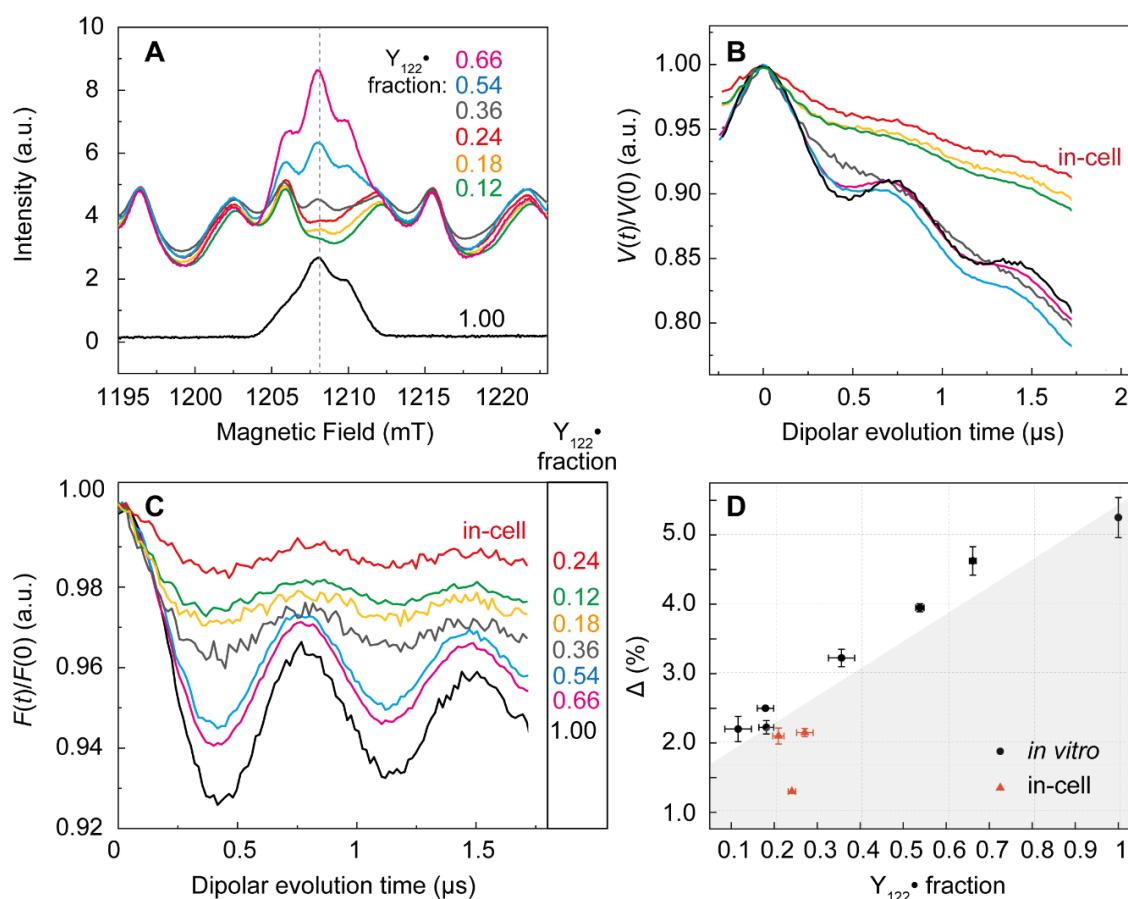


**Figure 3.10: Modulation depth analysis of *in vitro*  $\beta_2$  samples containing different equivalents of  $Mn^{II}$  compared to *in-cell* samples.** (A) Q-band field-swept EPR spectra of RNR/ $Mn^{II}$  mixtures and an *in-cell* sample (red trace) recorded via refocused spin echo with the pump pulse applied at the primary echo position. Spectra are normalized to  $Mn^{II}$  intensity. (B) Primary DEER traces and (C) form factors of the corresponding samples. (D) Calibration curve for the modulation depth as a function of relative  $Y_{122}^\bullet$  contribution to the refocused echo. The area below the curve is shaded as a guide to the eye.

Another fact to note is that the background slope of the primary DEER traces (**Figure 3.10B** and **Figure A.5**) of *in-cell* data does not exceed the steepness of the *in vitro* traces, which excludes high local spin concentrations.<sup>134,228</sup> The slope of the *in-cell* background is in a comparable range to the mimics, while samples with higher radical concentrations (70  $\mu$ M grey and 150  $\mu$ M black, pink, and blue in **Figure 3.10**) exhibited significantly

steeper backgrounds. This shows that the local  $Y_{122}\bullet$  concentration is substantially lower than  $70\ \mu\text{M}$  and implies that RNR  $\beta 2$  is homogeneously distributed within the cells, as supported by  $T_m$  measurements (**Figure A.6**). This result is in perfect agreement with the calculated intracellular radical concentration from Section 3.3.2.

### 3.3.8. The effect of chloroform on radical yield and cell viability

In previous in-cell EPR experiments performed on  $[2\text{Fe-2S}]$  clusters, it was proposed that the addition of chloroform enhances cell permeability so that reducing agents could be effectively delivered into the cytosol.<sup>193,229</sup> Sodium dithionite is required as a reducing agent to make  $[2\text{Fe-2S}]$  clusters accessible for EPR spectroscopy. In their studies, 10% (v/v) chloroform was added to the cells immediately prior to freezing the samples. In the case of RNR, no sodium dithionite is needed; however, adding chloroform might also facilitate the iron supply to the cells. To test this hypothesis and to probe whether chloroform addition thus leads to higher radical yields, samples were prepared with different amounts, ranging from 0.5 to 10%, directly added after iron addition. Subsequently, X-band cw-EPR spectra were recorded, as shown in **Figure 3.11A**. In the next step, double integrals of the spectra were plotted as a function of chloroform content (**Figure 3.11B**). Except for the sample with 5% chloroform, all samples show reduced signal intensity compared to the chloroform-free sample. Intriguingly, the addition of chloroform decreases the in-cell  $Y_{122}\bullet$  concentration instead of increasing the yield. This observation is supported by Q-band measurements performed with a second wt- $\beta 2$  expression batch (**Figure A.7**).

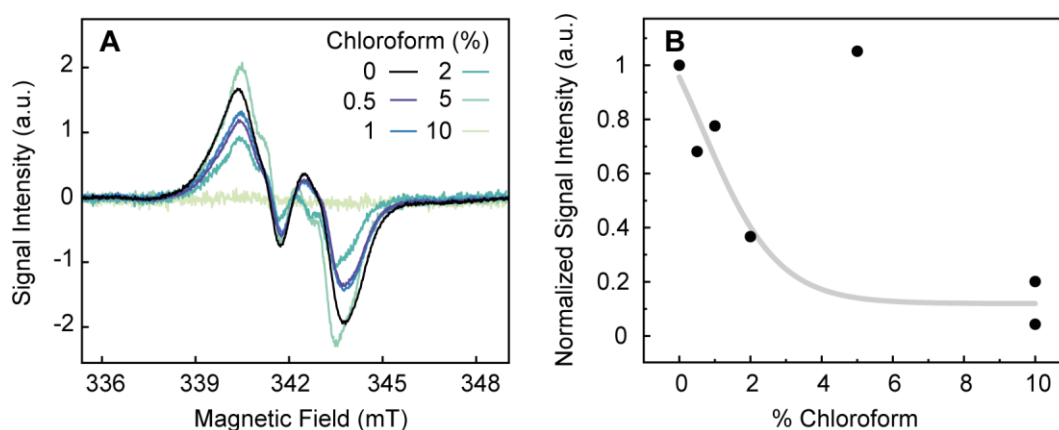


**Figure 3.11: Cw-EPR spectra of in-cell samples supplemented with chloroform showing signal intensities as a function of chloroform content.** (A) 9 GHz spectra of  $Y_{122}\bullet$  in cells after the addition of different amounts of chloroform. (B) Double integrals normalized to 1, plotted against the chloroform content. The sample containing 10% chloroform was prepared as a duplicate. Experimental conditions: 9.6 GHz, 100 K, 31.6 mW power, 1.5 G modulation amplitude, 100 kHz modulation frequency, 5.12 ms as time constant, and 19.9 ms conversion time.

Furthermore, it can be seen from the X-band spectra that the addition of chloroform causes slight changes in the EPR lineshape, such as the additional spectral features centered around 342 mT. Their appearance could well be caused by the presence of the underlying manganese signal. In order to analyze the lineshape more precisely, W-band spectra of samples containing 0% and 1% chloroform were compared (**Figure 3.12**). As can be seen from the figure, both spectra highly agree in their EPR lineshape. For example, the  $g_x$  value (shown with a solid gray line) is unchanged and the  $C\beta$ -methylene proton couplings, which provide essential information about  $Y^\bullet$  conformations, are also consistent (shown with dashed gray lines). However, it is important to note that not all of these couplings are resolved in the spectra, such as those at 3343 mT. These couplings cannot be absent since the splitting scheme must be symmetric around  $g_x$ , as shown previously in **Figure 3.3**. The reason for the invisibility of these couplings is the suppressed, underlying manganese signal, which can only be separated by a complex background subtraction (**Figure A.8**). A direct influence of chloroform on the protein structure and thus on the EPR lineshape can consequently not be verified. It is possible that the presence of different  $Mn^{II}$  species causes the observed differences.

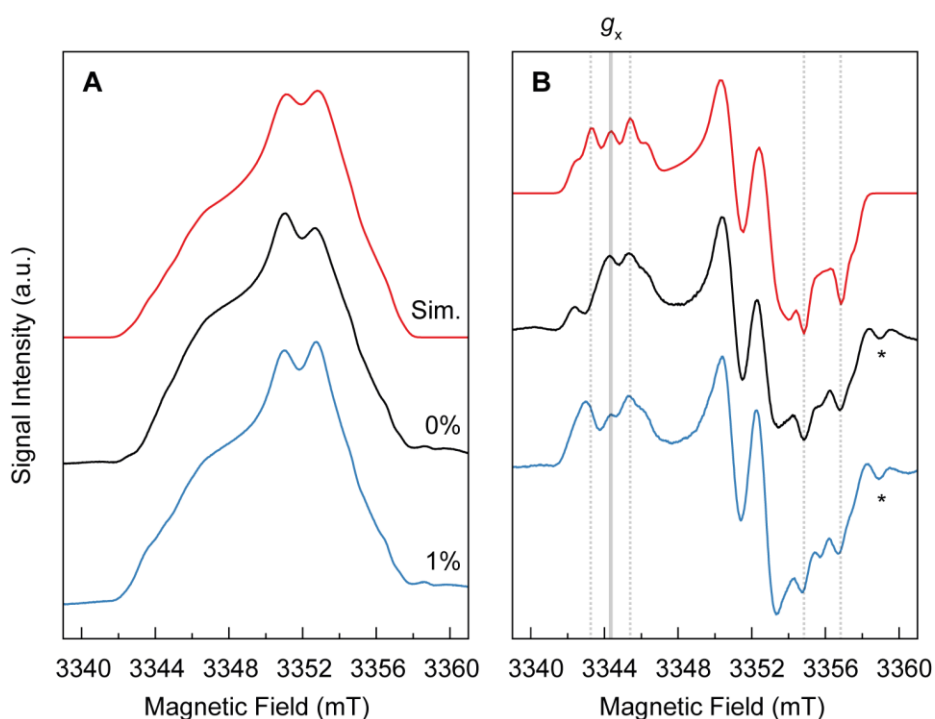


**Figure 3.12: ESE spectra of  $Y_{122}^\bullet$  in *E. coli* cells measured at 94 GHz.** (A) Absorption spectra and (B) pseudomodulated spectra (modulation amplitude = 5 G) of *E. coli* cell samples expressing wt- $\beta 2$  and containing either no (black) or 1% chloroform (blue), shown together with spectral simulations (red). Simulations were performed by EasySpin, using parameters shown in **Table 3.2**. Solid gray vertical line indicates the position of the  $g_x$  value. Dashed lines show the positions of  $C\beta$ -methylene protons couplings.  $Mn^{II}$  signals are marked with an asterisk \*. Acquisition parameters: Temperature = 20 K,  $\pi = 32$  ns,  $\tau = 320$  ns, srt = 15 ms, spp = 80.

Another factor that must be considered when utilizing chloroform is cell viability. To check this property, 20  $\mu\text{L}$  of cell suspension were plated up to a  $10^{10}$  dilution onto LB-agar plates and allowed to incubate overnight at 37 °C. No colonies were observed for chloroform-containing samples, whereas the chloroform-free samples showed strong growth. Furthermore, liquid cultures were prepared by inoculating 5 mL of chloroform containing LB medium with a single colony, followed by incubation at 37 °C overnight. Only the samples with 0% and 0.5% chloroform resulted in cloudy solutions, indicative of cell growth, whereas all other samples remained clear. SDS-PAGE analysis of these samples illustrates that a chloroform content of 0.5% is already sufficient to increase protein leakage marginally, as an increase in extracellular protein content is observed (**Figure 3.13**).

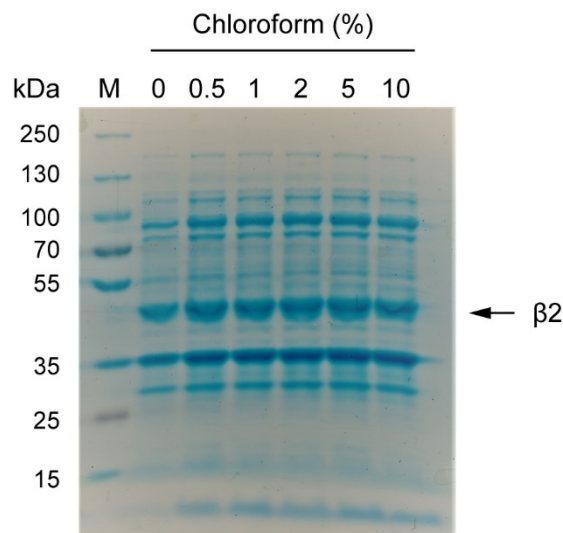


**Figure 3.13: SDS-PAGE analysis of the supernatant of *E. coli* cells treated with different amounts of chloroform.** An *E. coli* cell-suspension overexpressing wt- $\beta 2$  in  $\text{Fe}^{\text{II}}$ -containing buffer was enriched with chloroform. The cells were kept on ice for approximately 5 min, and afterward, cells were separated at 2000  $\times g$  for 5 min at 4 °C. 9  $\mu\text{L}$  of supernatant were taken for SDS-PAGE analysis (15% Gel).

In conclusion, these observations show that chloroform leads to cell death, which is a well-known fact.<sup>230</sup> Its damaging effect is attributed to its ability to modify membrane lipid matrix properties.<sup>231,232</sup> Therefore, its use is not suitable for in-cell experiments when preservation of the cellular structure is requested.

### 3.3.9. Detection of $F_3Y_{122}^{\bullet}$ and $F_3Y_{122}^{\bullet}$ - $F_3Y_{122}^{\bullet}$ pairs within the cells

The next important step for in-cell studies is understanding RNR's activity and active structure in the cellular environment. The use of unnatural amino acids is a key element in this process. The incorporation of  $F_3Y_{122}$  was fundamental to enable investigations on the *in vitro* radical transfer mechanism and to obtain the cryo-EM structure of the  $\alpha 2\beta 2$  complex. Therefore, in the next step, 2,3,5- $F_3Y$  was incorporated in position 122, and apo- $F_3Y_{122}$  was overexpressed in the cells. The cell growth on the LB-agar with the *E. coli* cell suspension containing 2,3,5- $F_3Y_{122}$  overexpression plasmid was at least  $6 \cdot 10^{10}$  cells per mL cell suspension. Slightly lower survivability in mutants is to be expected compared to wt- $\beta 2$  overexpression.  $Fe^{II}$  and  $O_2$  treatment of the washed cell cultures led to the generation of  $F_3Y_{122}^{\bullet}$  as verified by 9.6 and 34 GHz EPR spectra, while no detectable amounts of radical could pass the cell wall (**Figure 3.14**). Spin quantification experiments yielded a  $17 \pm 5 \mu M$  in-cell bulk concentration of  $F_3Y_{122}^{\bullet}$  in good agreement with the wt- $\beta 2$  in-cell samples.

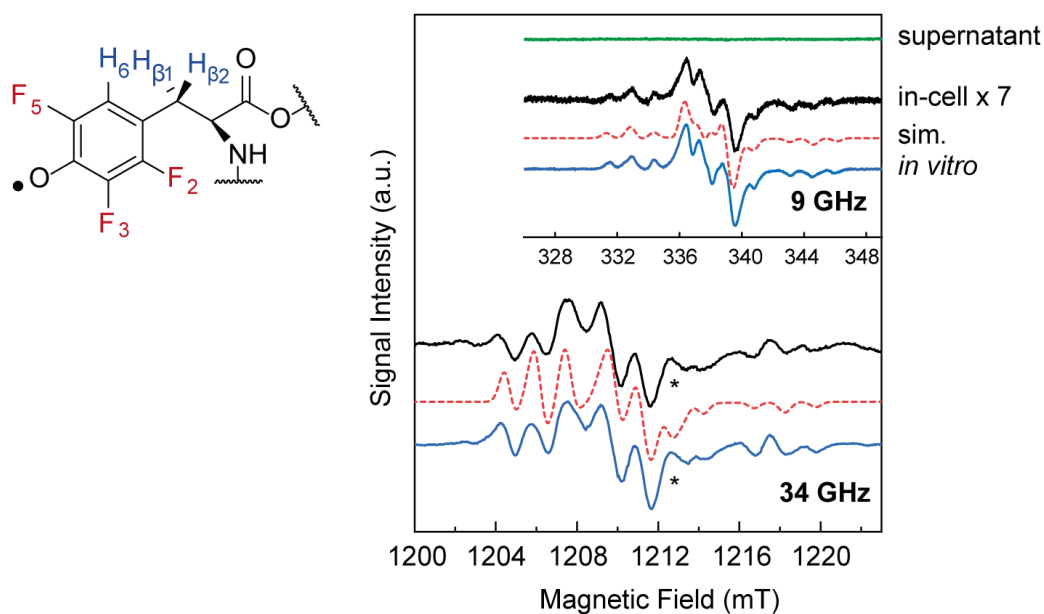


**Figure 3.14:** Cw- and derivative pulse EPR spectra of  $F_3Y_{122}^{\bullet}$  measured at 9.6 and 34 GHz. In-cell (black) and *in vitro* (blue) data are shown along with corresponding simulations (red dashed lines) and the supernatant spectrum (green). Simulation parameters reported in literature<sup>35,233</sup> are changed minimally during spectral simulations (see **Table 3.4**). Asterisks denote couplings seemingly absent in the experimental spectra due to a background signal. Schematic representation of  $F_3Y_{122}^{\bullet}$  shown left with the numbering of magnetically coupled nuclei included in the EPR spectral simulations in red and blue. Experimental conditions: 9 GHz: 2.5 mW power (31.6 mW power for green), 1.5 G modulation amplitude, 100 kHz modulation frequency, 5.12 ms as time constant, and 19.9 ms conversion time at 100 K, 50 scans (black), 20 scans (blue), 100 scans (green). 34 GHz:  $\pi = 32$  ns,  $\tau = 300$  ns, srt = 4 ms, spp = 10 and 20 mW power, 1 scan.

**Table 3.4: Hyperfine coupling parameters used for spectral simulations of multi-frequency EPR spectra of 2,3,5-F<sub>3</sub>Y<sub>122</sub>• in whole *E. coli* cells.** Best agreement with the experimental data was achieved with  $g_{x,y,z} = 2.0085(5), 2.0045(2), 2.0022(3)$ . Hyperfine parameters used for simulating the 9.6 GHz and 34 GHz data are given in regular and italic font, respectively. The minor differences between the two sets are likely due to the presence of the second conformation. The Euler angles  $\alpha$ ,  $\beta$ , and  $\gamma$  are defined within the EasySpin  $z, y', z''$  convention and refer to rotation from the  $g$ -tensor into the hyperfine tensor frames. Positive angles are clockwise rotations viewed along the rotation axis. The hf coupling uncertainty was at most 20%.

Nucleus	$A_x$ (MHz)	$A_y$ (MHz)	$A_z$ (MHz)	$\alpha$	$\beta$	$\gamma$
C <sub>1</sub> $\beta$ -H	56	39	40			
	<i>56</i>	<i>39</i>	<i>40</i>			
C <sub>2</sub> $\beta$ -H	0.5	0.5	3			
	<i>0.5</i>	<i>0.5</i>	<i>3</i>			
F <sub>2</sub> ring	-3	16	-45	0	0	60
	<i>-3</i>	<i>16</i>	<i>-45</i>			
F <sub>3</sub> ring	-3	-40	150	0	0	-45
	<i>-3</i>	<i>-40</i>	<i>155</i>			
F <sub>5</sub> ring	-3	-25	180	0	0	135
	<i>-3</i>	<i>-25</i>	<i>184</i>			
H <sub>6</sub> ring	5.8	5.5	2	0	0	-120
	<i>5.8</i>	<i>5.5</i>	<i>2</i>			

Subsequently, in-cell and *in vitro* DEER measurements with samples containing F<sub>3</sub>Y<sub>122</sub>• were performed. Four *in vitro* DEER traces were recorded at different  $g$ -tensor orientations (**Figure 3.15B**), which were summed up to eliminate orientation-selection effects (**Figure 3.15C** blue). Further details of these measurements are given in **Figure A.9**. Because of poor S/N ratios, such orientation-selective DEER measurements were not feasible with the in-cell sample. Instead, an in-cell DEER trace (**Figure 3.15C** black) at a molecular orientation at which the distance vector  $r_{F_3Y_{122}\bullet-F_3Y_{122}\bullet}$  is perpendicular to the magnetic field was recorded, marked as position 1. It was stated earlier that the correct mean distances can be determined directly from dipolar frequencies at this orientation.<sup>234</sup> The distance analysis of this trace resulted in a mean distance of 3.37 nm (**Figure 3.15D**). Please note that the standard deviation of the in-cell distance distribution can not be given as a comparison since its value is not entirely reliable in the presence of orientation-selectivity.<sup>235</sup> The detected in-cell distance agrees to a high degree with the *in vitro* distance detected here (3.36 with  $\sigma = 0.11$  nm) and with the distance between oxygen atoms of two F<sub>3</sub>Y<sub>122</sub>S in the recent crystal structure of F<sub>3</sub>Y<sub>122</sub>- $\beta$ 2 (**Figure 3.15A**). Hence, this distance can be assigned to the F<sub>3</sub>Y<sub>122</sub>•-F<sub>3</sub>Y<sub>122</sub>• pair in *E. coli* RNR. The agreement between the *in vitro* and *in vivo* F<sub>3</sub>Y<sub>122</sub>•-F<sub>3</sub>Y<sub>122</sub>• distance, as well as with the wild-type Y<sub>122</sub>•-Y<sub>122</sub>• distance indicates that incorporation of the unnatural amino acid does not significantly affect the protein structure in the cell.

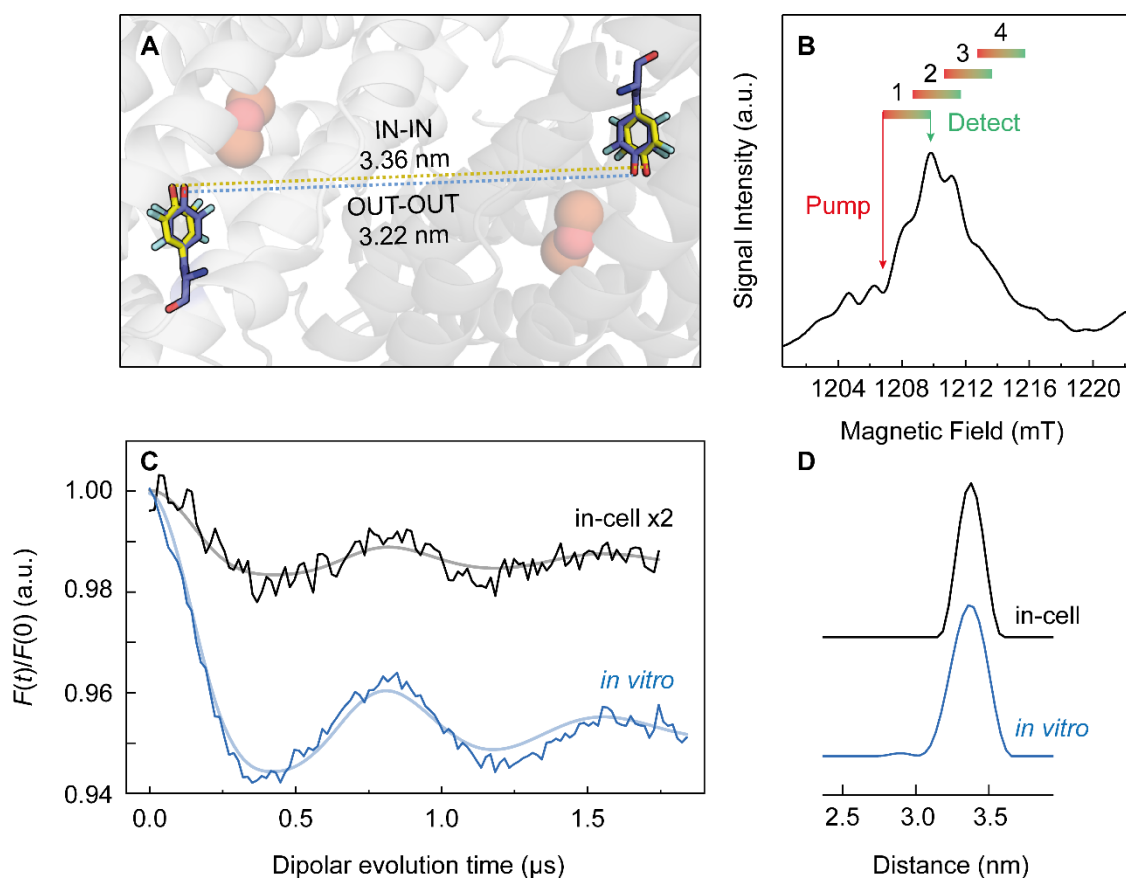


**Figure 3.15: Distance determination between the  $F_3Y_{122}\bullet$ - $F_3Y_{122}\bullet$  pair in *E. coli* RNR.** (A) Crystal structure of the  $F_3Y_{122}\text{-}\beta_2$  variant of *E. coli* RNR (PDB: 5CI3<sup>35</sup>) overlaid with the wt- $\beta_2$  structure (PDB: 5CI4<sup>35</sup>) to reproduce the homodimeric complex. IN and OUT conformers of  $F_3Y_{122}$  are shown in yellow and blue, respectively. (B) ESE-detected EPR spectrum of an in-cell sample recorded at 10 K. Four consecutive measurements for an *in vitro* sample were spaced by 20 G. Detect (D1, D2, D3, and D4) and pump (P1, P2, P3, and P4) positions for *in vitro* orientation-selective DEER measurements are indicated with green and red marks, respectively. Frequency separations between detection and pump positions were 84 MHz. DEER measurements for the in-cell sample were carried out at the first detect and pump position (D1/P1). (C) Background- and phase-corrected, normalized 34 GHz in-cell (black) and orientation-averaged *in vitro* (blue) DEER traces of  $F_3Y_{122}\bullet$ - $\beta_2$  subunit of *E. coli* RNR with fits overlaid in pale shade. The original in-cell trace is magnified by a factor of two for better visualization. (D)  $F_3Y_{122}\bullet$ - $F_3Y_{122}\bullet$  distance distributions. Details are given in **Figure A.9**.

The crystal structure of the  $F_3Y_{122}\text{-}\beta_2$  variant of *E. coli* RNR was overlaid with the wt- $\beta_2$  structure by using PyMOL to reproduce the homodimeric complex. In the crystal structure, two conformations of  $F_3Y_{122}$  are present, termed IN (yellow) and OUT (blue), as shown in **Figure 3.15A**. Earlier X-ray crystallographic investigations showed that the electron density of 2,3,5- $F_3Y_{122}$  cannot be modeled accurately by a single conformation of the residue. Instead, two conformations were found that differ by a 180° rotation around the  $C\beta$ - $C\gamma$  bond and a slight shift within the hydrophobic pocket.<sup>35</sup> Accordingly, the  $C\beta$ -proton hyperfine couplings differ for both conformers (**Table 3.5**).

**Table 3.5: C $\beta$ -proton hyperfine couplings for 2,3,5-F<sub>3</sub>Y<sub>122</sub>- $\beta$ 2 IN and OUT conformers as determined by Oyala *et al.*<sup>35</sup>**

Conformation	Proton	A <sub>x</sub> (MHz)	A <sub>y</sub> (MHz)	A <sub>z</sub> (MHz)	Relative abundance	$\rho_{C1}$	$\theta^{o**}$
IN	C <sub>1</sub> $\beta$ -H	57	51	54	80%	0.386	21.7
	C <sub>2</sub> $\beta$ -H	0.5	0.5	3			
OUT	C <sub>1</sub> $\beta$ -H	43	38	38	20%	0.357	34.1
	C <sub>2</sub> $\beta$ -H	-0.5	-0.5	2			

The distance for two IN conformers (3.36 nm) corresponds to the *in vitro* and in-cell distances detected in this work through DEER measurements. The distance between two OUT F<sub>3</sub>Y<sub>122</sub>• conformers is 3.22 nm, which is not detected by the presented DEER measurements. These results support that the IN conformation is the predominant state in whole cells, as already suggested for *in vitro* in the literature.<sup>35</sup> Simulations of the multi-frequency data support this observation, where hyperfine coupling values corresponding to the IN-conformation were utilized.

It should be noted that the distances between the IN-IN and OUT-OUT conformers are captured between two oxygen atoms of F<sub>3</sub>Y<sub>122</sub>• in the crystal structure, which does not correspond to the center of spin density,<sup>201,236</sup> but still provides reliable results. The distances measured for a Y<sub>122</sub>•-Y<sub>122</sub>• pair based on the spin density gravity center and based on the O atoms in the crystal structure are 3.26 and 3.29 nm, respectively. Thus, a discrepancy of 0.03 nm is expected. The spin density is estimated to remain about the same for Y<sub>122</sub>• ( $\rho_{C1} = 0.387^{35}$ ) and F<sub>3</sub>Y<sub>122</sub>•. Compared to the difference between IN and OUT conformers (0.14 nm), the discrepancy of 0.03 nm is negligible. Thus, distance calculations based on the oxygen atoms of F<sub>3</sub>Y<sub>122</sub>• in the crystal structure are valid.

Furthermore, background slopes of the in-cell and *in vitro* DEER traces were compared. Similar to the results obtained with Y<sub>122</sub>• in the wild-type enzyme, this analysis showed that the local F<sub>3</sub>Y<sub>122</sub>• concentration within the cells must be substantially lower than the detected *in vitro* concentration of  $130 \pm 30 \mu\text{M}$ .

---

\*\* Values were determined from EPR measurements.

### 3.3.10. Optimization of $F_3Y_{122}^{\bullet}$ expression conditions

Previous  $F_nY$ - $\beta 2$  expression protocols suggested using *E. coli* TOP10 cells and only 0.05% arabinose to induce protein expression.<sup>35</sup> The first attempts of expressing and detecting  $F_3Y_{122}^{\bullet}$  in *E. coli* were thus performed in TOP10 cells. However, this resulted in low radical yields and poor S/N ratios of the DEER data. To enhance the  $F_3Y_{122}^{\bullet}$  radical yield, different expression conditions were tested. The overall expression procedure was kept as described in Section 3.2.2, introducing changes at specific points.

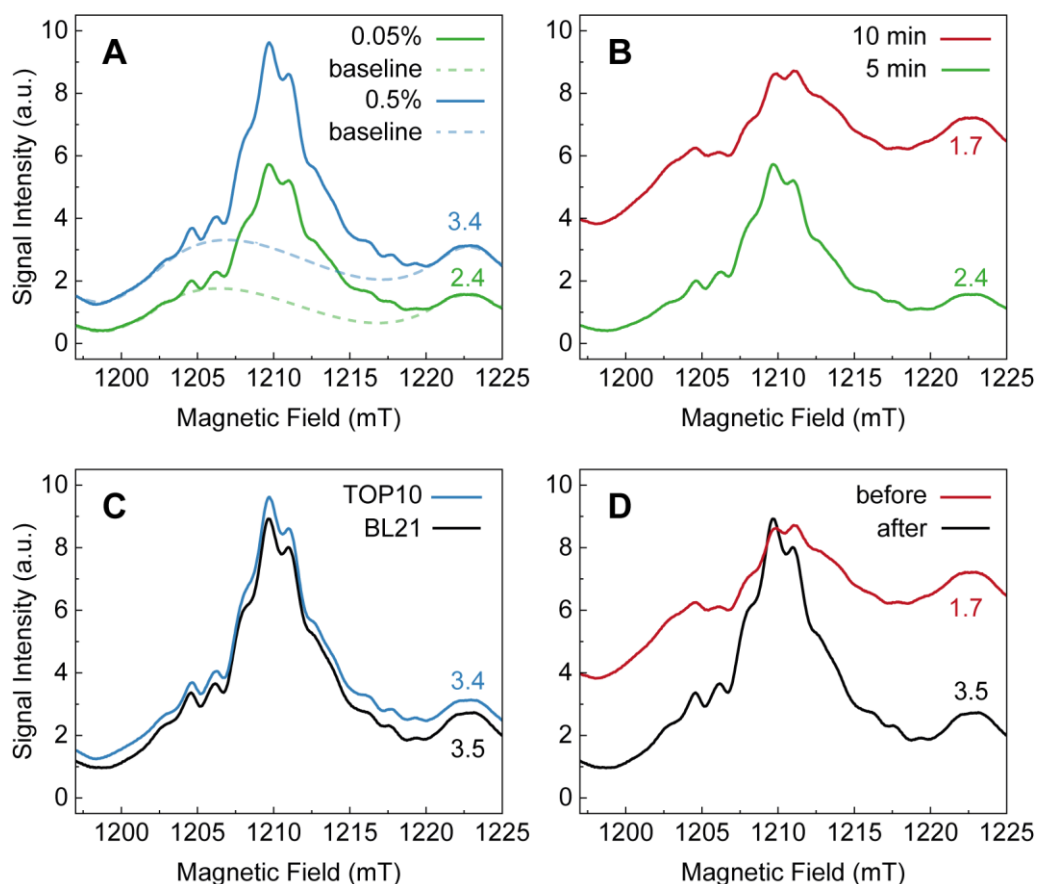


**Figure 3.16: 34 GHz ESE spectra of  $F_3Y_{122}^{\bullet}$ - $\beta 2$  expressed under different conditions.** (A) Either 0.05% or 0.5% arabinose was used to induce protein expression. An exemplary background correction is shown in dashed lines. (B) The cell suspension was either allowed to incubate for 10 or 5 min with iron. (C) TOP10 or BL21(DE3)-Gold cells were employed for protein overexpression. (D) comparison of samples before and after optimization of the expression protocol. Values next to the spectra indicate integrals of  $F_3Y_{122}^{\bullet}$  signal after background subtraction. Sample details: green: TOP10, 0.05% arabinose, 5 min; blue: TOP10, 0.5% arabinose, 5 min; red: TOP10, 0.05% arabinose, 10 min; black: BL21, 0.5% arabinose, 5 min. Signals are scaled to number of scans, spp, and videogain. Acquisition parameters:  $\pi = 32$  ns,  $\tau = 300$  ns, srt = 8 ms, spp = 100 and 20 mW power, 1 scan.

First, the arabinose content for  $F_3Y_{122}$ - $\beta 2$  overexpression in *E. coli* TOP10 cells was varied using either 0.05% or 0.5% arabinose. Subsequently, 34 GHz ESE spectra were recorded (Figure 3.16A). The spectra reveal the presence of two paramagnetic species,  $F_3Y_{122}^{\bullet}$  and  $Mn^{II}$ . To allow the comparison of generated  $F_3Y_{122}^{\bullet}$  yields, a background correction for

Mn<sup>II</sup> was performed (exemplarily shown as dashed lines in **Figure 3.16A**), and the integral of the F<sub>3</sub>Y• signal was determined (values shown next to the spectra). Accordingly, using 0.5% arabinose instead of only 0.05% drastically enhances the radical yield in the cells. Next, the incubation time between iron addition and sample freezing varied between 5 and 10 min (**Figure 3.16B**). Integration of the F<sub>3</sub>Y<sub>122</sub>• signal reveals a remarkable increase in radical content for the shorter incubation time. Finally, the employed *E. coli* strain was altered from TOP10 to BL21 cells, causing only a negligible enhancement in F<sub>3</sub>Y<sub>122</sub>• radical yield (**Figure 3.16C**).

The direct comparison before and after optimization of the expression conditions (**Figure 3.16D**) unveils approximately a doubling of F<sub>3</sub>Y<sub>122</sub>• signal intensity and an enhanced relative intensity compared to the Mn<sup>II</sup> EPR signal, which should consequently lead to an increase in S/N ratios and modulation depth in DEER experiments. Indeed, DEER traces recorded for the F<sub>3</sub>Y<sub>122</sub>•-F<sub>3</sub>Y<sub>122</sub>• pairs in TOP10 cells revealed a dampened modulation depth with  $\Delta = 0.5\%$  (**Figure 3.17A**). The modulation depth of the DEER trace of BL21 cells is enhanced by the factor of two ( $\Delta = 0.9\%$ ) and is only slightly lower than for wt- $\beta 2$  expression. *In vitro* experiments already showed that the maximum radical yield of F<sub>3</sub>Y<sub>122</sub>• is 0.9 F<sub>3</sub>Y•/ $\beta 2$ , in contrast to the usual 1.2 Y•/ $\beta 2$  for the wild-type enzyme,<sup>35</sup> which could be a possible reason for the reduced modulation depth observed with F<sub>3</sub>Y<sub>122</sub>•. The lower radical concentration in TOP10 cells causes a poor signal-to-noise ratio.

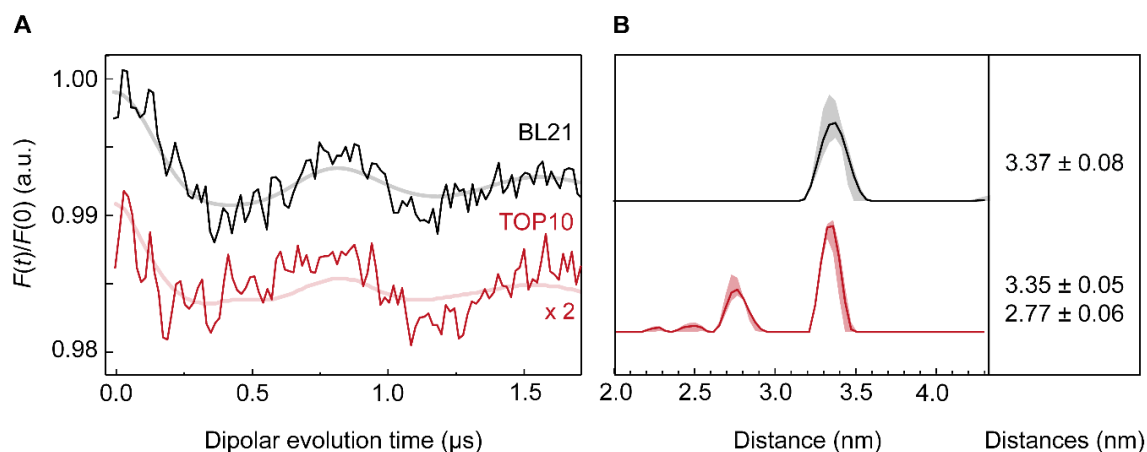


**Figure 3.17:** 34 GHz DEER measurements of F<sub>3</sub>Y<sub>122</sub>• expressed in *E. coli* BL21(DE3)-Gold or TOP10 cells. (A) Background- and phase-corrected, normalized 34 GHz DEER traces of F<sub>3</sub>Y<sub>122</sub>•- $\beta 2$  subunit of *E. coli* RNR overexpressed in BL21 with 0.5% arabinose (black) or TOP10 with 0.05% arabinose (red) cells. Fits obtained by DeerAnalysis are overlaid in pale shade. (B) F<sub>3</sub>Y<sub>122</sub>•-F<sub>3</sub>Y<sub>122</sub>• distance distributions together with detected distances. Bulk radical concentration: 17  $\mu$ M (black), 7  $\mu$ M (red).

Analysis of the DEER traces of BL21 and TOP10 samples results in a main peak in the distance distribution at 3.37 and 3.35 nm, respectively (**Figure 3.17B**). However, a smaller distance at 2.8 nm is observed in TOP10 cells, which already emerged in the orientation-

averaged traces of the wild-type protein, this time with increased relative intensity and again validated. In conclusion, these results highlight that using 0.5% arabinose is more suitable for investigating  $F_3Y_{122}\bullet$  in *E. coli* cells via EPR. Moreover, we prefer the *E. coli* strain BL21 for in-cell EPR as it is a standard strain for protein expression.

### 3.4. Conclusion and outlook

This chapter reports on the characterization of the essential tyrosyl radical of *E. coli* class Ia RNR in whole *E. coli* cells by using advanced EPR techniques. This goal was achieved by overexpressing the wt- $\beta 2$  subunit in intact, living cells. Multi-frequency EPR and  $^1\text{H}$  Davies ENDOR measurements revealed that the structure and electrostatic environment of the di-iron tyrosyl radical cofactor  $Y_{122}\bullet$  in *E. coli* RNR are identical under *in vivo* and *in vitro* conditions. DEER distance measurements within the  $Y_{122}\bullet$ - $Y_{122}\bullet$  pair provided insights into the in-cell structure and conformational rigidity of the  $\beta 2$  subunit. Such orientation-selective DEER measurements performed on a native paramagnetic center in the cells are, to the best of our knowledge, the first of their kind. Most importantly, these dipolar experiments shed light on a distinct in-cell radical distribution within this subunit. The presence of  $\beta 2$  subunits having only one  $Y_{122}\bullet$  strongly supports a model in which *E. coli* RNR activity is regulated via modulation of  $Y\bullet$  concentrations in the cells. These results serve as a basis for future experiments aiming to detect and manipulate the factors influencing in-cell RNR activity.

Additionally, the spectroscopic detection of an unnatural amino acid radical in whole cells,  $F_3Y_{122}\bullet$ , was presented. It could be shown that  $F_3Y$  incorporation does not affect the *in vivo* protein structure. A successful generation of  $F_3Y_{122}\bullet$  within the cells is the first step toward gaining unique insights into RNR catalysis under physiological conditions. Trapping the intermediate  $Y_{356}\bullet$  within the cells would be substantial to investigate its function in the PCET inside a living system. Initial hints indicate that the overexpressed  $\beta 2$  subunit is catalytically active within the cells, and  $Y_{356}\bullet$  might be detectable (**Figure 3.18**). Since these preliminary data are still characterized by a poor S/N ratio and a strong  $\text{Mn}^{\text{II}}$  background, additional spectroscopic and biochemical work is necessary to confirm this hypothesis with certainty.

*In vivo* formation and detection of  $F_nY\bullet$ s will not only be crucial for RNR but, furthermore, showcases the possibility of unraveling the *in vivo* structure and role of tyrosyl radicals involved in other fundamental processes such as photosynthesis,<sup>237</sup> reduction of  $\text{O}_2$  to water,<sup>238</sup> and DNA repair<sup>239</sup> by unnatural amino acid incorporation.

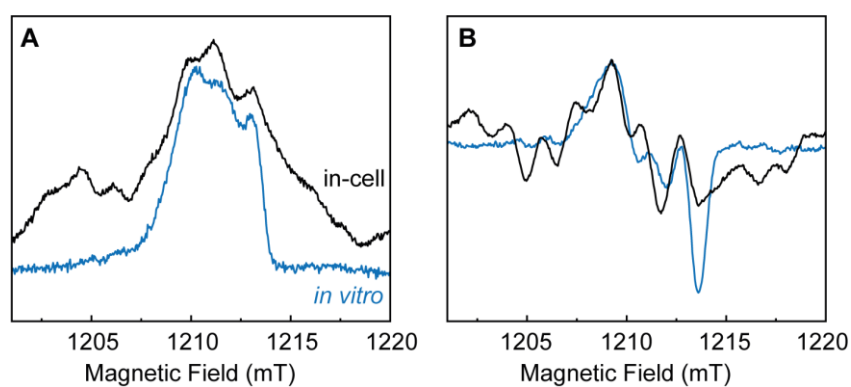


**Figure 3.18: An outlook for trapping of  $Y_{356}\bullet$  investigated by 34 GHz ESE spectra.** (A) Absorption spectra and (B) pseudomodulated spectra. For *in vitro*  $Y_{356}\bullet$  generation, the reaction of  $F_3Y_{122}\bullet$ - $\beta 2$  with wt- $\alpha 2$  was manually freeze quenched as described by Nick *et al.*<sup>70</sup> Proximity of  $F_3Y_{122}\bullet$  to the di-iron cluster alters its relaxation properties so that at 80 K mostly  $Y_{356}\bullet$  can be monitored (blue). In-cell measurements of the  $F_3Y_{122}\bullet$  variant (black) at 70 K reveal a spectrum with similar lineshape compared to  $Y_{356}\bullet$  on top of the  $Mn^{II}$  EPR pattern.

# 4.

## Role of manganese ions in tuning the radical generation in ribonucleotide reductase

---

Parts of the results presented in this chapter are in preparation for publication:

Meichsner, S. L., Kasanmascheff, M. Mismetallation or regulation? Role of manganese ions in tuning the radical generation in ribonucleotide reductase, in preparation.

### 4.1. Introduction

*E. coli* encodes two class I RNRs, Ia (NrdA and NrdB) and Ib (NrdE and NrdF). Class Ia is expressed under normal aerobic growth conditions, whereas the Ib enzyme takes over the catalysis under iron-limited and oxidative stress conditions.<sup>18</sup> Surprisingly, under these conditions, class Ia is also expressed in levels comparable to those detected in iron-rich media. The presence of class Ia  $\beta_2$  in large amounts with low activity remains puzzling.

The universal binding of transition metals in the +II oxidation state is described in terms of the Irving-Williams series with  $Mn^{II} < Fe^{II} < Ni^{II} < Co^{II} < Cu^{II} > Zn^{II}$ .<sup>240</sup>  $Mn^{II}$  and  $Fe^{II}$  in general exhibit relatively low binding affinities, so mismetallation of iron sites with manganese and the reverse case is a well-known problem.<sup>241–243</sup>  $Mn^{II}$  and  $Fe^{II}$  both offer relatively similar ionic radii (0.80 Å for  $Mn^{II}$  and 0.74 Å for  $Fe^{II}$ ), similar coordination numbers, and redox activities in the physiological pH.<sup>244</sup> Previous studies of the  $\beta_2$  subunit of *E. coli* class Ia RNR have demonstrated that  $Mn^{II}$  can bind tightly in the protein's metal-binding site with the same amino acids involved in the ligation as for  $Fe^{II}$ .<sup>99</sup> This in turn inhibits the formation of the stable  $Y_{122}\bullet$  on the Mn-occupied binding site.<sup>99,100</sup> To date, there is no exact answer to how nature minimizes or regulates such a mismetallation in the protein. However, understanding its activity regulation is essential because of RNR's central role in every living organism.

Some of the presented facts already demonstrated that a type of activity regulation of *E. coli* RNR is present in living cells. So far, the maximum possible yield of 2  $Y_{122}^{\bullet}$  and 4 Fe per  $\beta 2$  was observed in crude cell extracts titrated with reduced YfaE exclusively.<sup>101</sup> Yet, only substoichiometric  $Y_{122}^{\bullet}$  levels ( $0.1 - 0.3 Y_{122}^{\bullet}/\beta 2$ ) were detected inside the cells, although the overexpressed  $\beta 2$  was almost completely loaded with the diferric cluster.<sup>101</sup> Moreover, the results obtained in Chapter 3 displayed that overproduction of NrdB in *E. coli* cells under iron-limiting conditions results in a distinct radical distribution of  $Y_{122}^{\bullet}$  in the cells,<sup>192</sup> compared to the two or none model *in vitro*. These results suggest a model in which RNR activity is regulated via modulation of  $Y_{122}^{\bullet}$  concentrations, possibly influenced by metal availabilities. These studies aim to address the question about the interplay between available metal ions and radical formation, thus RNR activity, *in vitro* and *in vivo*.

## 4.2. Materials and methods

### 4.2.1. In-cell sample preparation

The former in-cell samples were produced under iron-limiting conditions. In this chapter, a second set of samples was prepared, in which iron was available during protein expression ( $n = 3/\text{group}/\text{point}$  in time). For both samples, *E. coli* BL21(DE3)-Gold cells were grown in 600 mL LB-medium. For iron chelation, 1,10-Phenanthroline was added to a final concentration of 100  $\mu\text{M}$  in the medium at OD600  $\sim 0.9$ . After 20 min, while an OD600 of around 1.1 was detected, protein expression was induced with 0.5 mM isopropyl-1-thio- $\beta$ -galactopyranoside (IPTG). For the other samples, no phenanthroline was added, and protein expression was directly induced at OD600  $\sim 1.1$ . For both samples, protein overproduction was accomplished for 4 h, and afterward, the cells were harvested by centrifugation at 3000  $\times g$  for 20 min at 4  $^{\circ}\text{C}$ . A typical 3 – 9 and 6 – 7 g cell paste/L media was obtained for iron-chelated and iron-available samples each. The cell pellet was resuspended in 50 mM Tris pH 7.6 with 5% glycerol using 3 mL of buffer per g cell paste. 0.15 mM  $\text{Fe}^{\text{II}}(\text{NH}_4)_2(\text{SO}_4)_2$  was added to this buffer. After 10 min incubation on ice, all samples were transferred to 2.8 mm O.D. EPR tubes and frozen in liquid  $\text{N}_2$  at the same time to ensure equal incubation times.  $Y_{122}^{\bullet}$  yield and the amount of free  $\text{Mn}^{\text{II}}$  were quantified by cw-EPR spectroscopy at 9.6 GHz (**Table 4.1**).

**Table 4.1:  $Y_{122}^\bullet$  yield,  $Mn^{II}$  and OD600 of *E. coli* in-cell samples expressing wt- $\beta 2$  RNR for 4 h under iron chelated and iron available conditions.** Mean values and standard deviation of three individual expression batches are listed.

Iron	$Y_{122}^\bullet$ ( $\mu M$ )	$Mn^{II}$ ( $\mu M$ )	OD600 (a.u.)
chelated	$20 \pm 5$	$20 \pm 4$	$1.6 \pm 0.2$
available	$58 \pm 23$	$26 \pm 12$	$2.2 \pm 0.3$

#### 4.2.2. Monitoring of cell density, tyrosyl radical, and manganese content in the cells

During the growth of the in-cell samples from Section 4.2.1, aliquots were taken at distinct time points after initiation of protein expression to determine the  $Y_{122}^\bullet$  radical content and the amount of EPR-detectable  $Mn^{II}$  species by cw-EPR, as well as the OD600 value. Cells were allowed to grow for at most 20 h. After sampling, the cells were again harvested by centrifugation at  $3000 \times g$  for 20 min at 4 °C. The cell pellet was resuspended in 50 mM Tris pH 7.6 with 5% glycerol using 3 mL of buffer per g cell paste. 0.15 mM  $Fe^{II}(NH_4)_2(SO_4)_2$  was added to this buffer. After 10 min incubation on ice, all samples were transferred to 2.8 mm O.D. EPR tubes and frozen in liquid  $N_2$  at the same time.

#### 4.2.3. *In vitro* sample preparation

First, protein concentration was determined via UV-Vis spectroscopy. 150  $\mu M$  of apo- $\beta 2$  were titrated with the corresponding amount of  $Mn^{II}$ . Manganese was supplied in the form of  $MnCl_2$ , prepared freshly for each experiment. The protein-manganese mixture was incubated on ice for 10 min. Subsequently, 5 equivalents of  $Fe^{II}$  per dimer were added in the form of  $Fe^{II}(NH_4)_2(SO_4)_2$ . The iron solution was prepared freshly before its use in degassed buffer via  $N_2$  bubbling for at least one hour. If not stated otherwise, the solution was mixed and incubated for 2 h in an open 1.5 mL Eppendorf tube to ensure  $O_2$  availability. For EPR measurements, 100  $\mu L$  protein solution was transferred to 2.8 mm O.D. EPR tubes and shock frozen in liquid  $N_2$ .

#### 4.2.4. UV-Vis measurements

UV-Vis experiments were conducted at a Jasco V-650 spectrometer equipped with a temperature control unit. 30  $\mu M$  of apo- $\beta 2$  were titrated with the corresponding amount of  $MnCl_2$ , prepared freshly for each experiment. The solution was incubated on ice for 10 min. Subsequently, 5 equivalents of  $Fe^{II}$  per dimer were added in the form of  $Fe^{II}(NH_4)_2(SO_4)_2$ . The iron solution was prepared freshly before its use in degassed buffer

via N<sub>2</sub> bubbling for at least one hour. The solution was mixed and measured immediately afterwards with a dead-time of around 1 min after iron addition. Spectra were acquired at 20 °C every 3 min between 1 – 30 min, every 5 min between 30 – 60 min, and then every 10 min. The Y<sub>122•</sub> contribution at A<sub>410nm</sub> (Y<sub>122•</sub>) to the absorbance spectrum was determined by baseline subtraction for each spectrum. The background intensity is constantly changing because of ongoing iron oxidation (**Figure B.5A**); hence a new background needs to be created for every time point. This background was created by omitting the data points between approx. 400 to 420 nm. Using the background corrected data, the Y<sub>122•</sub> yield per β<sub>2</sub> could then be obtained by

$$\frac{c(Y_{122\bullet})}{c(\beta_2)} = \frac{A_{410nm}(Y_{122\bullet})}{\epsilon \cdot d \cdot c(\beta_2)} \quad (4.1)$$

with  $\epsilon(410nm) = 2110 \text{ M}^{-1} \text{ cm}^{-1}$ .<sup>88</sup>

#### 4.2.5. Size exclusion chromatography for β<sub>2</sub> dimer and monomer identification

To distinguish monomeric and dimeric β-subunits, size exclusion chromatography was performed with a Superdex 75 Increase 10/300 GL column using a flow rate of 0.5 mL/min on a cooled ÄKTA go chromatography system. Prior to the analysis, a calibration was accomplished by using a molecular marker kit containing Albumin, Alcohol Dehydrogenase, β-Amylase, Carbonic Anhydrase, Cytochrome c, and Blue dextran. Subsequently, either 30 μM or 150 μM protein solution was incubated for 10 min with the indicated amount of Mn<sup>II</sup> on ice. After different time points of iron addition, the solution was applied to the column.

#### 4.2.6. Dephosphorylation of azido-CTP

The N<sub>3</sub>CDP activity assay requires the 5'-diphosphate form of 2'-azidonucleotide for binding to the active site of α<sub>2</sub>. This compound is not commercially available, though the 5'-triphosphate can be purchased. The terminal phosphate group can be cleaved enzymatically by myosin.<sup>245</sup> Therefore, 5 mM azido-CTP was incubated with 5 mM CaCl<sub>2</sub> and 0.65 μM myosin (65 μl/ml) in 50 mM Tris HCl, pH 8.0, for 9 hours at 37 °C and 300 rpm. This reaction was performed in a standard volume of a total 200 μL. After incubation, the mixture was placed on ice for some minutes to stop the reaction, which led to calcium phosphate precipitation. The white precipitate was spun down at 10 000 xg for 2 min at 20 °C. In the following, myosin could be separated from the nucleotide by centrifugation in an Amicon® centrifugal filter unit with 10 kDa cutoff once with 8 mL fresh 50 mM Tris HCl pH 7.6 buffer for 3000 xg for 15 min at 4 °C. Afterwards, two further washing rounds were performed in a smaller Amicon® with 1 mL Buffer at 3000 xg for 30 min at 4 °C. The nucleotide-containing filtrate was then

frozen in a 15 ml plastic tube and lyophilized overnight. The dry powder was stored at  $-20\text{ }^{\circ}\text{C}$  until use. The nucleotide was then dissolved in a minimal amount of 50 mM Tris HCl pH 7.6. To check nucleotide concentration, 1  $\mu\text{L}$  is mixed with 99  $\mu\text{L}$  0.01 M HCl, followed by the absorption measurement at 279 nm. At pH 2.0,  $\epsilon(279\text{ nm}) = 13\ 700\ \text{M}^{-1}\ \text{cm}^{-1}$  can be applied. The cleavage efficiency is checked by thin layer chromatography (TLC) using TLC Silica gel 60 F<sub>254</sub> as the stationary phase and 0.3 M  $(\text{NH}_4)_2\text{CO}_3$  as mobile phase. The separation of di- and tri-phosphates is monitored by potassium permanganate staining. The purity is close to 100%, as no traces of triphosphates were observed on the TLC plate (**Figure B.1**).

#### 4.2.7. N<sub>3</sub>CDP-based activity assay

In order to test the activity of manganese-bound  $\beta_2$  subunits, N<sub>3</sub>CDP as substrate analogon was used. The assay conditions used were 50  $\mu\text{M}$   $\beta_2$ , 50  $\mu\text{M}$   $\alpha_2$ , 50  $\mu\text{M}$  dTTP, 1 mM N<sub>3</sub>CDP, 15 mM Mg-acetate, and 1.25 mM DTT in 50 mM Tris-HCl pH 7.6. Therefore,  $\beta_2$  was first incubated with the corresponding amount of MnCl<sub>2</sub> for 10 min, followed by iron addition and incubation at RT for 2 h. Subsequently, the radical yield was checked via UV-Vis. In the next step, one reaction vessel was prepared, containing the  $\alpha_2$ -subunit, dTTP, DTT, and Mg-acetate. In a second vessel,  $\beta_2$  was mixed with N<sub>3</sub>CDP and Mg-acetate. The reaction was started by mixing both solutions, which were then quickly transferred in EPR tubes and, after 1 min reaction time, frozen in liquid N<sub>2</sub>.

For the detection of Y<sub>122</sub>• signal decay, 40  $\mu\text{L}$  of the sample volume was filled in 1.6 mm O.D. EPR tubes, which were frozen in liquid N<sub>2</sub> after 1 min incubation at room temperature. The Y<sub>122</sub>• content was quantified by cw-EPR measurements at 9.6 GHz. Afterward, the sample was allowed to thaw at 20  $^{\circ}\text{C}$  for 1 min, followed by freezing and measuring. This cycle was repeated for 20 min in total.

As the N• radical is not stable over the observed period,<sup>66</sup> sample preparation was different for efficient N• detection. Therefore, 80  $\mu\text{L}$  of the reaction mix was filled in 2.8 mm O.D. EPR tubes and frozen after 6 min incubation time at room temperature. After this 6 min, Y<sub>122</sub>• and N• were detected via cw-EPR. The isolated EPR spectrum of N• is obtained via subtraction of the remaining Y<sub>122</sub>• from the cw-EPR spectrum.

#### 4.2.8. Size exclusion chromatography to probe $\alpha_2\beta_2$ complex assembly

Separation of  $\alpha_2$ ,  $\beta_2$ , and  $\alpha_2\beta_2$  can be achieved by utilizing a Superdex 200 Increase 10/300 GL column connected to a cooled ÄKTA go chromatography system with a flow rate of 0.5 mL/min. The samples were the same as used for the activity assay, prepared for N• detection. After the cw measurements, samples were thawed on ice and directly diluted to 600  $\mu\text{L}$  sample volume, yielding around 3  $\mu\text{M}$  protein concentration. Afterward, the solution was applied to the column and eluted with 0.5 mL/min flow. Calibration of the column was achieved by a molecular marker kit containing Albumin,

Alcohol Dehydrogenase,  $\beta$ -Amylase, Carbonic Anhydrase, Cytochrome c, and Blue dextran.

#### 4.2.9. Detail of the EPR experiments

**X-band:** X-band cw-EPR measurements were carried out at  $T = 100$  K using a Bruker EMX-Nano Benchtop spectrometer equipped with a continuous-flow nitrogen cryostat.

**Q-band:** Q-Band pulse EPR measurements were carried out at  $T = 10$  K using a Bruker Eleksys E580 spectrometer equipped with a 150 W TWT amplifier, Bruker ER 5106QT-2 resonator, Bruker SpinJet AWG, Oxford Instruments CF935 continuous-flow helium cryostat and Oxford Instruments MercuryTC temperature controller.

**Orientation-selective DEER experiments** were performed using the 4-pulse DEER pulse sequence with 16-step phase cycling and Gaussian pulses. The frequency separation  $\Delta f = f_{\text{pump}} - f_{\text{det}}$  was 84 MHz, and an overcoupled resonator with  $f_{\text{pump}}$  set to the center of the resonator dip was used. Pump and detect positions are marked in the spectrum in **Figure 4.1**. Optimal  $\pi$ -pulse lengths were determined using transient nutation experiments, typically 28 ns for the pump pulse and 70 ns for the detection. DEER time traces were background-corrected by using an empirical second-order polynomial fitting. The protein concentration of  $\beta 2$  used was 150  $\mu\text{M}$  if not stated otherwise.

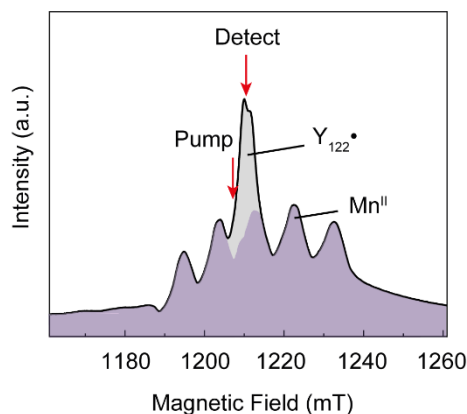


**Figure 4.1: Detect and pump position used for DEER experiments in this chapter.** An exemplary pulse EPR spectrum recorded at 34 GHz and 10 K displaying spectral features contributed by  $\text{Y}_{122}\bullet$  (gray) and  $\text{Mn}^{\text{II}}$  (purple). Detect and pump positions of a typical DEER experiment are indicated by arrows.

### 4.3. Results and discussion

#### 4.3.1. Relation between cellular metal concentration and $Y_{122}^{\bullet}$ radical yield

The influence of transition metals such as iron and manganese being present during wt- $\beta 2$  expression in *E. coli* cells on the tyrosyl radical formation efficiency was tested by choosing two different expression procedures. One of those corresponds to the one already shown in Chapter 3, namely apo- $\beta 2$  expression under iron-limiting conditions. In the second approach, no metals are chelated. Thus, the amount of available metal ions corresponds to physiological conditions in *E. coli* cells. *E. coli* cells grown in LB-medium usually contain a 10-fold excess of iron compared to manganese,<sup>246</sup> which therefore corresponds to a holo- $\beta 2$  expression. After different time points of protein expression, samples were taken and investigated for their cell density via OD600 measurements (**Figure 4.2A**), the restored amount of tyrosyl radical  $Y_{122}^{\bullet}$  (**Figure 4.2B**), and the EPR-detectable amount of  $Mn^{II}$ -species (**Figure 4.2C**). Notably, biomolecule-bound manganese is characterized in many cases by broad and/or complex EPR lineshapes,<sup>247-249</sup> which were not observed in this case. Since the  $\beta 2$  subunit is the only overexpressed enzyme in the cells, EPR signals of other metallocofactors are below the detection limit. Thus, the detected amount of  $Mn^{II}$  in the in-cell samples should mainly represent free, bioavailable  $Mn^{II}$ . A constant increase in OD600 over the observation period is seen for both expression batches (**Figure 4.2A**). The phenanthroline-free cell sample features a higher cell density, which can be explained by phenanthroline's cytotoxicity.<sup>250</sup> The strongest cell growth is observed within the first three hours of overexpression.

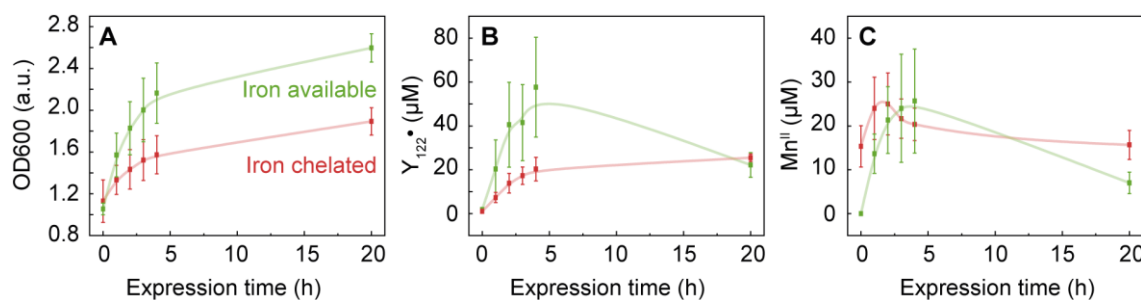


**Figure 4.2: Different parameters monitored during 20 h wt- $\beta 2$  expression in *E. coli* cells.** (A) OD600, (B)  $Y_{122}^{\bullet}$  concentration, and (C)  $Mn^{II}$  content with iron available (green) or chelated (red) during protein expression.  $Y_{122}^{\bullet}$  and  $Mn^{II}$  content were assessed via cw-EPR measurements.

Next, the in-cell  $Y_{122}^{\bullet}$  concentration is investigated (**Figure 4.2B**). Before doing so, it should be noted that all samples contained approximately the same amount of cell mass, which is why changes in  $Y_{122}^{\bullet}$  concentration should not be confused with changes in cell density. Similar to the observation for the cell density, the observed  $Y_{122}^{\bullet}$  content strongly increases within the first three hours. Samples produced under conditions with iron available reveal approximately twice the  $Y_{122}^{\bullet}$  concentration of samples with iron chelator. Astonishingly, both expression batches seem to agree on a mutual equilibrium

of roughly  $24 \pm 5 \mu\text{M Y}_{122}\bullet$  after 20 h overproduction. This observation could indicate an active regulation of the radical content in the cells.

For the iron-chelated samples, approximately  $15 \mu\text{M Mn}^{\text{II}}$  is detected at the starting point of protein expression, whereas for iron-available samples, the  $\text{Mn}^{\text{II}}$  was below the detection limit (**Figure 4.2C**). It has already been observed that under iron-limiting conditions, the manganese importer MntH together with the small protein MntS is expressed in order to increase the intracellular manganese concentration.<sup>211</sup> In iron-available samples, the progression of the manganese concentration is analogous to the  $\text{Y}_{122}\bullet$  content, while the manganese concentration in iron-chelated samples remains at a constant level within the error margins. Only a minor increase is observed in the first three hours. A straightforward interpretation of the time-dependent free manganese concentration is not feasible due to multiple factors in the cell. What is striking, however, is that the intracellular manganese content changes as a function of iron availability during protein expression. Since RNR is the only overexpressed protein in this experiment, there might be a correlation to the monitored metal concentration. The available metal pool could be influenced, for example, by the binding of iron but also manganese to RNR, which will be the research subject in this chapter.

#### **4.3.2. Metal ion availability influencing the $\text{Y}_{122}\bullet$ radical distribution in the cells**

In the next step, DEER measurements were accommodated for cell suspensions prepared under unaffected metal availability to compare the present  $\text{Y}_{122}\bullet$  radical distribution to those grown under iron-limiting conditions from Chapter 3. The background slope is steeper for the sample containing free iron than for the iron chelated one since its radical concentration is higher ( $77 \mu\text{M}$  vs.  $22 \mu\text{M}$  bulk  $\text{Y}_{122}\bullet$  concentration). A second *in vitro* mimic sample containing  $72 \mu\text{M Y}_{122}\bullet$  (see **Table 3.1** and **Figure 4.3** gray) owns a comparable background slope and thus indicates that no high local protein concentration is present in these samples either. The modulation depth and the fraction of  $\text{Y}_{122}\bullet$  in the refocused echo were again plotted on the calibration curve (**Figure 4.3D**).

Surprisingly, the samples where iron was available during protein expression match the *in vitro* calibration curve. This implies that once free iron is available during the expression of wt- $\beta 2$  in *E. coli* cells, a radical distribution according to two or none is present. However, iron chelation during protein expression results in a distinct radical distribution in the cells, other than two or none, and thus provides direct evidence for the influence of metal availability on RNRs *in vivo* radical distribution.

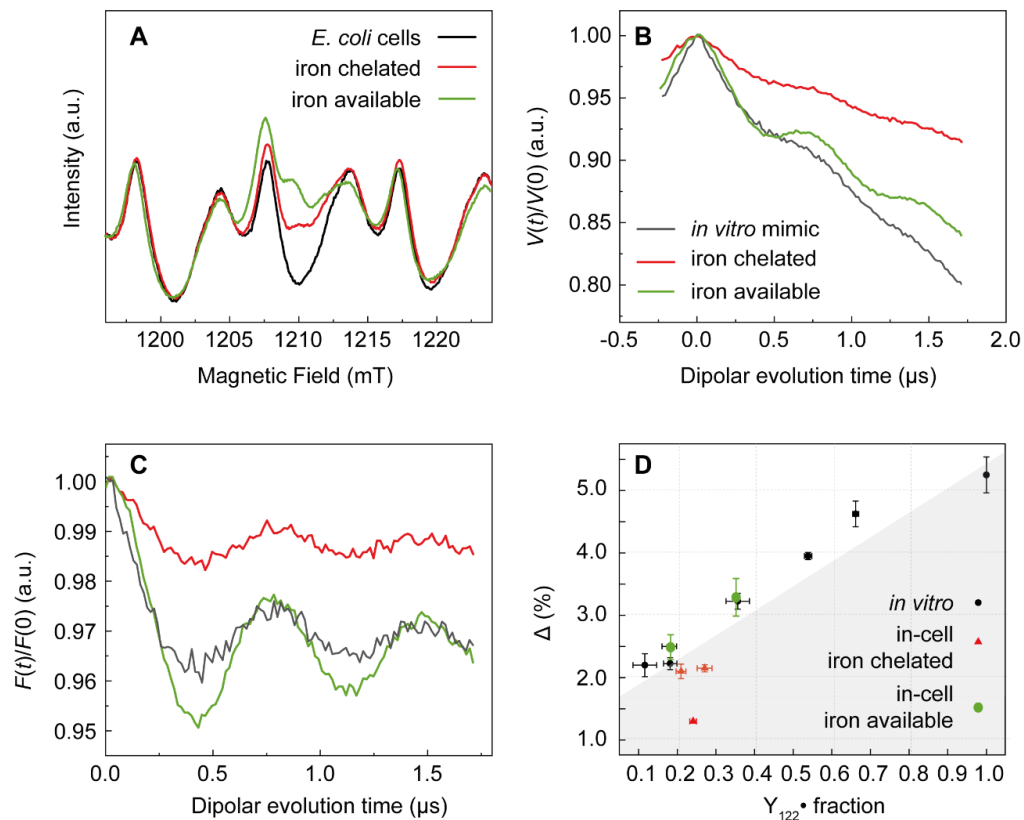


**Figure 4.3: Modulation depth analysis of in-cell samples expressing the  $\beta_2$ -subunit of *E. coli* RNR under iron-chelated and iron-available conditions.** (A) Q-band field-swept EPR spectra of in-cell samples produced under iron-limiting (red) or iron-available (green) expression conditions. Spectra were recorded via the refocused spin echo with pump pulse applied. A spectrum of *E. coli* cells without protein overexpression is shown in black as comparison. (B) Primary DEER traces and (C) form factors of the corresponding samples. An *in vitro* sample mimicking the iron-available sample is shown in grey as comparison. (D) Calibration curve for different in-cell samples compared to *in vitro*. Iron was either limited (red) or available (green) during the protein expression of the cells. Details are given in **Figure B.2**.

#### 4.3.3. $Y_{122}\bullet$ radical distribution *in vitro* as a function of manganese concentration

To gain a detailed understanding of such a complex mechanism as  $Y\bullet$  level regulation in dependence on metal availability is hard to be clarified solely via *in vivo* experiments. Various factors, such as intracellular metal and protein levels, would need to be controlled, and reliable *in vivo* activity assays would need to be applied, which do not exist yet. Therefore, a different approach was chosen to understand the underlying basics: the cellular conditions were mimicked by *in vitro* experiments. Therefore, apo- $\beta_2$  RNR was first titrated with  $Mn^{II}$ .

The presence of the diiron center in *E. coli* RNR is a prerequisite for the radical state of  $Y_{122}$  and, thus, protein catalytic activity. Self-assembly of the metallocofactor *in vitro* from apo- $\beta_2$  by the addition of  $Fe^{II}$  and  $O_2$  results in the reconstitution of the active diiron tyrosyl radical cofactor (**Figure 4.4A**). However, the protein can also bind manganese

with a quite similar ligand environment as the iron complex, forming an inactive dimanganese ( $\text{Mn}^{\text{II}}\text{Mn}^{\text{II}}$ ) cofactor. The EPR fingerprint of this Mn-cofactor is characterized by a broad EPR signal with a peak-to-peak linewidth of 500 G centered at  $g = 1.95$  (Figure 4.4A), consistent with earlier results.<sup>99,100</sup> The ground state of an antiferromagnetically coupled  $\text{Mn}^{\text{II}}\text{Mn}^{\text{II}}$  center is EPR silent ( $S = 0$ ). However, when the exchange coupling is small, this allows excited spin states of the manifold to be accessed at cryogenic temperatures.<sup>21</sup> These spin manifolds have total spin quantum numbers of  $S = 0, 1, 2, 3, 4,$  and  $5$ , given by:

$$S = |S_1 + S_2|, |S_1 + S_2 - 1|, \dots, |S_1 - S_2|.^{251} \quad (4.2)$$

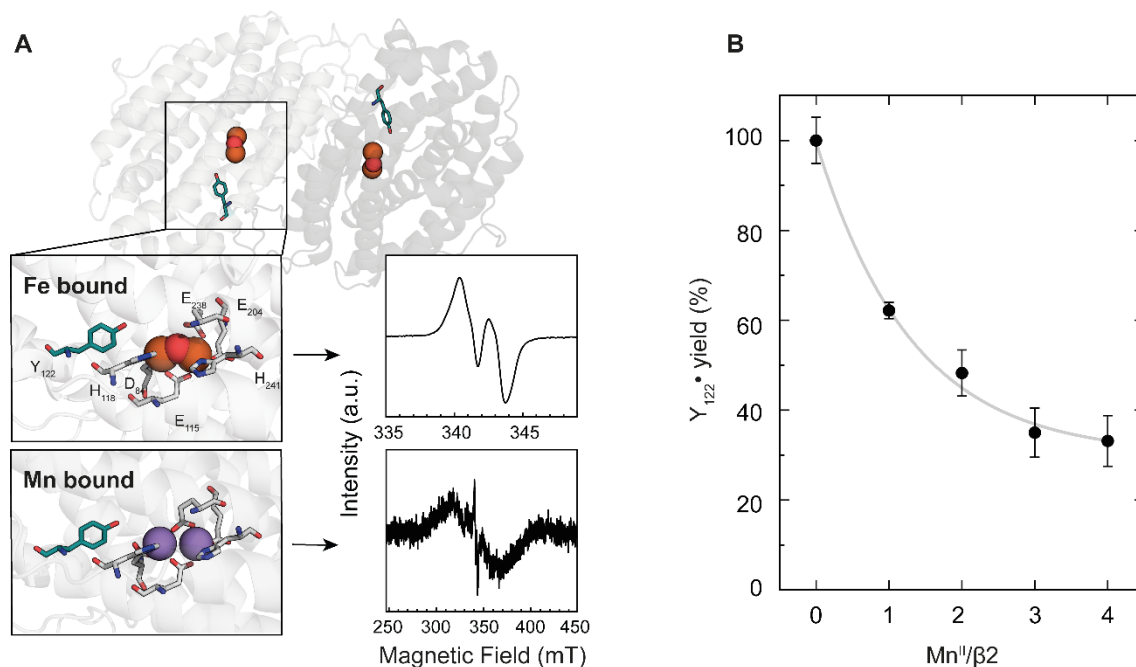


**Figure 4.4: Iron or manganese bound in the homodimeric  $\beta_2$  subunit of *E. coli* RNR.** (A) Cw-EPR spectrum of  $\beta_2$  after the addition of  $\text{Fe}^{\text{II}}$  (top) or  $\text{Mn}^{\text{II}}$  (bottom) under aerobic conditions. Note the different spectral widths of  $\text{Y}_{122}\bullet$  and  $\text{Mn}^{\text{II}}\text{Mn}^{\text{II}}$ . Spectra were recorded at 9.6 GHz and 100K. (B)  $\text{Y}_{122}\bullet$  yield generated by the addition of 5 equivalents  $\text{Fe}^{\text{II}}$  to the  $\beta_2$  subunit of *E. coli* RNR, previously incubated with 1 – 4 equivalents  $\text{Mn}^{\text{II}}/\beta_2$  under aerobic conditions. Yields were determined by the amplitude of the  $\text{Y}_{122}\bullet$  cw-EPR signal at 9.6 GHz. Data points show mean values together with standard deviation.

EPR signals of these excited states appear quite characteristic but, at the same time, diverse.<sup>21,252,253</sup> The EPR signature of  $\text{Mn}^{\text{II}}\text{Mn}^{\text{II}}$  in *E. coli* class Ia RNR differs from most of the reported spectra of dinuclear  $\text{Mn}^{\text{II}}$  centers in proteins, such as those of RNR class Ib or R2c,<sup>17,21</sup> which might be explained by weaker coupling.<sup>23</sup> An isotropic exchange coupling of  $J = -1.8 \text{ cm}^{-1}$  was found earlier for  $\text{Mn}^{\text{II}}\text{Mn}^{\text{II}}$  in *E. coli* class Ia RNR.<sup>100</sup> Indeed,

the spectral lineshape is more consistent with the one of  $\text{Mn}^{\text{II}}$  in concanavalin A<sup>254</sup> with  $|J| = 0.9 \text{ cm}^{-1}$  rather than the one from Mn-catalase ( $|J| = 14 \text{ cm}^{-1}$ )<sup>255</sup>.

The following experiments were performed next to further mimic the process of in-cell sample preparation: First, various equivalents (eq.) of  $\text{Mn}^{\text{II}}$  were added to *in vitro* apo- $\beta 2$  under aerobic conditions to allow manganese binding in the iron-binding sites of the protein. Afterward, the radical formation was initiated by the addition of 5 eq.  $\text{Fe}^{\text{II}}$  per  $\beta 2$  and the radical yield was determined by cw-EPR after 2 h incubation (**Figure 4.4B**). As seen in the data, the addition of  $\text{Mn}^{\text{II}}$  to apo- $\beta 2$  prior to iron reduces the radical generation efficiency. However, the observed effect is not as drastic as reported earlier, where 2 eq.  $\text{Mn}^{\text{II}}$  were already sufficient to almost fully inhibit the radical formation (ca. 10% radical yield vs. 50% here).<sup>99</sup> The different outcomes can be explained by varying experimental conditions as in the previous studies, significantly higher amounts of glycerol (20%) have been used in the buffer, compared to 5% used here. Glycerol was shown to affect the allostery between the two  $\beta$ -subunits and thus leads to a distinct metal distribution in the homodimeric protein.<sup>100</sup> For high glycerol levels, manganese is incorporated equally in both subunits and binding of up to 4 eq.  $\text{Mn}^{\text{II}}$  was observed. Only one site was found to bind  $\text{Mn}^{\text{II}}$  at low glycerol contents, and thus, a maximum of 2  $\text{Mn}^{\text{II}}/\beta 2$  is detected.<sup>100</sup>

Furthermore, it was manifested that oxygen availability plays a crucial role in the cofactor assembly mechanism. In the absence of oxygen, only two metals, either being  $\text{Mn}^{\text{II}}$  or  $\text{Fe}^{\text{II}}$ , could be bound in  $\beta_{\text{I}}$ , whereas  $\beta_{\text{II}}$  remains in the apo state. If  $\text{Fe}^{\text{II}}$  is bound in  $\beta_{\text{I}}$ ,  $\text{Mn}^{\text{II}}$  can be added and subsequent  $\text{O}_2$  saturation of the sample will lead to an asymmetric assembly with diiron cofactor in  $\beta_{\text{I}}$  and a dimanganese one in  $\beta_{\text{II}}$ . Furthermore, metal exchange, also described as scrambling, was suggested to take place during the reaction with  $\text{O}_2$  to form an active diferric cofactor with its tyrosyl radical on one side and a di-manganese cofactor on the other side of the dimer.<sup>256</sup> This process is only feasible in the presence of oxygen. However, no direct spectroscopic evidence has been presented for this hypothesis yet.

Among the two metal-binding sites within a single  $\beta$ -monomer, the  $\text{Fe}_{\text{B}}$  site possessed an approximately 5-fold higher binding affinity than the  $\text{Fe}_{\text{A}}$  site.<sup>97</sup> Apo- $\beta 2$  with one equivalent of  $\text{Mn}^{\text{II}}$  thus results in  $\text{Mn}^{\text{II}}_{\text{B}}\text{-}\beta 2$ , bound in  $\beta_{\text{I}}$ , which does not exhibit any cw-EPR signal at 100 K and 9.6 GHz (**Figure 4.5A**). Typically, a characteristic EPR spectrum of  $\text{Mn}^{\text{II}}$ -RNR is expected,<sup>100</sup> which scales inversely with temperature<sup>100</sup> and is therefore no longer detectable at 100 K in this case. The addition of iron leads to the detection of three different paramagnetic species (**Figure 4.5A**): I) tyrosyl radical (cut out for better visualization), II) a broad EPR signal, characteristic of the dimanganese  $\text{Mn}^{\text{II}}\text{Mn}^{\text{II}}\text{-}\beta 2$ , and III) free  $\text{Mn}^{\text{II}}$ . The appearance of these signals after iron addition indicates that rearrangement of the metals bound in the subunits must occur, allowing  $\text{Y}_{122}\bullet$  formation.

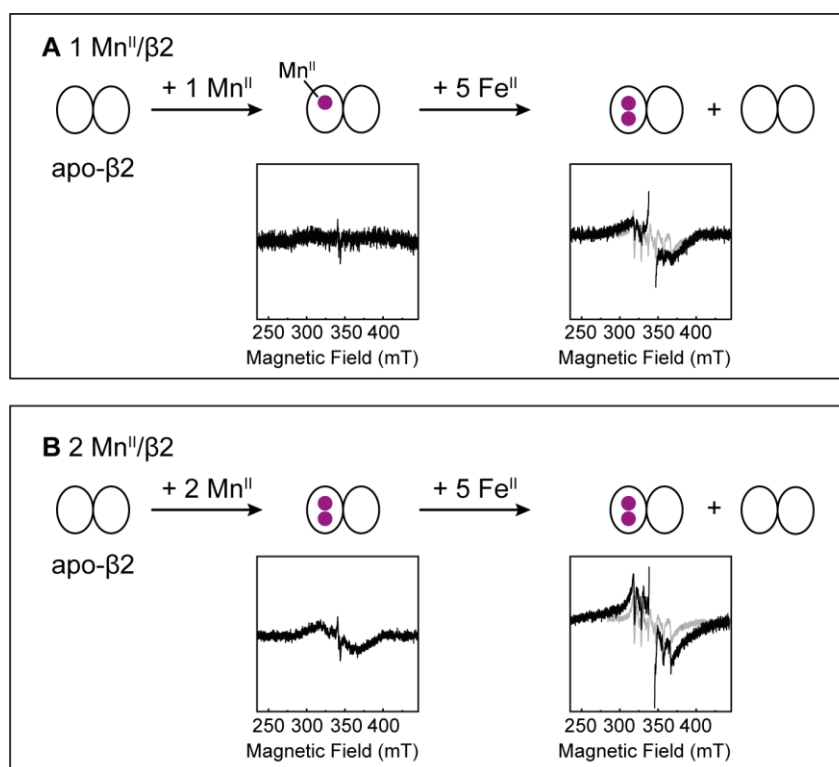


**Figure 4.5:** Cw-EPR spectrum before and after adding Fe<sup>II</sup> to Mn<sup>II</sup>-bound *E. coli* RNR. Signals are shown for the addition of (A) 1 equivalent Mn<sup>II</sup> per β<sub>2</sub> or (B) 2 equivalents. Y<sub>122</sub>• signal is cut out for better visualization. Free aqueous Mn<sup>II</sup> is overlaid in gray for comparison to bound Mn<sup>II</sup> species. Data were recorded at 9.6 GHz at 100 K. Experimental conditions: 1 mW power, 3.5 G modulation amplitude, 100 kHz modulation frequency, 20.48 ms as time constant, and 34.84 ms conversion time, 15 scans (1 Mn<sup>II</sup>), 34 scans (1 Mn<sup>II</sup> + 5 Fe<sup>II</sup>), 50 scans (2 Mn<sup>II</sup>), 80 scans (2 Mn<sup>II</sup> + 5 Fe<sup>II</sup>).

When RNR is supplemented with 2 eq. Mn<sup>II</sup>, the Mn<sup>II</sup>Mn<sup>II</sup>-β<sub>2</sub> signal is already detected even without iron addition (**Figure 4.5B**). No or only minor amounts of Y<sub>122</sub>• and free Mn<sup>II</sup> are observed. Adding iron again leads to the observation of the three species (Y<sub>122</sub>•, Mn<sup>II</sup>Mn<sup>II</sup>, and free Mn<sup>II</sup>), supporting a hypothesis of metal rearrangement in combination with radical formation.

These results allow a conclusion on the binding mechanism of Mn<sup>II</sup> in *E. coli* RNR in the presence and absence of iron, as depicted schematically in **Figure 4.5**. First, all Mn<sup>II</sup><sub>B</sub> binding sites are occupied in β<sub>I</sub>, followed by binding in the A-site in β<sub>I</sub> upon adding the second equivalent of Mn<sup>II</sup>. However, the addition of Fe<sup>II</sup> leads to manganese scrambling so that in all cases, Mn<sup>II</sup><sub>A</sub>Mn<sup>II</sup><sub>B</sub> centers are tried to be formed. Note that A and B sites, as well as β<sub>I</sub> and β<sub>II</sub>, are not labeled in the scheme below, as their allocation after metal scrambling is unknown. These findings strongly support an unprecedented, asymmetric radical distribution to be present in the β<sub>2</sub> dimer with a diiron-Y<sub>122</sub>• cofactor on one side and a dimanganese cofactor on the other side of the dimer. Such an asymmetric cofactor arrangement seems surprising as it has not been observed in RNR yet.

#### 4.3.4. An asymmetric cofactor assembly and radical generation in *E. coli* RNR verified via *in vitro* DEER measurements

The data so far strongly suggest asymmetric cofactor formation in *E. coli* RNR. However, there is still the possibility that the observed tyrosyl radicals are generated in manganese-free subunits only. The distance between the tyrosyl radical and the dimanganese cofactor is expected to be  $\sim 2.9$  nm based on the available crystal structure (Figure 4.6A and Figure B.3), which lies within the accessible range of DEER spectroscopy. If the formation of an asymmetric cofactor assembly in the  $\beta 2$  dimer is the case, a distance between  $Y_{122}\bullet$  and  $Mn^{II}Mn^{II}$  should be easily resolved. Therefore, apo- $\beta 2$  samples pretreated with 1 – 4 eq.  $Mn^{II}/\beta 2$  were supplemented with iron, incubated for 2 h, and subsequently investigated by orientation-selective DEER measurements (Figure 4.6B).

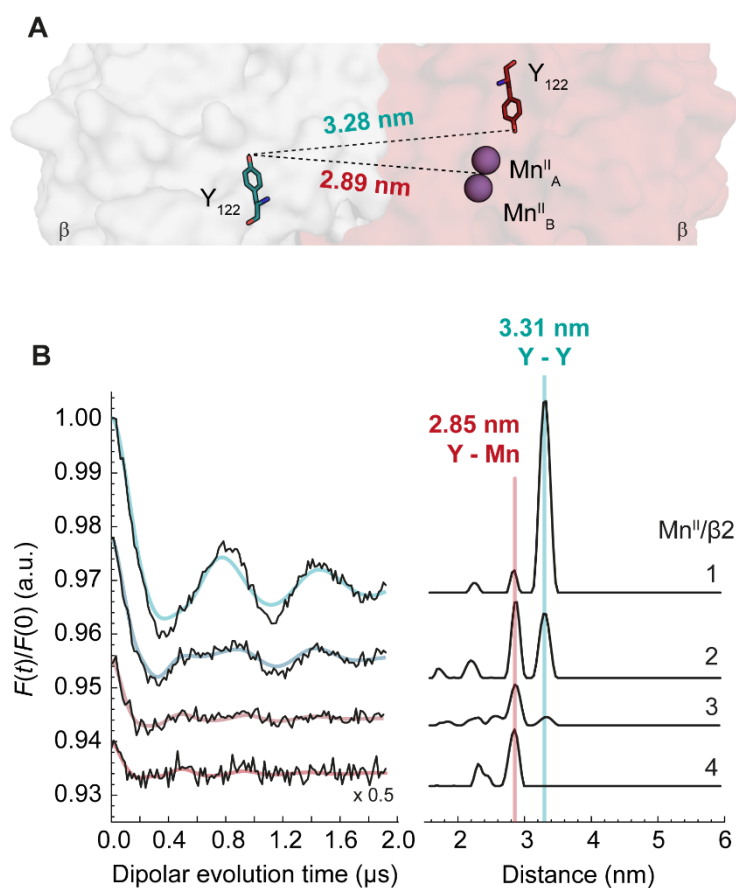


**Figure 4.6: Detection of a  $Y_{122}\bullet$ - $Mn^{II}Mn^{II}$  distance in *E. coli* RNR via DEER measurements.** (A) Crystal structure of *E. coli* RNR  $\beta 2$  in its iron (gray) and manganese (red) bound form, along with distances between two  $Y_{122}\bullet$ s and between  $Y_{122}\bullet$  and  $Mn^{II}Mn^{II}$  (dashed lines). (B) Background- and phase-corrected, normalized 34 GHz DEER traces of apo- $\beta 2$  supplemented with one to four equivalents  $Mn^{II}$  per dimer together with obtained distance distributions. Detected main distances are marked with colored lines. Fits obtained by DeerAnalysis are overlaid in light color. Details of the experiments and analyses are given in Figure B.4.

Distance measurements of manganese-containing RNR revealed two main distances, one located at around 3.3 nm and a second smaller distance at 2.9 nm. The first one can be immediately assigned to the  $Y_{122}\bullet$ - $Y_{122}\bullet$  pair, termed Y-Y in the following.<sup>64</sup> The second distance matches the predicted distance for a  $Y_{122}\bullet$ - $Mn^{II}Mn^{II}$  pair based on the crystal structure. Additionally, the 2.9 nm distance gains relative intensity compared to the Y-Y distance with increasing amounts of manganese. These observations strongly suggest that the identity of this smaller distance is a  $Y_{122}\bullet$ - $Mn^{II}Mn^{II}$  pair (shortly Y-Mn) originating from asymmetric cofactor assembly. However, this distance was only observed for samples where  $Mn^{II}$  was added prior to iron. DEER measurements of samples with reverse order of metal addition revealed only one distance, the Y-Y pair.<sup>192</sup>

Another possibility giving rise to additional distances in the distance distribution<sup>73</sup> could be a distinct  $Y_{122}\bullet$  conformation. This possibility is unlikely, as it would be reflected in a change in the EPR lineshape, which could not be observed. However, to rule out this possibility entirely, further DEER experiments were performed, in which the power of the pump pulse was reduced. The previous pulses were optimized for  $Y_{122}\bullet$  detection. However, metal species possess distinct relaxation behaviors and saturate quickly under the chosen experimental conditions. Therefore, the sharp six lines characteristic of  $Mn^{II}$  are not visible when applying a  $\pi = 28$  ns pulse of 90% power at 20 mW for detection. Hahn echo-detected field sweep spectra (Figure 4.7) revealed an optimal power of around 20 to 30% with  $\pi = 28$  ns for manganese detection. At these power levels,  $Mn^{II}$  shows six spectral lines originating from the  $m_s = -1/2 \leftrightarrow +1/2$  transitions.

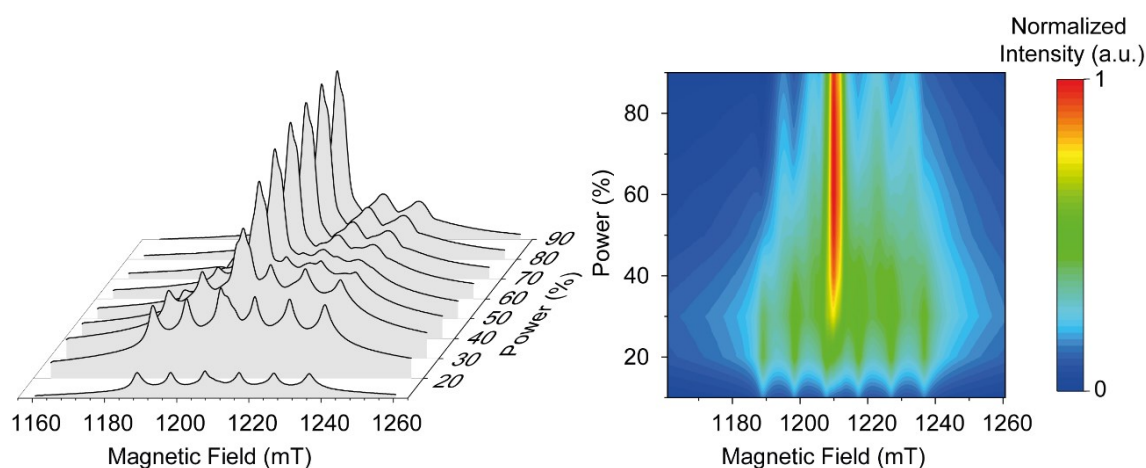


**Figure 4.7:** ESE spectra of  $Mn^{II}$  added to  $Y_{122}\bullet$  in *E. coli* RNR performed at 34 GHz and 10 K depending on the microwave pulse power applied. Spectra are illustrated as a 3D plot (left) or a heatmap (right).

The experimental inversion efficiency  $\lambda_{\text{exp}}$  can be calculated via the following equation:

$$\lambda_{\text{exp}} = \frac{1 - \frac{B}{A}}{2} \quad (4.3)$$

with A being the echo amplitude before the generation of microwave pulses and B the echo intensity at the corresponding time point. Nutation experiments, performed at the field position with maximum signal intensity of  $Y_{122}\bullet$ , were implemented by varying power levels of the inversion pulse  $t_p$  and unraveled a reduction in inversion efficiency from 0.83 to 0.41 (30% power) or 0.25 (20% power) (Figure 4.8A). This means that by reducing the pump pulse power in the DEER experiment, the tyrosyl radical is pumped less effectively than the metal species, highlighting the Y-Mn distance against the Y-Y pair in relative intensities. If both distances result from two distinct Y-Y conformations, both distances would scale equally in relative intensity. In fact, the corresponding DEER experiments prove that the first scenario is true, so the smaller distance at 2.9 nm must result from dipolar coupling of the metal species (Figure 4.8B).

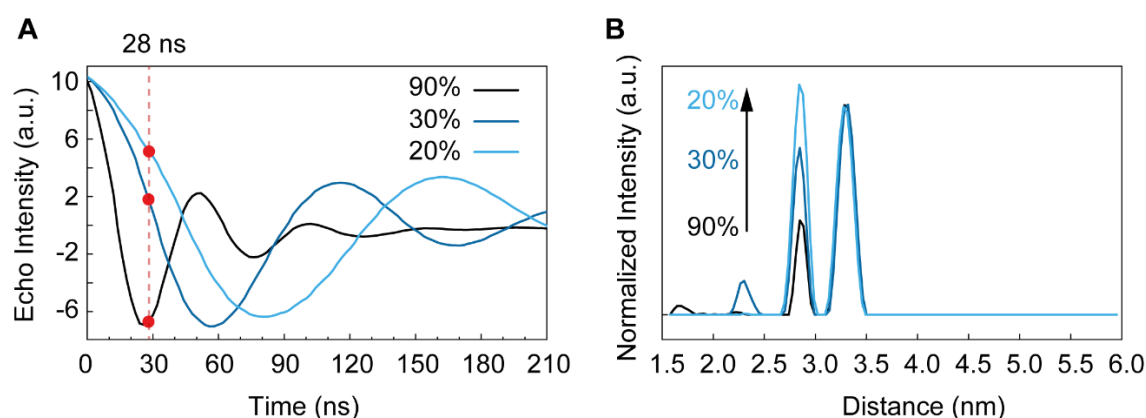


**Figure 4.8: Power-dependent DEER experiments for  $Mn^{II}$ -bound *E. coli* class Ia RNR, proving a  $Y_{122}\bullet$ - $Mn^{II}Mn^{II}$  distance.** (A) Microwave nutation experiments with 90% (black), 30% (blue), and 20% (light blue) power of the initial  $\pi$ -pulse  $t_p$ . (B) Obtained distance distributions normalized to intensities at 3.3 nm.

These findings provide proof of the first spectroscopic detection of a  $Y_{122}\bullet$ - $Mn^{II}Mn^{II}$  distance in *E. coli* RNR and thus support an unprecedented asymmetric radical distribution in the presence of manganese. The lack of any spectroscopic detection of a  $Mn^{II}Mn^{II}$ - $Mn^{II}Mn^{II}$  pair with an expected distance of 2.5 nm demonstrates an asymmetric metal-binding process in which one side of the dimer ( $\beta_I$ ) is able to bind manganese but prevents further metal incorporation into  $\beta_{II}$ , as suggested by Pierce *et al.*<sup>100</sup> A maximum of 2  $Mn^{II}$  bound per  $\beta_2$  as detected by cw experiments supports these findings.

It is important to note that a smaller distance of around 2.2 – 2.3 nm is detected in some cases. This distance can be assigned to an orientation-selectivity artifact of the  $v_{II}$  component, as the observed distance resembles the one extracted by DeerAnalysis for  $\theta = 0^\circ$ . This observation provides proof of strong orientation selectivity and, consequently, a rigidity that must be present in the system under consideration. This is not surprising, considering the strong orientation selectivity of  $Y_{122}\bullet$  detected in the cells

as well. Similarly, this shows that the manganese is systematically and tightly coordinated in RNR's metal-binding pocket.

In addition, the narrow peak of the Y-Mn distance indicates a considerably localized spin density in the dimetal center. Distances between  $Y_{122}\bullet\text{-Mn}^{\text{II}}_{\text{A}}$  and  $Y_{122}\bullet\text{-Mn}^{\text{II}}_{\text{B}}$  based on the crystal structure are 2.92 and 2.86 nm, respectively (**Table B.1**). Considering an error in distance determination of approximately 0.3 nm, based on the Y-Y distance determined experimentally and by the crystal structure, the experimental Y-Mn distance of 2.85 nm indicates a spin density more localized at  $\text{Mn}^{\text{II}}_{\text{B}}$ . This might suggest that the determined distance can also originate from a single bound  $\text{Mn}^{\text{II}}$  ion. However, this explanation seems unlikely since two metals are observed to bind upon the addition of 4 eq. of manganese in a  $\text{Mn}^{\text{II}}_{\text{A}}\text{Mn}^{\text{II}}_{\text{B}}$  arrangement, and thus, a peak broadening or a shift of the mean distance should be observed, which is not the case (**Figure 4.6**). The correct spin density distribution could be clarified by density functional theory (DFT) calculations.

Apart from a distance, DEER experiments deliver information on the fraction of spin pairs in a sample provided by the experimental modulation depth  $\Delta$ . As outlined in Chapter 3, the effect of the manganese content on the modulation depth of *E. coli* can be described by a linear calibration curve. A comparison of these new results to the established calibration curve demonstrates that all data points constantly fall below the modulation depth expected for a two or none radical distribution (**Figure 4.9**). This implies that a radical distribution different from two or none must be present in these samples. The reduction of  $\Delta$  can be explained by the presence of the Y-Mn distance. As  $\text{Mn}^{\text{II}}$  is characterized by a broad EPR spectrum, the fraction of  $\text{Mn}^{\text{II}}$ -species inverted by the pump pulse  $\lambda_{\text{Mn}^{\text{II}}}$  is much smaller than for a tyrosyl radical, holding a narrow spectral width. Hence, the maximum  $\Delta$  for a Y-Mn distance will be smaller than for a Y-Y pair. These observations again provide direct proof of an asymmetric cofactor assembly. Remarkably, all data points align and therefore demonstrate that the metal binding and, thus also, mismetallation in *E. coli* RNR is a controlled process. Otherwise, if manganese were bound in some cases and free in solution in others, the data points would be scattered over the entire graph.

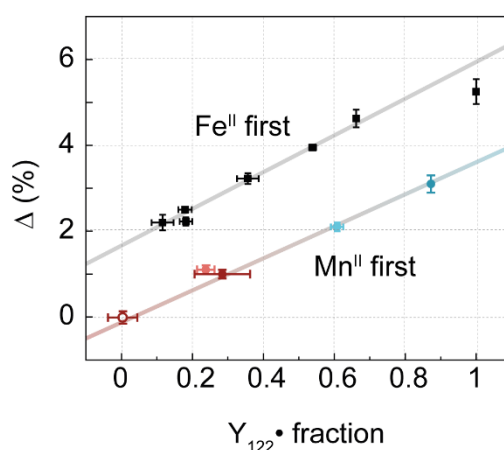


**Figure 4.9: Calibration curve for *E. coli* RNR *in vitro* prepared under different metal-availabilities, mimicking cellular conditions.** Fe<sup>II</sup> (black) or Mn<sup>II</sup> (blue to red) was first added to apo-β<sub>2</sub>, followed by the addition of the other metal respectively. Black data points were recorded 10 min after Mn<sup>II</sup> addition, while colored data points were recorded 2 h after Fe<sup>II</sup> addition. Data shown in red with a filled or open symbol differ in the sample preparation. For details, see supporting information **Figure B.4**.

#### 4.3.5. Elucidating the time-dependent *in vitro* radical generation process

Diferric Y<sub>122</sub>• formation in *E. coli* class Ia RNR is usually completed within a few seconds.<sup>88</sup> However, if a metal exchange were to take place, it could happen within hours. Such a phenomenon has been showcased in, for example, cadmium carbonic anhydrase. Zn can substitute the bound Cd while the replacement takes place within a timeframe of several hours to finally reach a new equilibrium *in vitro* after approximately one day of incubation.<sup>257</sup> Detecting the occurrence of such an exchange mechanism would be an essential element for understanding the mechanistic implications of metal cofactor assembly in *E. coli* RNR. To check the incidence of metal exchange and a resulting recovery of the protein, time-dependent UV-Vis measurements were performed (**Figure 4.10A**) to characterize the Y• yield. UV-Vis spectra of holo-β<sub>2</sub> are characterized by a sharp absorption maximum at 410 nm caused by Y<sub>122</sub>• and bands at 320 and 365 nm resulting from the μ-oxodiiron<sup>III</sup> cofactor.<sup>86,87</sup> The Mn<sup>II</sup>-bound β<sub>2</sub>-subunit does not exhibit any specific absorption features (**Figure B.5B**) and consequently allows differentiation of the two states. For the experiments, apo-β<sub>2</sub> was first incubated with 1 – 4 eq. of Mn<sup>II</sup> for 10 min. Subsequently, 5 eq. Fe<sup>II</sup> were added, and UV-Vis spectra were recorded immediately afterward. In order to extract the contribution of Y<sub>122</sub>• to the total absorption at 410 nm, a dropline correction is often used for subtracting Fe<sup>II</sup>-O-Fe<sup>II</sup> contributions.<sup>88</sup> However, for manganese-containing samples, the UV-Vis lineshape is changed, and the established dropline correction might be inaccurate. Consequently, a modified version of background correction needs to be done by creating a new

background for each individual dataset. The obtained radical yield can then be represented as a function of time (**Figure 4.10B**).

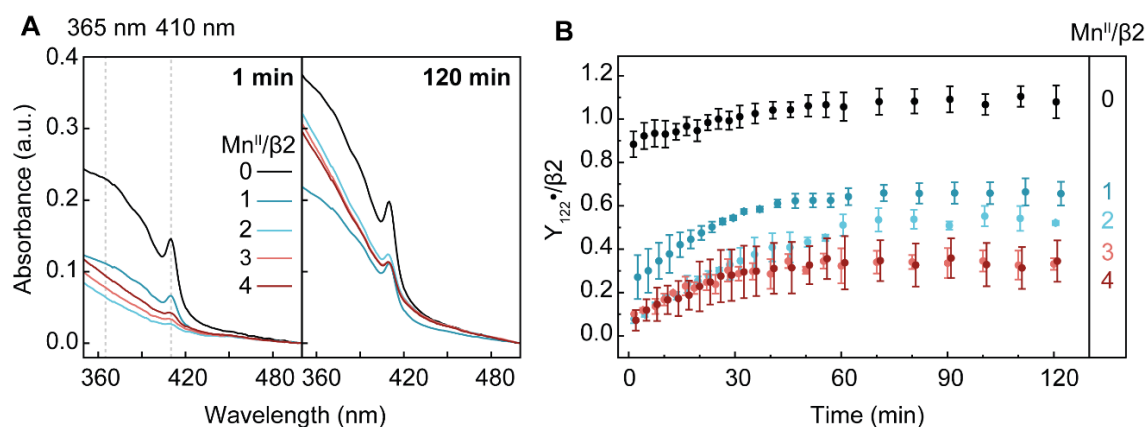


**Figure 4.10: Influence of  $Mn^{II}$  on the time-dependent radical formation of  $Y_{122}\bullet$  in *E. coli* RNR.** (A) UV-Vis spectra of the  $\beta_2$  subunit supplemented with different equivalents of  $Mn^{II}$  recorded 1 min (left) or 120 min (right) after  $Fe^{II}$  addition. (B) Time-dependent detection of the  $Y_{122}\bullet/\beta_2$  yield as a function of added  $Mn^{II}$ . Errors in the graphs are given by the standard deviation of duplicates.

In all manganese-containing samples,  $Y_{122}\bullet$ -formation is inhibited in the first few minutes after iron addition, whereas the manganese-free samples already displayed a radical yield of  $0.9 Y_{122}\bullet/\beta_2$ . A subsequent increase in radical concentration is observed over a period of approximately 1 hour, independent of the manganese content. Holo- $\beta_2$  without additional manganese reaches a radical yield of  $1.1 Y_{122}\bullet/\beta_2$  after 2 h incubation, consistent with the previously reported maximum yield of  $1.2 Y_{122}\bullet/\beta_2$ .<sup>86</sup> In contrast, all manganese-containing samples exhibit lower radical yields. 2 equivalents of  $Mn^{II}$  were already sufficient to initially inhibit the radical generation process ( $0.1 Y_{122}\bullet/\beta_2$  at 1 min). However, a rise of 0.4 units can be observed after 2 h incubation.

Surprisingly, high amounts of glycerol prevent this recovery effect (**Figure 4.11**). Even in the absence of manganese, glycerol reduces the maximal radical yield, decreasing it from 1.2 to  $0.8 Y_{122}\bullet/\beta_2$ . In the presence of manganese, both samples initially display a radical yield of around  $0.3 Y_{122}\bullet/\beta_2$ , which remains stable in the case of 20% glycerol but increases to  $0.6 Y_{122}\bullet/\beta_2$  for 5% glycerol. These results demonstrate a reduced radical formation caused by glycerol. Interestingly, activity measurements of the  $\alpha_2\beta_2$  complex revealed that a glycerol content of 18% already reduces the catalytic activity by about 50% compared to assays performed in a glycerol-free buffer.<sup>74</sup> An increase of the glycerol content to 27% results in a residual activity of approx. 30% only.<sup>74</sup> These findings support the hypothesis that glycerol influences RNR's allosteric regulation and consequently activity.

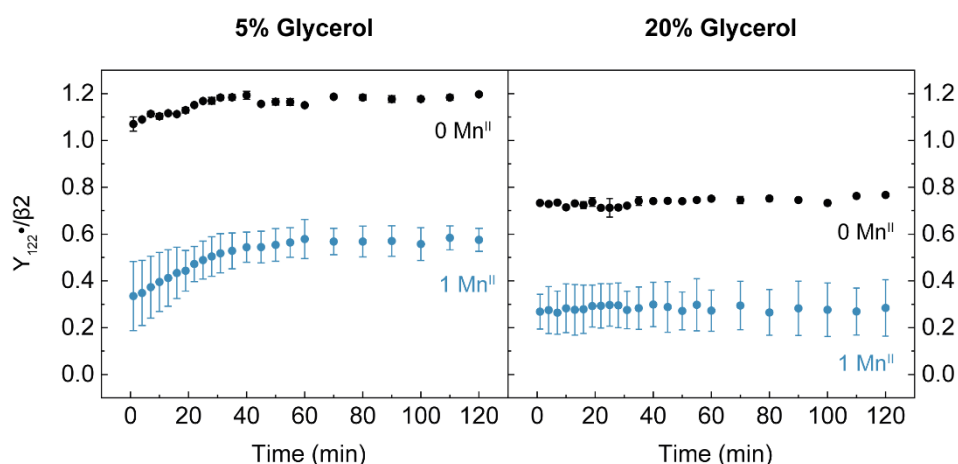


**Figure 4.11: Time-dependent detection of the  $Y_{122}\bullet/\beta_2$  yield in the presence and absence of  $1 \text{ Mn}^{\text{II}}/\beta_2$ , obtained via UV-Vis measurements.** Samples were prepared in Tris buffer, either containing 5% or 20% glycerol. Data are mean values and standard deviation of two experiments.

The formation of a tyrosyl radical, despite manganese binding, is surprising, as it was previously predicted that manganese would completely prevent radical formation.<sup>99</sup> In contrast to the experiments shown here, previous ones did not consider time-dependent effects. Therefore, it is interesting to identify and understand factors that enable radical generation over time. One way to approach this question is to trace the different manganese species. Thus, cw-EPR spin counting experiments of the free aqueous  $\text{Mn}^{\text{II}}$  were performed (**Figure 4.12**), revealing that radical generation is accompanied by  $\text{Mn}^{\text{II}}$  release. After 2 h of iron incubation, around 40% of the initially added manganese is released. Previous studies report on 20% free  $\text{Mn}^{\text{II}}$  after iron addition and a few minutes of incubation, consistent with our observations.<sup>256</sup> In contrast, manganese-bound  $\beta_2$  incubated for 2 h without iron does not show such a release. Thus,  $\text{Mn}^{\text{II}}$  must be tightly bound in the protein, but  $\text{Fe}^{\text{II}}$  must have a slightly higher binding affinity, as already proposed in the Irving-William Series. In turn, this process allows metal displacement with accompanying radical generation as a regulatory mechanism for protein mismetallation.

However, not all bound manganese is released, but only about 40% at a time. The limitation in metal release could be linked to the fact that iron oxidizes very quickly under aerobic conditions. Hence, the radical yield was also investigated after the second addition of 5 eq.  $\text{Fe}^{\text{II}}$  to the sample (**Figure 4.13A**). This supplementary addition of iron causes a further increase in radical yield of about 0.1 – 0.2 units. Furthermore, DEER spectra were recorded at equilibrium after the first (5 eq.  $\text{Fe}^{\text{II}}$ ) and the second addition of iron (10 eq.  $\text{Fe}^{\text{II}}$ ) to a sample containing 2 eq.  $\text{Mn}^{\text{II}}$  (**Figure 4.13B**). For 10 eq.  $\text{Fe}^{\text{II}}$ , the fraction of  $Y_{122}\bullet$  in the refocused echo decreases compared to 5 eq.  $\text{Fe}^{\text{II}}$  since  $\text{Mn}^{\text{II}}$  continues to be released (ca. 10% released as determined by cw-EPR experiments).

Comparing both samples to the calibration curve points out that the second iron addition causes an approach back to the calibration curve, meaning the quantity of Y-Y pairs increases relative to Y-Mn pairs. This indicates that once there is sufficient  $\text{Fe}^{\text{II}}$  present, the protein can completely reverse mismetallation and return to its active, diiron-bound form.

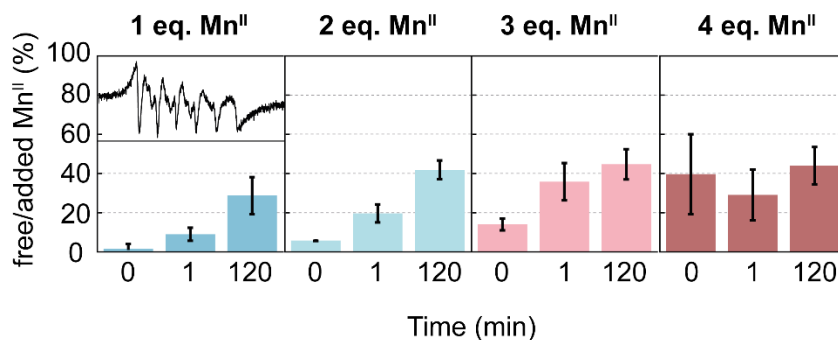


**Figure 4.12:** Percentage of free  $\text{Mn}^{\text{II}}$  before (0 min), directly after (1 min), and 2 h after the addition of  $\text{Fe}^{\text{II}}$  to *E. coli* RNR. Data are obtained by cw-EPR spin counting experiments, comparing the spectra to that of a standard sample of  $\text{MnCl}_2$  in Tris buffer (inset). Spectra were recorded at 9.6 GHz and 100 K.

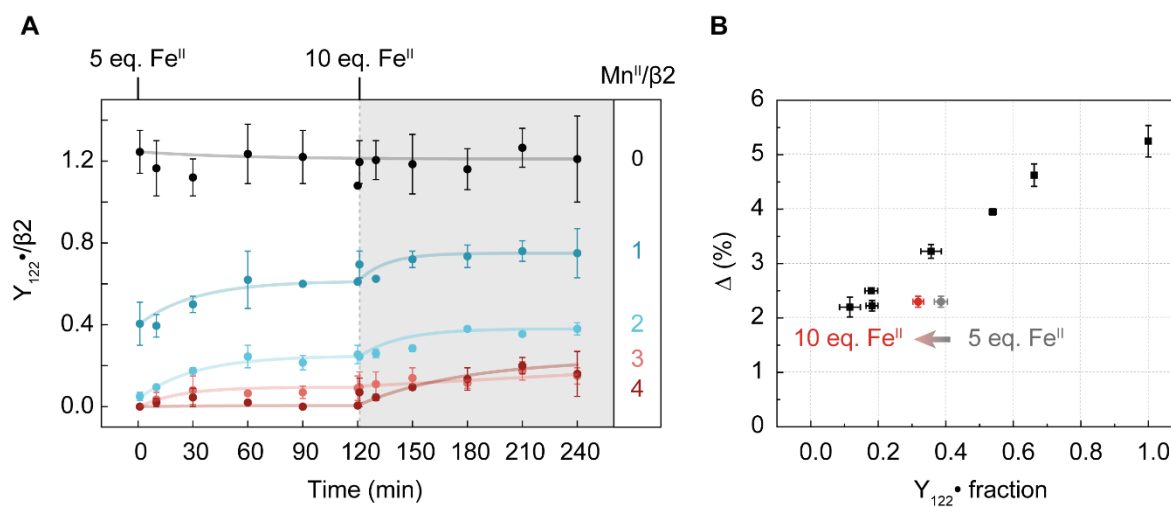


**Figure 4.13:** The effect of further addition of  $\text{Fe}^{\text{II}}$  to  $\text{Mn}^{\text{II}}$ -mismetallated RNR  $\beta_2$ . (A) Time-dependent detection of the  $\text{Y}_{122}\bullet/\beta_2$  yield as a function of added  $\text{Mn}^{\text{II}}$  obtained by UV-Vis measurements. Iron was added at two different time points (0 and 121 minutes), indicated by the gray shaded area. Mean values and standard deviation of two experiments each are shown. (B) Comparison of samples containing either 5 eq. (gray) or 10 eq. (red)  $\text{Fe}^{\text{II}}$  and 2 eq.  $\text{Mn}^{\text{II}}$  to the calibration curve. Details of the experiments are shown in Figure B.6.

#### 4.3.6. Relative binding affinities of manganese and iron

The previous experiments suggest that iron has a slightly higher binding affinity to the metal binding site of *E. coli* class Ia RNR than manganese. To test for their relative binding affinities, 5 equivalents of both metals were added to apo  $\beta 2$  at the same time, followed by detection of the radical yield via UV-Vis (**Figure 4.14A**). Surprisingly, the radical yield did not reveal changes over time but instead a constant yield of  $\sim 0.2 Y_{122\bullet}/\beta 2$ . This shows that some tyrosyl radicals can still be formed even with excess manganese. However, both metals must have comparable binding affinities and compete against each other, as binding of only one of the two metals is not observed.

The radical and metal distribution can further be elucidated by DEER spectroscopy. Prior to the measurements, the sample must be desalted since the large amounts of manganese prohibit the detection of a dipolar modulation. The distance distribution of a desalted sample is illustrated in **Figure 4.14B**, along with a comparison to the calibration curve (**Figure 4.14C**).

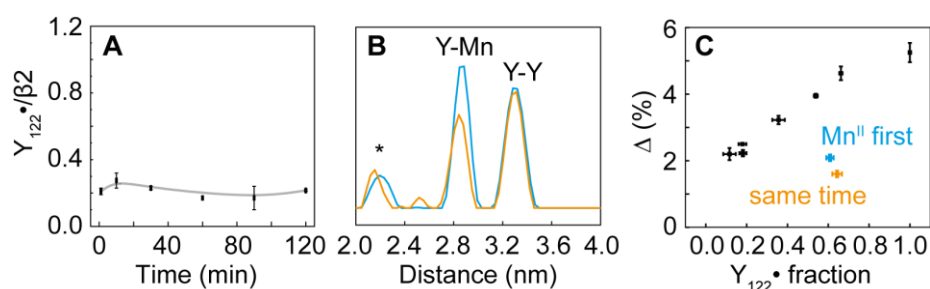


**Figure 4.14: 5 equivalents of iron and manganese added simultaneously to apo- $\beta 2$ .** (A) Time-dependent detection of the  $Y_{122\bullet}/\beta 2$  yield. Mean values and standard deviation of two experiments are shown. (B) Distance distribution obtained by the DEER measurements of samples with 5 eq.  $Fe^{II}$  and  $Mn^{II}$  each added to apo- $\beta 2$  after 2 h incubation (orange). A sample with 2 eq.  $Mn^{II}$  added prior to iron (blue) is selected as comparison. Y-Y and Y-Mn pair distances are marked, as well as the orientation-selection artifact, marked by an asterisk \*. (C) The modulation depth  $\Delta$  was plotted against the fraction of  $Y_{122\bullet}$  determined by the refocused echo. Details of the DEER measurements are given in **Figure B.7**.

DEER data of this sample are compared to a previously shown sample with 2 eq.  $Mn^{II}$  added prior to iron. These samples exhibited comparable modulation depths in the DEER experiments. DEER measurements of the sample prepared under the simultaneous presence of both metals provide evidence for Y-Y and Y-Mn pairs (**Figure 4.14B** orange data), with the ratios of the two peaks being comparable to those of the sample with 2  $Mn^{II}$  (**Figure 4.14B**, blue data). These results indicate that in both cases, an asymmetric radical distribution must be present with a  $Mn^{II}Mn^{II}$  cofactor on one side of the dimer and the ferrous tyrosyl radical on the other. In general, the procedure of metal incorporation thus behaves similarly during the presence of both metals at the same time, compared to individual addition. Furthermore, these DEER experiments demonstrate that the binding affinities of  $Mn^{II}$  and  $Fe^{II}$  to *E. coli* RNR are in a comparable

range. If iron were bound predominantly, only a Y-Y distance would be observed. However, due to the rapid oxidation of Fe<sup>II</sup>, it is challenging to make a definite statement.

In addition, the distance distribution of the sample prepared under the simultaneous addition of Mn<sup>II</sup> and Fe<sup>II</sup> displays a minor fraction of a smaller distance located at around 2.5 nm, which is also validated. According to the crystal structure, such a distance would agree with a Mn<sup>II</sup>Mn<sup>II</sup>-Mn<sup>II</sup>Mn<sup>II</sup> pair distance (see **Table B.1**). As previously explained, metal-based distances can be identified by lowering the power of the pump pulse used. If this distance originates from a Mn<sup>II</sup>Mn<sup>II</sup>-Mn<sup>II</sup>Mn<sup>II</sup> pair, it should gain relative intensity with lower power of the pump pulse compared to the Y-Y distance, just as shown for the Y-Mn pair (Section 4.3.4). A DEER experiment with only 30% power of the pump pulse (**Figure 4.15**) reveals three main distances. First, the Y-Y distance at about 3.3 nm is detected, this time with a much broader distribution than all data shown in this work. The width can be explained by the low S/N ratio of the data. Furthermore, two distances at 2.9 and 2.4 nm are detected, which gain relative intensity compared to the Y-Y distance. The distance at 2.9 nm can be assigned to the Y-Mn pair, as already described several times. A clear assignment of the smaller distance is challenging due to the high noise content of the data. This distance is probably not originating from the orientation-selectivity artifact, as this one does not scale with the used power (see **Figure 4.8**). Hence, these data suggest a Mn<sup>II</sup>Mn<sup>II</sup>-Mn<sup>II</sup>Mn<sup>II</sup> pair to be the origin of the 2.4 nm distance. Blocking all four metal-binding sites would complicate the mechanism of metal exchange, which might explain the low, unrecoverable radical yield.

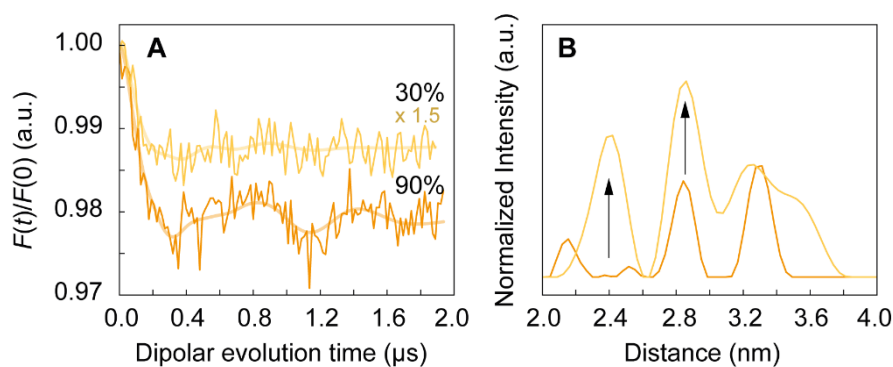


**Figure 4.15: Power-dependent DEER experiments for samples in which iron and manganese were added simultaneously to apo-β2.** (A) Background-corrected DEER traces with either 90% (orange) or 30% (yellow) power of the pump pulse. The yellow trace is magnified by 1.5 for better visualization. (B) Obtained distance distributions normalized to intensities at 3.3 nm. Acquisition times: 24 h (orange), 42 h (yellow).

These data suggest that the cofactor assembly and metal exchange process is less controlled and thus less effective in the simultaneous presence of excess free manganese and iron. These findings would explain the low radical yield observed. Potentially,

combinations of wrong metal cofactors could be assembled during conformational changes, e.g., two dimanganese centers on each side of the dimer, which blocks the radical recovery. These experiments propose that the regulation of mismetallation in RNR is not solely determined by metal binding affinities.

#### 4.3.7. Time-dependent DEER experiments allow summarizing the regulatory mechanism of mismetallation

So far, the results obtained in this work illustrate that mismetallation is not irreversibly inhibiting *E. coli* RNR, but the cofactor constitution is being modulated. This observation leads to a hypothesis about the regulatory mechanism, where two processes are crucial for the recovery from mismetallation by manganese. I) Fe<sup>II</sup> possesses a slightly higher binding affinity for the metal binding site in *E. coli* class Ia RNR, thereby competing with and releasing manganese. II) Metals switch subunits, thus allowing maximum radical yield formation.

Such a process should be easy to determine by time-dependent distance measurements between the Mn<sup>II</sup>Mn<sup>II</sup> cofactor and the tyrosyl radical. The previously shown time-dependent UV-Vis experiments were recorded with 30 μM protein concentration, but higher concentrations are needed for DEER measurements. Consequently, a concentration-dependent effect was excluded first by monitoring the radical yield prior to dipolar measurements (**Figure B.8**). The subsequent DEER measurements recorded for 1 and 2 equivalents of Mn<sup>II</sup> added to apo-β2 allow to ultimately conclude on the recovery mechanism when compared to the calibration curve (**Figure 4.16**):

As explained earlier in Section 4.3.3, the addition of 1 eq. Mn<sup>II</sup> per β2 subunit leads to the formation of a fraction of dimers containing a Mn<sup>II</sup>Mn<sup>II</sup> cofactor and another manganese-free fraction in the presence of iron and oxygen. The latter ones are able to rapidly form the native diiron tyrosyl radical cofactor in both subunits. Manganese-containing dimers remain Y<sub>122</sub>• free for the moment. This hypothesis is supported by the presence of a single Y-Y distance in the distance distribution and a radical distribution according to two of none observed in the calibration curve at the 1 min datapoint. Over time, Y<sub>122</sub>•s are slowly formed in manganese-containing β2s, verified by the growth of the Y-Mn pair distance and the shift of data points away from the calibration curve.

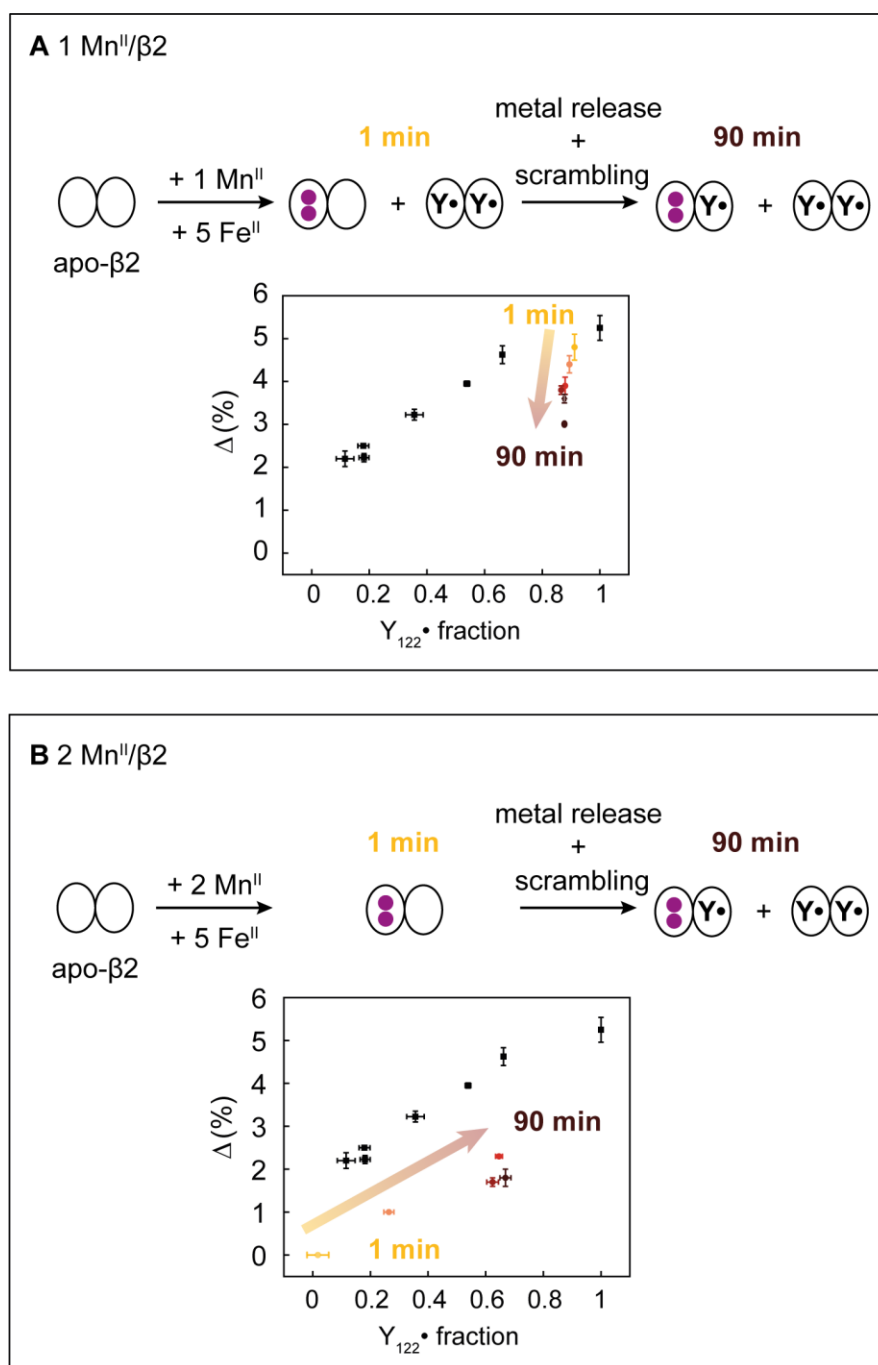


**Figure 4.16: *E. coli* class Ia RNR recovers from Mn<sup>II</sup> mismetallation via metal release and scrambling.** (A) 1 eq. Mn<sup>II</sup>/β<sub>2</sub> was added, followed by the addition of 5 eq. Fe<sup>II</sup>. DEER measurements were recorded after 1, 10, 30, 60, and 90 min iron incubation at RT. Data are compared to the calibration curve. (B) Experiments identical to those described in (A) were performed for 2 Mn<sup>II</sup>/β<sub>2</sub>. Details are given in Figure B.9.

For two equivalents, the data behave differently, which is consistent with the previous hypothesis. Upon addition of 2 Mn<sup>II</sup>/β<sub>2</sub>, β's metal coordination sites are fully saturated by manganese, which initially inhibits Y<sub>122</sub>• radical formation. No pair distances between paramagnetic centers are detected in this case. The described combination of

metal release and scrambling leads to the formation of manganese-free  $\beta_2$  subunits, represented by Y-Y distances, and  $\beta_2$ s with asymmetric metal cofactors, represented by Y-Mn distances. However, this process takes a relatively long time, as already observed with one equivalent  $Mn^{II}$ , which is why the modulation depth increases only slowly in this case. Both processes, release and scrambling, must coincide or at least depend on each other. If, for example, the release would take place in a much faster time frame, the modulation depth would have to switch instantaneously to a two-or-none distribution in the calibration curve. Overall, these findings demonstrate that the metal cofactor assembly is a highly controlled and regulated process, as all data points are characterized by a clear trend and are not randomly distributed.

#### 4.3.8. $\beta_2$ remains a rigid dimer during recovery from mismetallation

Exchanging metals could be accompanied by swapping the individual dimeric  $\beta_2$  subunits, possibly resulting in monomers as intermediates. To distinguish monomeric from dimeric  $\beta$ -subunits, size exclusion chromatography using a Superdex 75 Increase 10/300 GL column can be performed. Either 30  $\mu M$  or 150  $\mu M$  protein solution was incubated for 10 min with the indicated amount of  $Mn^{II}$  on ice. After different time points of iron addition, the solution was applied to the column (**Figure 4.17**). A single peak is observed in the elution profile corresponding to dimeric  $\beta_2$  with 88 kDa for all samples. Monomeric  $\beta$ -subunits with 44 kDa and  $V_e/V_0 = 1.3$  are not detected in any samples. These size exclusion experiments demonstrate that only dimers are present at any time during the reaction.

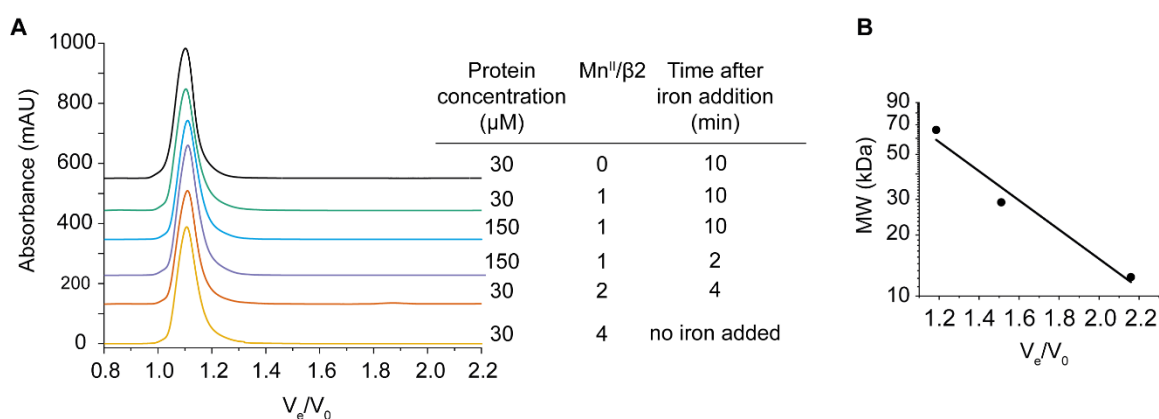


**Figure 4.17: Detection of oligomeric states of the  $\beta_2$  subunit in *E. coli* RNR upon mismetallation.** (A) Size exclusion chromatography of *E. coli* RNR  $\beta_2$  supplemented with different amounts of  $Mn^{II}/\beta_2$ . (B) Calibration with standard samples.

#### 4.3.9. Testing the activity of mismetallated RNR using the N<sub>3</sub>CDP assay

All class Ia RNRs are characterized by a half-site reactivity, in which the two halves of the  $\alpha\beta\beta$  complex cannot be assembled simultaneously.<sup>34,258</sup> The radical transfer and catalysis initially occur within a single  $\alpha\beta$  pair. After conformational changes and product release, the other  $\alpha\beta$  pair is subject to the catalytic reaction. Therefore, it might seem logical that the radical formed in asymmetric cofactors could undergo one catalytic turnover. One way to assess RNR activity is to use the mechanism-based inhibitor 2'-azido-2'-deoxycytidine diphosphate (N<sub>3</sub>CDP).<sup>43,66,245</sup> This substrate analog binds in the active site and, during catalysis, is converted to a nitrogen-centered nucleotide radical (N•) covalently bound to a cysteine in the active site. The reaction of  $\alpha 2$ ,  $\beta 2$ , N<sub>3</sub>CDP, and TTP consequently results in 50% conversion of Y<sub>122</sub>• to the EPR active N•, and the other 50% of Y<sub>122</sub>• remains unchanged (**Figure 4.18A**).<sup>259</sup> The activity can be assessed either by monitoring the decrease of Y<sub>122</sub>• or the appearance of the N• EPR signal. The first method is more suitable for quantitative statements since the N• radical is not very stable at room temperature.

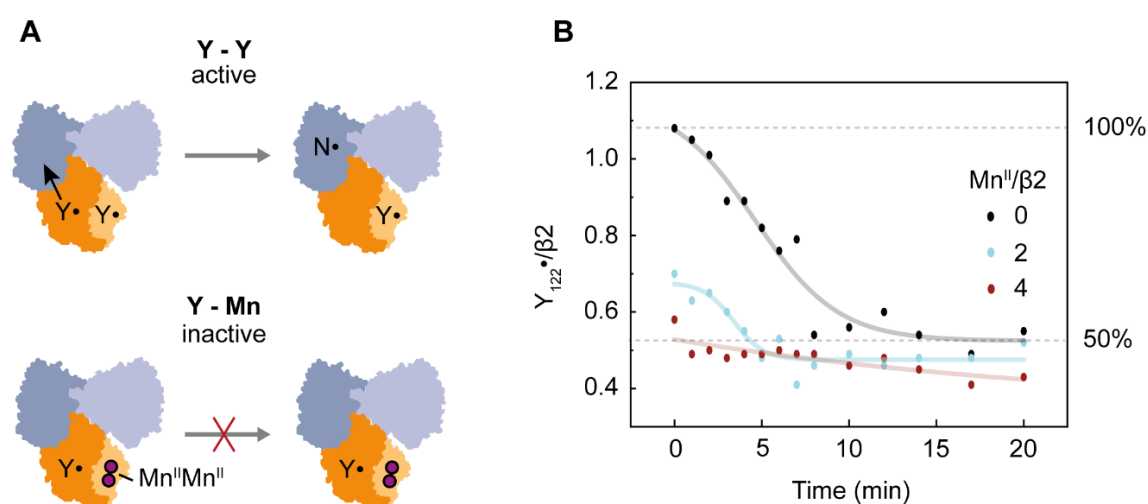


**Figure 4.18: Probing the catalytic activity of mismetallated RNR using the N<sub>3</sub>CDP assay, monitoring the Y<sub>122</sub>• decay.** (A) Schematic representation of the reaction of  $\alpha 2\beta 2$  complexed with N<sub>3</sub>CDP. (B) Y<sub>122</sub>• yield as a function of time during the reaction with N<sub>3</sub>CDP observed via cw-EPR at 9.6 GHz.

For the first analysis pathway, it is true that the Y<sub>122</sub>• radical is stable at room temperature for several days. Hence, a decrease in radical yield in the presence of N<sub>3</sub>CDP is caused by the formation of N• during catalytic turnover only, completed after ca. 20 min. The expected decrease from 1.1 to ca. 0.5 Y•/β2 was observed in manganese-free samples (**Figure 4.18B**). In contrast, a sample supplemented with 2 eq. Mn<sup>II</sup> shows a decrease of only 0.2 Y•/β2. The presence of 4 eq. Mn<sup>II</sup> leads to almost no detectable changes in Y<sub>122</sub>• signal intensities. However, all samples exhibit similar radical yields at equilibrium, regardless of their manganese content. Previous DEER experiments of

samples supplemented with 4 eq.  $\text{Mn}^{\text{II}}$  displayed Y-Mn pairs only. Therefore, their Y-Y content must be below the detection limit. If Y-Mn pairs would be catalytically active, the  $\text{Y}_{122}\bullet$  yield should be almost zero after the reaction, which could not be observed. Instead, a total yield of one  $\text{Y}_{122}\bullet$  per dimer can be determined after the incubation time of 20 min, which demonstrates that mismetallated  $\beta 2$  subunits are inactive. Accordingly, a sample with only 2 equivalent  $\text{Mn}^{\text{II}}$  still offers residual activity as it contains fractions of Y-Y pairs, as proven by the previous DEER experiments.

In a second experiment,  $\text{N}\bullet$  formation in mismetallated protein was monitored. As the reaction with  $\text{N}_3\text{CDP}$  leads to 1  $\text{N}\bullet/\beta 2$  in combination with 1  $\text{Y}\bullet/\beta 2$ , a mixed EPR spectrum of both species is observed.  $\text{N}\bullet$ 's EPR signature can be extracted by subtracting the remaining  $\text{Y}_{122}\bullet$  signal, as demonstrated in **Figure 4.19A**. For all samples,  $\text{N}\bullet$  is detected (**Figure 4.19B**), whereas signal intensities decrease with increasing amounts of manganese. These findings are consistent with catalytically inactive mismetallated  $\beta 2$  subunits. Otherwise, one would expect identical signal intensities for all samples.

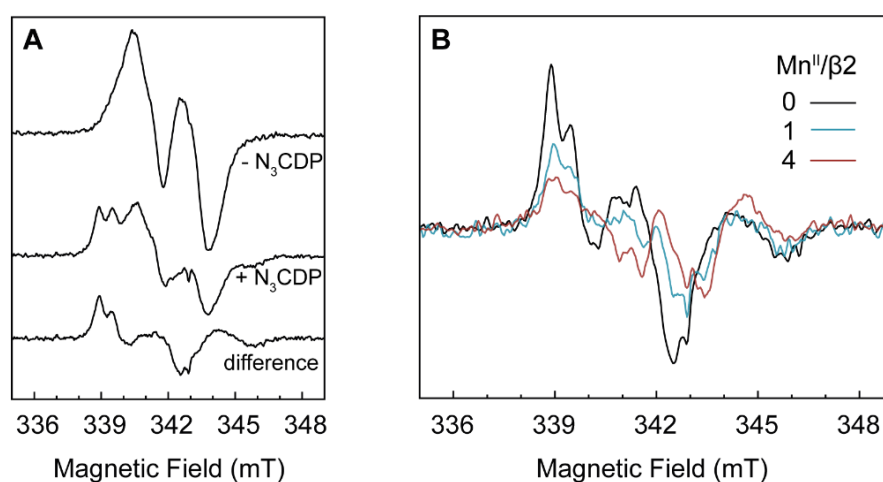


**Figure 4.19: Determination of the catalytic activity of mismetallated RNR using the  $\text{N}_3\text{CDP}$  assay, monitoring  $\text{N}\bullet$  formation.** (A) Cw-EPR spectra of radical signals obtained before and after incubation of the  $\alpha 2\beta 2$  complex with  $\text{N}_3\text{CDP}$ . Spectra were acquired at 9.6 GHz and 100 K. (B) Before  $\alpha 2\beta 2$  complex assembly,  $\beta 2$  was supplemented with the indicated amount of  $\text{Mn}^{\text{II}}$ . Afterward,  $\text{N}\bullet$  was monitored as described in (A). Experimental conditions are: 0.1 mW power, 2 G modulation amplitude, 100 kHz modulation frequency, 20.48 ms as time constant, and 20.01 ms conversion time.

Observing a weak  $\text{N}\bullet$  signal despite the addition of 4 eq. manganese seems surprising since DEER experiments detected only Y-Mn pairs present in the sample. However, residual activity can be explained by the presence of a minor fraction of Y-Y pairs below the detection limit, which also explains the slight decline in  $\text{Y}_{122}\bullet/\beta 2$  as observed in **Figure 4.18**.

#### 4.3.10. Active $\alpha\beta_2$ complex formation in mismetallated RNR

A possible explanation for the inactivity of manganese-containing class Ia RNR could be the lacking assembly of the active  $\alpha\beta_2$  complex (260 kDa), so that separated  $\alpha$  (86 kDa),  $\alpha_2$  (172 kDa), and  $\beta_2$  (88 kDa) subunits coexist in the solution. Whereas  $\alpha$  is present in monomeric and dimeric form depending on the nucleotide pool, monomeric  $\beta$  has never been observed.<sup>260</sup> Size exclusion chromatography allows the separation of  $\alpha_2$ ,  $\beta_2$ , and  $\alpha\beta_2$  by utilizing a Superdex 200 Increase 10/300 GL column. Therefore, samples containing  $\alpha_2$ ,  $\beta_2$ ,  $N_3$ CDP, and TTP plus the respective amount of manganese were applied to the column (**Figure 4.20A**). For each sample, a control experiment without  $N_3$ CDP was performed additionally.

Manganese-free samples revealed one main elution peak, matching successful  $\alpha\beta_2$  assembly with an apparent molecular weight of  $246 \pm 7$  kDa (**Figure 4.20** yellow). The error is given by the standard deviation of multiple experiments. SDS-PAGE analysis of the eluted fractions revealed bands characteristic for  $\alpha$  and  $\beta$  (**Figure 4.21** left). Their band intensities were compared to standard samples of the individual proteins by using GelAnalyzer 19.1 and exposed  $\alpha$ : $\beta$  ratios of 1:1, confirming the presence of  $\alpha\beta_2$ .

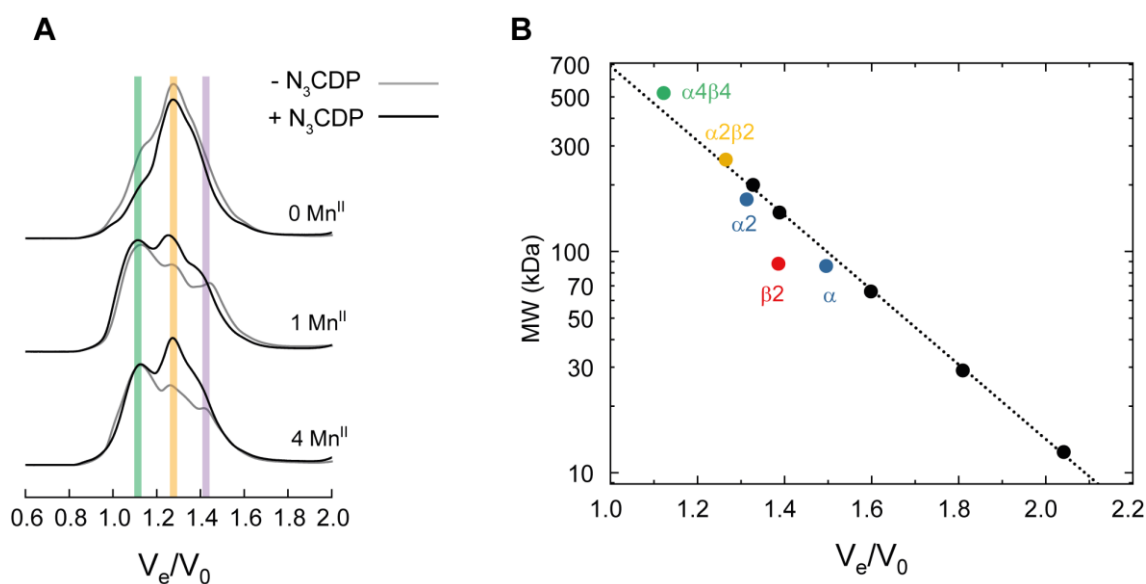


**Figure 4.20: *E. coli* RNR complex assembly investigated by size exclusion chromatography.** (A)  $\beta_2$  was supplemented with different amounts of  $Mn^{II}$ , and afterward, the  $\alpha\beta_2$  complex assembly was investigated in the absence (gray) and presence (black) of  $N_3$ CDP. Main elution peaks are indicated as vertical lines. Green:  $\alpha_4\beta_4$ , yellow:  $\alpha_2\beta_2$ . The identity of the peak marked in purple is ambiguous and can either be assigned to  $\alpha$  or  $\beta_2$ . The identity of the detected oligomeric species could be revealed by comparing it to the calibration curve depicted in (B). (B) Calibration of the column obtained with standard samples. Mean values of the detected species are plotted versus the expected molecular weight.

Surprisingly,  $\alpha_2\beta_2$  complex formation is also observed in manganese-containing samples, and even more remarkably, a higher-ordered structure with an apparent molecular weight of  $428 \pm 7$  kDa is observed additionally (**Figure 4.20** green). SDS-Page

analysis (**Figure 4.21** right) reveals a 1:1 ratio of  $\alpha$  to  $\beta$  for this complex, which proposes the inactive  $\alpha_4\beta_4$  complex (520 kDa) as the origin of this signal. Unfortunately, single  $\alpha$ s and  $\beta$ s cannot be distinguished due to the lack of resolution (**Figure 4.20** purple line).

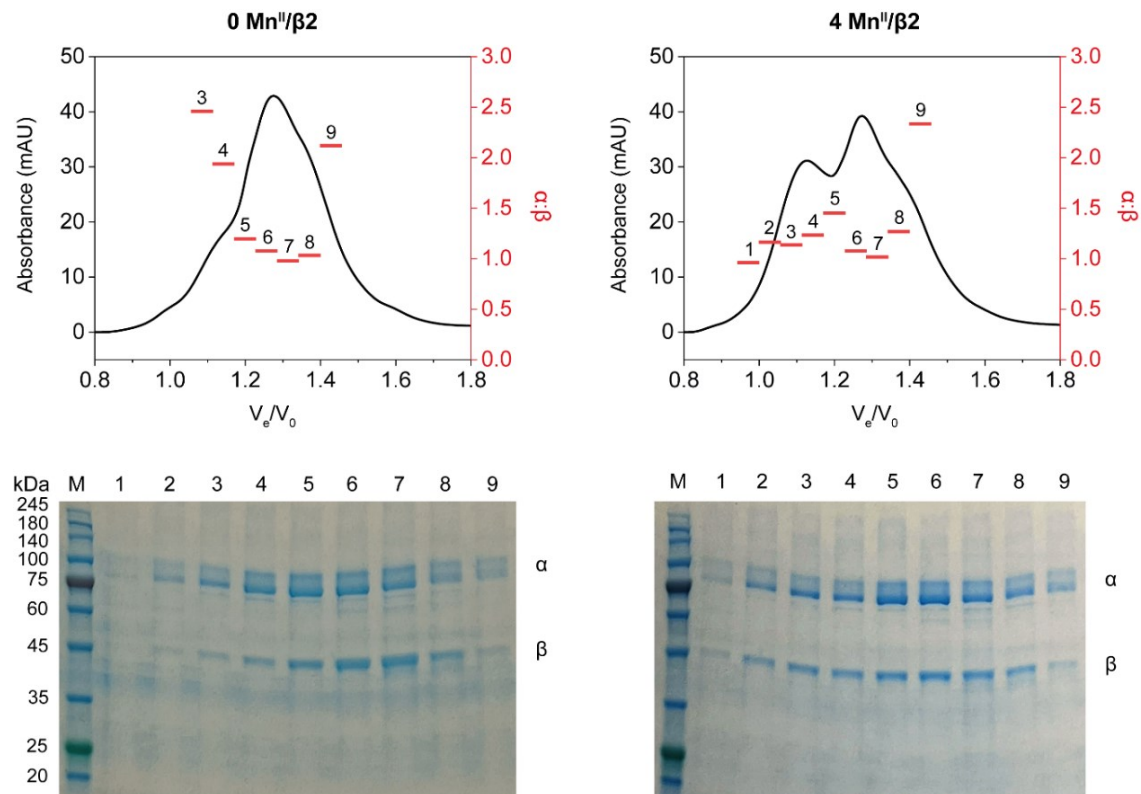


**Figure 4.21:** SDS-PAGE of fractions obtained after size exclusion column of *E. coli* supplemented with 0  $\text{Mn}^{\text{II}}/\beta_2$  (left) and 4  $\text{Mn}^{\text{II}}/\beta_2$  (right). Fractions 1 – 9 are shown along with the Marker (M). Fractions with weak band intensities were excluded from the analysis (fraction 1 and 2 left).

In summary, these data clearly demonstrate that subunit assembly takes place in mismetallated protein. Incomplete complex assembly can therefore be ruled out as the source of inactivity. Surprisingly, the fraction of  $\alpha_2\beta_2$  even increases upon  $\text{N}_3\text{CDP}$  addition in relation to  $\alpha_4\beta_4$  (**Figure 4.22**), seemingly being a regulatory reaction. This proposes a model in which RNR activity is highly regulated, possibly much more than expected until now. Not only the protein concentration<sup>31</sup> or nucleotide pools<sup>261</sup> may govern protein activity, but furthermore, the metal pool might be essential. The presence and allosteric regulation of  $\alpha_4\beta_4$  under these circumstances remain elusive.

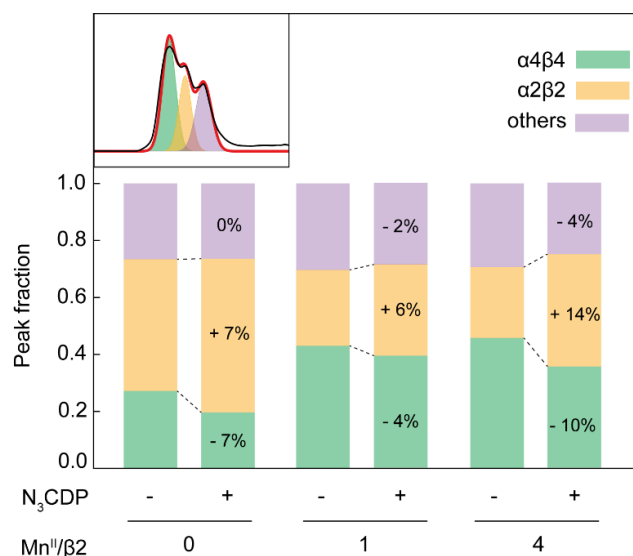


**Figure 4.22: Fraction of peaks detected by size exclusion chromatography.** Spectra shown in **Figure 4.20** were fitted with three different Gaussians, whereas the peak center was allowed to vary by  $\pm 0.05$  mL and full width at half maximum (FWHM) of maximal 1.3 mL ( $\alpha 4\beta 4$  and  $\alpha 2\beta 2$ ) or 1.5 mL (others). An exemplary fitting result is shown in the inset as red line.

#### 4.4. Conclusion and outlook

These studies highlighted the effect of mismetallation by manganese in *E. coli* RNR on its radical distribution and activity. As a basis for further investigations, it was first experimentally confirmed that mismetallation by manganese takes place as proposed by previous reports.<sup>99,100</sup> The two previously published studies are partly controversial as they either report on a maximum binding capacity of 2 or 4 equivalent Mn<sup>II</sup> per β<sub>2</sub> dimer. Here, binding of 2 eq. Mn<sup>II</sup> was observed as maximum, agreeing with the results from Pierce *et al.* The differences in the experimental outcomes from Atta *et al.*, which were attributed to the presence of high amounts of glycerol, could be confirmed in this work.

In contrast to the former studies, the results presented here demonstrate a recovery from mismetallation, allowing the formation of an asymmetric cofactor assembly with a Mn<sup>II</sup>Mn<sup>II</sup> center on one side of the β<sub>2</sub> subunit and Y<sub>122</sub>• formation in the other half. Such an asymmetric cofactor has never been observed in this enzyme but is substantial because it must be directly linked to RNR's half-site reactivity. Moreover, these results highlight one of the very few examples of a protein that can self-recover from mismetallation. Two main mechanisms allow for the recovery from mismetallation by manganese. First, Fe<sup>III</sup>'s slightly higher binding affinity for the metal binding site in *E. coli* class Ia RNR competes against Mn<sup>II</sup>, leading to manganese release. Second, the remaining bound manganese alternates its binding sites to allow the formation of maximum radical yield. Surprisingly, the β<sub>2</sub> subunit remains a stable dimer during this process, while no monomeric β<sub>s</sub> are observed.

Mismetallated  $\beta 2$  subunits do not exhibit catalytic activity, which is most probably related to the observation of  $\alpha 4\beta 4$  complex formation. An explanation for the presence of inactive  $\alpha 4\beta 4$  next to active  $\alpha 2\beta 2$  in mismetallated enzyme could not be found yet but is pivotal to understand RNR regulation in the cells. The preliminary in-cell results strongly support a hypothesis in which RNR radical distribution and thus its activity is strongly influenced by the metal availability in the cells. The observation of an intracellular radical distribution other than two or none, as well as the detection of a 2.8 nm distance inside the cellular environment, indicates that mismetallated protein with an asymmetric cofactor plays a role in the cellular machinery as well. Mismetallated protein must be of biological importance and may act as a kind of regulatory mechanism. These findings help decipher why class Ia expression levels are not down-regulated while class Ib RNR is expressed at high intracellular manganese levels.<sup>18</sup> With the results obtained here, it now seems reasonable that the present class Ia RNR is mismetallated under these conditions and can be restored to its original function if the iron content is sufficiently high. Such an intramolecularly self-rescue mechanism is exciting to observe, as it showcases the strong regulation of this vital enzyme. Self-rescue may be a certainly simpler but possibly also a less effective control pathway than, for example, relying on additional chaperones as observed in other systems.<sup>262</sup>

Further quantitative Western blot experiments would help to determine the amount of  $\beta 2$  expressed and quantify the  $Y\bullet/\beta 2$  ratio in the cells. Furthermore, adjustments of various factors, such as  $\alpha 2$  expression levels in the cell, are possible. Incorporating unnatural amino acids could further help determine intracellular protein activities as a function of protein- and metal concentrations. Moreover, expression levels of the manganese importer MntH and MntS or the exporter protein MntP<sup>211</sup> could be varied to modify the bioavailable manganese pool.

Experiments with 2,3,5-F<sub>3</sub>Y<sub>122</sub>- $\beta 2$  and Y<sub>731</sub>F- $\alpha 2$  mutants are currently underway to trap the radical during the forward transfer reaction. These studies should provide information on whether mismetallated  $\beta 2$  subunits are at least capable of initiating the radical transfer process. If this is the case, i.e., if Y<sub>356</sub>• is detected, the catalytic inactivity of the protein is due to the inability of the radical to pass the protein interface, which is probably caused by a distinct protein conformation. Such experiments can also be performed inside cells, supported by DEER experiments, which will provide significant advances in the field of in-cell structure elucidation of RNR and would thus help to understand intracellular activity regulation. However, these studies are not only fundamental for elucidating RNR catalysis but also with regard to the role of RNR in various cancers. Targeting the cofactor assembly rather than the enzymatic reaction may be an effective new pathway for drug development.

# 5.

## Development of a new rigid spin label

---

---

### 5.1. Introduction

As most biologically relevant targets are diamagnetic, they must be spin-labeled in order to be accessible for EPR spectroscopy. The development of site-directed spin labeling enabled EPR to be utilized for all biomolecules regardless of their form of magnetic state. Among all established EPR methods, pulse-dipolar techniques are currently the most frequently used procedures for *in vitro* and in-cell structure determination. Since the first pioneering work using MTSSL as a paramagnetic label, the field of spin label development has been under constant development.<sup>141,142</sup> Different approaches for in-cell DEER studies have been tested, such as inserting spin-labeled proteins in the cells via microinjection<sup>154,159,176,263</sup> electroporation,<sup>166,167</sup> or labeling membrane proteins on the outer cell surface.<sup>264–266</sup> Nowadays, many different labels exist, and the need for additional spin labels may not be obvious. However, as already briefly outlined in Section 2.5, many well-known spin labels come along with some disadvantages, which will be outlined in more detail in the following.

#### 5.1.1. The problem

##### I. The distance distribution

In most cases, spin labels are attached to their target via a linker, which possesses many rotational degrees of freedom, resulting in broad and incomprehensible distance distributions.<sup>148,267,268</sup> Hence, small distance changes are challenging to detect, and it is often difficult to determine whether the detected change originates from a protein conformational change or another rotamer of the spin label. Further analysis is needed to model and evaluate possible rotamers and compare them with experimental outcomes.<sup>269–273</sup> The simplest solution to this problem may be to shorten the linker group, but unfortunately, this often distorts the biomolecular target's structure and function.<sup>274</sup> Moreover, spin tags may also prefer specific conformers due to interactions with the

protein or its environment.<sup>274,275</sup> In this case, little can be said about the orientation of individual side chains or amino acid residues.

## II. The size of the spin label

Many established spin labels, such as trityl labels, are themselves quite bulky, making labeling in relatively inaccessible and cramped areas of the protein, such as the protein interior, impossible. Incorporation of spin labels may destabilize protein structure, giving rise to partially or fully unfolded fractions.<sup>276</sup>

## III. The site-specificity

To attach a spin label to a specific cysteine residue, all other accessible cysteines must be mutated to prevent nonspecific labeling. In addition to a high workload, this can also be accompanied by disruption of the natural protein structure. Therefore, performing activity assays with cysteine mutants and spin-labeled proteins prior to distance measurements is common practice.

## IV. In-cell suitability

The most common groups of spin labels, namely nitroxide-based ones, are susceptible to reduction and thus not stable in the cellular environment.<sup>154–158,277</sup> Although lifetimes can be extended by chemical shielding, regulatory mechanisms in living organisms that operate on a scale of hours often are of interest, e.g., mismetallation discussed in Chapter 4. Metal-based spin labels may also not be optimal when investigating a protein inside a living system, as metal release from the label into the cell interior has been observed previously.<sup>170</sup> Another point to consider is that introducing large amounts of metals can be toxic to cells.<sup>278–280</sup>

## V. The workload for in-cell measurements

In many in-cell examples, the protein must first be purified before it can be spin-labeled and reintroduced into the organism. Reintroduction into the cells can be achieved via microinjection, electroporation, and hypotonic swelling.<sup>154,165,166,169,263</sup> This procedure requires additional work and the necessary laboratory equipment.

### 5.1.2. The solution approach

Due to multiple challenges that come along with some of the spin labels, it becomes obvious why a new spin label is needed. The underlying idea for developing a new spin label is to use an unnatural amino acid, which is put into a paramagnetic state through light activation. Application of the basic concept of photocaged amino acids is inspired by the impressive work of Deiters<sup>281–283</sup>, Summerer<sup>284–286</sup>, and Chin<sup>287–289</sup>, to name a few. This thesis will refine these principles to allow their combination with EPR spectroscopy.

While designing the new spin label, the problems outlined above are addressed as follows.

### **I. The distance distribution**

As the UAA will not be attached to the protein via a linker but is directly incorporated into the nascent protein upon translation, its conformation flexibility will be similar to that of natural amino acids.

### **II. The size of the spin label**

The plan is to select an UAA that is as similar as possible to a natural variant so that there are little or no structural disturbances. For example, fluorotyrosines incorporated into the protein interior do not cause structural changes in ribonucleotide reductase in the cell, as showcased in Chapter 3.

### **III. The site-specificity**

The *in vivo* nonsense suppression method allows the UAA to be incorporated into the protein at any position with high precision. Interchanging mutations of other native amino acids can thus be avoided. Furthermore, high labeling efficiencies can be achieved.

### **IV. In-cell suitability**

The advantage of this method is that the spin label can be generated at any time if required, i.e., directly before its readout at cryogenic temperatures. Therefore, the label is resistant to quenching or reduction in the cell. One concern may be the response of the cells to the irradiation. However, *E. coli* cells can be exposed to high doses of laser radiation without significantly reducing their growth rate.<sup>290,291</sup> Ideally, only a short laser pulse is required for photoactivation of the new spin label so that the cells are harmed as little as possible.

### **V. The workload for in-cell measurements**

The principle of ncAA incorporation directly inside the cell facilitates sample handling enormously. The protein of interest can be expressed directly in the host together with its unnatural amino acid. Subsequent purification and reintroduction into an organism are not required but can, of course, still be performed if desired. This procedure is particularly advantageous for membrane proteins that cannot be reintroduced and consequently rely on *in situ* labeling.<sup>170</sup>

For the development of the spin label, the  $\beta 2$  subunit of *E. coli* class Ia ribonucleotide reductase is chosen as a model system. First, due to the dimeric form of the protein, only one spin labeling position is required for DEER distance measurements. Second, structural data under *in vitro* and in-cell conditions were elaborated over the year,

especially in this thesis, which tremendously facilitates data analysis and troubleshooting.

Apart from the fact that spin labels are useful for all kinds of biomolecules, RNR research can particularly benefit from this new label. As highlighted in Section 3.1, studying *E. coli* RNR in a host system other than its original one often leads to quenching of Y<sub>122</sub>•. A spin label would thus be required to study RNRs structure under these conditions, yet many labels are not suitable for attachment to all sites of RNR. Even purification tags such as StrepII or (His)<sub>6</sub> introduced at the N-terminal tail lead to low protein and radical yields.<sup>292</sup> Furthermore, especially the flexible C-terminal tail is very sensitive to modifications.<sup>43</sup> A small, rigid label could allow significant advances in resolving RNR structure and dynamics.

## 5.2. Materials and methods

### 5.2.1. Sample preparation and photolysis

Samples were prepared at pH 7.6 in 50 mM Tris, containing 5% Glycerol. The solution was degassed with N<sub>2</sub> gas for 1 h. Afterward, the sample was filled in 2.8. mm O.D. EPR tubes and subsequently snap frozen in liquid nitrogen at 77 K. Photolysis was performed with a LOT QuantumDesign LSB610U 100 W Hg arc lamp (250 to > 2500 nm) either inside the cavity of the EPR spectrometer of the EMX-Nano Benchtop spectrometer (as shown in **Figure 5.1**) or in a self-built irradiation setup (all other measurements). For the first variant, the samples were each exposed for 2 min at 100 K. For the latter alternative, samples were irradiated at 77 K for 10 min in liquid nitrogen and rotated 180° after 5 min to ensure uniform sample irradiation. Afterward, the irradiated samples were stored in liquid nitrogen, and EPR measurements were performed as fast as possible to prevent radical quenching over time.

### 5.2.2. Details of the EPR experiments

**X-band:** X-band cw-EPR measurements shown in **Figure 5.1** were carried out at T = 100 K using a Bruker EMX-Nano Benchtop spectrometer equipped with a continuous-flow nitrogen cryostat. Experimental conditions were: 3.981 mW microwave power, 3 G modulation amplitude, 100 kHz modulation frequency, 5.12 ms as time constant, 45.0 ms conversion time.

The X-band cw-EPR measurements shown in **Figure 5.2** were carried out at T = 15 K using a Bruker Elexsys E580 spectrometer equipped with a Bruker ER 4118X-MD5 resonator and an Oxford Instruments ER 4118CF cryostat. Experimental conditions were: 0.95 mW microwave power, 10 G modulation amplitude, 100 kHz modulation frequency, 50.0 ms conversion time.

**Q-band:** Q-band pulse EPR measurements were carried out using a Bruker Elecsys E580 spectrometer equipped with the ER 5106QT-2 resonator, operating at  $T = 10$  K. 34 GHz DEER experiments were performed at 10 K using the 3-pulse DEER pulse sequence with 8-step phase cycling and Gaussian pulses. The frequency separation  $\Delta f = f_{\text{pump}} - f_{\text{det}}$  was 84 MHz in an overcoupled resonator with  $f_{\text{pump}}$  set to the center of the resonator dip. The optimal  $\pi$ -pulse lengths were determined using transient nutation experiments, being 20 ns for the pump pulse and 40 ns for the detection. DEER time traces were background-corrected, assuming an exponential background with dimensionality equal to 3.

### 5.2.3. Incorporation of azF in $\beta 2$ class Ia *E. coli* RNR

The incorporation protocol was extended to RNR on the basis of Widder *et al.*<sup>150</sup> *E. coli* BL21(DE3)-Gold (Invitrogen) were transformed with pBAD-*nrdB*<sub>122TAG</sub> and pEVOL-pCNPhe and plated on LB-agar plates with 100  $\mu\text{g}/\text{mL}$  carbenicillin (Carb) and 35  $\mu\text{g}/\text{mL}$  chloramphenicol (Cm) at 37 °C. Positive clones were selected, and a starter culture (3 mL) was grown for 7 h in LB-medium enriched with Carb and Cm at 37 °C and 180 rpm until saturation. An intermediate culture (100 mL) was enriched with 1 mL of the starter culture, grown overnight at 37 °C and 180 rpm. The expression culture was grown with a 200-fold dilution of the intermediate culture in LB-medium containing Carb and Cm. At OD<sub>600</sub> ~0.3, azF was added to a final concentration of 0.6 mM. After 20 min, 100  $\mu\text{M}$  1,10-phenanthroline was added to chelate iron. After a further 20 min, protein expression was induced with 0.5% (w/v) L-arabinose. After 20 h of protein overproduction, the cells were harvested by centrifugation at 17 000  $\times g$  for 15 min at 4 °C resulting in 1.8 g cell paste/L media. The cell pellet was stored at -80 °C until protein purification. The protein construct was purified by two anion-exchange chromatography steps as described for wt- $\beta 2$  in Section 8.2.4, resulting in approximately 13 mg protein/g cell paste.

## 5.3. Results and discussion

### 5.3.1. Amino acid photolysis investigated via 9 GHz cw-EPR measurements

Four amino acids are known to form catalytically active, one-electron oxidized radicals: tyrosine, tryptophan, cysteine, and glycine.<sup>3</sup> Tyrosyl and tryptophan radicals can artificially be generated via UV photolysis in frozen solutions.<sup>293–295</sup> This concept was used as the basis to induce radical formation in fluorotyrosines, which displayed broader EPR signals than  $\text{Y}\bullet$ . Their EPR lineshapes differ depending on the degree and position of fluorination.<sup>60</sup> Furthermore, substituting the aromatic protons of tyrosine with fluorine results in a blue shift of the UV-Vis absorption maximum. As this shift is quite small, tyrosine and tryptophan radical generation in UAA-bearing protein samples via photolytic radical formation is difficult to avoid. Previous experiments on the irradiation

of the  $\alpha 2$  subunit of *E. coli* RNR already demonstrated the generation of several organic radicals, exhibiting a quite similar lineshape compared to photolyzed 2,3,5-trifluorotyrosine (Bachelor thesis Dustin Schlüter and **Figure C.1**).

These findings have driven us to search for unnatural amino acids that meet at least one of the two following criteria for being a suitable candidate for spin-labeling. Either the efficiency of creating the label's paramagnetic state should exceed that of natural amino acid residues so that the label is the predominant radical species. Otherwise, the lineshape or at least the relaxation behavior of the resulting radical species should be sufficiently different from natural amino acid radicals to allow their spectroscopic discrimination. In order to test for these criteria, a 200  $\mu\text{M}$  solution of tryptophan (**Figure 5.1** as **4**) or tyrosine **5** in Tris buffer was prepared. Photolysis was performed inside the cavity of the X-band EPR spectrometer using a Hg arc lamp, followed by subsequent investigation via 9.6 GHz cw-EPR experiments. Moreover, the same procedure was carried out for some unnatural amino acids **1** – **3**, resembling native tyrosine (**Figure 5.1**).

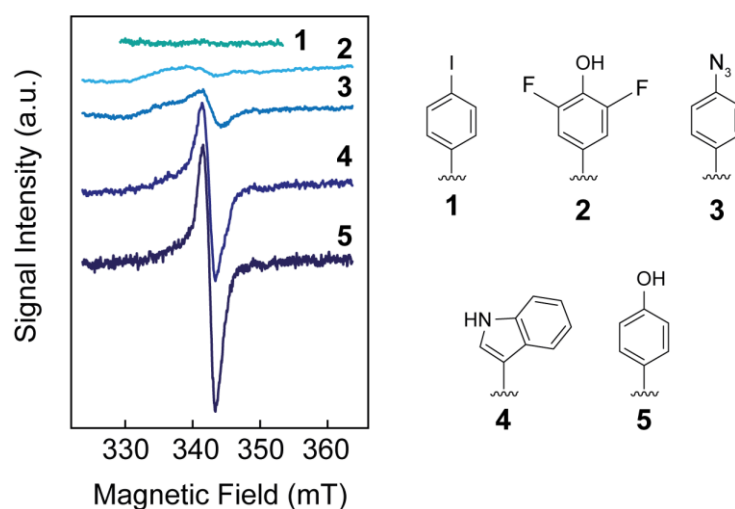


**Figure 5.1:** 9.6 GHz cw-EPR spectra of different amino acid radicals formed via photolysis at 100 K. Photolysis was carried out on 4-iodo-L-phenylalanine (IF) **1**, 3,5-difluorotyrosine (F<sub>2</sub>Y) **2**, 4-azido-L-phenylalanine (azF) **3**, tryptophan (W) **4**, and tyrosine (Y) **5**.

Two minutes of light exposure were sufficient for the formation of radical species in Y and W solutions, whereas a higher signal amplitude was detected for the tyrosyl sample. Both samples exhibit a single sharp EPR line with a peak-to-peak linewidth of around 1.9 mT centered at  $g = 2.007$ , in accordance with previous reports.<sup>293,296,297</sup>

Next, radical formation in an aqueous solution of 4-iodophenylalanine (IF) **1** was tested. The C-I bond in IF has a much lower binding energy ( $213 \text{ kJ mol}^{-1}$ )<sup>298</sup> than an O-H bond ( $390 \text{ kJ mol}^{-1}$ )<sup>299</sup> in tyrosine. Consequently, formation of a phenyl-type radical was predicted earlier with an almost quantitative yield.<sup>300</sup> Iodine generally has the lowest binding energy among all halogens, which favors its bond cleavage by homolysis. In

principle, this homolytic cleavage should lead to the formation of a radical at the respective cleaved atoms. However, only a barely visible EPR signal was observed when tracing the photolytic radical formation via cw-EPR (**Figure 5.1**). Therefore, this UAA can be excluded as a spin label candidate.

Second, 3,5-difluorotyrosine was investigated after irradiation for 2 min (**Figure 5.1** as **2**). In this case, a weak EPR signal was observed, which, however, exceeds the intensity of IF. Since this signal is very weak, an exact  $g$ -value and linewidth cannot be read from the spectra. Previous Q-band studies with longer irradiation times revealed that the signal is centered around  $g = 2.0016$  (**Figure C.1**). Because of the ability to generate an EPR signal from  $F_nY_s$ , an attempt was made to measure the distance between the  $F_3Y_{122}$ - $F_3Y_{122}$  pair of mutant  $\beta 2$  *E. coli* RNR by DEER spectroscopy (data not shown) after the photolysis. However, all attempts to extract a distance remained unsuccessful. Since the EPR spectrum does not significantly differ from that of  $Y\bullet$  and  $W\bullet$  and the radical generation is less efficient, both criteria for the spin label are not met, so  $F_nY_s$  are ruled out as candidates.

Finally, 4-azidophenylalanine **3**, azF for short, was investigated using the same means. The azide unit of this UAA is a popular functional group for click chemistry and has been used to attach spin labels onto user-defined sites in proteins.<sup>150,151,301</sup> The photo-activated unnatural amino acid displays a cw-EPR signal at  $g = 2.007$  with a peak-to-peak linewidth of ca. 2.7 mT, comparable to  $W$  and  $Y$ , whereas its intensity is weaker than those of the natural amino acids. However, this azF exhibits the strongest signal intensity among the non-canonical amino acids studied. A wide-field scan of this sample revealed two spectral features at approximately 337 and 716 mT, which equals  $g = 2.01$ , and 0.94 (**Figure 5.2A**).

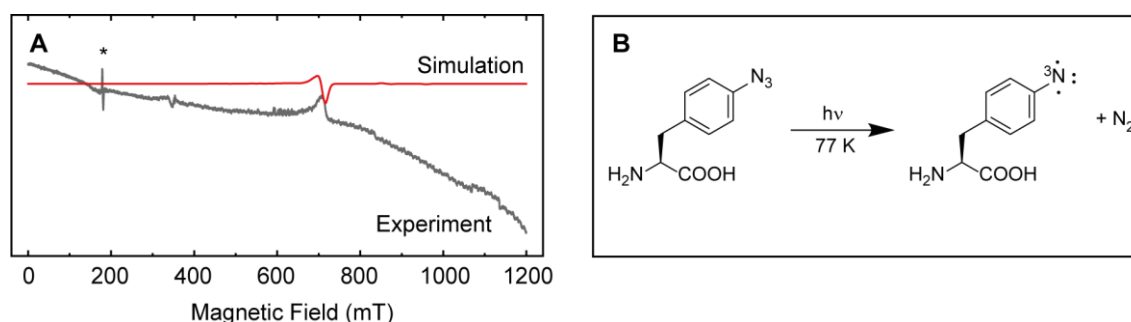


**Figure 5.2: X-band studies of the photolysis product of 4-azido-L-phenylalanine.** (A) Azidophenylalanine was irradiated at 77 K for 10 min and measured via 9 GHz cw-EPR at 15 K. 200  $\mu$ M amino acid solution was prepared in 50 mM Tris + 5% glycerol. Asterisk \* marks signal arising from resonator background. Simulations were obtained by the EasySpin ‘pepper’ routine with  $S = 1$ ,  $g_{iso} = 2.02$ ,  $D/hc = 1.110$   $\text{cm}^{-1}$ ,  $E/hc = 0$   $\text{cm}^{-1}$ . (B) UV light exposure at 77 K of azidophenylalanine induces a triplet nitrene, giving rise to zero-field splitting, as detected in (A).

The low-field signal at 180 mT can be assigned to the resonator background, whereas the signals at  $g = 2.01$  and  $0.94$  originate from the sample. Such a low  $g$ -value of  $0.94$  is uncommon for an organic radical and therefore points to the presence of zero-field-splitting. Previous studies revealed that phenylazides are able to form triplet nitrenes when exposed to UV light  $> 310$  nm (**Figure 5.2B**). The triplet state can only be observed under cryogenic conditions, whereas the singlet state is predominant at room temperature.<sup>302,303</sup> Furthermore, such a triplet has been observed for azidophenylalanine incorporated in T4 lysozyme.<sup>304</sup> The occurrence of undefined paramagnetic side products with  $S = 1/2$ , corresponding to the signal at around  $g = 2$  in **Figure 5.1** and **Figure 5.2**, was also reported in earlier studies.<sup>304,305</sup> The triplet nitrene can be reproduced by simulating a spin system  $S = 1$  with  $D/hc = 1.110$  cm<sup>-1</sup> and  $E/hc = 0$  cm<sup>-1</sup>, in agreement with previously reported data ( $D/hc = 0.990$  cm<sup>-1</sup> and  $E/hc = 0$  cm<sup>-1</sup> for phenylazide)<sup>303</sup>. The resonance field of the triplet nitrene differs from that of ordinary organic radicals, meeting the second criterion for a suitable UAA-based spin label.

### 5.3.2. AzF- $\beta$ 2 RNR investigated via 34 GHz pulse EPR measurements

The unnatural amino acid azidophenylalanine was selected as a suitable candidate for a new, rigid spin label due to its unusual property of triplet formation. To test its suitability as a molecular protein marker, the UAA was incorporated into the  $\beta$ 2 subunit of class Ia *E. coli* RNR at position 122. AzF<sub>122</sub>- $\beta$ 2 was irradiated at 77 K for 10 min and subsequently studied by pulse EPR at 34 GHz (**Figure 5.3**). Further, free azF and apo wt- $\beta$ 2 were investigated using the same method to allow an assignment to signals originating from azF<sub>122</sub> in the protein only (**Figure 5.3**). Samples containing azF, either in the protein or free in solution, exhibit several absorption features in the low-field region between approx. 100 to 800 mT. The negative control, wt- $\beta$ 2, does not display any absorption in this region. These results verify the successful incorporation and triplet state generation of azF inside the protein.

In addition, both protein-containing samples feature broad spectral absorption between 1000 to 1400 mT. Measurements pre- and post-irradiation uncover that this signal originates from protein-bound manganese. The presence of a strong manganese signal in apo- $\beta$ 2 is to be expected since the sample was not treated with EDTA but only with phenanthroline during the protein expression. Our internal laboratory data illustrated that subsequent EDTA treatment of  $\beta$ 2 significantly reduces the manganese content. The resonance fields of the triplet and manganese differ substantially so that the analysis of the triplet signal is not disturbed by the metal contamination. Nevertheless, the contribution of manganese can be subtracted by using the spectrum prior to light exposure. These first-derivative spectra of azF in solution and incorporated into RNR obtained in this way are depicted in **Figure 5.4**.

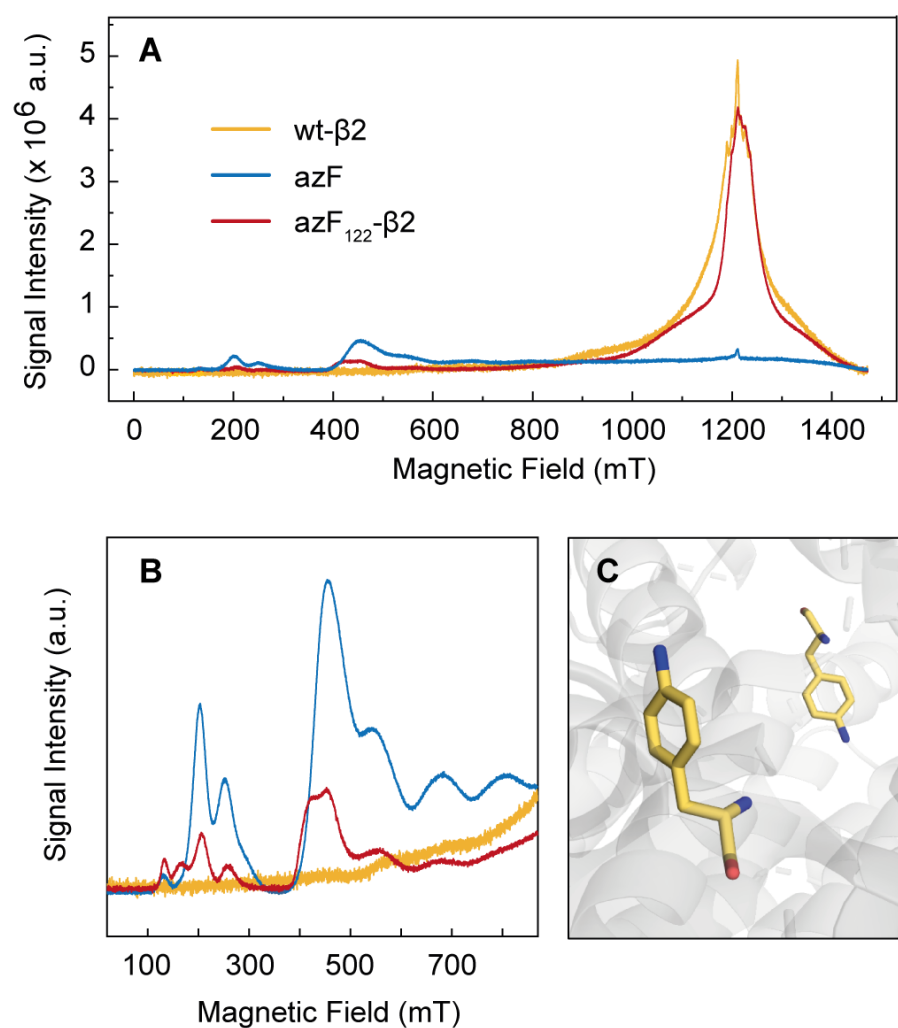


**Figure 5.3: EPR investigation of azidophenylalanine in different environments.** 34 GHz ESE spectra of azidophenylalanine either free in solution (blue) or incorporated into the  $\beta 2$  subunit of *E. coli* RNR (red). Furthermore, apo wt- $\beta 2$  was investigated under the same conditions, serving as a negative control (yellow). (A) shows the complete field sweep, whereas (B) shows an inset of the low-field region. The photolyzed product of azF<sub>122</sub>- $\beta 2$  is demonstrated in (C). Signals were normalized to 34 GHz, sample concentrations, number of scans, and spp. Acquisition parameters: Temperature = 10 K,  $\pi$  = 26 ns (A) or 20 ns (B),  $\tau$  = 200 ns, Attenuation = 5 dB (A) or 0 dB (B), srt = 1 ms, spp = 10.

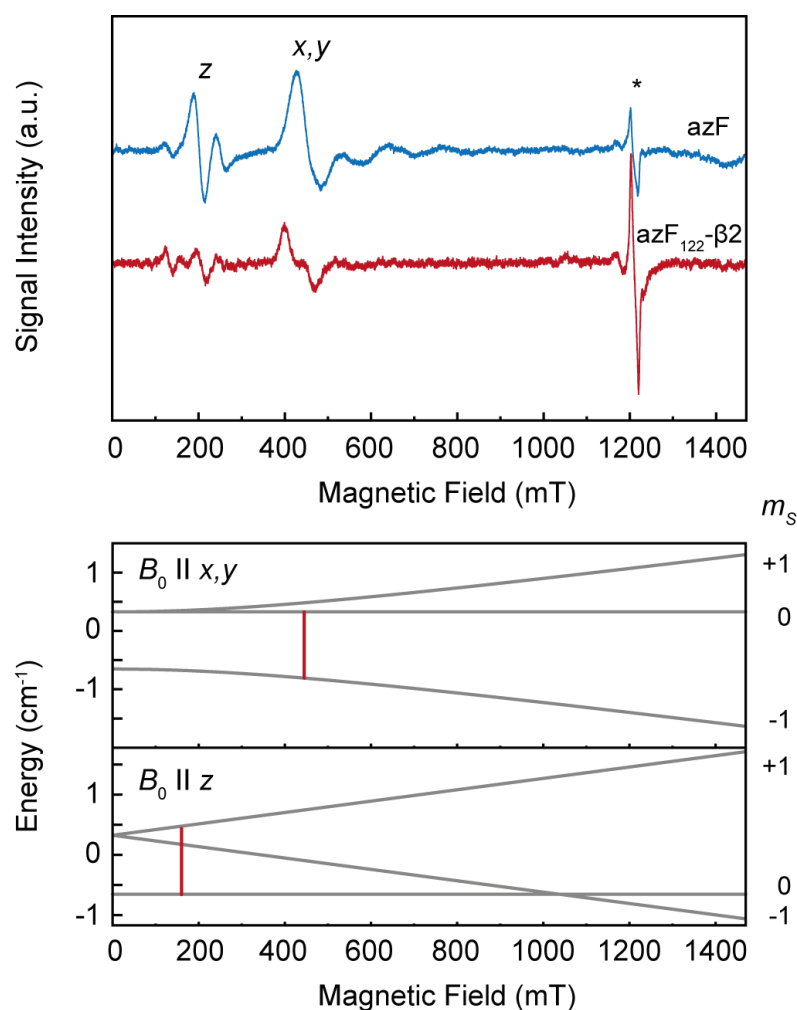


**Figure 5.4: Analysis of generated triplet species.** Top: Pseudomodulated ESE spectra of azidophenylalanine in Tris buffer (blue) and azF<sub>122</sub>-β2 (red) after photolysis. Asterisk marks  $S = 1/2$  side products. Bottom: Energy levels for  $S = 1$  with  $g_{\text{iso}} = 2.02$ ,  $D/hc = 0.978 \text{ cm}^{-1}$  and  $E/hc = 0 \text{ cm}^{-1}$ . Allowed EPR transitions (denoted as  $z$  and  $x,y$ ) are shown for  $B_0 \parallel x,y$  and  $B_0 \parallel z$  in red, respectively. Modulation amplitude = 20 mT. Acquisition parameters: Temperature = 10 K,  $\pi = 26 \text{ ns}$ ,  $\tau = 200 \text{ ns}$ , Attenuation = 5 dB,  $\text{srt} = 1 \text{ ms}$ ,  $\text{spp} = 10$ .

Exact simulations for both signals are not feasible due to the multitude of small unassigned signals that most likely arise from nuclear modulation artifacts due to hyperfine interactions with the  $^{14}\text{N}$  nucleus.<sup>306</sup> All attempts to fit EPR transitions, spectral widths, and signal intensities simultaneously remained unsuccessful. However, the detected transitions can be roughly described by an  $S = 1$  system with  $D/hc = 0.978 \text{ cm}^{-1}$  and  $E/hc = 0 \text{ cm}^{-1}$  (Figure 5.4), matching the usually reported large  $D$  for triplet nitrenes and their axial symmetry.<sup>307–310</sup>

These data report the first spectroscopic detection of a triplet nitrene generated from photolyzed azidophenylalanine inside *E. coli* RNR, which was found to be stable for at least two weeks when stored at liquid nitrogen temperatures. Therefore, an attempt was made to determine the distance between an azF<sub>122</sub>-azF<sub>122</sub> pair by 4-pulse DEER at the

maximum intensity of the triplet signal (data not shown). However, no modulation could be detected due to low spin concentration and fast  $T_m$  times. Furthermore, 3-pulse DEER was used, which is particularly useful for fast-relaxing species.<sup>311,312</sup> Likewise, no distance could be extracted, but a weak modulation with a modulation depth of approximately 1% was visible (**Figure 5.5**). Although the modulation is very weakly pronounced, the trace differs from background measurements. The data are characterized by a low S/N ratio due to the short measurement time. However, the discovery of a weak modulation at Q-band frequencies is promising and opens the way for further optimization. This measurement serves as the first step for using a UAA-based triplet species as a protein spin label. Moreover, it should be noted that this measurement was not performed on a simplified model system such as a short peptide, as is sometimes the case, but on a protein.

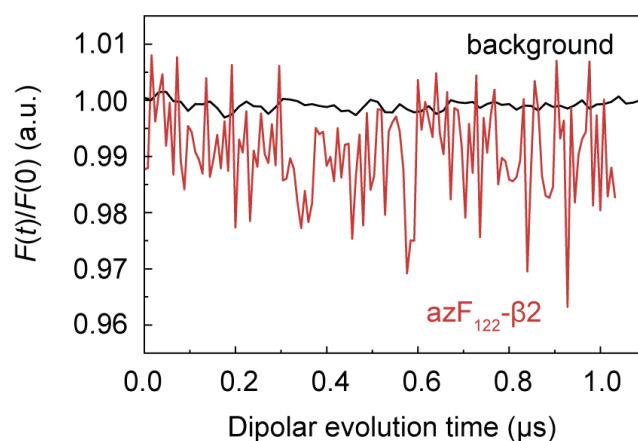


**Figure 5.5: Background-corrected 3-pulse DEER trace of azF<sub>122</sub>-β<sub>2</sub> detected at 450 mT and 34 GHz.** A background-corrected 4-pulse DEER experiment without any dipolar modulation is shown as a comparison (black). This trace was obtained from apo wt-β<sub>2</sub> overexpressed in *E. coli* cells, as shown previously in **Figure 3.6**. Acquisition times: 5 h (red), 15 h (black).

#### 5.4. Conclusion and outlook

This chapter provided insights into the development of a new, rigid spin label designed in particular for prospective in-cell EPR distance measurements. This study aimed to find a photoactivatable unnatural amino acid that would meet several criteria for a suitable label, such as rigidity, specificity, and in-cell suitability. Therefore, photolysis via a Hg arc lamp was tested for different unnatural amino acids, while three candidates were presented: 4-iodophenylalanine, 3,5-difluorotyrosine, and 4-azidophenylalanine. Among these candidates, the unnatural amino acid 4-azidophenylalanine (azF), with its ability to form a triplet nitrene, proved to be by far the most promising.

Q-band pulse experiments have proven the successful site-specific incorporation of azF into the protein and triplet nitrene generation within the protein environment. The UAA's unusual property of triplet formation opens up the possibility for further investigations, aiming to elucidate protein structures and dynamics. This label could combine some of the most critical features required for EPR spin labels, such as high rigidity and site-specific tagging. Furthermore, the triplet signal is outside the manganese spectral range, so azF-labeled protein and intracellular manganese should not interfere in in-cell DEER experiments.

These studies serve as the first important steps toward establishing azF as a spin label. Different attempts to measure the distance between two azFs in the  $\beta$ 2-subunit of *E. coli* RNR using 3- and 4-pulse DEER at Q-band were unsuccessful until now due to several factors. First, the generated signal is relatively weak in intensity, resulting in a poor S/N ratio. An increase in protein concentration and an improvement in the irradiation protocol could help overcome these problems. Employed wavelength and exposure times could be varied. Second, the transversal relaxation time of the triplet species is quite fast. This issue can be overcome by deuteration of the sample. Furthermore, the generated triplet signal is very broad, at least at Q-band frequencies. Hence, the excited fraction of spins is low with common microwave pulses. This should be less of a problem at X-band frequencies, where only a single, relatively narrow EPR transition was detected. X-band DEER measurements might therefore be more suitable for distance determination when using azF. However, if distance measurements at Q-band are needed, shaped pulses could be implemented to overcome this issue. Unfortunately, the complete triplet spectrum will never be excited by a single EPR pulse, but using shaped pulses such as WURST (wideband, uniform rate, smooth truncation) pulses could provide a slight improvement.<sup>313</sup> Another technique that does not rely on the excitation width of a pump pulse is LaserIMD. If, for example, a nitroxide radical is selected as the detected species, the triplet state can be activated by a laser pulse, acting like a pump pulse in a usual DEER experiment.

Furthermore, using an azide group to generate a paramagnetic species may not only be limited to phenylalanine since other azide-containing compounds, such as  $\beta$ -azido-propionophenone or 1-azidoadamantane, also form triplet nitrenes upon UV light exposure.<sup>314,315</sup> In previous work, azido-derivatives of tryptophan, cysteine, and lysine have been successfully incorporated into proteins, which could, in combination, eventually pave the way for various UAA-based spin labels.<sup>316</sup>

# 6.

## Investigating *E. coli* ribonucleotide reductase with high-pressure EPR

---

### 6.1. Introduction

#### 6.1.1. Pressure affecting protein structures

The effect of pressure on a system is characterized by Le Chatelier's principle. Accordingly, a system tends to minimize and counteract the effect of external perturbing factors at equilibrium state, which in the case of pressure application, leads to a reduction of the system's volume. In the equilibrium state, generally

$$\Delta G = -RT\ln(K) = \Delta U + p\Delta V - T\Delta S \quad (6.1)$$

is valid with the changes in Gibbs free energy  $G$ , internal energy  $U$ , volume  $V$ , and entropy  $S$ .<sup>317</sup>  $R$  is the gas constant and  $K$  the equilibrium constant, while  $T$  is temperature and  $p$  pressure. Pressure affects the volume of a system that changes between state A and B in equilibrium, given by

$$\Delta V = V_B - V_A = \left(\frac{\partial \Delta G}{\partial p}\right)_T = -RT \left(\frac{\partial \ln(K)}{\partial p}\right)_T. \quad (6.2)$$

In analogy to this equation, the activation volume  $\Delta V^\ddagger$  can be written as

$$\Delta V^\ddagger = -RT \left(\frac{\partial \ln(k)}{\partial p}\right)_T \quad (6.3)$$

with the rate constant  $k$ .<sup>318,319</sup> Characteristic values for  $\Delta V$  or  $\Delta V^\ddagger$  in biochemical processes are around +50 to -50 mL mol<sup>-1</sup>.<sup>317,320</sup>

The volume of a protein is dominated by three main components: the volume of the individual atoms (constitutive volume), the void volume of internal cavities, and contributions arising from the solvation effects of peptide bonds and amino acid side

chains. Pressure will influence the protein volume and induce local and global conformational changes and/or subunit dissociation-association processes, which finally leads to denaturation of the protein. 1 to 2 kbar is mostly sufficient to induce dissociation of oligomeric proteins.<sup>321</sup> Denaturation of small monomeric proteins is typically observed in the range of 3 – 8 kbar.<sup>317,322</sup> This implies that pressures up to 3 kbar mainly influence quaternary protein structures, whereas higher pressures affect secondary and tertiary structures. Primary structures remain undisturbed by pressures up to 20 kbar.<sup>323</sup> Pressure-induced unfolding is explained mainly by void volumes in the protein structure arising from imperfect packing. The application of pressure eliminates these void spaces, decreasing the system volume.<sup>324</sup> An additional reason for pressure unfolding might be water penetration into the protein interior, weakening hydrophobic interactions.<sup>323</sup> On the other hand, pressure-induced dissociation may be explained by the imperfect packing of atoms located at the subunit interface and also disruption of polar and ionic bonds at the subunit interfaces leading to negative volume changes.<sup>323</sup> The transitions of folded to unfolded state, induced by external factors such as pressure and temperature, are often visualized with the aid of phase diagrams, exemplarily shown in **Figure 6.1**, which deliver information about stability and unfolding mechanisms.

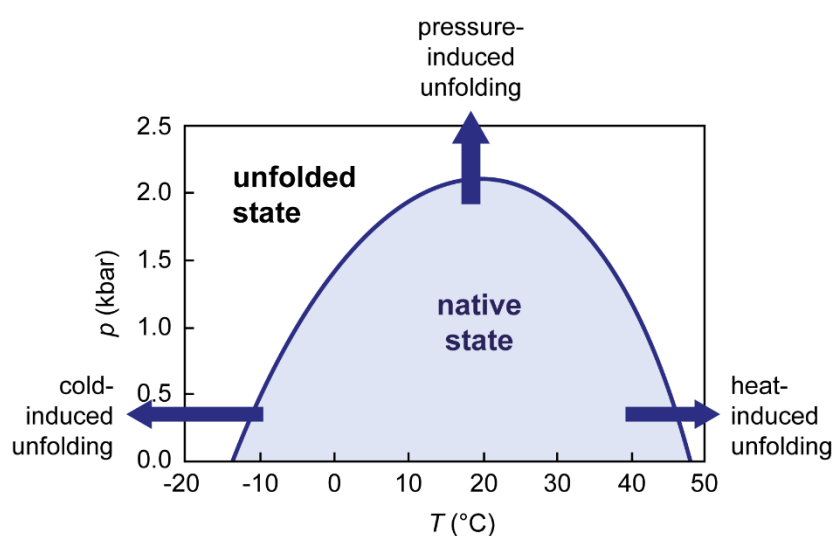


**Figure 6.1:** Exemplary  $p,T$ -stability diagram of SNase at pH 5.5. Figure adapted from Winter *et al.*<sup>323</sup>

In addition to its usage in unfolding studies, pressure is often employed to populate higher-energy conformational states, namely excited states.<sup>325–328</sup> In many proteins, intermediate structures are difficult to characterize due to their low population and short lifetimes. Pressure represents one way to artificially induce these conformational changes, thus leading to a higher population in these states. This principle becomes comprehensible if one considers the energy landscape of proteins, described by the

folding funnel (**Figure 6.2**). The entire allowed conformational space of a protein is covered by the folding funnel, with the x-axis describing the conformational entropy of the system and the y-axis describing the conformational order, i.e., the internal energy, in an aqueous solvent.<sup>329</sup> The landscape is represented as hills and valleys. Roughly speaking, if the landscape is smooth, the natively folded protein is expected to display only marginal conformational variations. If the landscape is rough, the ensemble of underlying structures might include conformers entirely different from the native one.<sup>330</sup>

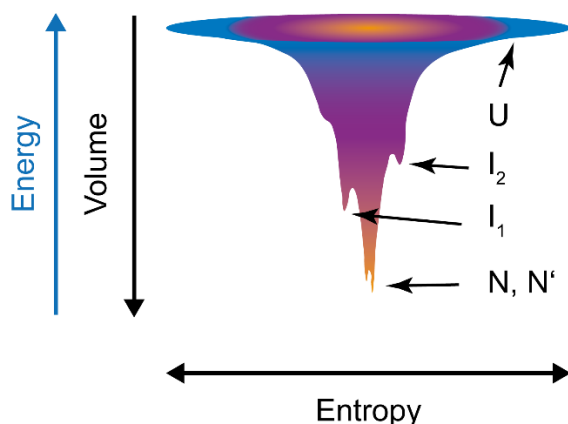


**Figure 6.2:** Exemplarily folding funnel for  $\beta$ -lactoglobulin with the five major conformations: native (N), the low-lying excited state (N'), two intermediate states (I<sub>1</sub> and I<sub>2</sub>), and the unfolded state (U). Molar volumes decrease in the order  $N > N' > I_2 > I_1 > U$ . Figure adapted from Akasaka.<sup>329</sup>

### 6.1.2. Excited states in ribonucleotide reductase

In ribonucleotide reductase, high-energy intermediate states might be present during the catalytic reaction, and hence, pressure application might be beneficial for their detection. Of course, it has already been outlined in the previous chapters that unnatural amino acids can be used to capture intermediate steps. Nevertheless, this always requires a protein mutation, which does not correspond to the protein's natural state, even though the change may be minor. The assistance of pressure would allow the usage of the wild-type enzyme. In addition, other previously hidden conformers could be unraveled. Conformational changes could either be observed throughout altered EPR lineshapes, distance measurements, or by changes in the electrostatic environment, e.g., caused by water penetration.

In addition, it is interesting to investigate the complex stability of multimeric RNR for two reasons. First, RNR dissociation and reassociation of  $\alpha 2\beta 2$  into dimers is a fundamental aspect of its regulation. Understanding and manipulating these mechanisms are vital for therapeutic treatment. Second, it is known that the  $\alpha 2$  subunit of *E. coli* RNR can be found as monomers in solution, whereas  $\beta 2$  is found exclusively as a dimer. It is unclear why the protein favors this behavior. Pressure could be used to

manipulate dimer-monomer equilibria in the sample and thus gain insights into dissociation constants and processes.

### 6.1.3. High-pressure EPR

While the combination of high-pressure setups with spectroscopic detection is already well-established in several biophysical spectroscopies (e.g., NMR, SF setups, FT-IR, or CD)<sup>317</sup>, EPR currently lacks standard accessories for this application. Therefore, Simon Schumann constructed a self-built setup in our laboratory based on the idea of Lerch *et al.*<sup>325,331</sup> Briefly, sample-containing EPR tubes are sealed with a silicon piston and pressurized inside a high-pressure setup. After reaching the desired pressure, the sample is frozen, which allows trapping of the sample in its high-pressure state, even after removing it from the pressurization setup. This technique allows the investigation of liquid samples under high hydrostatic pressures via EPR spectroscopy at cryogenic temperatures.

## 6.2. Materials and methods

### 6.2.1. Sample preparation

First, a radical yield of  $1.2 \text{ Y}\bullet/\beta 2$  was achieved by mixing a  $190 \mu\text{M}$  solution apo- $\beta 2$  in  $50 \text{ mM}$  Tris pH 7.6 with 5 eq.  $\text{Fe}^{\text{II}}$  and  $\text{O}_2$ . Previous test experiments with the high-pressure setup revealed that samples must contain 25% (v/v) glycerol to prevent EPR sample tubes from bursting. Hence, the protein solution was supplemented with glycerol to a final concentration of 25%, yielding a protein concentration of  $140 \mu\text{M}$   $\beta 2$ . Ca.  $200 \mu\text{L}$  of the sample was then transferred to  $2.8 \text{ mm}$  O.D. EPR tubes and stored at  $4 \text{ }^\circ\text{C}$  until pressure application. It is important to note that air bubbles inside the EPR tube must be avoided.

### 6.2.2. Sample pressurization

The sample-containing EPR tube was sealed with a silicon piston, which was pressed down to the sample, so that little to no air was trapped between the sample and the piston. Ethanol is layered over the piston, which prevents the sample and ethanol from mixing. To externally control the sample position within the pressure bomb, the EPR tube is provided with a magnetic collar. The sample tube is then inserted into the high-pressure apparatus filled with ethanol. First, the sample was positioned at the top of the pressure bomb, while the desired pressure could be adjusted manually. After reaching the desired pressure, the system was allowed to equilibrate for 5 – 10 min. The pressure bomb was then cooled down with a mixture of dry ice/isopropanol, and the sample was positioned in the lower part of the pressure bomb. The sample was then allowed to

freeze for around 20 – 25 min. Finally, the bomb was depressurized, and the sample was removed from the system and quickly transferred to liquid nitrogen. The magnetic collar was removed before EPR measurements.

### **6.2.3. Details of the EPR experiments**

**Q-band:** Q-band pulse EPR measurements were carried out at  $T = 10$  K using the Bruker ER 5106QT-2 resonator. DEER experiments were performed using the 4-pulse DEER pulse sequence with 16-step phase cycling and Gaussian pulses. The frequency separation  $\Delta f = f_{\text{pump}} - f_{\text{obs}}$  was 84 MHz in an overcoupled resonator with  $f_{\text{pump}}$  set to the center of the resonator dip. DEER time traces were background-corrected by using an empirical second-order polynomial fitting. For orientation averaging, each primary time trace was first normalized to the same signal intensity at zero time. Afterward, these time traces were normalized to the signal intensity of the Hahn echo at the pump position. The summation of orientation-selective DEER time traces thus led to the orientation-averaged traces. Validation of the distance distributions was obtained by varying the starting value of the background fit by  $\pm 50\%$  in 10 steps and the background dimensionality in 10 steps by  $\pm 0.5$  concerning the initial value chosen for the data analysis.

### 6.3. Results and discussion

#### 6.3.1. The effect of glycerol on *E. coli* RNR protein structure

As demonstrated in earlier chapters, glycerol influences the radical formation efficiency and may thus also affect the protein structure. However, the use of glycerol for the high-pressure setup is unavoidable according to the current state of the art. To exclude changes in the EPR lineshape caused by glycerol itself, a comparison of 34 GHz ESE of holo- $\beta 2$  samples containing either 5% or 25% glycerol in the buffer is presented in **Figure 6.3**. Both samples displayed a radical yield of  $1.2 Y_{\bullet}/\beta 2$ . It should be noted that no pressure has been applied to these samples yet.

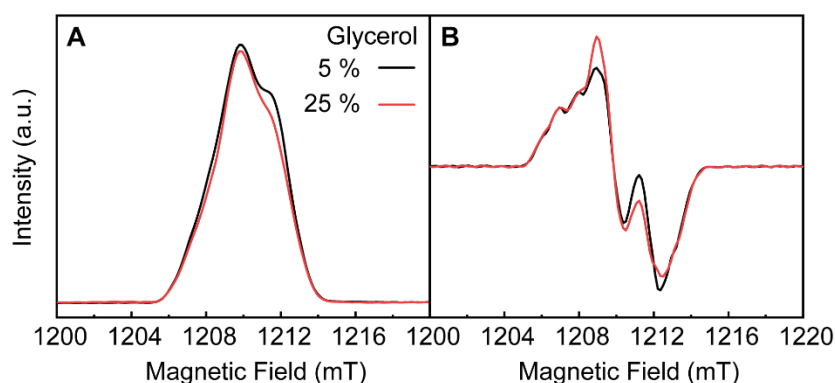


**Figure 6.3:** Pulse EPR spectra of  $Y_{122}\bullet$  in the  $\beta 2$ -subunit of *E. coli* RNR as a function of glycerol content in the buffer, recorded at 34 GHz and 10 K. Spectra are shown as absorption spectra (A) or as first derivative (B). Samples either contain 5% (black) or 25% (red) glycerol in the buffer. Spectra are scaled to protein concentration, number of scans, videogain, and srt. Experimental conditions:  $\pi = 28$  ns;  $\tau = 300$  ns;  $srt = 4$  ms;  $spp = 100$ ; microwave power = 20 mW.

The absorption spectra show only minor deviations in their integral, which is proportional to the number of spins in a sample, and are within the usually given 10 – 30% error for quantitative EPR.<sup>332,333</sup> Hence, adding glycerol does not affect the spin concentration, which is to be expected. It should be noted that glycerol was added after generating the radical species and thus cannot affect the radical formation process and efficiency itself. Further, no significant changes in the EPR lineshape are observed since, for example,  $g$ -values and large hyperfine couplings remain the same.  $T_2$  measurements revealed almost identical relaxation times with 1.2 and 1.3  $\mu$ s for 5% and 25% glycerol, respectively.

Next, orientation-selective DEER measurements of holo- $\beta 2$  were carried out to investigate the spatial orientation of the  $Y_{122}\bullet$ - $Y_{122}\bullet$  pair in the  $\beta 2$  dimer and to determine the fraction of  $Y_{122}\bullet$ - $Y_{122}\bullet$  pairs. The second point in particular is of concern, as previous studies from our laboratory have proven that glycerol contents  $\geq 20\%$  influence the communication between the respective subunits in the  $\beta 2$  dimer (Master thesis Viktoria

Gocke). Orientation-selective DEER measurements with the 25% glycerol sample, shown in **Figure 6.4**, were thus compared to a sample containing 5% glycerol.

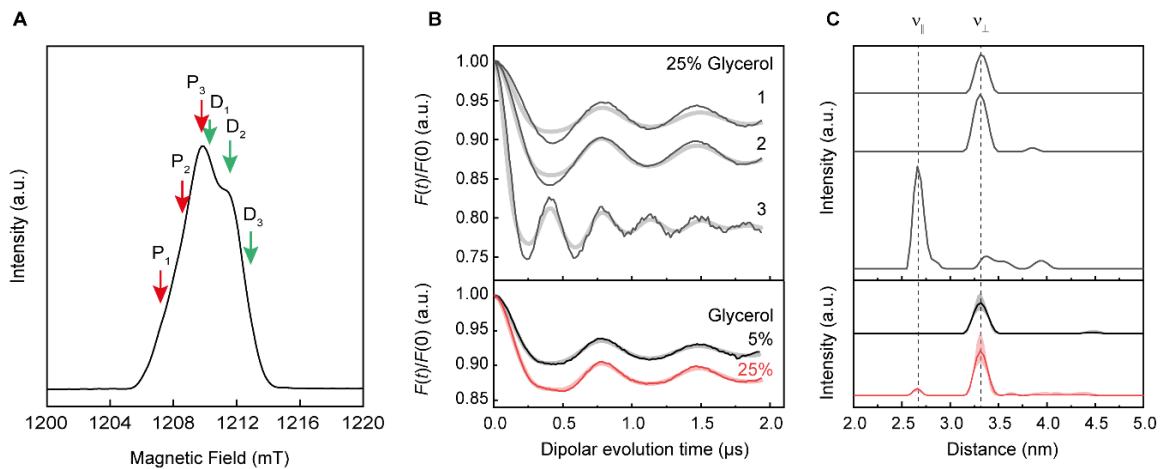


**Figure 6.4: DEER distance measurements for *E. coli* RNR supplemented with different amounts of glycerol.** (A) DEER measurements were performed at three consecutive field positions (labeled 1, 2, 3). P indicates pump, and D detect positions. (B) Background- and phase-corrected, normalized orientation-selective (top), and orientation-averaged (bottom) 34 GHz DEER traces. Data are displayed in dark shade, and fits obtained by DeerAnalysis are overlaid in paler shade. (C) Distance distribution obtained by the analysis. Validation of the distance distribution (paler shade) was performed in DeerAnalysis. Top part (grey data) shows data obtained for the sample containing 25% glycerol. Bottom part shows a comparison of orientation-averaged data for 5% (black) versus 25% (red) glycerol. Acquisition time = 5 h (1), 16 h (2), 6 h (3).

First, the focus is set on the distances obtained to address the first question of spatial orientation. Only one main distance of  $3.31 \pm 0.07$  nm is observed for the sample containing 5% glycerol, whereas two validated main distances are observed in the sample containing 25% glycerol. The predominant distance is located at  $3.33 \pm 0.07$  nm, whereas a smaller one is detected at  $2.66 \pm 0.04$  nm. In both samples, the 3.3 nm distance can be assigned to the  $Y_{122}\bullet$ - $Y_{122}\bullet$  pair, while the smaller distance might most probably originate from an orientation-averaging artifact. Even though the primary time traces were scaled before summation, the distance arising from  $\theta = 0^\circ$  ( $v_{\parallel}$ ) might still be overpronounced. The slight deviation of 0.02 nm for the  $Y_{122}\bullet$ - $Y_{122}\bullet$  pair in both samples is within error and, therefore, negligible.

Surprisingly, a glycerol content of 25% leads to several unvalidated distances between 3.5 and 4.6 nm, whereas for 5% glycerol, the distance distribution is very precisely defined. Note that both the spin concentration (about 240  $\mu$ M for 5% and 170  $\mu$ M for 25%) and acquisition times do not vary much between samples, which would otherwise affect S/N ratios and thus explain the occurrence of measurement artifacts. However, a higher S/N ratio of 33 is indeed observed for the sample with 25% glycerol compared to 20 for 5% glycerol.

Furthermore, the modulation depth  $\Delta$  can be read from the DEER measurements. According to equation 2.41:

$$\Delta = 1 - (1 - \lambda_B)^{(N-1)} \quad (2.41)$$

$\Delta$  depends on the inversion efficiency  $\lambda_B$  and the number of spins  $N$ . As all experimental conditions are kept constant, and the spectral lineshape does not vary among the experiments,  $\lambda_B$  remains constant. The experimentally determined  $\Delta$  increases from 7.9% to 11.6% with increasing glycerol levels (**Figure 6.4**). Consequently, a larger modulation depth implies a higher number of spin pairs  $N$ . This observation seems strange since maximum modulation depth should already be achieved at 5% glycerol due to two or none radical distribution. Distances other than the  $Y_{122}\bullet$ - $Y_{122}\bullet$  pair have never been observed in similar experiments. To interpret both, the multiple larger distances and the enhanced modulation depth caused by glycerol, three possible scenarios were evaluated.

#### I. Different $Y_{122}\bullet$ conformers

Glycerol is known to induce conformational changes in proteins.<sup>334</sup>  $Y_{122}\bullet$  may adopt different conformations, resulting in shorter and/or longer distances, depending on the flipped angle. However, this must be a defined conformation since an ensemble of many different conformers with only slight spatial deviations would lead to broadening of the main distance at 3.3 nm, which is not observed. To probe this hypothesis, different possible rotamers of  $Y_{122}$  were calculated by the software PyMOL, restricting the calculation to 'backbone dependent rotamers'. For the highest-ranked rotamer, the angle between the two  $\pi$ -planes of both conformations changes by around  $104^\circ$  (**Figure 6.5B**). The distance between these flipped  $Y_{122}$ - $Y_{122}$  conformers measured at the O atom results in around 4.4 nm (**Figure 6.5C**). Strikingly, the analysis of the DEER trace without validation of the fit results in a sharp distance of around 4.0 nm (**Figure 6.5A**). Such a distance of around 4 nm has also been observed in similar studies, further described in Viktoria Gocke's Master thesis, and agrees with the distance observed for the yellow rotamer within an error of 10% accuracy of distance determination.

However, one fact that is not consistent with this hypothesis is the increase in modulation depth. As determined from the pulse EPR spectra, the spin concentration does not change upon the increase of glycerol content. Hence, the only factor that can change is the ratio between blue and yellow conformers. This ratio will not affect the modulation depth, as  $N$  stays constant.<sup>132,220</sup> Moreover, major conformational changes should be reflected in the EPR lineshape.

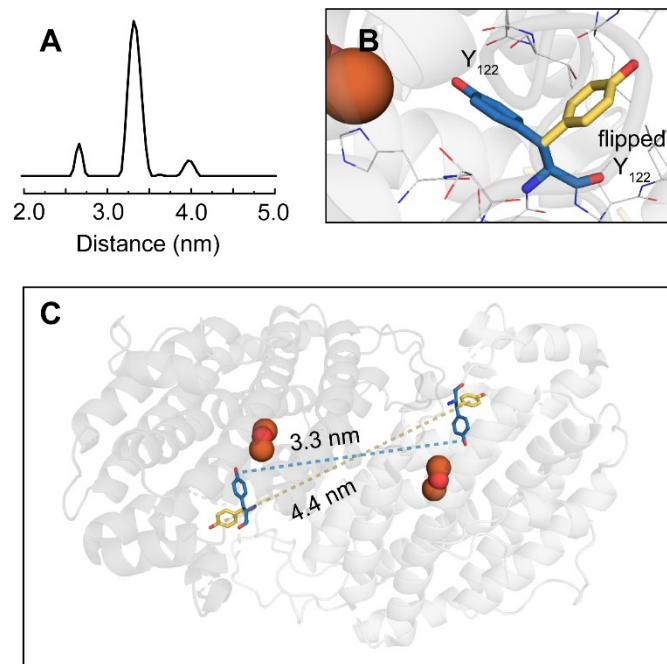


**Figure 6.5: Analysis of obtained distances.** (A) Distance distribution as obtained by DEER measurements without validation of the fit. A minor distance is observed at around 4.0 nm. (B) Different conformations of Y<sub>122</sub> in *E. coli* RNR. The conformer found in the wild-type protein is shown in blue, whereas the yellow conformer was obtained by rotamer calculations in PyMOL. The diiron cluster is represented by spheres. Nearby residues are depicted as thin lines. (C) Distances between Y<sub>122</sub>-Y<sub>122</sub> are 3.3 nm (blue-blue) and 4.4 nm (yellow-yellow). PDB: 5CI4<sup>35</sup>.

## II. Dimer disruption

Y<sub>122</sub> remains rigid, and its structure is not affected, but glycerol penetrates the protein-protein interface and thus disrupts the dimeric interaction. This may lead to a larger distance between the Y<sub>122</sub>•s. Glycerol is often used as a cosolvent for high protein stability and to prevent aggregation.<sup>335,336</sup> This is achieved by the interaction of glycerol with large hydrophobic areas, where glycerol functions as an amphiphilic interface between the hydrophobic surface and the polar solvent. However, it was reported that glycerol often shifts the native protein to more compact states, which would contradict the experimental observations of larger distances. Although the effect of glycerol penetrating the protein interface would explain the noncooperative behavior observed during the diiron cofactor assembly and the larger distance, this scenario is unlikely. The additional solvent layer of glycerol would more likely shift the main distance to longer distances rather than cause an additional one. Furthermore, the modulation depth would remain constant in this case, or even more likely,  $\Delta$  decreases if dimers lose their interaction and fall apart.

### III. Oligomerization

Glycerol may induce the formation of higher-ordered structures, giving rise to several longer distances. The cosolvent glycerol can mediate the formation of strong non-covalent interactions with protein subunits, which promotes contact between monomers, further leading to oligomeric structures.<sup>337</sup> No tri- or tetrameric structures have yet been reported for *E. coli* RNR. However, a  $\beta_4$  tetramer has been found to be part of the regulatory machinery in class I *Leeuwenhoekiella bladensis* RNR.<sup>338,339</sup> Similarly, in *Facklamia ignava* RNR, also a class I enzyme, tetramer formation is promoted in the presence of dATP.<sup>340</sup> To test whether oligomers and their radical pair distances in *E. coli* RNR are within the detectable range of DEER measurements, docking models of trimers and tetramers were constructed by ClusPro.<sup>341–344</sup> Exemplarily, three models with the highest scoring are pictured each (**Figure 6.6**). Please note that these models are not intended to prove the correctness of the docked structure, but instead, they demonstrate that even different orientations of the monomers in the oligomer lead to quite similar distances between the Y<sub>122</sub>S. For the trimers, all distances are located between 3.0 and 3.5 nm. A distance of 3.1 – 3.8 nm between two neighboring subunits and a diagonal distance of 4.4 – 5.4 nm can be observed in tetramers. All these distances are consistent with those obtained by DEER measurements. On top of that, the occurrence of additional spin pairs increases  $N$ , leading to a higher experimental modulation depth. Moreover, the slight increase in  $T_2$  times of around 0.1  $\mu$ s could indicate a higher local spin concentration upon raising the glycerol content.

Out of the three possible explanations, option 2 seems to be the least likely, as it does not fully agree with the experimental findings. Likewise, a residue as solvent-protected as Y<sub>122</sub> is unlikely to be affected by glycerol to such an extent that it changes its conformation by more than 90°. Hence, explanation number 3 seems most likely, as it agrees with all experimental data. However, a combination of the different effects might also be possible, for example, glycerol first penetrating the interface, thus allowing conformational changes. As for all these scenarios, the orientation of the inter-spin vector  $r$  changes, orientation-averaging of the individual traces is not straightforward, which explains the occurrence of an orientation-averaging artifact. Further experiments are needed to understand the effect of glycerol on the protein structure. However, probing this is challenging because high levels of glycerol interfere with numerous analytical methods or are at least not optimal (size exclusion chromatography, mass spectrometry, and small-angle X-ray scattering, as a few examples).<sup>345–347</sup>

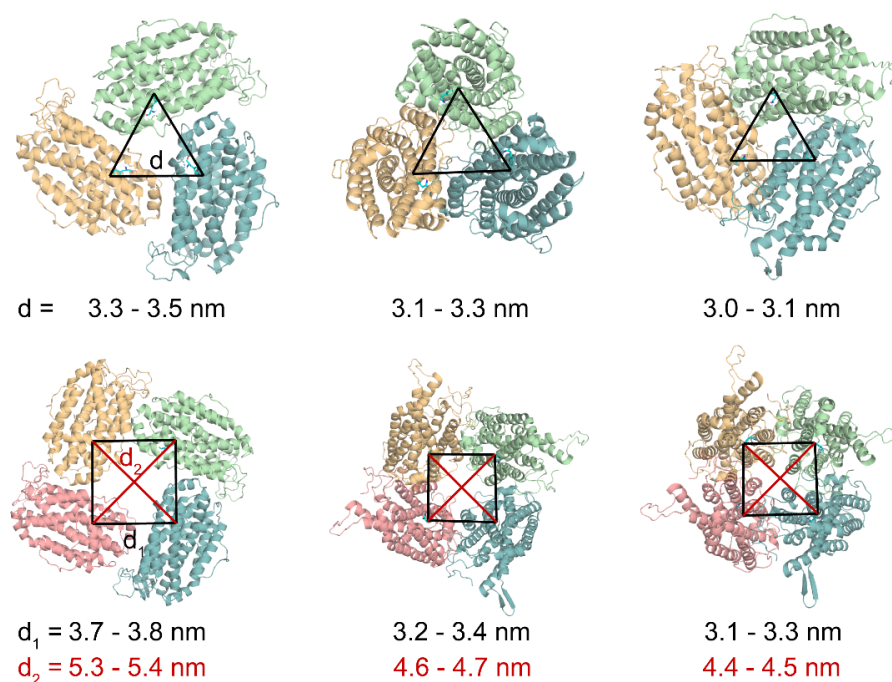


**Figure 6.6: Trimers (top row) and tetramers (bottom row) of the  $\beta$ -subunit of *E. coli* RNR.** Models were obtained by protein-protein docking via ClusPro of the wt- $\beta$ 2 subunit (PDB: 5CI4<sup>35</sup>). One single distance (black line) between Y<sub>122S</sub> in each subunit is observed for trimers. Tetramer formation allows the detection of two distinct distances (black and red). Only three docking models with the highest scoring out of ten are presented exemplarily for each assembly. All other models revealed distances in a similar range.

Even though it cannot be ruled out that glycerol does not interfere with the structure of *E. coli* RNR, these effects do not seem to be the dominant factors for protein structure (no change in lineshape and Y<sub>122</sub>•-Y<sub>122</sub>• distance observed). Hence, pressure was applied to the system in the next step.

### 6.3.2. *E. coli* RNR under different pressures

Since no pressure studies on RNR are known to date, a region of suitable pressure must first be identified in which the protein is not denatured to ultimately identify excited states. As described above, pressures > 2 kbar often influence tertiary protein structures, so 2 and 4 kbar were considered interesting starting points for this study. 4 kbar is the maximum achieved with the pressure setup. The subsequently recorded 34 GHz pulse EPR spectra are presented in **Figure 6.7**, along with their pseudomodulation.

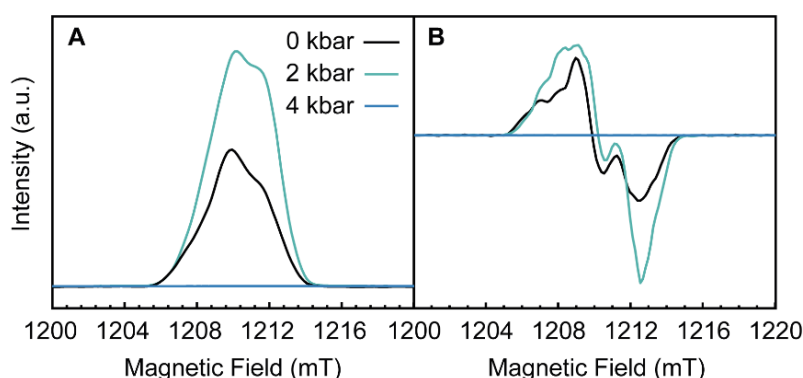


**Figure 6.7: Pulse EPR spectra of  $Y_{122}\bullet$  in the  $\beta_2$ -subunit of *E. coli* RNR under pressure, recorded at 34 GHz and 10 K.** Spectra are presented as absorption spectra (A) or as first derivative (B). Samples were either measured under atmospheric pressure (0 kbar) or after pressure application (2 and 4 kbar). Spectra are scaled to protein concentration (140  $\mu\text{M}$  each), number of scans, videogain, and srt. Experimental conditions:  $\tau = 28$  ns;  $\tau = 300$  ns; srt = 4 ms; spp = 100; microwave power = 20 mW.

Exerting 4 kbar pressure leads to a complete loss of the EPR signal intensity. Either water has penetrated the protein's interior, which leads to quenching of  $Y_{122}\bullet$ , or the protein has completely unfolded. Either way, it becomes clear that 4 kbar is too high if  $Y_{122}\bullet$  should be detected via EPR. At 2 kbar, a sharp EPR signal is observed, which increases in relative intensity compared to 0 kbar (**Figure 6.7A**). Integration of the 2 kbar spectrum and comparison to reference samples reveals a spin concentration of  $316 \pm 36 \mu\text{M}$ . Furthermore, a change in lineshape becomes apparent when comparing their first derivative spectra (**Figure 6.7B**). This suggests that there is a second underlying paramagnetic species in addition to the  $Y_{122}\bullet$  signal, which could explain the increase in spin concentration evident from the absorption spectrum. Subtraction of the 0 kbar EPR spectrum (**Figure 6.8B**) from the one obtained after 2 kbar pressure application (**Figure 6.8A**) allows characterization of the underlying signal (**Figure 6.8C**). Furthermore, a Hahn echo was recorded at the detect frequency  $\nu_{\text{det}}$  (**Figure 6.8D**) used for DEER experiments later in this chapter. The longer pulses used at  $\nu_{\text{det}}$  seem to be more optimal for detecting the unknown radical species, as this is the main species detected. The first derivative spectra reveal global maxima and minima at around  $g = 2.0088$  and  $2.0015$  for both the subtraction spectrum and the one recorded at  $\nu_{\text{det}}$ . The signals exhibit a linewidth comparable to that of  $Y_{122}\bullet$ , suggesting an organic radical as the origin of this signal.

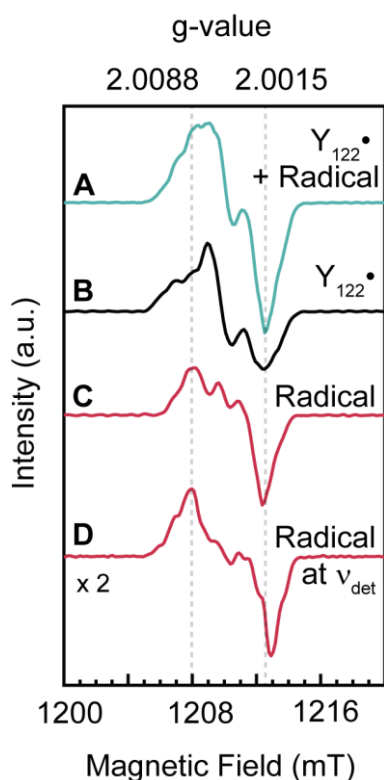


**Figure 6.8:** First derivative spectra of  $Y_{122}\bullet$  and an unknown radical species, recorded at 34 GHz and 10 K. (A) 2 kbar pressure applied to the  $\beta$ 2-subunit of *E. coli* RNR. The pulse EPR signal is a mixture of  $Y_{122}\bullet$  and the unknown radical species. Subtraction of  $Y_{122}\bullet$  (B) results in the radical spectrum (C). (D) Pulse EPR spectrum recorded at the detect frequency  $\nu_{\text{det}}$  mostly exhibits a signal of the unknown radical. Spectra (A) – (C) were recorded at 34.0025 GHz with  $\pi = 28$  ns, whereas spectrum (D) was recorded at 33.9185 GHz with  $\pi = 70$  ns. Spectra were shifted horizontally for better visualization.

Typically, protein-based radicals can be traced back to either tryptophan or tyrosyl radicals. Thus, the radical signal was simulated using typical parameters for tryptophan or tyrosine residues from literature to determine its identity (**Figure 6.9**). The spectrum shown in **Figure 6.8D** was used for this purpose, as the unknown radical signal is best isolated here.

In *E. coli* RNR, a neutral tryptophan radical at  $W_{111}$  can be formed in the reconstitution reaction of apo- $Y_{122}\text{F}$  with  $\text{Fe}^{\text{II}}$  and oxygen.<sup>348,349</sup> This radical can be readily distinguished from  $Y_{122}\bullet$  by high-field EPR studies since  $W_{111}$  offers a much smaller  $g$ -anisotropy than tyrosyl.<sup>349</sup> However, Q-band does not provide the required resolution of single  $g$ -values to differentiate in our case. Simulation of  $W_{111}\bullet$  at 34 GHz unravels a similar lineshape and linewidth as the unknown radical signal. Nevertheless, all  $g$ -values for  $W_{111}\bullet$  would need to be shifted by +0.002 to match the experimental spectrum. This deviation is outside the range of all reported tryptophan radicals; hence, tryptophan can be ruled out as the origin of the unknown radical.<sup>297,350</sup>

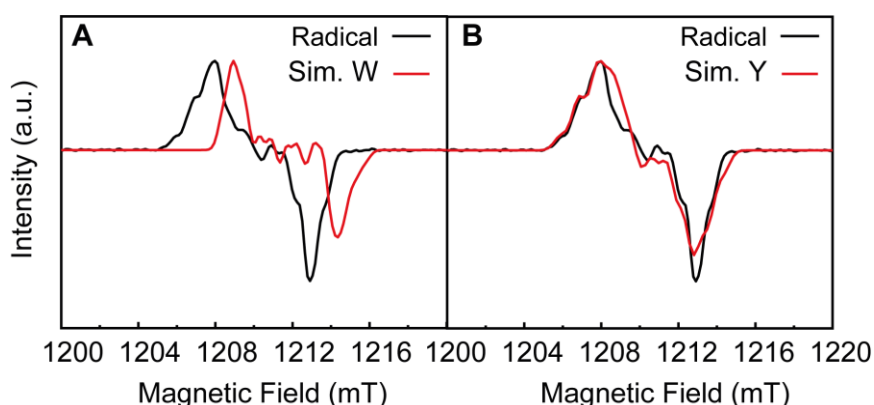


**Figure 6.9: Simulation of the radical species.** Comparison of the unknown radical species (black) to simulations for  $W\bullet$  (A) or  $Y\bullet$  (B). Simulations, colored in red, were created by the EasySpin ‘pepper’ routine. Parameters for (A) were reported by Lenzian *et al.*<sup>348</sup> and Bleifuss *et al.*<sup>349</sup> Parameters used for the simulation of (B) are given in **Table 6.1**.

An algorithm has been proposed earlier for tyrosyl radicals, which aids in simulating and understanding any tyrosyl radical EPR signal.<sup>351</sup> This algorithm calculates typical hyperfine coupling values for different orientations of the tyrosyl ring plane based on the McConnell relation, previously designated as equation 3.1 in Chapter 3.<sup>207</sup>

$$a_{\text{iso}}^{\beta} = \rho_{\text{C1}}(B' + B'' \cos^2 \theta) \quad (3.1)$$

Accordingly, coupling values of  $C\beta$ -methylene protons (**Figure 6.10A**) are affected by the rotation angle  $\theta$  and the spin density  $\rho$  on atom C1.  $B'$  and  $B''$  are constants, whereas  $B'$  is commonly neglected in practical applications, and  $B''$  equals 58 G.<sup>352</sup> Hyperfine splitting constants for the ring protons and their corresponding Euler angles are assumed conserved for all tyrosyl radicals and are thus kept constant. The simulation algorithm also assumes axial symmetry as a simplification. The only parameters that need to be specified in the algorithm are the spin density  $\rho_{\text{C1}}$  and the angle  $\theta$ . The algorithm then provides both, theoretical  $g$ -tensors and hyperfine coupling constants, which can be used for simulating the EPR spectra. Alternatively,  $\rho_{\text{C1}}$  and  $\theta$  can be obtained by giving isotropic hyperfine coupling values of  $a_{\text{iso}}^{\beta 1}$  and  $a_{\text{iso}}^{\beta 2}$ .

For  $Y_{122}\bullet$ ,  $\rho_{\text{C1}}$  equals 0.38<sup>351</sup> and the best match with previously reported hyperfine coupling values was obtained at  $\theta = 16.6^\circ$  and  $-76.6^\circ$  (**Table 6.1**). An angle of  $16.6^\circ$  is in good agreement with the published crystal structure (**Figure 6.10C**). For simulating the radical signal, starting values were taken from tyrosyl radicals in cytochrome *c* oxidase and bacterioferritin, as they have similar lineshapes.<sup>353,354</sup> The  $g_x$  value and hyperfine coupling constants of the  $C\beta$ -protons were then varied in order to obtain the best fit (**Figure 6.9B**).  $g_y$  and  $g_z$  were retained for  $Y_{122}\bullet$  since these two parameters vary only slightly for most tyrosyl radicals.<sup>351,355</sup> As proposed by the simulation algorithm, axial

symmetry was maintained for hyperfine couplings. All other parameters were kept constant during the fitting procedure as compared to  $Y_{122}\bullet$ . Based on the algorithm,  $\rho_{C1}$  changed to 0.45, and now  $\theta$  can be either  $-8.5^\circ$  or  $-51.5^\circ$  (**Table 6.1**).

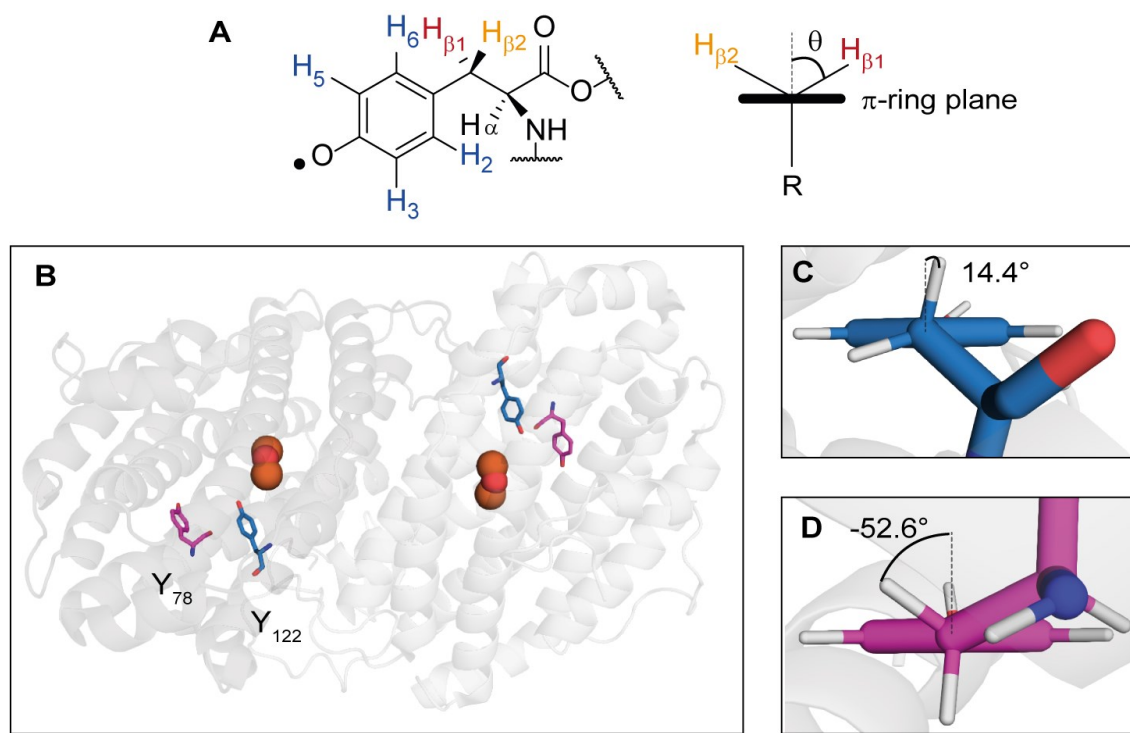


**Figure 6.10: Tyrosine  $Y_{122}$  and  $Y_{78}$  in *E. coli* class Ia RNR.** (A) Left: Schematic representation of protons generally included for the simulation of a tyrosyl radical. Protons with conserved hyperfine couplings constants (blue) are located at the aromatic ring. Coupling values for  $\beta$ -methylene protons (orange and red) are strongly dependent on the angle  $\theta$ . Right:  $\theta$  is defined by the dihedral angle between the  $C\beta$ -H bond and the  $p_z$  orbital axis of  $C1$ . (B) Residues  $Y_{122}$  (blue) and  $Y_{78}$  (pink) in the *E. coli* RNR  $\beta_2$  subunit. Angle  $\theta$  depicted for  $Y_{122}$  (C) and  $Y_{78}$  (D).

A lower  $g_x$  value may indicate H-bonds between the tyrosyl radical and solvating water molecules. One explanation thus might be that pressure allows water to enter the protein, followed by the formation of an H-bond with  $Y_{122}\bullet$ . In this case, mostly the unknown radical should be visible, and the native  $Y_{122}\bullet$  should decrease in relative intensity. However, spectra utilized for the subtraction in **Figure 6.8** were employed with their original intensities, and thus, a significant decrease in  $Y_{122}\bullet$  concentration is not verified. This fact indicates that the unknown signal does not originate from the tyrosine at position 122 but from another tyrosyl residue. However, the radical cannot be transferred from  $Y_{122}$  to this other tyrosine since then,  $Y_{122}\bullet$  should again decrease in intensity. Hence, the generation process of this radical species remains unclear.

**Table 6.1: Simulation parameters.** Parameters used for spectral simulations of the 34 GHz EPR spectra of  $Y_{122}^\bullet$  as first reported by Tkach *et al.* in comparison to the simulation shown in **Figure 6.9B**.<sup>71</sup> The Euler angles  $\alpha$ ,  $\beta$ , and  $\gamma$  are defined within the EasySpin  $z, y', z''$  convention. Furthermore, the predicted spin density  $\rho_{C1}$  and the rotation angle  $\theta$  are listed.

Species	Parameters						
	$g_x$	$g_y$	$g_z$	$\rho_{C1}$	$\theta / ^\circ$		
$Y_{122}^\bullet$	2.00915	2.00460	2.00225	0.38	16.6 -76.6		
Simulation of unknown $Y^\bullet$	2.00780	2.00460	2.00225	0.45	-8.5 -51.5		
		$A_x / \text{MHz}$	$A_y / \text{MHz}$	$A_z / \text{MHz}$	$\alpha$	$\beta$	$\gamma$
$Y_{122}^\bullet$	$C_1\beta\text{-H}$	59.0	55.0	56.0	0	0	0
	$C_2\beta\text{-H}$	8.0	-1.0	-1.0	70	4	-7
	$C_3/C_5$	-27.2	-7.9	-19.8	0	0	-25/-155
	$C_2/C_6$	4.9	7.7	1.7	0	0	25/155
Simulation of unknown $Y^\bullet$	$C_1\beta\text{-H}$	72.0	70.0	70.0	0	0	0
	$C_2\beta\text{-H}$	28.0	28.0	28.0	70	4	-7
	$C_3/C_5$	-27.2	-7.9	-19.8	0	0	-25/-155
	$C_2/C_6$	4.9	7.7	1.7	0	0	25/155

To identify possible residues, all tyrosines resolved in the crystal structure of *E. coli* RNR (15 in a  $\beta$ -monomer) were examined for their angular conformation of the  $C\beta$ -protons, while one residue ( $Y_{78}$ ) was found to be reasonably consistent with  $\theta$  of  $-51.5^\circ$ . This residue, which is depicted in **Figure 6.10D**, is approximately 1.1 nm away from  $Y_{122}$ . Furthermore,  $Y_{78}$  is located closer to the protein surface than  $Y_{122}$  (see **Figure 6.10B**), which agrees with the smaller  $g_x$  value proposed by the simulations. The pair distances between  $Y_{78}$ - $Y_{78}$  (4.6 nm) and  $Y_{122}$ - $Y_{78}$  (4.0 nm) are larger than the  $Y_{122}$ - $Y_{122}$  pair distance (3.3 nm). If  $Y_{78}$  forms a radical under pressure, this should be verifiable via DEER spectroscopy. Still, it should be noted that any other residue that has changed its conformations due to pressure also qualifies as a candidate.

### 6.3.3. Pressure-dependent DEER measurements

Orientation-selective DEER traces were recorded under the same conditions as in Section 6.3.1 to ensure comparability of the results. Background-corrected time traces and the resulting distance distributions of 0 and 2 kbar samples are illustrated in **Figure 6.11**.

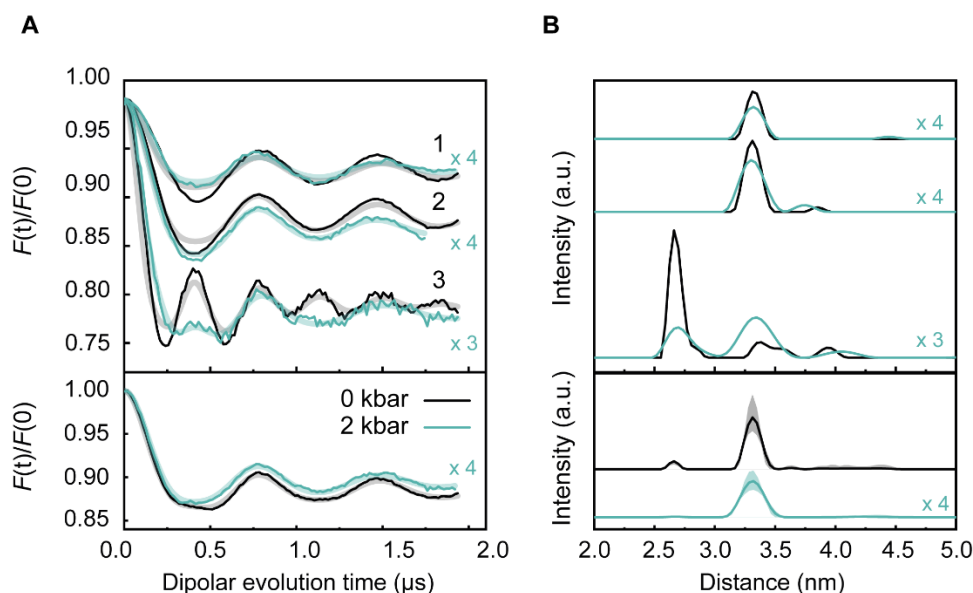


**Figure 6.11: DEER distance measurements of *E. coli* RNR under ambient (0 kbar, black) or 2 kbar (turquoise) pressure.** Signals for 2 kbar were magnified for better visualization. (A) Background- and phase-corrected, normalized orientation-selective (top) and orientation-averaged (bottom) 34 GHz DEER traces. Data are shown in dark shade, and fits obtained by DeerAnalysis are overlaid in a paler shade. (B) Distance distribution obtained by the analysis. Validation of the distance distribution (paler shade) was performed in DeerAnalysis. As indicated in **Figure 6.4** and **Figure 3.5**, measurements were performed at three consecutive field positions (labeled 1, 2, 3). Acquisition time: 0 kbar = 5 h (1), 16 h (2), 6 h (3); 2 kbar = 18 h (1), 28 h (2), 30 h (3).

One main distance at  $3.32 \pm 0.09$  nm is detected at 2 kbar. This distance is consistent with the  $Y_{122}\bullet$ - $Y_{122}\bullet$  pair distance detected at 0 kbar ( $3.33 \pm 0.07$  nm), while the nonsignificant broader distance distribution indicates a persisting rigidity of  $Y_{122}\bullet$ . This supports the hypothesis that the unknown radical species arising after 2 kbar of pressure cannot arise from a distinct  $Y_{122}$  conformation since it would be reflected in a distinct main distance or broadening. Surprisingly, all other previously discussed distances detected at 0 kbar disappear at 2 kbar pressure. The 2.7 nm distance can be observed only at an extremely high signal magnification. The absence of additional distances implies that no distance from the unknown signal is detected.

Remarkably, the modulation depth drops drastically upon the application of pressure. For the orientation-averaged traces, the experimentally determined  $\Delta$  is 2.6% as compared to 11.6% (25% glycerol) and 7.9% (5% glycerol) at 0 kbar. The presence of the unknown radical can suppress the modulation depth if there is no dipolar coupling to any other spin. Furthermore, dimer dissociation into monomers will also lead to a

reduction in modulation depth. As  $Y_{122}\bullet$  and the unknown radical show different spectral widths, their inversion efficiencies  $\lambda_B$  in a DEER experiment differ, which forbids an accurate quantification according to equation 2.42.

$$\Delta = \frac{\sum_i s_i x_i \Delta_i}{\sum_i s_i x_i} \quad (2.42)$$

However, the effect of the unknown species on  $\Delta$  can roughly be approximated by several assumptions:<sup>\*</sup>

- I. The maximum  $\Delta_A$  obtained by  $Y_{122}\bullet$ - $Y_{122}\bullet$  pairs equals 7.9%.
- II. Spin B exhibits no dipolar coupling, thus  $\Delta_B = 0$ .
- III. 2 kbar pressure has no effect on  $Y_{122}\bullet$  concentration, which remains approx. 170  $\mu\text{M}$ . A total spin concentration of ca. 320  $\mu\text{M}$  was detected. Consequently, the unknown radical has a concentration of ca. 150  $\mu\text{M}$ . Thus  $x_A = 0.53$  and  $x_B = 0.47$ .
- IV. Spin A and Spin B are characterized by similar  $T_2$  times. Thus  $s_A = s_B$ .
- V.  $Y_{122}\bullet$  is distributed according to two or none.

The equation thus simplifies to  $\Delta = 0.53 \cdot 7.9\%$ , and consequently, the theoretical modulation depth is expected to be around 4.2%, which is higher than the experimental value. If all of these assumptions are true, this result implies that the presence of the unknown radical species cannot be the sole reason for the decreased modulation depth. Then, dissociation of dimers would also contribute to the reduction in modulation depth. This hypothesis is in line with the experimental findings. If oligomerization is the reason for multiple distances observed at 0 kbar in the presence of 25% glycerol, then pressure may induce dissociation of these multimeric structures, leading to the disappearance of the larger distances  $> 3.3$  nm. The dissociation of protein subunits caused by pressure is a well-known effect and may thus not be a surprising observation in *E. coli* RNR.<sup>356-359</sup>

---

<sup>\*</sup> Spin A is  $Y_{122}\bullet$ , Spin B is the unknown radical species. No other spins are present in the sample.

## 6.4. Conclusion and outlook

This chapter demonstrated the power of high-pressure studies combined with EPR spectroscopy. Therefore, the stable tyrosyl radical, located in the  $\beta 2$ -subunit of *E. coli* ribonucleotide reductase, was investigated by pulse EPR in combination with high hydrostatic pressures up to 4 kbar. As RNRs have not been explored under pressure before, these studies deliver unique insights into protein stability under extreme conditions. By coupling high hydrostatic pressure to EPR investigations, the typically stable radical  $Y_{122}\bullet$  was shown to be quenched at 4 kbar. In contrast, the radical was observed to remain stable at 2 kbar, while surprisingly, an additional paramagnetic species could be monitored. This species is most probably not a distinct  $Y_{122}$  conformer and cannot be generated by radical transfer from  $Y_{122}$  to another residue. To the best of our knowledge, the generation of an additional radical species by pressure has not yet been reported in the literature and thus remains an unsolved mechanism. The identity of this species remains elusive, even though the experimental results suggest that a tyrosyl radical is responsible for it. Often, extensive experimental effort is connected to the procedure of identifying unknown radical signals. In EPR spectroscopy, multi-frequency investigations are a frequently used tool to specify  $g$ -tensors in an unknown system. However, this is not possible given the current state of the art. W-band sample tubes have a narrow diameter and are so fragile that they sometimes break upon sample loading. These sample tubes would not withstand the high pressure and would break, which we have already observed several times with 2.8 mm O.D. Q-band tubes. However, isotope labeling and site-directed mutagenesis would be potential tools for identifying possible radical candidates.<sup>293,360–362</sup>

Moreover, EPR distance measurements revealed a decrease in modulation depth upon applying 2 kbar pressure. This effect is most probably caused by dissociation of the dimeric subunits of the  $\beta 2$  protein, which delivers exciting insights into dimer stability under such extreme conditions. However, the active  $\alpha 2\beta 2$  complex assembly is required to identify reactive intermediates involved in the catalytic reaction, while pressure-induced dissociation would forbid its spectroscopic investigation.

In summary, this chapter demonstrates that the combination of EPR and pressure reveals unique findings that are important for gaining structural insights and therefore serves as an expansion to the established pool of biophysical tools. Some of the results may be challenging to explain, and furthermore, the effect of stabilizing agents such as glycerol on the system must be understood first. Interactions with the cosolvent, as in the case of RNR, complicate the data analysis tremendously. Therefore, it is essential to study the system under investigation with additional biophysical methods, as has been shown several times in the literature.<sup>363,364</sup>

# 7.

## Long-lived C<sub>60</sub> radical anion stabilized inside a molecular coordination cage

---

---

Parts of the results presented in this chapter are published in:

Hasegawa, S., Meichsner, S. L., Holstein, J. J., Baksi, A., Kasanmascheff, M., Clever, G. H. Long-Lived C<sub>60</sub> Radical Anion Stabilized Inside an Electron-Deficient Coordination Cage. *J. Am. Chem. Soc.* **143**(26), 9718 – 9723 (2021).<sup>365</sup>

### 7.1. Introduction

#### 7.1.1. Fullerenes and their functionalization

Fullerenes are cage-like hollow molecules consisting of a mesh of five- and six-membered rings of carbon atoms. They are denoted by their empirical formula C<sub>*n*</sub>, with *n* being the number of carbon atoms forming the cage. Buckminsterfullerene, a C<sub>60</sub> football-shaped molecule, is the namesake for this group of molecules and the family's most famous member. C<sub>60</sub> was first discovered in 1985 by Kroto *et al.*, and since then, this group of molecules has gained considerable attention over the last three decades, even though their existence was initially judged critically.<sup>366,367</sup> Finally, the Nobel Prize in Chemistry was awarded to Robert F. Curl, Sir Harold W. Kroto, and Richard E. Smalley in 1996 for their “discovery of fullerenes”.<sup>368–370</sup> Fullerenes, one of the most stable allotropes of carbon, are soluble in organic solvents such as carbon disulfide, toluene, o-dichlorobenzene, or chlorobenzene, whereas they are insoluble in water.<sup>371</sup> Due to their curved π-conjugated surfaces and their exceptional suitability as electron acceptors, they offer versatile applications such as molecular electronics, photovoltaics, and battery materials.<sup>372–375</sup> Also, fullerenes are an attractive candidate for medical application, such as an antioxidant for reactive oxygen species, whose applicability has so far been limited due to their water insolubility. Thus, water-soluble derivatives through functionalization have become a much-addressed problem.<sup>376</sup> These modifications can be either installed inside the cavity (endohedral) or attached to the outer surface

(exohedral). The standard notation for endohedral fullerenes is  $X@C_n$ , where  $X$  is the species located inside the cage.<sup>377</sup> In most published examples,  $X$  is a mono- or bimetallic metal center, which leads to altered reactivities and electrochemical properties. Moreover, unique synthetic routes can generate small-molecule fullerenes such as  $H_2O@C_{60}$  and  $H_2@C_{60}$ .<sup>378</sup> Numerous examples of exohedral functionalization of fullerenes can be found in the literature ranging from the attachment of small polar functional groups, such as amination, up to large synthetic constructs.

### 7.1.2. Encapsulated fullerenes

Another point limiting the applicability of fullerenes is tedious purification protocols, peculiar solubility, and limited control over regioselective derivatization, accompanied by time-expensive chromatographic separation methods. Therefore, many approaches from the field of supramolecular chemistry have been dedicated to constructing molecular fullerene receptors that should facilitate selective purification and derivatization.<sup>379–381</sup> Most of these host compounds must be synthesized in a complicated, time-consuming process, whereas self-assembling binders comprise much simpler building blocks.<sup>382,383</sup> Hence, metal-mediated rings and cages have moved into focus, remarkably adaptable depending on their modular construction. Recently, a metallo-supramolecular receptor has been presented based on the well-known  $[Pd_2L_4]^{4+}$  coordination cage motif.<sup>384,385</sup> This receptor is advantageous in three points compared to other receptors: it possesses a lower molecular weight than existing hosts, it is uncomplicated to synthesize and derivatize, and last but not least, capable of discriminating different fullerenes and dissolving them in a variety of organic solvents.<sup>386,387</sup>  $Pd^{II}$  cations in assembly with pyridyl terminated, phthalimide-based, bent ligands  $L$  tend to form a  $[Pd_2L_4]^{4+}$  coordination cage, highly selective for  $C_{60}$ . Moreover, the individual components of the receptor cage can be varied to allow binding of larger molecules such as  $C_{70}$ . Bowl-shaped structures were developed, which can also be dimerized to form pill-shaped cages, encapsulating two fullerenes simultaneously. The bowl-shaped structures may also serve as a supramolecular protection group, allowing selective monofunctionalization of its fullerene guest.<sup>387</sup> These metallo-supramolecular receptors allow the solubility of fullerenes in acetonitrile, acetone, nitromethane, and dimethylformamide. As some of these solvents are still toxic, solubility in alcohols or even water is a goal for future developments.

### 7.1.3. The fullerene radical anion

In organic devices, single-electron transfer from donors to C<sub>60</sub> generates the C<sub>60</sub><sup>•-</sup> radical anion. Moreover, this species can also be generated via photochemical reduction, whereas 1-Benzyl-1,4-dihydronicotinamide (BNAH) is the most suitable one-electron reductant as described by Fukuzumi *et al.*<sup>388</sup> C<sub>60</sub><sup>•-</sup> plays a vital role as a carrier for efficient charge harvesting and may be used as a near-infrared (NIR) dye, with potential applications in bioimaging and photodynamic therapy.<sup>389–391</sup> The C<sub>60</sub><sup>•-</sup> radical anion is generally short-lived, with a maximal lifetime of a few seconds.<sup>392,393</sup> For this range of applications and to enable the characterization of the radical species, it is of general interest to increase the lifetime of C<sub>60</sub><sup>•-</sup>. Previous studies of C<sub>60</sub> encapsulated in a cationic metallo-supramolecular cage [Pd<sub>2</sub>1<sub>4</sub>]<sup>4+</sup> (Figure 7.1) revealed a positive shift for the first reduction potential compared to bulk C<sub>60</sub>.<sup>386,387</sup> This observation could be indicative of C<sub>60</sub><sup>•-</sup> being stabilized within the coordination cage. The aim of this work is thus first to characterize the photochemically generated paramagnetic species via EPR and, in the following, to determine its lifetime.

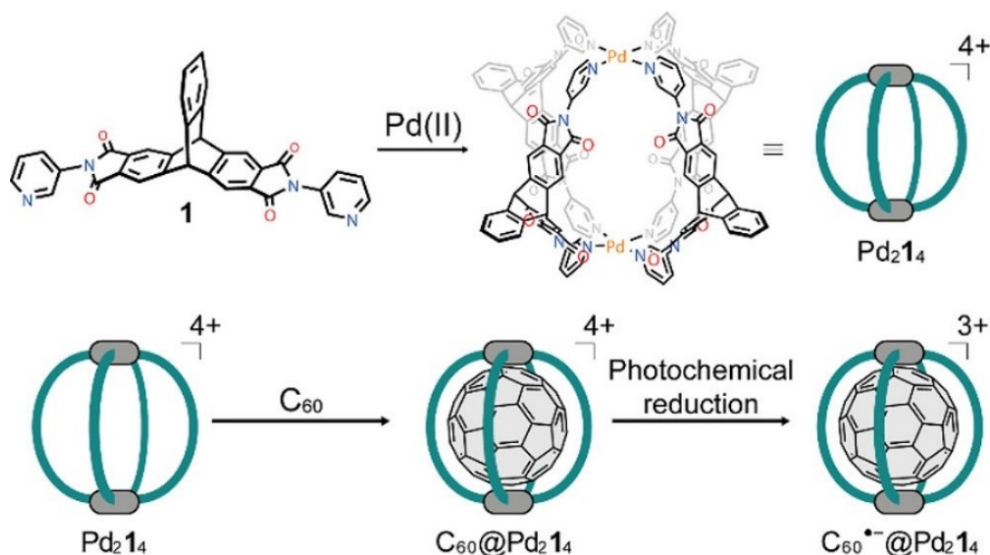


**Figure 7.1: Structures of Fullerene C<sub>60</sub> and the coordination cage.** Structures of ligand **1** and cage Pd<sub>2</sub>1<sub>4</sub> with a schematic depiction of fullerene binding, followed by photochemical single electron reduction. The figure is taken from Hasegawa *et al.*<sup>365</sup>

## 7.2. Materials and methods

Ligand synthesis, sample preparation, and verification of the cage assembly were done by Shota Hasegawa, a member of the Clever lab at TU Dortmund. Details of this part can be found in the supporting information of the respective publication.<sup>365</sup>

### 7.2.1. Sample preparation for EPR measurements

$C_{60}@Pd_{214}$  (0.70 mM, 0.60 mL, 0.42  $\mu$ mol) was prepared in acetonitrile. Afterward, an acetonitrile solution of 1-benzyl-1,4-dihydronicotinamide (BNAH) (20.0 mM, 10.5  $\mu$ L, 0.2  $\mu$ mol) was added in the dark, and the mixture was transferred to 2.8 mm O.D. EPR tubes. The solution was irradiated with a white LED light source for 2 min while slowly turning the sample to ensure irradiation from all sides. Subsequently, the sample was frozen in liquid nitrogen immediately to prevent quenching of the generated species, followed by EPR measurements. Samples were measured as fast as possible to prevent radical quenching during storage (< 24 h).

For samples produced in inert atmosphere, the samples were handled and transferred to 2.8 mm O.D. EPR sample tubes in a glove box filled with  $N_2$  gas. Irradiation was performed similarly to aerobic conditions. Furthermore, the samples were sealed and frozen inside the glove box to avoid oxygen contamination.

### 7.2.2. Details of the EPR experiments

**X-band:** X-band cw-EPR measurements were carried out at  $T = 100$  K using a Bruker EMX-Nano Benchtop spectrometer equipped with a continuous-flow nitrogen cryostat. If not stated otherwise, experimental conditions were: 1 G modulation amplitude, 100 kHz modulation frequency, 1.28 ms as time constant, 15.0 ms conversion time. Spectral simulations were performed with the EasySpin 'pepper' routine.

## 7.3. Results and discussion

### 7.3.1. Generation of the $C_{60}^{\bullet-}$ radical

To generate  $C_{60}^{\bullet-}$ , BNAH was used as a one-electron reductant.  $C_{60}$  itself acts as a photosensitizer to activate BNAH by an energy transfer from its excited triplet state, as depicted in **Figure 7.2**. One equivalent of BNAH is sufficient for the conversion of two  $C_{60}$ s.  $^1H$  NMR thereby revealed that  $C_{60}@Pd_{214}$  is stable in the presence of 0.5 eq. BNAH in darkness. Only irradiation of the mixture with a white LED light source for 2 min led to broadening of the  $C_{60}@Pd_{214}$   $^1H$  NMR signals, while BNAH entirely transformed to the corresponding oxidized species.  $^1H$  NMR signals appear broadened in the presence of radicals due to accelerated nuclear spin relaxation processes.<sup>394,395</sup>

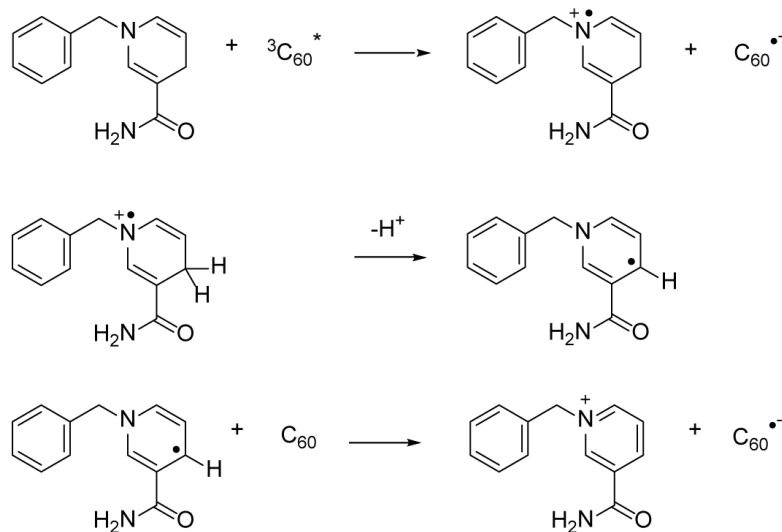


**Figure 7.2: The one-electron photoreduction of C<sub>60</sub> by BNAH.** The first step is a photoinduced electron transfer from BNAH to  ${}^3\text{C}_{60}^*$ , resulting in the first equivalent of  $\text{C}_{60}^{\bullet-}$ . In the second step, deprotonation of  $\text{BNAH}^{\bullet+}$  leads to  $\text{BNA}^{\bullet}$ .  $\text{BNA}^{\bullet}$  in the third step further reduces a second  $\text{C}_{60}$  to  $\text{C}_{60}^{\bullet-}$ . The reaction mechanism was reported by Fukuzumi *et al.*<sup>388</sup>

To ensure that the encapsulated  $\text{C}_{60}^{\bullet-}$  is the only radical species created, three control experiments were performed by using cw-EPR (**Figure 7.3**). The host-guest complex without BNAH was measured before and after irradiation. These samples did not result in any detectable EPR signals. This result demonstrates that BNAH is needed as a photoreductant to initiate radical formation. Similarly, irradiation of Pd<sub>2</sub>1<sub>4</sub> together with BNAH (but without C<sub>60</sub>) showed no EPR signal. Finally, the irradiated host-guest assembly  $\text{C}_{60}@\text{Pd}_21_4$  was the only sample that displayed a strong EPR signal. The only combination missing in these measurements is C<sub>60</sub> with BNAH without the coordination cage. However, this mixture is not soluble in the chosen solvent, which is acetonitrile. In conclusion, a combination of all three components (host, guest, and photoreductant) is required to generate a radical species. These findings are in accordance with <sup>1</sup>H NMR data of empty Pd<sub>2</sub>1<sub>4</sub>.<sup>365</sup>

Furthermore, these control experiments strongly suggest that the encapsulated C<sub>60</sub> is reduced rather than the cage, resulting in  $\text{C}_{60}^{\bullet-}$ . The  $\text{C}_{60}^{\bullet-}$  radical anion usually displays a characteristic absorption in the near-infrared region.<sup>396–398</sup> UV-Vis-NIR spectra of the encapsulated C<sub>60</sub> showed absorption at 546 and 599 nm before reduction, whereas new absorption bands at 975 and 1111 nm were observed after the reduction.<sup>365</sup> These observed spectral characteristics highly agree with  $\text{C}_{60}^{\bullet-}$  absorption spectra presented earlier.<sup>396–398</sup>

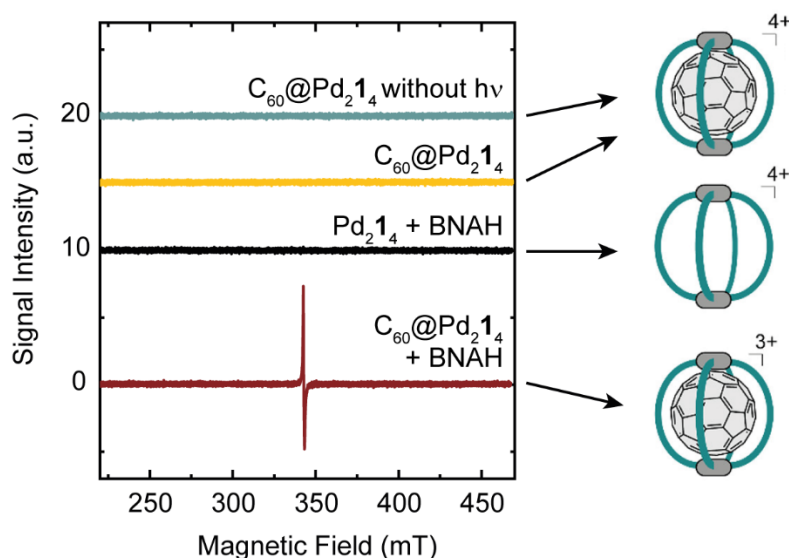


**Figure 7.3: Cw-EPR control experiments of different compounds performed at X-band under aerobic conditions.** First, the host-guest complex without BNAH was measured before (blue) and after (yellow) irradiation. Measurements after irradiation of the empty cage in combination with BNAH are displayed in black. Only the complete assembly of  $C_{60}@Pd_21_4$  in acetonitrile (0.35 mM, 0.50 mL, 0.17  $\mu$ mol) in the presence of BNAH (10 mM, 8.8  $\mu$ L, 0.08  $\mu$ mol) after irradiation (red) revealed an EPR spectrum. Spectra were shifted horizontally for better visualization. All spectra were recorded at 0.32 mW power, 1 scan each.

$^1H$  NMR and UV-Vis-NIR spectra already suggest  $C_{60}\bullet^-$  as being the generated radical species. However, the method of choice for identifying and characterizing paramagnetic species is EPR.

Previous reports showcased that  $C_{60}\bullet^-$  is sensitive to oxygen, forming EPR active side products.<sup>399,400</sup> Hence, samples were produced in either inert atmosphere (**Figure 7.4A**) or under aerobic conditions (**Figure 7.4B**) to exclude contaminating paramagnetic species in the sample. Whereas for samples prepared in  $N_2$  atmosphere, a single cw-EPR signal with a peak-to-peak linewidth of approximately 0.6 mT is observed, two overlapping signals are detected for the samples produced under aerobic conditions. The spectral lineshape could be reproduced by simulation of two different species with  $S = 1/2$ , colored in yellow and blue (**Figure 7.4**). A yellow-to-blue ratio of approximately 1 resulted in the complete simulation of  $C_{60}\bullet^-@Pd_21_4$  prepared under aerobic conditions. The spectrum obtained for  $C_{60}\bullet^-@Pd_21_4$  prepared under  $N_2$  atmosphere could be entirely reproduced using only the blue species. The species displayed in yellow with  $g_{iso} = 2.001$  has a much narrower linewidth than the one marked in blue, which possesses a  $g_{iso}$  of 1.999. The Lorentzian broadened linewidth (0.3 and 1.1 mT) is given by the full width at half maximum (FWHM).

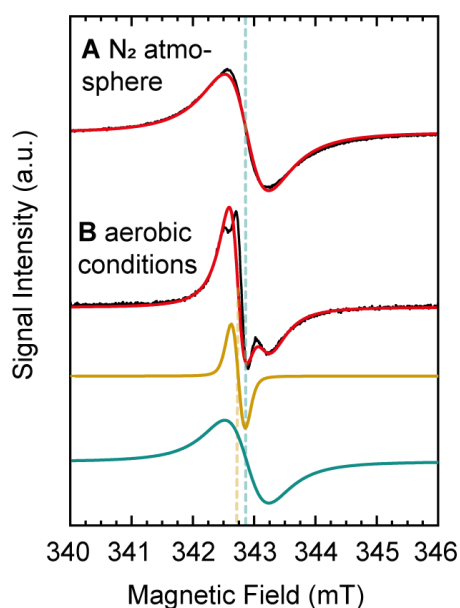


**Figure 7.4: X-band EPR analysis of generated radicals.** X-band cw-EPR spectra of C<sub>60</sub>•<sup>-</sup> @Pd<sub>214</sub> in acetonitrile (0.35 mM) prepared under N<sub>2</sub> atmosphere (A) and aerobic conditions (B) along with their corresponding simulations (red). Spectra were simulated by using two different species (yellow and blue). Simulation parameters: yellow:  $g_{\text{iso}} = 2.001$ ,  $lw = 0.3$  mT, blue:  $g_{\text{iso}} = 1.999$ ,  $lw = 1.1$  mT. Dotted lines indicate the positions of the  $g_{\text{iso}}$  values of the respective species. Spectra and simulations were shifted horizontally for better visualization. Spectra were recorded at 0.79 mW with 20 scans each.

The only possible hyperfine couplings in C<sub>60</sub>•<sup>-</sup> could be due to an interaction of the unpaired electron spin with the <sup>13</sup>C isotope with only 1.1% abundance. These interactions are not resolved under the experimental conditions; thus, the  $g$ -tensor is the decisive parameter.<sup>401</sup> The signal with an isotropic  $g$ -value of 1.999 detected in both samples can undoubtedly be assigned to C<sub>60</sub>•<sup>-</sup>.<sup>392,402,403</sup> In general, reduction of the C<sub>60</sub> molecule diminishes the  $g$ -value relative to  $g_e$ . It is known that the  $g$ -value is sensitive to bond deformation (bending) as well as to delocalization of the unpaired spin.<sup>404</sup> Bending of the double bond leads to an increase in the  $\sigma$ -character of the bond, resulting in a decrease of the  $g$ -value relative to  $g_e$ .<sup>405</sup> Delocalization of the unpaired spin from the carbon atom to neighboring atoms, on the other hand, leads to increasing  $g$ -values. Due to bond deformation on the C<sub>60</sub> skeleton, the  $g$ -value for C<sub>60</sub>•<sup>-</sup> is shifted towards lower values with respect to  $g_e$ .

As mentioned, an additional signal with  $g_{\text{iso}} = 2.001$  is observed in the sample prepared under aerobic conditions. Such an additional signal in fullerene samples has been observed in several cases, yet, most theories failed to explain its origin.<sup>406</sup> Lately, it has been shown that this signal originates from an oxygenated fullerene species. The here detected  $g$ -value and spectral linewidth match the reported values for the oxygen-bridged fullerene dimer C<sub>120</sub>O<sup>-</sup> ( $g_{\text{iso}} = 2.0013$ , peak-to-peak linewidth 0.1 mT).<sup>399,407</sup> The

presence of such an oxygenated species is also confirmed by electrospray ionization mass spectrometry analysis.<sup>365</sup>

### 7.3.2. Saturation behavior of the radical signals

The intensity of a cw-EPR spectrum depends on the properties of the spin system under investigation. The first parameter that determines the spectral intensity is the Boltzmann population. Furthermore, relaxation processes essentially determine the microwave power dependence of the signal intensity. These parameters determine the steady-state population difference between the two resonant spin states. If the microwave power is too high or the spin-lattice relaxation is too slow, the spin system will saturate, and the observed signal becomes weaker. The power dependence of the peak-to-peak amplitude of a first-derivative cw-EPR signal  $I$  is determined by

$$I \propto \frac{\sqrt{P}}{\left(1 + \frac{P}{P_{\frac{1}{2}}}\right)^{\frac{b}{2}}} \quad (7.1)$$

with the microwave power  $P$ .<sup>116</sup>  $P_{\frac{1}{2}}$  is the power at which the saturation factor  $s$ , introduced in equation 2.36, equals 1/2.

$$s = \frac{1}{1 + \gamma_e^2 B_1^2 T_1 T_2} \quad (2.36)$$

Furthermore,  $b$  is defined by the lineshape and may vary between 3 for homogeneously broadening and 1 for inhomogeneously broadened lines. When the rate of the microwave-induced transitions is much less than the relaxation rate, meaning at low power levels, the signal intensity reveals a linear dependence on  $\sqrt{P}$  and an undistorted lineshape is recorded. When saturation becomes significant, the signal intensity increases less than linearly with  $\sqrt{P}$  until finally, the signal amplitude even may decrease.<sup>115</sup> According to these correlations, the saturation curve contains information on the product of longitudinal and transverse relaxation times  $T_1 T_2$ .

Power saturation curves of  $C_{60}\bullet^-$  and the oxygenated species were recorded to characterize the obtained signals. Therefore, the power-dependent spectra were simulated by EasySpin first, followed by reading out the peak-to-peak amplitude of each species (**Figure 7.5**). Microwave powers higher than 0.8 mW led to saturation of the oxygenated species, whereas  $C_{60}\bullet^-$  was not saturated in the observed range. These results clearly demonstrate the distinct relaxation properties of  $C_{60}\bullet^-$  and the oxygenated species.

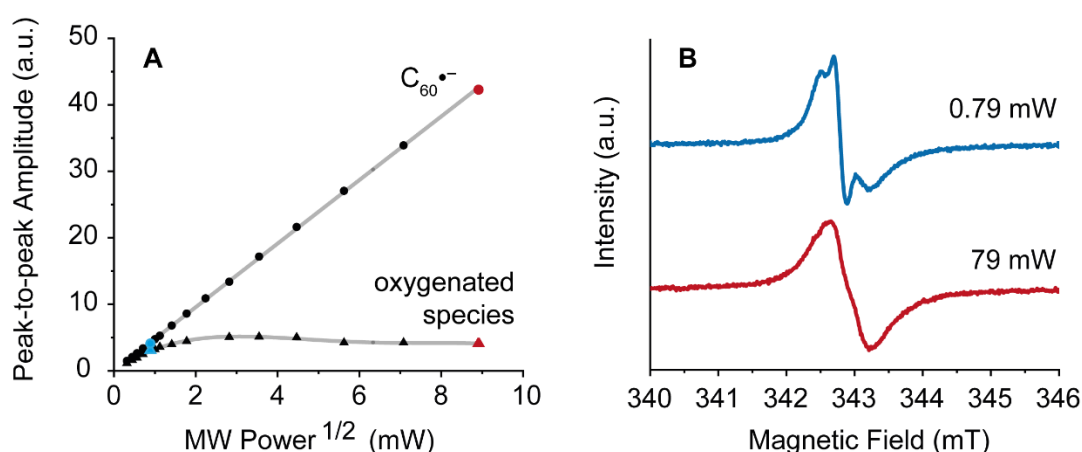


**Figure 7.5: Power saturation behavior of generated radicals.** (A) Cw power saturation curves for C<sub>60</sub>•<sup>-</sup>@Pd<sub>2</sub>14 in acetonitrile (0.35 μM) and its oxygenated species. (B) Cw-EPR spectra recorded at different microwave power levels. Experiments that were shown in **Figure 7.4** were recorded at 0.79 mW power (blue point in A), which is the ideal power for detecting both species. The same spectrum is shown in blue in (B). The red spectrum shown in (B) was acquired with 79 mW power (shown as a red data point in A) and shows the encapsulated C<sub>60</sub>•<sup>-</sup> only. Spectra depicted in (B) are scaled to maximum intensity.

Another factor influenced by the applied microwave power is the width of the EPR line. At low power, where  $I$  is proportional to  $\sqrt{P}$ , the linewidth is essentially determined by  $T_2$  and is unaffected by the microwave power. A homogeneously broadened absorption line is Lorentzian with a FWHM of  $1/\pi T_2$ .<sup>115</sup> Upon saturation, the spectral width is broadened. As the oxygenated species is almost invisible at high power levels, its power-dependent linewidth can not be determined. However, when comparing widths of C<sub>60</sub>•<sup>-</sup>'s EPR spectra at 0.79 mW and 79 mW, no change is notable, showing that saturation is not reached in the observed power range.

### 7.3.3. Half-lifetime determination of C<sub>60</sub>•<sup>-</sup>

The observation of different relaxation properties of C<sub>60</sub>•<sup>-</sup> and the oxygenated species allowed separation of the respective EPR signals, and thus in the next step, to determine the half-lifetime of C<sub>60</sub>•<sup>-</sup> by tracing the decay of the peak-to-peak amplitude of the EPR signals. Therefore, cw X-band spectra were recorded at different time points after radical generation for samples prepared under N<sub>2</sub> atmosphere and under aerobic conditions. Spectra were assimilated at 0.79 mW (which are depicted in **Figure 7.6**) and 79 mW power each. Furthermore, time-dependent UV-Vis-NIR data were collected as a second controlling experiment performed by Shota Hasegawa. As described, C<sub>60</sub>•<sup>-</sup> displays strong absorption bands at 975 and 1111 nm. The half-lifetime of C<sub>60</sub>•<sup>-</sup> can thus be estimated by following the decline of the 1111 nm absorption at 295 K.

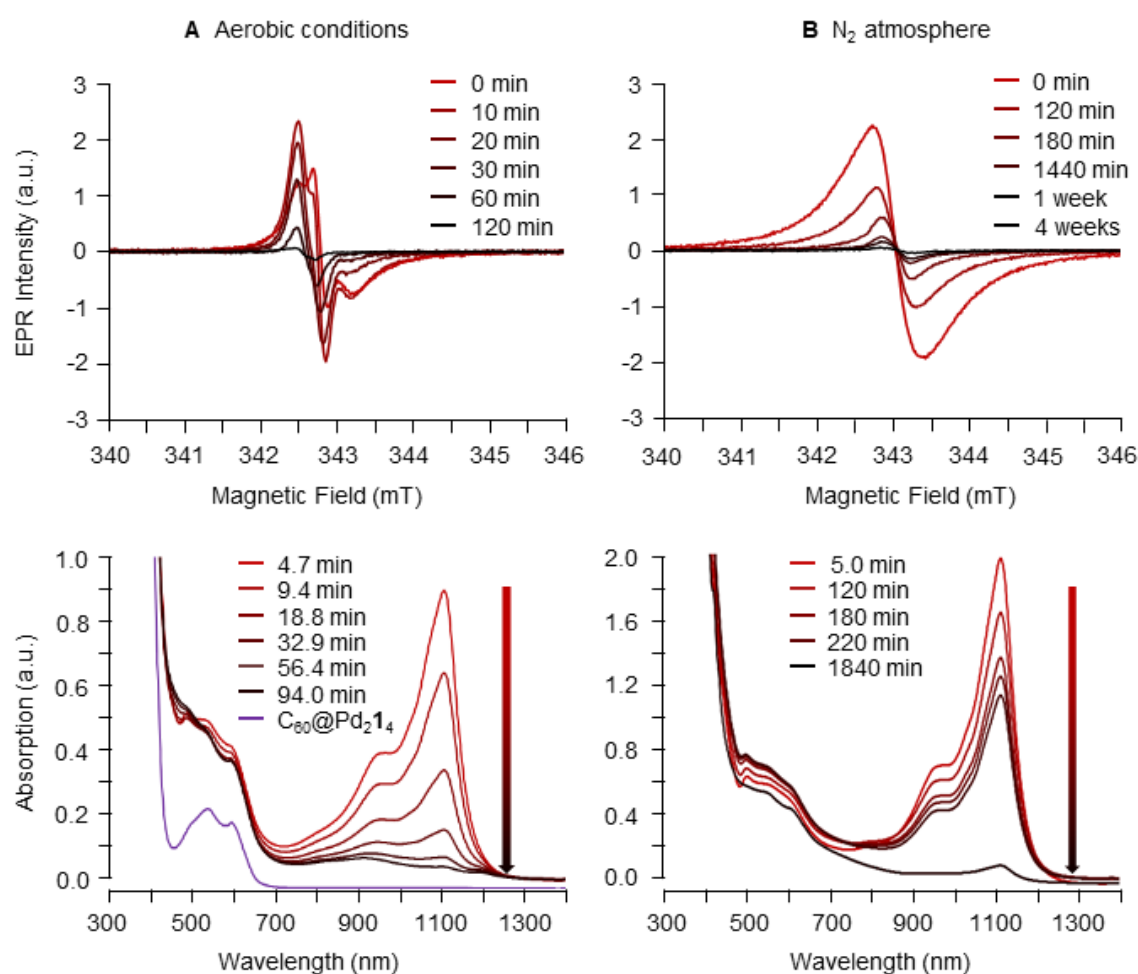


**Figure 7.6: Half-lifetime determination of  $C_{60}\bullet^-$ .** Time-dependent cw-EPR (top) and UV-Vis-NIR spectra (bottom) of  $C_{60}\bullet^-@Pd_{214}$  in acetonitrile (0.35 mM) prepared under (A) aerobic conditions and (B) under  $N_2$  atmosphere. Microwave power: 0.79 mW.

First, the focus is placed on samples prepared under aerobic conditions. Spectra were recorded in 10 min intervals for the first hour, followed by measurements once an hour. After two hours, no EPR signal is observed anymore. EPR spectra recorded at 0.79 mW display changes in the relative weights between  $C_{60}\bullet^-$  and the oxygenated species. All spectra were simulated with the parameters given in **Figure 7.4** with varying weight percentages of the two species (**Figure 7.7**). Consequently, the oxygenated species exhibit a longer lifetime than pure  $C_{60}\bullet^-$  so that after approximately 40 min, only the oxygenated species is detected.

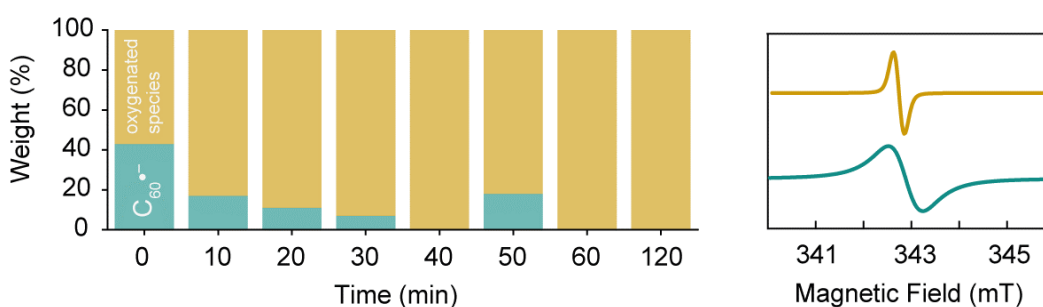


**Figure 7.7:** Relative weight of C<sub>60</sub>•<sup>-</sup> (blue) and its oxygenated species (yellow) in samples produced under aerobic conditions as determined by spectral simulations. For simulation parameters see Figure 7.4.

In the next step, the lifetime of C<sub>60</sub>•<sup>-</sup> is determined by plotting the peak-to-peak amplitude of the cw-EPR spectra acquired at 79 mW (Figure 7.8). Datapoints were fitted by utilizing an exponential decay function based on earlier reports.<sup>408</sup> The half-lifetime of encapsulated C<sub>60</sub>•<sup>-</sup> under aerobic conditions was estimated to be 14 min, in complete agreement with the value obtained by UV-Vis-NIR spectroscopy under the same conditions (13 min).

For C<sub>60</sub> encapsulated under anaerobic conditions, duplicates from two different sample preparations were measured. Here, their mean values are plotted together with their standard deviation. Surprisingly, an EPR signal of the encapsulated C<sub>60</sub>•<sup>-</sup> could still be observed even after one month (Figure 7.8). Spin quantification reveals an initial spin concentration of  $106 \pm 10 \mu\text{M}$  (mean value of duplicates with standard deviation) and approx.  $0.1 \pm 0.1 \mu\text{M}$  after 4 weeks. These values were obtained by comparing the double integral of the cw EPR spectra to a 1 mM CuSO<sub>4</sub> standard, using 1 mW power at 100 K under nonsaturating conditions. A value of  $< 1 \mu\text{M}$  radical concentration is close to the detection limit of the EMX-Nano X-band spectrometer, and hence the error is high due to the low S/N ratio. The exponential fit of the data points delivers a lifetime of 893 min (corresponding to ca. 15 h). However, when calculating the remaining spins  $N(t)$  after time  $t$  in dependence on the initial spin concentration  $N_0$  with the half-lifetime  $t_{1/2}$  and an exponential decay according to:

$$N(t) = N_0 2^{-\frac{t}{t_{1/2}}} \quad (7.2)$$

the sample would have a spin concentration of  $0.04 \mu\text{M}$  after one week and  $3 \cdot 10^{-9} \text{ nM}$  after 4 weeks, far below the EPR detection limit in the low micromolar range. This tremendous deviation of the experimental data from theoretical values might be caused by the experimental conditions. Presumably, this process is explained by radical scavengers co-existing in the same system, further oxidizing C<sub>60</sub>•<sup>-</sup>. This will lead to a faster decay within the first hours. As the total amount of radical scavengers decreases

over time, the decay rate also decreases. If the half-lifetime is determined within the initial decay period between 0 and 48 h (**Figure 7.8** inset), the fit resulted in a value of 785 min (ca. 13 h). Fitting only the decay between 24 h to 4 weeks leads to very long half-lifetimes  $> 67$  h, in agreement with biphasic decay. The encapsulated  $C_{60}\bullet^-$  radical anion under anaerobic conditions shows a significantly longer half-lifetime than the one generated under aerobic conditions. These results impressively demonstrate that protection from air further increases the lifetime of  $C_{60}\bullet^-$ . Such a half-lifetime of several hours is the longest lifetime reported to date for a  $C_{60}\bullet^-$  radical anion in all conscience.

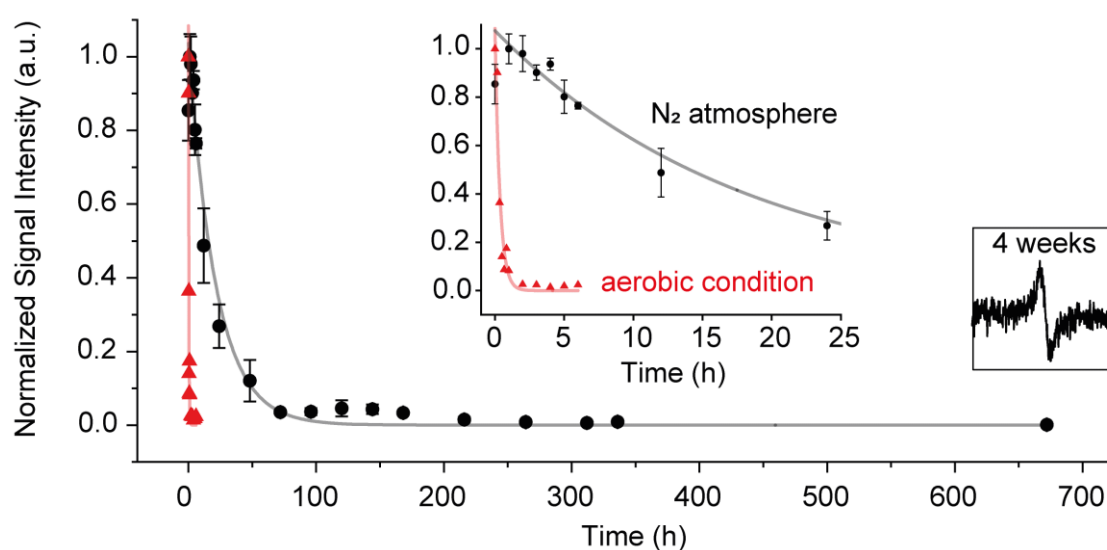


**Figure 7.8: Half-lifetimes of  $C_{60}\bullet^-$  under different conditions.** The time-dependent EPR spectra of  $C_{60}\bullet^-@Pd_{214}$  prepared under aerobic conditions and in  $N_2$  atmosphere are used to calculate the half-lifetime of the encapsulated  $C_{60}\bullet^-$  radical anion (aerobic: 14 min, anaerobic: 893 min). The data were normalized by dividing double integral values of each spectrum by the maximum obtained value. Inset: magnification of the first 24 h of data acquisition. Data were recorded at 79.43 mW power, 20 to 100 scans each.

Astonishingly, UV-Vis-NIR measurements provided a half-lifetime of around 300 min for encapsulated  $C_{60}\bullet^-$  under  $N_2$  atmosphere, shorter than the value determined by EPR. This difference can most likely be attributed to the different sample preparation conditions: In both cases, samples were prepared similarly in the glovebox. Then, UV-Vis-NIR measurements were performed in a plugged cuvette outside the glovebox while keeping the sample at room temperature. It cannot be ruled out that the ambient air contaminates the sample during the measurement time, leading to a shortened lifetime. Such impurities are, in contrast, unlikely in the EPR measurements. The sample tubes remained in the glovebox, and aliquots were taken at respective time points. The samples were removed from the glovebox sealed, and immediately snap frozen in liquid nitrogen.

#### 7.4. Conclusion and outlook

The experiments presented in this chapter deliver proof of an exceptional long-lived C<sub>60</sub><sup>•-</sup> radical anion encapsulated in a lantern-shaped coordination cage. The radical form was generated by photochemical activation of C<sub>60</sub> by BNAH. The electron-deficient cage Pd<sub>2</sub>1<sub>4</sub> tightly binds the anionic guest and serves as a protecting group to shield the radical species. This is most likely achieved by kinetically hindering the access of oxidants. Protection of the fullerene, leading to prolonged lifetimes, has been verified using a [10]cycloparaphenylene nanobelt encircling C<sub>59</sub>N<sup>•</sup>. The highly reactive radical can be shielded, resulting in a half-lifetime of 100 min in degassed 1-chloronaphthalene.<sup>409</sup> However, the half-life determined for our system far exceeds any previously reported lifetimes. These findings represent a decisive step toward the application of C<sub>60</sub><sup>•-</sup> for various chemical, spectroscopic, and imaging purposes. For example, this well-functioning spin system might be attractive for materials science applications.

The system presented here could also be advantageous as a spin label in EPR spectroscopy. An example of a fullerene-based spin label application has been presented earlier.<sup>410,411</sup> However, these techniques employ the EPR active triplet state of fullerenes, requiring a spectrometer-connected laser setup, which is not accessible to every laboratory. Once the coordination cage is soluble in water, it might easily be attached to proteins or other biomolecules. The encapsulated C<sub>60</sub><sup>•-</sup> radical is stable and, more importantly, detectable at room temperature. Its narrow linewidth might offer high S/N ratios in pulsed dipolar distance determination. However, one problem could be relaxation times. Since no power saturation was observed for C<sub>60</sub><sup>•-</sup>, its relaxation time might be relatively short, which is non-ideal for some types of dipolar distance measurements.<sup>126</sup> Besides, the label might be quite space-consuming. Nevertheless, this type of molecule offers versatile applications, not only in EPR spectroscopy.

# 8.

## Materials and methods

---

### 8.1. Materials

#### 8.1.1. Hosts and vectors

All bacterial strains used in this work are non-enteropathogenic *Escherichia coli* B or K-12 isolates, donated by Prof. Dr. D. Summerer and coworkers (**Table 8.1**). Genetic material (**Table 8.2**) transformed into the recipient hosts agreed with biosafety level 1 regulations.

**Table 8.1: Bacterial strains used in this work.**

Strain	Genotype, Origin, and Notes
BL21-Gold(DE3)	F <sup>-</sup> <i>hsdS<sub>B</sub></i> (r <sup>-</sup> BM <sup>-</sup> B) <i>gal dcm<sup>+</sup> endA1 ompT λ(DE3) Tet<sup>r</sup> Hte</i> Agilent Technologies (Waldbronn, Germany), cat. no. 230132. B isolate engineered for high transformation efficiency and high protein yields with T7 RNA polymerase.
DH10B (TOP10 <sup>TM</sup> )	F <sup>-</sup> <i>mcrA Δ(mrr-hsdRMS-mcrBC) φ80lacZΔM15 Δ(lac)X74 recA1 endA1 araD139 Δ(araA-leu)7697 galU galK rpsL(Str<sup>r</sup>) nupG</i> Invitrogen <sup>TM</sup> Thermo Fisher Scientific (Schwerte, Germany), cat. no. C404003. K-12 isolate for uptake of large plasmids as deoxyribose is constantly synthesized.

**Table 8.2: Plasmids used in this work.** Km: kanamycin, Amp: ampicillin, Cm: chloramphenicol. Carbenicillin was used as an ampicillin substitute during protein expression.

Name	Purpose	Marker	Provided by
pET24- <i>nrdA</i>	Expression of <i>E. coli</i> class Ia RNR $\alpha$ 2	Km <sup>r</sup>	J. Stubbe
pTB- <i>nrdB</i>	Expression of <i>E. coli</i> class Ia RNR $\beta$ 2	Amp <sup>r</sup>	J. Stubbe
pBAD- <i>nrdB</i> <sub>122TAG</sub>	Expression of <i>E. coli</i> class Ia RNR Y <sub>122X</sub> - $\beta$ 2	Amp <sup>r</sup>	J. Stubbe
pEVOL-F <sub>n</sub> YRS-E3	tRNA/aaRS pair for incorporation of F <sub>n</sub> Y	Cm <sup>r</sup>	J. Stubbe
pEVOL-pCNPhe	tRNA/aaRS pair for incorporation of azF	Cm <sup>r</sup>	D. Summerer
pTZTPL	Expression of TPL	Amp <sup>r</sup>	J. Stubbe

### 8.1.2. Instruments

**Table 8.3: Laboratory equipment in alphabetical order.**

Instrument	Model	Company
Balance	PM400	Mettler-Toledo
Balance, analytical	ABJ-NM	Kern
Bunsen burner	1040/1	Carl Friedrich Usbeck KG
Centrifuge, benchtop with cooling	5804R	Eppendorf
Centrifuge, benchtop with cooling	5430R	Eppendorf
Chromatography column	XK 16/40	Cytiva
Chromatography refrigerator	TC 601-E	tritec
Chromatography system	ÄKTA go	Cytiva
Electrophoresis system	Rotiphorese® PROclamp MINI with Roth power supply STANDARD	Carl Roth
Electroporator	Eporator®	Eppendorf
Heating block	AccuTherm I-4001-HCS-230V	Labnet
Incubator	INE 600	Memmert GmbH
Incubator shaker	New Brunswick™ I26	Eppendorf

Lamp	LSB610U 100 W	LOT-QuantumDesign
Micropipette	Research plus	Eppendorf
Microwave oven	Tecnolux ED 8525 exquisit	Verbeken & Fils
pH electrode	LE420	Mettler-Toledo
pH meter	FiveEasy Plus FP20	Mettler-Toledo
Photometer	BioPhotometer® plus	Eppendorf
Q-band EPR	Elexsys E580	Bruker
Resonator	ER 5106QT-2	Bruker
Resonator	EN 5107D2	Bruker
Rocker	Enduro MiniMix™	Labnet
Size exclusion column	Superdex™ 75 Increase 10/300 GL	Cytiva
Size exclusion column	Superdex™ 200 Increase 10/300 GL	Cytiva
Size exclusion column	HiPrep™ 26/60 Sephacryl® S-200 HR	Cytiva
Spectrometer, UV-Vis	NanoDrop™ 2000	Thermo Fisher
Spectrometer, UV-Vis	V-650	Jasco
Thermocycler	T-Personal	Biometra
Ultracentrifuge	Sorvall™ LYNX™ 6000	Thermo Fisher
Vortex mixer	Vortex-Genie 2	Scientific Industries
X-band EPR	EMX-Nano	Bruker

### 8.1.3. Buffers, reagents, and kits

Table 8.4: Commercial kits and ready-to-use mixtures in alphabetical order.

Product (Brand)	Company
Kit for molecular weights 12 000 – 200 000	Sigma-Aldrich
LB-agar (Lennox)	Carl Roth
LB-broth (Lennox)	Carl Roth
NucleoSpin® Plasmid EasyPure	Macherey-Nagel
Q-PAGE 10% TGN Midi	Carl Roth
Roti® Blue quick	Carl Roth
Roti® Mark Tricolor	Carl Roth
Rotiphorese® 10x SDS-PAGE buffer	Carl Roth

Table 8.5: Chemicals and CAS registry numbers.

Compound	CAS No.	Company
Acetic acid	64-19-7	Carl Roth
Adenosine 5'-triphosphate disodium salt (ATP)	34369-07-8	Sigma-Aldrich
Agarose LE, molecular biology grade	9012-36-6	Biozym Scientific
Ammonia 32%	7664-41-7	VWR Chemicals
Ammonium acetate	631-61-8	Sigma-Aldrich
Ammonium carbonate	8000-73-5	Sigma-Aldrich
Ammonium hydroxide	1336-21-6	VWR Chemicals
Ammonium sulfate	7783-20-2	Sigma-Aldrich
Ammonium iron(II) sulfate hexahydrate	7783-85-9	Sigma-Aldrich
2'-Azido-2'-deoxycytidine-5'-triphosphate (N <sub>3</sub> -dCTP)	62192-83-0	tebu-bio
4-Azido-L-phenylalanine (AzF)	33173-53-4	Sigma Aldrich
L(+)-arabinose	5328-37-0	Carl Roth
1-Butanol	71-36-3	Fisher Scientific
Calcium chloride dihydrate	10035-04-8	Carl Roth
Carbenicillin, disodium salt	4800-94-6	Carl Roth
Chloramphenicol	56-75-7	Carl Roth
Cytidine-5'-diphosphate trisodium salt (CDP)	34393-59-4	Alfa Aesar
1,4-dithiothreitol (DTT)	3483-12-3	Carl Roth
Ethanol, absolute, p.a.	64-17-5	Merck
Ethyl-acetate	141-78-6	Fisher Scientific
Ethylenediaminetetraacetate (EDTA)	6381-92-6	Sigma-Aldrich
2,6-Difluorophenol	28177-48-2	Thermo Scientific
2,3,6-Trifluorophenol	113798-74-6	Thermo Scientific
Glycerol	56-81-5	Alfa Aesar
Hydrochloric acid 37%	7647-01-0	Chemsolute®
Imidazole	288-32-4	Abcr
4-Iodo-L-phenylalanine	24250-85-9	Abcr
Isopropanol	67-63-0	Fisher Scientific
Isopropyl-β-D-thiogalactopyranosid (IPTG)	367-93-1	Carl Roth
Magnesium acetate tetrahydrate	16674-78-5	Alfa Aesar
Magnesium chloride	7791-18-6	Sigma-Aldrich

## Materials

Manganese(II) chloride tetrahydrate	13446-34-9	Sigma-Aldrich
$\beta$ -Mercaptoethanol	60-24-2	Merck
$\beta$ -Nicotinamide-adenine dinucleotide phosphate tetrasodium salt, reduced (NADPH)	2646-71-1	Carl Roth
Ninhydrin	485-47-2	Merck
1,10-Phenanthroline	66-71-9	Sigma-Aldrich
Phenylmethsulfonyl fluoride (PMSF)	329-98-6	Carl Roth
Pyridoxal 5-phosphate hydrate	853645-22-4	Sigma-Aldrich
Pyruvic acid	127-17-3	Sigma-Aldrich
Potassium tetraborate tetrahydrate	12045-78-2	Sigma-Aldrich
Sodium chloride	7647-14-5	Merck
Sodium hydroxide	1310-73-2	Chemsolute®
Sodium pyruvate	113-24-6	Sigma-Aldrich
Streptomycin sulfate	3810-74-0	VWR Chemicals
Thymidine 5'-triphosphate sodium salt (TTP)	18423-43-3	Sigma-Aldrich
2-amino-2-(hydroxymethyl)propane-1,3-diol (Tris, Trizma base), buffer grade	77-86-1	Sigma-Aldrich
L-Tryptophan	73-22-3	Sigma-Aldrich
L-Tyrosine	60-18-4	Sigma-Aldrich

---

**8.1.4. Software and online tools**

Table 8.6: Software utilized in this work.

<b>Software</b>	<b>Publisher</b>
Adobe Illustrator	Adobe Inc. (2020). <i>Adobe Illustrator</i> . Retrieved from <a href="https://adobe.com/products/illustrator">https://adobe.com/products/illustrator</a>
Citavi	Version 6.12, Swiss Academic Software GmbH
ClusPro	Vajda Lab and ABC Group, Boston University and Stony Brook University
DeerAnalysis2019	G. Jeschke <i>et al.</i> <sup>235</sup>
EasySpin	S. Stoll <i>et al.</i> <sup>412</sup>
GelAnalyzer 19.1	( <a href="http://www.gelanalyzer.com">www.gelanalyzer.com</a> ) by Istvan Lazar Jr., PhD and Istvan Lazar Sr., PhD, CSc
Matlab R2017b	MATLAB. (2017). <i>version 9.3.0 (R2017b)</i> . Natick, Massachusetts: The MathWorks Inc.
MS-Office 2016	Microsoft Corporation. (2018). <i>Microsoft Word</i> . Retrieved from <a href="https://products.office.com/word">https://products.office.com/word</a>
OriginPro 2022	Origin(Pro), Version 2022. OriginLab Corporation, Northampton, MA, USA.
PeldorFit 2019	D. Abdullin <i>et al.</i> <sup>413</sup>
PyMOL	The PyMOL Molecular Graphics System, Version 2.2.3 Schrödinger, LLC.
Xepr	Bruker Corporation, Billerica, MA, USA.

## 8.2. Methods

### 8.2.1. Transformation of competent *E. coli* cells

Transformation of plasmids into competent bacterial cells was done via electroporation. Therefore, 0.1 – 10 ng plasmid was added to 25  $\mu$ L aliquot of competent cells. The suspension was transferred to a pre-chilled electroporation cuvette, followed by electroporation at 1.8 kV for 4.1 – 4.4 ms. The cell suspension was immediately recovered with 500  $\mu$ L prewarmed S.O.C. medium with subsequent incubation at 37 °C at 800 rpm for ca. 1 h. Finally, 25  $\mu$ L of bacterial culture was spread onto antibiotic-containing agar plates.

### 8.2.2. Plasmid isolation from bacterial strains

Plasmids were isolated via a silica column purification provided by the commercially available plasmid purification kit NucleoSpin® Plasmid EasyPure according to the manufacturer's instructions.

### 8.2.3. Expression and purification of *E. coli* class Ia RNR (His)<sub>6</sub>- $\alpha$ 2

Expression and purification was performed as previously described.<sup>51</sup> If not stated otherwise, 50 mM Tris buffer containing 5% glycerol and 2 mM DTT at pH 7.6 was used for all purification steps, shortly termed Tris in the following.

*E. coli* BL21(DE3)-Gold were transformed with pET28a-*nrdA* and plated on LB-agar plates with 50  $\mu$ g/mL kanamycin (Km) at 37 °C. Positive clones were selected and a starter culture (5 mL) was grown overnight in LB-medium enriched with Km at 37 °C until saturation. An intermediate culture (100 mL) was enriched with 1 mL of the starter culture, also grown overnight. The expression culture was grown with a 200-fold dilution of the intermediate culture in LB-medium containing Km. At OD<sub>600</sub> ~0.6, protein expression was induced with 0.5 mM IPTG. After 5 h of protein overproduction, the cells were harvested by centrifugation at 17 000  $\times$ g for 15 min and 4 °C. A typical 1 – 2 g cell paste/L media was obtained, in agreement with previously reported yields.<sup>51</sup>

The cell pellet was resuspended in 3.5 – 5 mL/g cell pellet Tris buffer, supplemented with 1 mM PMSF. Next, the suspension was lysed via four passages through a French pressure cell press. Insoluble debris was removed at 3200  $\times$ g for 30 min at 4 °C. DNA was precipitated by adding 0.2 vol eq. of a 6% (w/v) streptomycin solution dropwise, followed by centrifugation at 3200  $\times$ g for 30 min at 4 °C. The clear supernatant was loaded onto a pre-equilibrated Ni-NTA column (Ni-Sepharose™ High Performance, GE Healthcare). Tris buffer containing 20 mM imidazole and 200 mM NaCl was used for equilibration. After loading the protein solution, the column was first washed with the same buffer, and finally, the protein was eluted by raising the imidazole concentration to 250 mM. Afterward, the protein was precipitated by 60% saturation with (NH<sub>4</sub>)<sub>2</sub>SO<sub>4</sub>

(39 g/100 mL). The salt was slowly added for over 10 minutes and stirred for an additional 15 minutes on ice. Then, the protein was isolated at 3200 xg for 30 min at 4 °C and resolubilized in a minimal amount of Tris buffer. Desalting was performed using a PD-10 column (Sephadex® G-25 Medium, Cytiva), preequilibrated with Tris buffer. The purified protein was concentrated in an Amicon® centrifugal filter unit with 30 kDa cutoff (Millipore), and the concentration was screened via UV-Vis with  $\epsilon(280 \text{ nm}) = 189\,000 \text{ M}^{-1} \text{ cm}^{-1}$ . Aliquots were flash frozen in liquid nitrogen and stored at -80 °C. A typical yield of 2 – 4 mg protein/g cell paste was obtained, lower than in previous reports.<sup>292,414</sup> However, as the alpha subunit was rarely used in this study, no further attempts were made to optimize expression and purification conditions.

#### 8.2.4. Expression and purification of *E. coli* class Ia RNR apo- $\beta$ 2

The expression and purification procedure was slightly modified compared to earlier protocols.<sup>415</sup> If not stated otherwise, 50 mM Tris buffer containing 5% glycerol at pH 7.6 was used for all purification steps, shortly termed Tris in the following.

*E. coli* BL21(DE3)-Gold were transformed with pTB-*nrdB* and plated on LB-agar plates with 100  $\mu\text{g/mL}$  carbenicillin (Carb) at 37 °C. Positive clones were selected and a starter culture (5 mL) was grown overnight in LB-medium enriched with Carb at 37 °C until saturation. An intermediate culture (100 mL) was enriched with 1 mL of the starter culture, also grown overnight. The expression culture was grown with a 200-fold dilution of the intermediate culture in LB-medium containing Carb. At OD<sub>600</sub> ~0.9, 1,10-Phenanthroline was added to a final concentration of 100  $\mu\text{M}$  to chelate iron. After 20 min, protein expression was induced with 0.5 mM IPTG. After 4 – 20 h of protein overproduction, the cells were harvested by centrifugation at 17 000 xg for 15 min and 4 °C. A typical 2 – 3 g cell paste/L media was obtained, in excellent agreement with the previously reported yield considering 1,10-Phenanthroline addition.<sup>35</sup>

For protein purification, the cell pellet was resuspended in 3.5 – 5 mL/g cell pellet Tris buffer containing 0.5 mM PMSF. Next, the suspension was lysed via four passages through a French pressure cell press. Insoluble debris was removed at 3200 xg for 30 min at 4 °C. DNA was precipitated by adding 0.2 vol eq. of a 6% (w/v) streptomycin solution dropwise, followed by centrifugation at 3200 xg for 30 min at 4 °C. Protein was precipitated by 60% saturation with (NH<sub>4</sub>)<sub>2</sub>SO<sub>4</sub> (39 g/100 mL) by slowly adding the salt for over 10 minutes and stir for an additional 15 minutes on ice. Then, the protein was isolated at 3200 xg for 30 min at 4 °C and resolubilized in a minimal amount of Tris buffer. Desalting was performed using a PD-10 column (Sephadex® G-25 Medium, Cytiva), preequilibrated with Tris buffer. Protein-containing fractions were then loaded onto a preequilibrated anion exchange column (DEAE Sepharose™ Fast Flow, GE Healthcare), connected to a cooled chromatography system. Equilibration and subsequent washing of the column were performed with Tris buffer, enriched with 100 mM NaCl. Protein elution was carried out with a gradient of 100 to 500 mM NaCl.

Protein-containing fractions were pooled and diluted 1:1 with Tris buffer to avoid high salt concentrations. Furthermore, the protein solution was purified via a second anion exchange column (Q Sepharose™ Fast Flow, GE Healthcare), also connected to the chromatography system. Tris buffer supplemented with 150 mM NaCl was used for equilibration and washing of the column, and elution was performed with a NaCl gradient from 150 to 500 mM. Protein concentration was checked via UV-Vis, and EDTA was added to the solution to a final concentration of 100-times the protein concentration, followed by incubation for 2 h at 4 °C. Finally, EDTA was removed by washing with an Amicon® centrifugal filter unit with 30 kDa cutoff (Millipore) several times. After successful EDTA removal and reaching the desired protein concentration, aliquots were frozen in liquid nitrogen and stored at -80 °C. A typical yield of 9 – 18 mg protein/g cell paste was obtained, in good agreement with earlier results considering apo-expression.<sup>292,414,415</sup> For the apo-protein, an extinction coefficient of  $\epsilon(280 \text{ nm}) = 120\,000 \text{ M}^{-1} \text{ cm}^{-1}$  was used.

### 8.2.5. Reconstitution of apo- $\beta$ 2 to form the diferric-Y• cofactor

Apo- $\beta$ 2 was supplemented with 5 eq. Fe<sup>II</sup> in the form of Fe<sup>II</sup>(NH<sub>4</sub>)<sub>2</sub>(SO<sub>4</sub>)<sub>2</sub>. As Fe<sup>II</sup> oxidizes quickly, the stock solution was prepared freshly before its use in degassed buffer via N<sub>2</sub> bubbling for at least 30 min. Protein and iron were mixed fastly and incubated for 10 min on ice. In some cases, the solution was further treated with O<sub>2</sub>, which did not affect the observed radical yield. Y<sub>122</sub>• exhibits a sharp characteristic absorption maximum at 410 nm, which can be quantified by the dropline correction method:<sup>86</sup>

$$c_{Y_{122}\bullet} = \frac{A_{410\text{nm}} - 0.5(A_{405\text{nm}} + A_{415\text{nm}})}{2110 \text{ M}^{-1}\text{cm}^{-1}} \cdot \text{dilution}. \quad (8.1)$$

For holo- $\beta$ 2,  $\epsilon(280 \text{ nm}) = 131\,000 \text{ M}^{-1} \text{ cm}^{-1}$  is used.

### 8.2.6. Expression and purification of tyrosine phenol lyase (TPL)

Purification procedures were slightly modified compared to earlier protocols.<sup>416,417</sup> *E. coli* SVS370 harboring the plasmid pTZTPL, which encodes for tyrosine phenol lyase (TPL), was plated on LB-agar plates with 100  $\mu\text{g}/\text{mL}$  carbenicillin (Carb) at 37 °C. Positive clones were selected and grown for 20 h in 1L LB-medium enriched with Carb at 37 °C. The cells were collected by centrifugation for 30 min at 10 000 xg at 4 °C and stored at -80 °C until used for purification. Typical yields were 4 – 5 g cell paste/L medium.

The thawed cells were suspended in 4 mL buffer (0.1 M potassium phosphate, 0.1 mM pyridoxal phosphate, 1 mM EDTA, 5 mM  $\beta$ -mercaptoethanol, pH 7.0) per g cell paste. Next, the suspension was lysed via four passages through a French pressure cell press. Insoluble debris was removed at 25 000 xg for 30 min at 4 °C. Then, DNA was

precipitated by adding 0.2 vol eq. of a 6% (w/v) streptomycin solution dropwise, followed by centrifugation at 25 000 xg for 30 min at 4 °C. Protein was precipitated by 60% saturation with (NH<sub>4</sub>)<sub>2</sub>SO<sub>4</sub> (39 g/100 mL) by slowly adding the salt for over 10 min and stir for an additional 15 min on ice. The resultant precipitate was collected by centrifugation at 25 000 xg, 30 min, 4 °C, and afterward resuspended in a minimal amount of buffer. The protein solution was desalted via overnight dialysis in buffer containing 144 g/L (NH<sub>4</sub>)<sub>2</sub>SO<sub>4</sub> (25% saturated). Next, the protein solution was loaded onto a size exclusion column (HiPrep™ 26/60 Sephacryl® S-200 HR), connected to a cooled chromatography system, with the buffer being 25% saturated with (NH<sub>4</sub>)<sub>2</sub>SO<sub>4</sub>. TPL-containing fractions were pooled, and protein was salted out via 75% saturation with (NH<sub>4</sub>)<sub>2</sub>SO<sub>4</sub>. After resolubilizing the protein in a minimal amount of buffer, the sample was desalted using a PD-10 column (Sephadex® G-25 Medium, Cytiva), preequilibrated with the standard buffer. Protein activity was assayed by a coupled spectrophotometric assay where a small volume of the fraction was added to an assay mixture containing 0.3 mM L-tyrosine, 1 mM DTT, 50 µM pyridoxal-5'-phosphate, 0.3 mg/mL lactate dehydrogenase and 0.2 mM NADH in 50 mM potassium phosphate at pH 8.0. The consumption of NADH was monitored at 340 nm, whereas one unit (U) of activity is defined as 1 µmol product/min. A total of ~90 U/g cell paste was obtained, in agreement with the previously reported yield.

### **8.2.7. SDS polyacrylamide gel electrophoresis**

Precast 10% (v/v) acrylamide SDS-PAGE gels were used to verify successful protein expression and purification. 5 µL samples were loaded per gel pocket, and separation was performed at 200 V for 40 min. After washing the gel with water, staining was performed for 20 min with Roti® Blue quick. Afterward, the gel was destained overnight in water, followed by imaging.

### **8.2.8. Enzymatic synthesis and purification of fluorotyrosines**

The workup procedure was conducted according to previously published protocols.<sup>418</sup> 1 L of 30 mM ammonium acetate and the appropriate fluorophenol with a final concentration of 10 mM was prepared. Pyruvic acid and β-mercaptoethanol were added to final concentrations of 60 and 5 mM, respectively. The reaction vessel was protected from light; afterward, the solution's pH was adjusted to 8.0 using ammonium hydroxide. 30 U of TPL was added together with pyridoxal-5'-phosphate to a final concentration of 40 mM, and the solution was allowed to stir for 3 – 4 days at room temperature. The light protection was removed from the reaction vessel, and the pH was lowered to 2 – 3 by using 6 N HCl, resulting in precipitation of TPL. Precipitated TPL was removed via a celite pad (Celite 545). The filtrate was then extracted once with 0.5 volumes of ethyl acetate, and the aqueous layer containing the F<sub>n</sub>Y was kept for further purification. The

fluorotyrosine was then separated from residual pyruvic acid and acetic acid throughout a cation exchange resin (AG50W-X8, 50-100 mesh, Bio-Rad) which was first prepared by washing with 10 CV of water. After loading the sample solution, the column was washed with 8 CV of water. F<sub>n</sub>Y was eluted with approx. 8 CV of a 10% ammonium hydroxide solution while collecting the eluted fractions. Fractions were tested for amino acid via the ninhydrin test. Therefore, a ninhydrin solution consisting of 0.19% (w/v) ninhydrin, 95% (v/v) n-butanol, 0.5% (v/v) acetic acid and 4.5% (v/v) water was prepared. The fractions were spotted onto a TLC plate, and the dry plate was dipped into the ninhydrin solution, followed by heating with a heat gun for 10 – 15 s. A purple/pink spot indicates the presence of free amine functionality. Fractions giving a positive ninhydrin test were concentrated in a rotary evaporator. The remaining solution was lyophilized to dryness. Successful amino acid synthesis was assessed by NMR spectroscopy (**Figure D.1** and **Figure D.2**). The resulting F<sub>n</sub>Y can be stored at 4 °C for several years.

### 8.2.9. Echo-detected EPR (ESE)

Pulse sequence:  $\pi/2 - \tau - \pi - \tau - \text{echo}$

The integrated echo is recorded as a function of the magnetic field  $B_0$ .

### 8.2.10. Microwave nutation

Pulse sequence:  $t_p - t_d - \pi/2 - \tau - \pi - \tau - \text{echo}$

The first pulse  $t_p$  is incremented in time. Mw nutation experiments were used to determine optimal pulse lengths for ESE experiments.

### 8.2.11. Phase memory time

Pulse sequence:  $\pi/2 - \tau - \pi - \tau - \text{echo}$

Time  $\tau$  is incremented. The phase memory time  $T_m$  was determined from a mono-exponential fit to the experimental data

$$I = I_0 \exp\left(-\frac{\tau}{T_m}\right) + C. \quad (8.2)$$

### 8.2.12. Davies ENDOR

Pulse sequence:  $\pi - T - \pi/2 - \tau - \pi - \tau - \text{echo}$

The RF pulse of variable frequency was applied during the time interval T and had a length of 17  $\mu$ s as determined from previous RF nutation experiments. The first  $\pi$  pulse was a rectangular-shaped inversion pulse of 190 ns. The radio frequency was swept stochastically during the experiment to avoid heating and saturation effects.

**8.2.13. DEER**

Pulse sequence:  $\pi/2_{\text{det}} - \tau_1 - \pi_{\text{det}} - (\tau_1 - T) - \pi_{\text{pump}} - (\tau_2 - T) - \pi_{\text{det}} - \tau_2 - \text{echo}$

4-pulse DEER experiments were performed by using 16-step phase cycling and Gaussian pulses. The frequency separation  $\Delta f = f_{\text{pump}} - f_{\text{det}}$  in an overcoupled resonator was adjusted with  $f_{\text{pump}}$  set to the center of the resonator dip. The optimal  $\pi$ -pulse lengths were determined using transient nutation experiments.

## Supporting information

### A. Supporting information to Chapter 3

#### Details of *in vitro* and in-cell DEER measurements

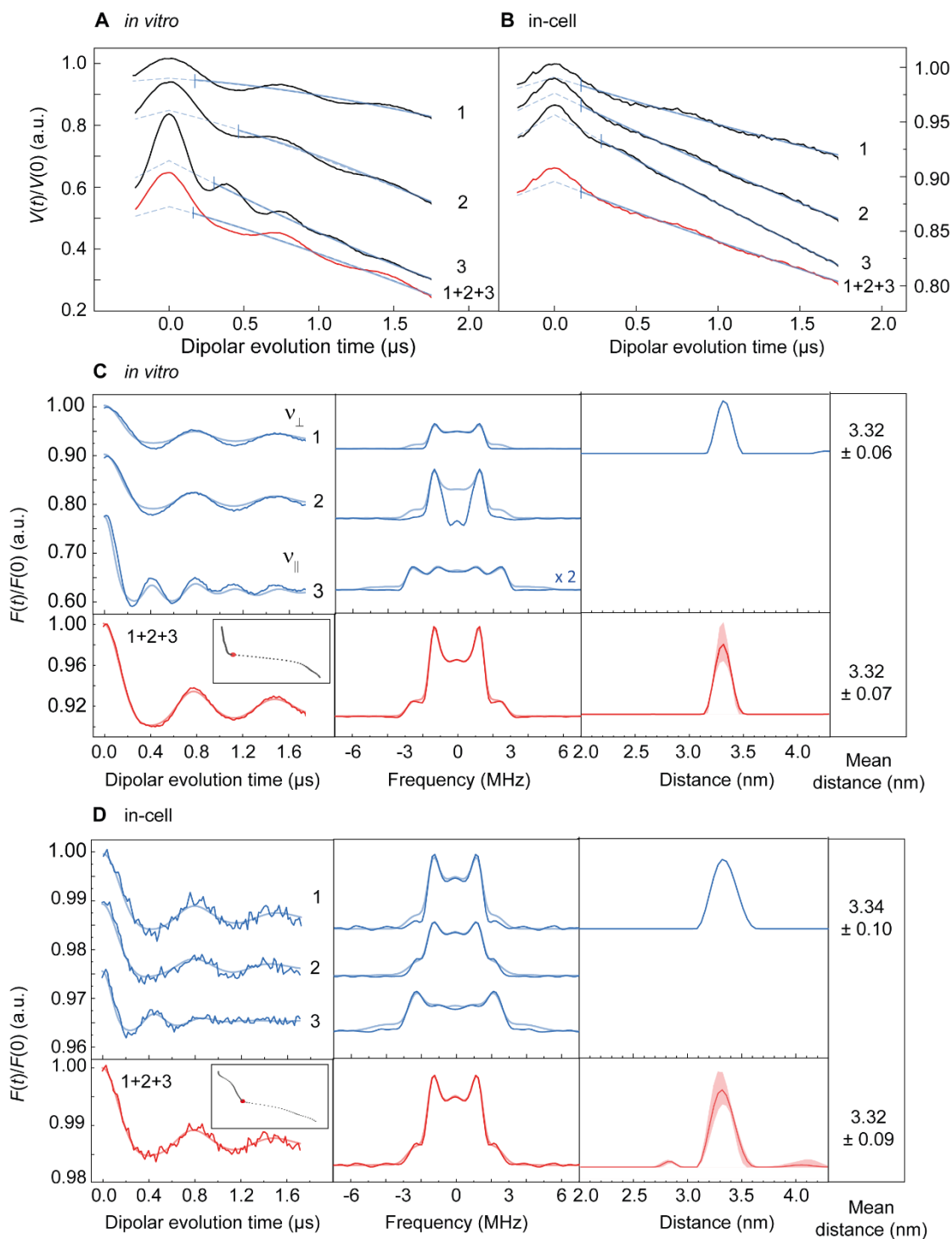


**Figure A.1: DEER measurements of  $Y_{122}^\bullet$  in *E. coli* RNR performed at 34 GHz and 10 K. (A) ESE-detected EPR spectrum of in-cell sample 1 recorded at 10 K. (A) Primary orientation-selective DEER traces (1, 2, and 3 shown with solid black lines) recorded with an *in vitro* sample shown along with the background functions (dashed blue lines). Field positions for traces 1, 2, and 3 are given in **Figure 3.5A**. For orientation averaging, each primary time trace was first normalized to the same signal intensity at zero time. Afterward, these traces were normalized to the signal intensity at the pump position. Summation led to the orientation-averaged time trace (red). (B) Primary DEER traces (1, 2, and 3 shown with solid black lines) recorded with the in-cell sample shown along with the background functions (dashed blue lines). (C) Analysis of the *in vitro* DEER data at three different positions (upper row) along with the orientation-averaged time trace (lower row, red). Left: Background- and phase-corrected, normalized (time signal  $V(t)$  divided by the signal at echo maximum  $V(0)$ ) DEER time traces are shown in dark colors. Fits obtained by DeerAnalysis using Tikhonov regularization are overlaid and displayed in paler shade. The inset shows the L-curve and the corresponding regularization parameter (red data point). Middle: Fourier transforms of the DEER data (blue) and their fits (paler shade). Right: obtained  $Y_{122}^\bullet$ - $Y_{122}^\bullet$  distance distributions, along with the mean distances and standard deviations. Validation of the distance distribution was obtained by varying the starting value of the background fit (vertical line in A) by  $\pm 50\%$  in 10 steps and the background dimensionality in 10 steps by  $\pm 0.5$  with respect to the initial value chosen for the data analysis. (D) Analysis for in-cell data, performed as explained in (C). Experimental conditions: Gaussian pulses,  $\tau_{\text{det}} = 70$  ns (D1), 68 ns (D2, D3);  $\tau_{\text{pump}} = 28$  ns (P1, P2, P3);  $\text{srt} = 4$  ms;  $\text{spp} = 100$ ; acquisition time = 19 h (in-cell position 1), 19 h (in-cell position 2), 19 h (in-cell position 3), 3 h (*in vitro* position 1), 3 h (*in vitro* position 2), 17 h (*in vitro* position 3).**

### Analysis of orientation-selective *in vitro* DEER data by PeldorFit

The data analysis was kindly assisted by Dr. Dinar Abdullin.

For the analysis of dipolar traces by PeldorFit, it is recommended to simulate the same data set several times with the same settings to ensure the reproducibility of the results. In this case, the optimization was performed three times with 500 optimization steps each, while the fitting score was always constant for more than the last 100 optimization steps, showing that the fit converged to its global minimum.

The fits of the data did not show any noticeable deviations from each other (**Figure A.2**). Distance,  $\xi$ , and  $\varphi$  were reproducible in three runs (**Table A.1**). Dr. Dinar Abdullin also performed the analysis with the newest version of PeldorFit, which yielded similar values for  $r$ ,  $\xi$ , and  $\varphi$  (3.31 nm, 24°, and 90°). These data are not shown here since this version is unpublished at the time of writing this thesis.

However, the Euler angles were not reproducible. Even when checking the 16 symmetry-related sets of angles provided by PeldorFit, no better match of the angles could be found. If the Euler angles from the literature were used and kept constant during the optimization, the fit could not reproduce the modulation observed at position 3. For the analysis shown in Section 3.3.5, the optimization result of run 2 was chosen as it showed the highest agreement compared to the literature and crystal structure.

**Table A.1:**  $Y_{122}\bullet\text{-}Y_{122}\bullet$  *in vitro* pair analysis derived from DEER experiments using PeldorFit. Results of three optimization runs are shown. The value in brackets indicates the error of the respective parameter. The error is determined by the range in which 110% of the minimal RMSD is reached. The first value per column is the mean value of the parameter, while the second value represents the uniform width (or in case of  $r$  the standard deviation) of each parameter.

Parameter		Value					
Optimization run		1		2		3	
$r$ (nm)	$\Delta r$ (nm)	3.31(0.03)	0.03(0.03)	3.31(0.03)	0.03(0.04)	3.30(0.03)	0.04(0.01)
$\xi$ (°)	$\Delta\xi$ (°)	26(3)	2(17)	28(9)	1(32)	27(19)	11(34)
$\varphi$ (°)	$\Delta\varphi$ (°)	88(19)	1(19)	94(13)	20(71)	86(19)	6(77)
$\alpha$ (°)	$\Delta\alpha$ (°)	110(21)	100(30)	172(12)	6(9)	146(17)	9(10)
$\beta$ (°)	$\Delta\beta$ (°)	3(7)	3(2)	30(6)	66(5)	22(4)	50(24)
$\gamma$ (°)	$\Delta\gamma$ (°)	82(41)	51(40)	7(5)	77(20)	38(25)	75(19)

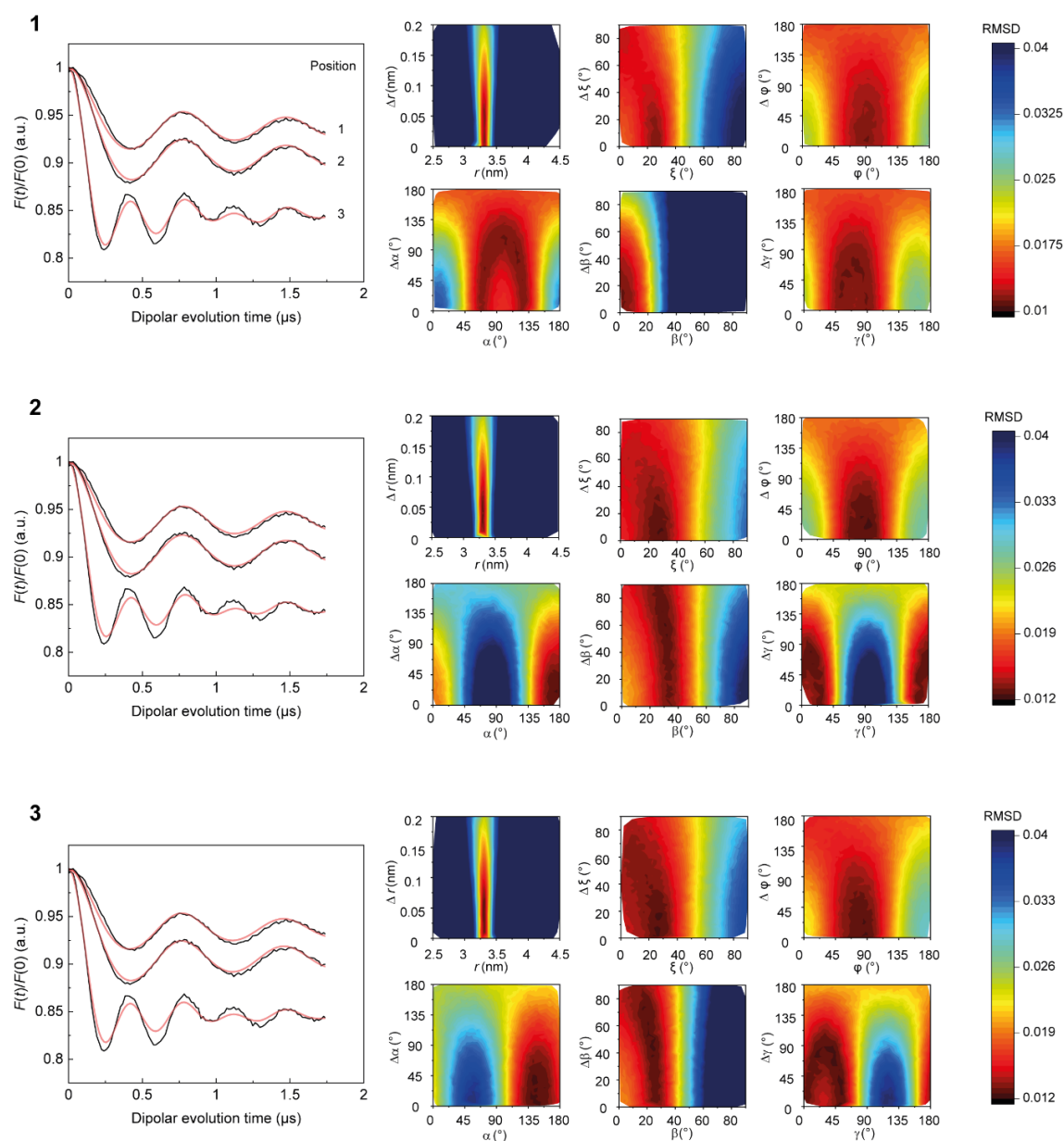


**Figure A.2:** Analysis of orientation-selective DEER data of  $Y_{122}\bullet$ - $Y_{122}\bullet$  in *E. coli* RNR *in vitro*. Optimization of three runs are shown, numbered from 1 to 3 in bold values. Left: Q-Band DEER time traces acquired at different field positions (1, 2, 3) overlaid with the PeldorFit simulations (red). Right: RMSD between experimental and simulated DEER time traces as a function of the geometric parameter of PeldorFit.

### Analysis of orientation-selective in-cell DEER data by PeldorFit

The same analysis procedure described for the *in vitro* data was carried out for the in-cell DEER traces. In **Table 3.3**, only the results of fitting run 3 are shown, as the highest agreement was observed in this case compared to the crystal structure.

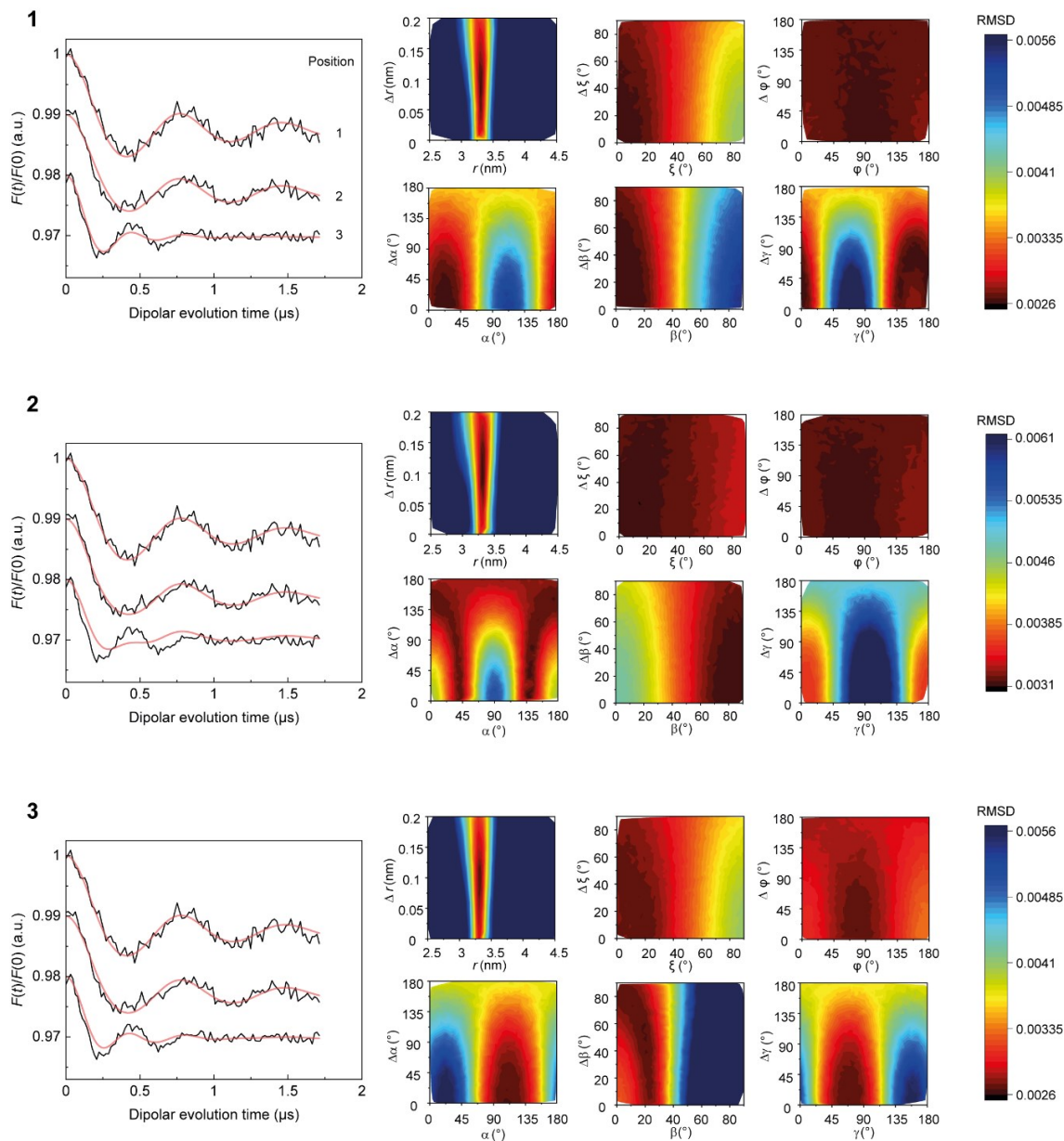
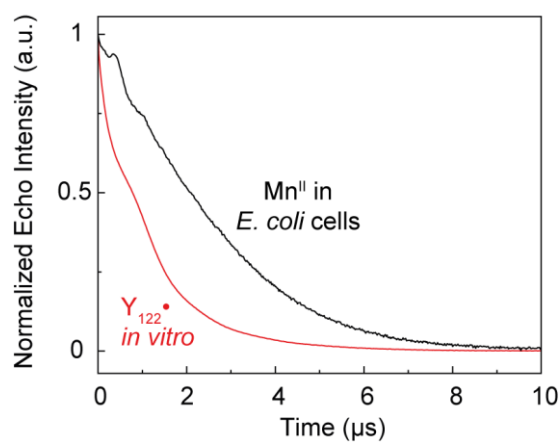


**Figure A.3:** Analysis of orientation-selective DEER data of  $Y_{122}^{\bullet}-Y_{122}^{\bullet}$  in *E. coli* RNR inside cells. Optimization of three runs are shown, numbered from 1 to 3 in bold values. Left: Q-Band DEER time traces acquired at different field positions (1, 2, 3), overlaid with the PeldorFit simulations (red). Right: RMSD between experimental and simulated DEER time traces as a function of the geometric parameter of PeldorFit.

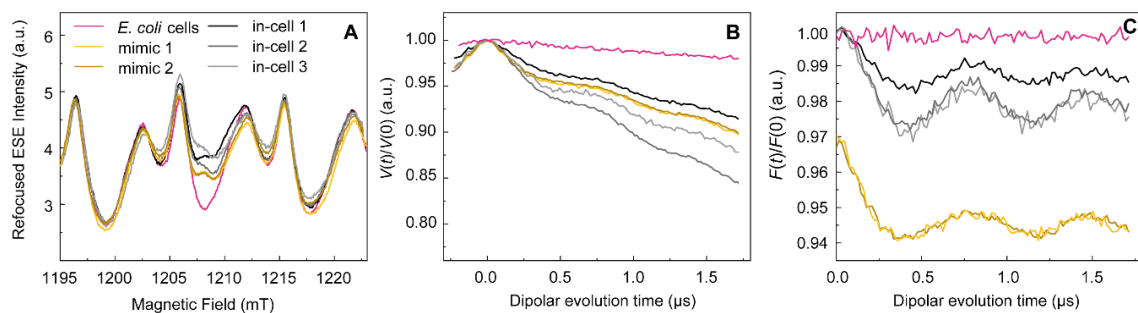
**Table A.2:  $Y_{122}^{\bullet}$ - $Y_{122}^{\bullet}$  in-cell pair analysis derived from DEER experiments using PeldorFit.** Results of three optimization runs are shown. The value in brackets indicates the error of the respective parameter. The error is determined by the range in which 110% of the minimal RMSD is reached. The first value per column is the mean value of the parameter, while the second value represents the uniform width (or in case of  $r$  the standard deviation) of each parameter.

Parameter		Value					
Optimization run		1	2	3	1	2	3
$r$ (nm)	$\Delta r$ (nm)	3.30(0.05)	0.09(0.06)	3.32(0.06)	0.11(0.03)	3.32(0.03)	0.10(0.05)
$\xi$ (°)	$\Delta\xi$ (°)	8(25)	0(26)	8(75)	2(33)	19(19)	8(14)
$\varphi$ (°)	$\Delta\varphi$ (°)	93(NA)	19(NA)	60(NA)	3(NA)	77(50)	11(84)
$\alpha$ (°)	$\Delta\alpha$ (°)	21(17)	12(71)	138(64)	6(154)	108(21)	4(42)
$\beta$ (°)	$\Delta\beta$ (°)	2(21)	60(8)	79(24)	4(14)	12(17)	74(46)
$\gamma$ (°)	$\Delta\gamma$ (°)	155(25)	80(19)	179(4)	35(56)	70(9)	1(98)

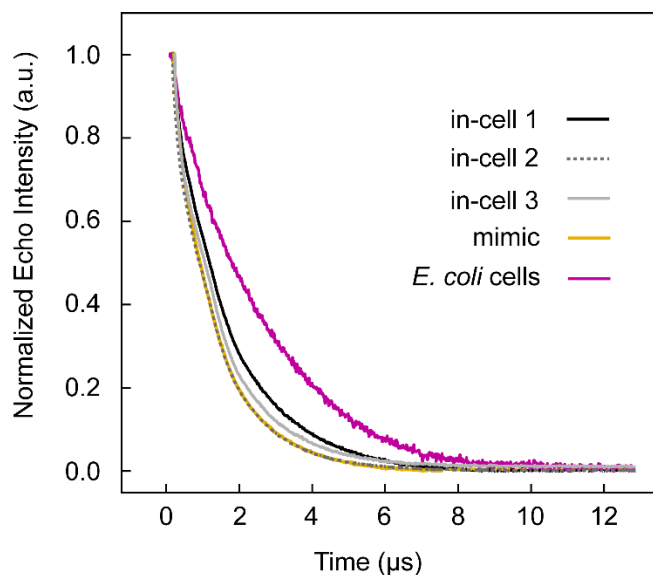
### Comparison of transversal relaxation times



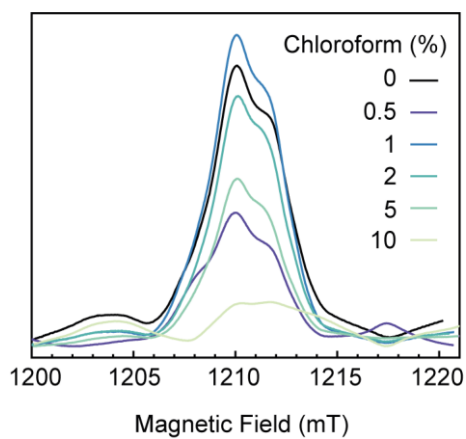
**Figure A.4:  $T_m$  measurements.** Two-pulse echo decay measurements of  $Y_{122}^{\bullet}$  *in vitro* (red) and  $Mn^{II}$  in *E. coli* cells lacking the overexpression plasmid (black).

In-cell samples compared to *in vitro* mimics

**Figure A.5: Modulation depth analysis of *in vitro*  $\beta 2$  mimic and in-cell samples compared to pure *E. coli* cells.** (A) 34 GHz field-swept EPR spectra of *E. coli* cells, *in vitro* mimic duplicates, and three different in-cell samples recorded via refocused spin echo. (B) Primary DEER traces and (C) form factors of the corresponding samples. Acquisition time: 15 h, 65 scans (*E. coli* cells); 14 h, 55 scans (mimic 1); 15 h, 62 scans (mimic 2); 19 h, 61 scans (in-cell 1); 22 h, 89 scans (in-cell 2); 25 h, 101 scans (in-cell 3).



**Figure A.6:  $T_m$  measurements of samples presented in Figure A.5.** Two-pulse echo decay measurements of  $Y_{122}\bullet$  in cells and *in vitro* (mimic 1). Data for *E. coli* cells without overexpression plasmid (purple) are shown for comparison.  $T_m$  of  $Y_{122}\bullet$  within the cells is either longer or the same as that of *in vitro* samples.

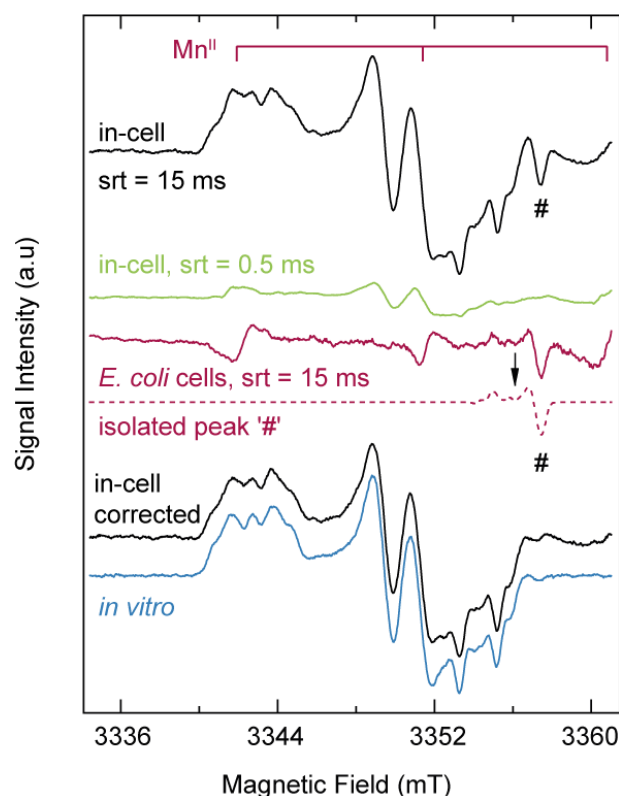
**The effect of chloroform investigated by 34 GHz EPR measurements**

**Figure A.7: 34 GHz ESE spectra of in-cell samples supplemented with chloroform.** A decrease in  $Y_{122\bullet}$  concentration is observed upon increasing amounts of chloroform are added. Experimental conditions: Temperature = 10 K,  $\pi = 24$  ns,  $\tau = 200$  ns, Attenuation = 8 dB, srt = 8 ms, spp = 100.

### Subtraction of the Mn<sup>II</sup> spectral features

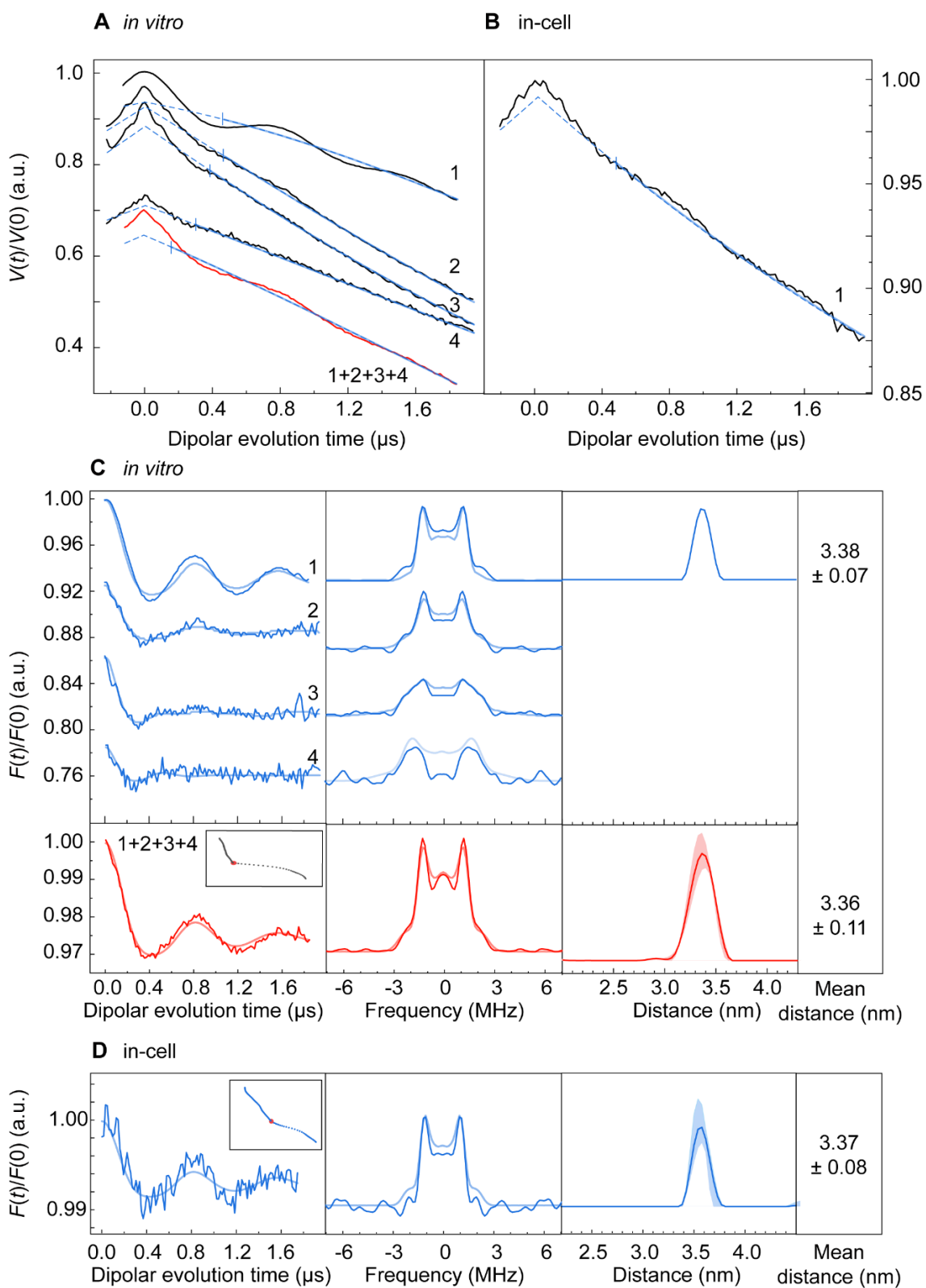
Measurements and analyses presented in this section were kindly performed by Dr. Yury Kutin.

Two ways of background measurements had to be performed for the background correction of W-band in-cell spectra. The unidentified background peak labeled with #, as well as the sharp hyperfine structure lines originating from the  $m_s = -1/2 \leftrightarrow +1/2$  transition of Mn<sup>II</sup> were both detected for the *E. coli* cells harvested prior to the radical generation. However, the Mn<sup>II</sup> EPR intensity is strongly dependent on the mw power. Since it was impossible to perfectly reproduce the same conditions for the background measurement, this background trace could only be used to isolate (dashed magenta trace) and subtract the background peak labeled with #. In the second step, the in-cell spectrum was remeasured with a shorter shot repetition time (green trace) to obtain a proper Mn<sup>II</sup> background. This procedure allows for suppressing the slowly relaxing Y<sub>122</sub>• contribution while reproducing the faster-relaxing Mn<sup>II</sup> background under the same conditions (microwave power and signal phase) as used for the in-cell Y<sub>122</sub>• measurement. This trace could subsequently be used to entirely suppress the Mn<sup>II</sup> spectral features in the in-cell Y<sub>122</sub>• spectrum.

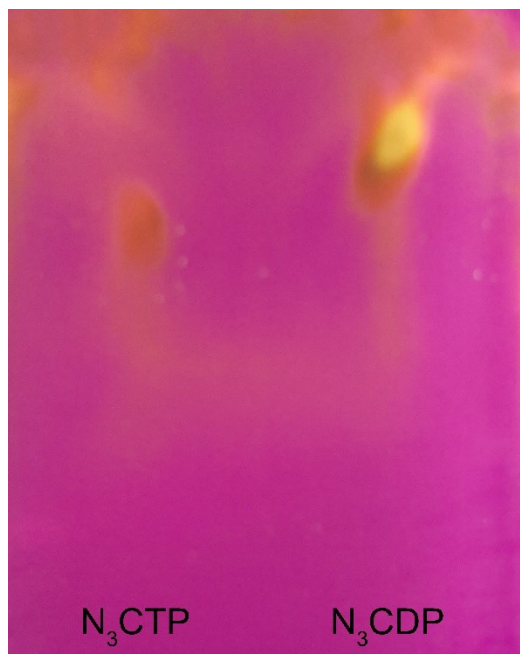


**Figure A.8: Background correction for the in-cell Y<sub>122</sub>• EPR spectra detected via primary spin echo at W-band.** From top to bottom: Black trace: EPR spectrum of Y<sub>122</sub>• in whole *E. coli* cells recorded at 94 GHz with a shot repetition time of 15 ms. Green trace: spectrum of the same sample, with the Y<sub>122</sub>• contribution suppressed by a short shot repetition time of 0.5 ms. Magenta trace: spectrum of *E. coli* cells harvested prior to the radical generation and containing only endogenous radical below the detection limit, recorded under approximately the same conditions as the in-cell Y<sub>122</sub>• spectrum. Magenta dashed line: isolated background signal labeled '#'. Black trace: background-corrected in-cell Y<sub>122</sub>• EPR spectrum, with an *in vitro* Y<sub>122</sub>• EPR spectrum (blue trace) for comparison.

### Details of the $F_3Y_{122}$ DEER measurements and analysis



**Figure A.9: DEER measurements of  $F_3Y_{122}\bullet$  in *E. coli* RNR performed at 34 GHz and 10 K.** (A) Primary orientation-selective DEER traces (1, 2, 3, and 4 shown with solid black lines) recorded with the *in vitro* sample shown along with the background functions. Summation led to the orientation-averaged time trace (red). (B) Primary DEER trace of the in-cell sample recorded at D1/P1 (solid black line) along with the background function (dashed blue line). (C) Analysis of the *in vitro* DEER data at four positions (upper row) along with the orientation-averaged time trace (lower row, red). Left: Background- and phase-corrected, normalized DEER time traces are shown in dark colors. Fits obtained by DeerAnalysis using Tikhonov regularization are overlaid and displayed in paler shade. L-curve and the corresponding regularization parameter (red data point) are shown in the inset. Middle: Fourier transforms of the DEER data along with their fits (paler shade). Right: Obtained  $F_3Y_{122}\bullet$ - $F_3Y_{122}\bullet$  distance distributions, along with the mean distances and standard deviations. Validation of the distance distribution was obtained by varying the starting value of the background fit (vertical line in A) by  $\pm 50\%$  in 10 steps and the background dimensionality in 10 steps by  $\pm 0.5$  with respect to the initial value chosen for the data analysis. (D) Analysis performed as explained in (C) for the in-cell data (D1/P1 position). Experimental conditions: Gaussian pulses,  $\pi_{\text{det}} = 74$  ns (D1), 68 ns (D2, D3), 62 ns (D4);  $\pi_{\text{pump}} = 32$  ns (P1, P2, P3, P4);  $\text{srt} = 8$  ms (in cell), 8 ms (*in vitro* position 1), 4 ms (position 2 – 4);  $\text{spp} = 100$ ; acquisition time = 44 h (in-cell), 10 h (*in vitro* position 1), 2.5 h (*in vitro* position 2), 4.5 h (*in vitro* position 3), 2 h (*in vitro* position 4).

**B. Supporting information to Chapter 4****TLC plate to monitor dephosphorylation of  $N_3$ CTP**

**Figure B.1:** TLC plate to monitor the dephosphorylation of  $N_3$ CTP. Educt and product were spotted on a plate TLC Silica gel 60 F<sub>254</sub>, followed by permanganate staining, which proves successful enzymatic dephosphorylation.

## Detail of the in-cell DEER measurements

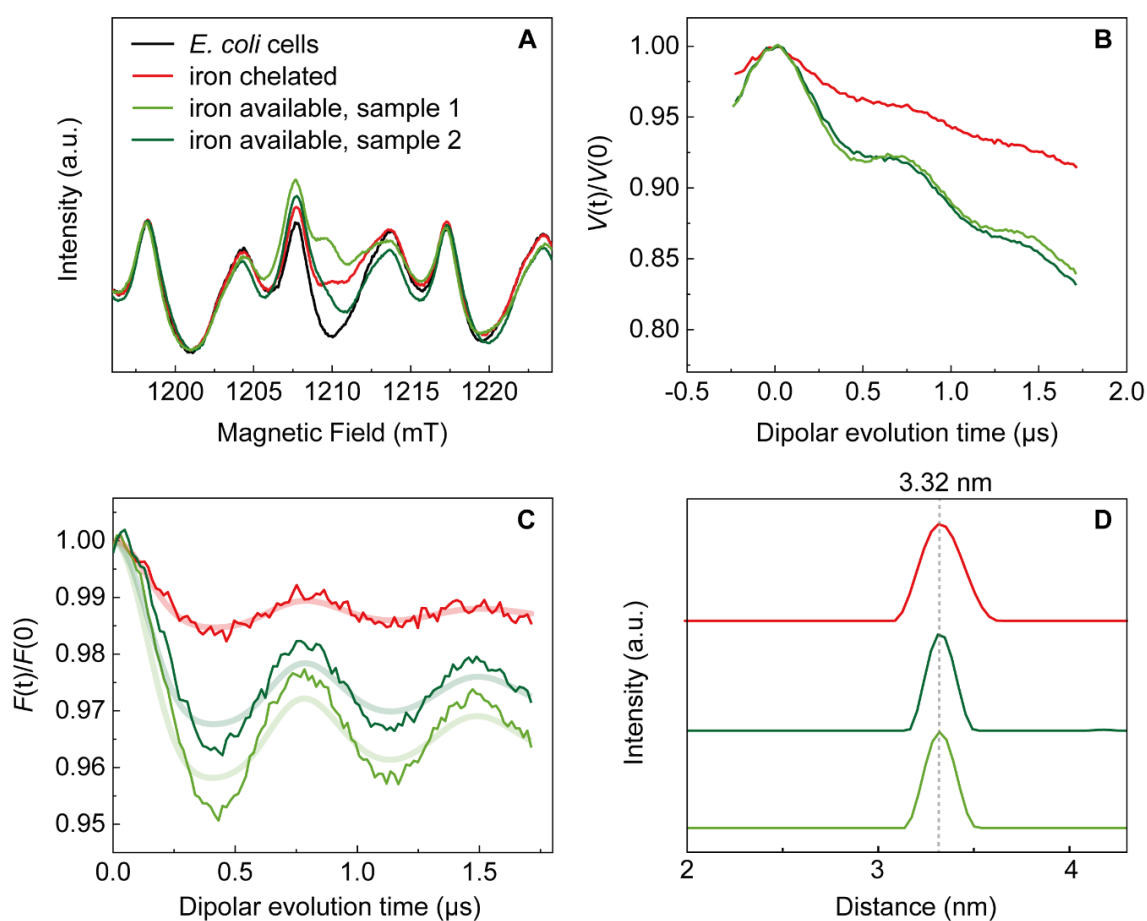


**Figure B.2: Modulation depth analysis of in-cell samples expressing the  $\beta 2$ -subunit of *E. coli* RNR under iron-chelated and iron-available conditions.** (A) Q-band field-swept EPR spectra of in-cell samples produced under iron-limiting (red) or iron-available (green) expression conditions. Spectra were recorded via the refocused spin echo with pump pulse applied. A spectrum of *E. coli* cells without protein overexpression is shown in black as comparison. (B) Primary DEER traces and (C) form factors of the corresponding samples. (D) Obtained distance distribution.  $Y_{122}^{\bullet}$  concentrations were  $77 \mu\text{M}$  (sample 1) and  $71 \mu\text{M}$  (sample 2). Free  $\text{Mn}^{\text{II}}$  in these samples was determined as  $40$  and  $26 \mu\text{M}$ , respectively. Experimental conditions: Gaussian pulses,  $\tau_{\text{det}} = 70 \text{ ns}$ ,  $\tau_{\text{pump}} = 28 \text{ ns}$ ,  $\text{srt} = 4 \text{ ms}$ ;  $\text{spp} = 100$ . Acquisition time:  $22 \text{ h}$  (red),  $21 \text{ h}$  (sample 1),  $17 \text{ h}$  (sample 2).

### Y-Mn distance in the crystal structure of manganese-bound RNR $\beta 2$

In order to obtain a structure of *E. coli* RNR with a diiron cofactor on one side and a dimanganese cofactor on the other side of the dimer, the crystal structure of the iron-bound holo- $\beta 2$  subunit (PDB: 5CI4<sup>35</sup>) was overlaid with the structure containing dimanganese centers in both subunits (PDB: 1MRR<sup>99</sup>) (**Figure B.3**). Subsequently, different possible distances were read out (**Table B.1**). The two manganese ions within one subunit possess different binding affinities and are therefore labeled as A and B. The Y<sub>122</sub>-Y<sub>122</sub> distance in 1MRR is slightly smaller than for the holo-protein (5CI4: 3.29 nm). This deviation is assigned to a conformational change that needs to be done for complete radical generation on both sites. Note that the distances are acquired between the oxygen atoms of Y<sub>122</sub>• in the crystal structure.

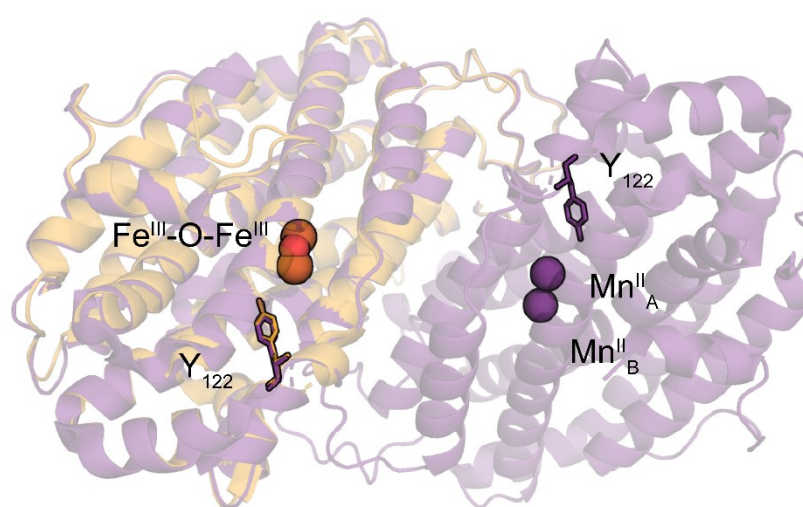


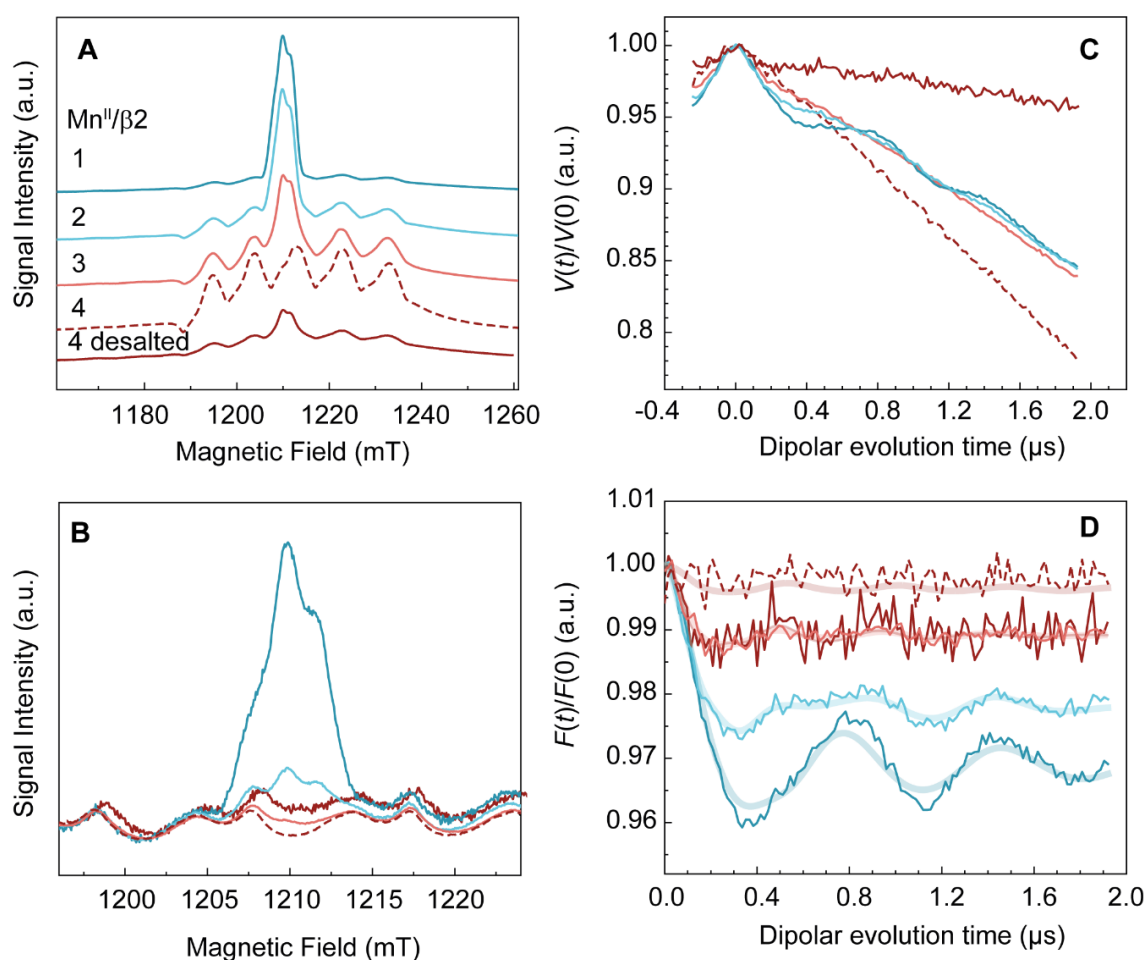
**Figure B.3: Manganese-bound *E. coli* class Ia  $\beta 2$  RNR.** Overlay of the crystal structures of *E. coli* RNR in iron-bound form (orange, 5CI4<sup>35</sup>) and manganese-bound form (purple, 1MRR<sup>99</sup>). Y<sub>122</sub> is illustrated by sticks, metal centers as spheres.

**Table B.1: Possible distances obtained by the crystal structures in Figure B.3.**

Paramagnetic centers	Distance (nm)		
	1MRR	5CI4	1MRR and 5CI4 merged
Y <sub>122</sub> •-Y <sub>122</sub> •	3.26	3.29	3.28
Y <sub>122</sub> •-Mn <sup>II</sup> <sub>A</sub>	2.91		2.92
Y <sub>122</sub> •-Mn <sup>II</sup> <sub>B</sub>	2.84		2.86
Mn <sup>II</sup> <sub>A</sub> -Mn <sup>II</sup> <sub>A</sub>	2.57		
Mn <sup>II</sup> <sub>A</sub> -Mn <sup>II</sup> <sub>B</sub>	2.54		
Mn <sup>II</sup> <sub>B</sub> -Mn <sup>II</sup> <sub>B</sub>	2.55		

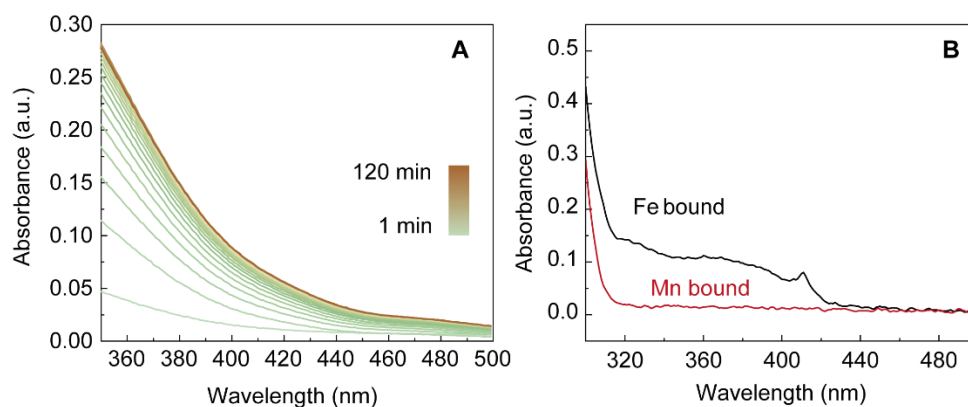
### DEER measurements on manganese-bound RNR

Adding 4 equivalents of  $\text{Mn}^{\text{II}}$  resulted in around 1.3 eq. of free  $\text{Mn}^{\text{II}}$  per  $\beta 2$ , suppressing the modulation depth to such an extent that no modulation is detected anymore. Hence, no distance can be extracted (see **Figure B.4** dashed line). This sample is represented by an open symbol in **Figure 4.9**. To overcome this problem, the sample was desalted by several washes using a centrifugal filter unit. The desalted sample (**Figure B.4** solid line and filled symbol in **Figure 4.9**) had a final protein concentration of  $40 \mu\text{M}$  and was not further concentrated because extensive centrifugation could potentially lead to manganese release. All other samples had a protein concentration of  $150 \mu\text{M}$ . As previously shown, different protein concentrations of *E. coli* RNR do not change the modulation depth parameter but the signal-to-noise ratio only,<sup>213</sup> allowing comparison of different sample concentrations.



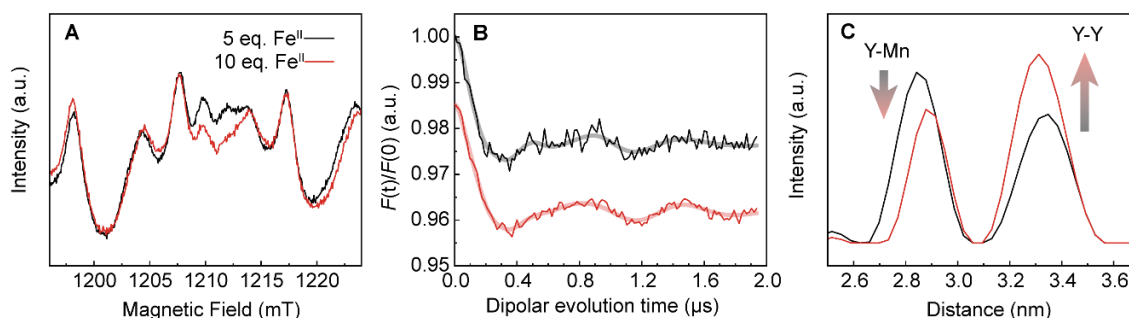
**Figure B.4: DEER measurements of  $\text{Y}_{122}^{\bullet}$  in *E. coli* RNR with different equivalents of  $\text{Mn}^{\text{II}}$  added, performed at 34 GHz and 10 K.** (A) ESE spectra of apo- $\beta 2$  supplemented with different equivalents of  $\text{Mn}^{\text{II}}$ . (B) Refocused echoes of the DEER experiments. (C) Primary orientation-selective DEER traces. (D) Background- and phase-corrected, normalized DEER time traces are shown in dark colors. Fits obtained by DeerAnalysis using Tikhonov regularization are overlaid and displayed in paler shade. Experimental conditions: Gaussian pulses,  $\pi_{\text{det}} = 70 \text{ ns}$ ;  $\pi_{\text{pump}} = 28 \text{ ns}$ ;  $\text{srt} = 4 \text{ ms}$ ;  $\text{spp} = 100$ ; acquisition time = 15 h (1), 18 h (2), 43 h (3), 17 h (4), 24 h (4 desalted).

### Details of UV-Vis measurements

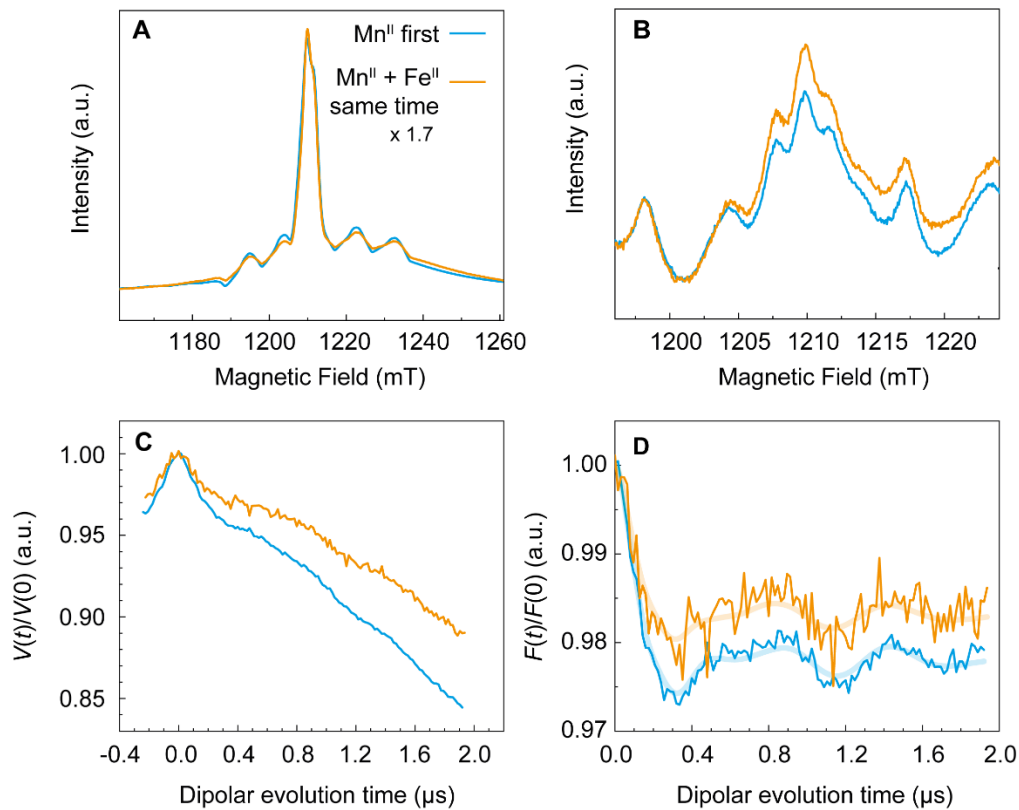


**Figure B.5: UV-Vis measurements of Fe<sup>II</sup> solutions and *E. coli* RNR  $\beta$ 2 in the Fe- or Mn-bound state.** (A) UV-Vis measurements of the autooxidation of 150  $\mu$ M Fe<sup>II</sup>(NH<sub>4</sub>)<sub>2</sub>(SO<sub>4</sub>)<sub>2</sub> in Tris Buffer under aerobic conditions. (B) UV-Vis spectra of *E. coli* RNR in the iron- (black) or manganese-bound (red) form.

### DEER experiments with different amounts of iron



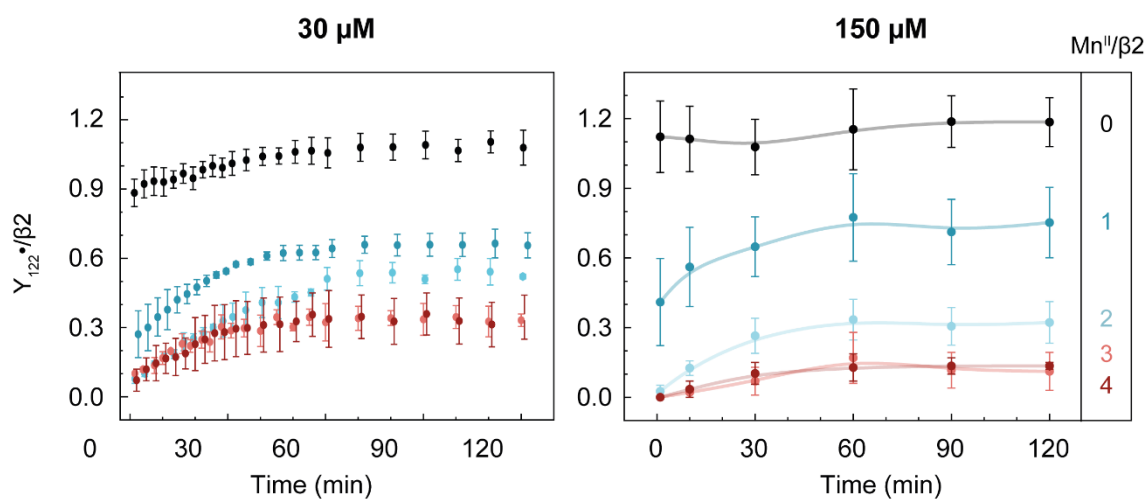
**Figure B.6: DEER experiments of manganese-bound  $\beta$ 2 (30  $\mu$ M) after first (5 eq. Mn<sup>II</sup>) and second (10 eq. Mn<sup>II</sup>) iron addition.** (A) Refocused echoes. (B) Background- and phase-corrected, normalized DEER time traces are shown in dark colors. Fits obtained by DeerAnalysis2019 using Tikhonov regularization are overlaid and displayed in paler shade. Traces were shifted vertically for visualization. (C) Distance distribution obtained by the analysis. Experimental conditions: Gaussian pulses,  $\pi_{\text{det}} = 70$  ns;  $\pi_{\text{pump}} = 28$  ns;  $\text{srt} = 4$  ms;  $\text{spp} = 100$ ; acquisition time = 18 h (black), 20 h (red).

**DEER measurements with iron and manganese added at the same time**

**Figure B.7: Apo- $\beta$ 2 (150  $\mu$ M) of *E. coli* RNR treated with iron and manganese in two different ways.** Samples were either supplemented with 2 Mn<sup>II</sup>/ $\beta$ 2 first, followed by 5 eq. Fe<sup>II</sup> (blue) or 5 Mn<sup>II</sup> and 5 Fe<sup>II</sup>/ $\beta$ 2 were added simultaneously (orange). Measurements were performed at 34 GHz and 10 K. (A) Hahn-echoes and (B) refocused echoes. (C) Primary orientation-selective DEER traces. (D) Background- and phase-corrected, normalized DEER time traces are shown in dark colors. Fits obtained by DeerAnalysis using Tikhonov regularization are overlaid and displayed in paler shade. Experimental conditions: Gaussian pulses,  $\pi_{\text{det}} = 70$  ns;  $\pi_{\text{pump}} = 28$  ns; srt = 4 ms; spp = 100; acquisition time = 18 h (blue), 24 h (orange).

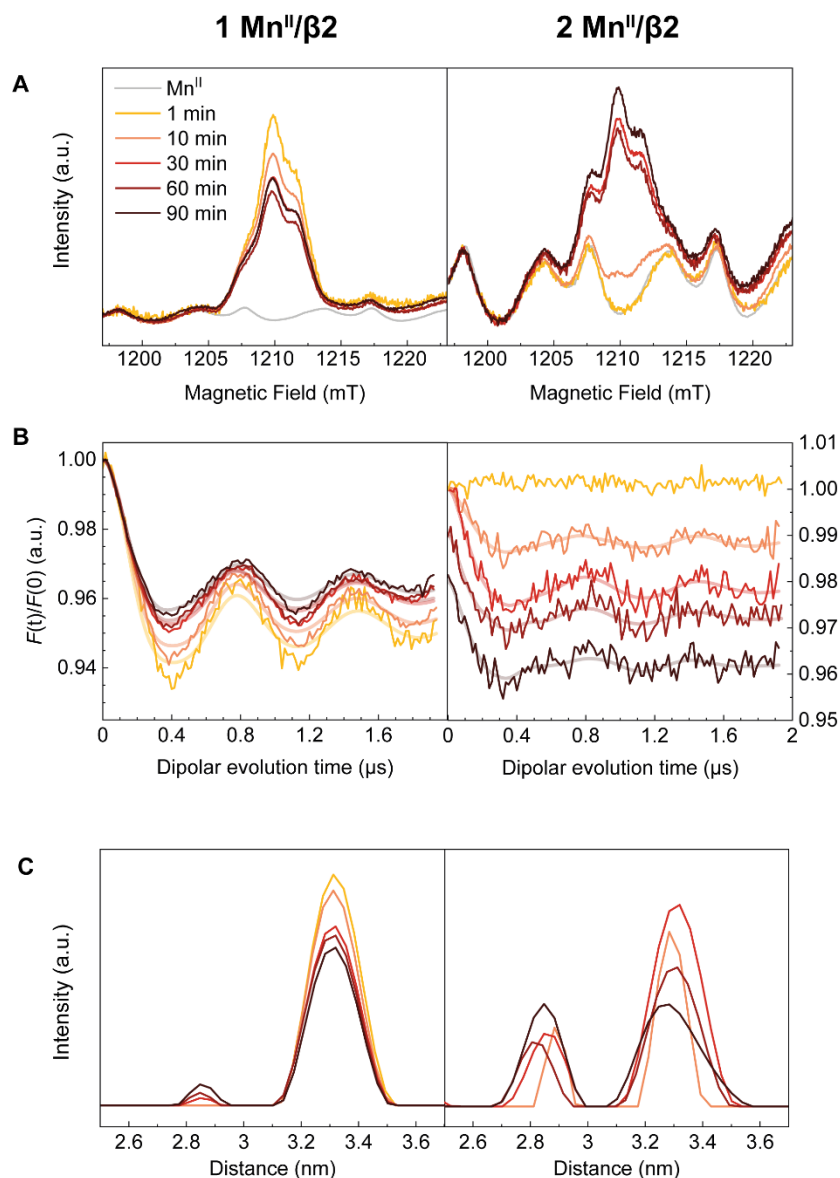
### Excluding concentration-dependent effects on radical recovery

Most of the EPR measurements were performed with samples of 150  $\mu\text{M}$  protein concentration. However, UV-Vis measurements contained 30  $\mu\text{M}$   $\beta\text{2}$ . To exclude a concentration-dependent effect, the same experiments were performed with 150  $\mu\text{M}$  but, this time, detected by the Nanodrop 2000 because of technical constraints of the Jasco V-650. The protein concentration does not affect radical yields and the time-dependent radical recovery (**Figure B.8**).



**Figure B.8:** Time-dependent detection of the  $\text{Y}_{122}\bullet/\beta\text{2}$  yield as a function of added  $\text{Mn}^{\text{II}}$ . Time-dependent radical formation was investigated for samples with either 30  $\mu\text{M}$  protein concentration (left, also shown in **Figure 4.10**) or 150  $\mu\text{M}$  (right). Samples with 150  $\mu\text{M}$  protein concentration were investigated via UV-Vis spectroscopy using the Nanodrop 2000. Mean values and standard deviations of 2 – 6 repeats are shown.

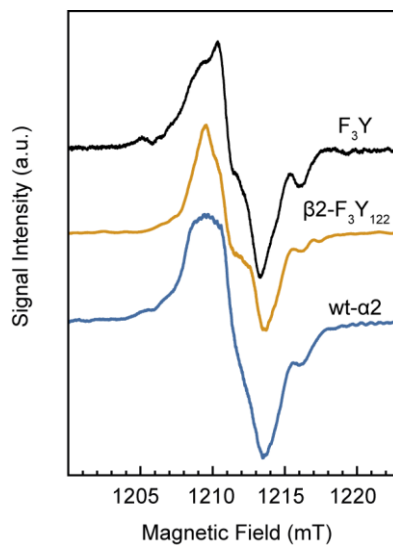
## Time-dependent radical recovery monitored by DEER measurements



**Figure B.9:** Reaction of *E. coli* RNR supplemented with 1 or 2 equivalents of  $\text{Mn}^{\text{II}}$  per  $\beta 2$ , followed by the addition of 5 equivalents  $\text{Fe}^{\text{II}}$ , monitored over time. Samples were frozen in liquid  $\text{N}_2$  after 1, 10, 30, 60, and 90 min of iron additions. Subsequently, time-dependent DEER measurements were performed at 34 GHz and 10 K. **(A)** Refocused echoes. **(B)** Background- and phase-corrected, normalized DEER time traces are shown in dark colors. Fits obtained by DeerAnalysis using Tikhonov regularization are overlaid and displayed in paler shade. For 2 eq.  $\text{Mn}^{\text{II}}/\beta 2$  DEER traces were shifted vertically for better visualization. **(C)** Obtained distance distributions. Experimental conditions: Gaussian pulses,  $\pi_{\text{det}} = 70$  ns;  $\pi_{\text{pump}} = 28$  ns;  $\text{srt} = 4$  ms;  $\text{spp} = 100$ . Acquisition time between 14 and 21 h for each trace.

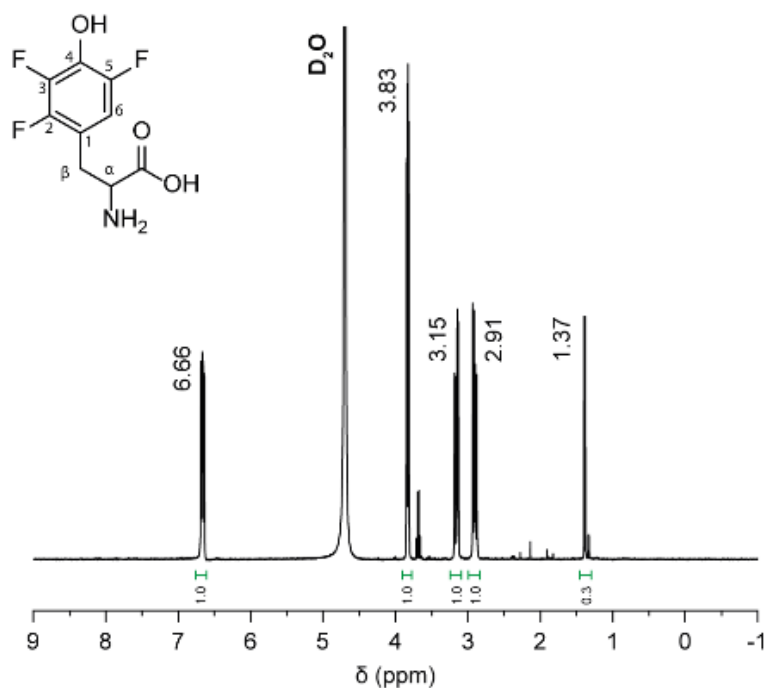
## C. Supporting information to Chapter 5

### Photolysis investigated by 34 GHz measurements



**Figure C.1:** First-derivative 34 GHz pulse EPR spectra of photolyzed 2,3,5-trifluorotyrosine (F<sub>3</sub>Y), *E. coli* RNR β<sub>2</sub>-F<sub>3</sub>Y<sub>122</sub>, and *E. coli* RNR α<sub>2</sub>. Photolysis was performed in the home-build irradiation setup in liquid nitrogen. Irradiation was conducted for 75 min by using a LOT LSB610U 100 W Hg arc lamp. Data were collected in the course of the Bachelor thesis from Dustin Schlüter.

## D. Supporting information to Chapter 8

NMR spectra of 2,3,5-F<sub>3</sub>Y

**Figure D.1:** <sup>1</sup>H-NMR of 2,3,5-F<sub>3</sub>Y. <sup>1</sup>H-NMR (400 MHz, D<sub>2</sub>O) δ (ppm) = 2.91 (dd, 1 H, Cβ (CH<sub>2</sub>), J = 14.9 MHz), 3.15 (m, 1 H, Cβ (CH<sub>2</sub>), J = 14.9 MHz), 3.83 (dd, 1 H, Cα (CH), J = 5.1 MHz), 4.75 (solvent), 6.66 (ddd, 1 H, C6 (CH), J = 11.6 MHz, J = 4.8 MHz). OH- and NH<sub>2</sub>-groups are not resolved in D<sub>2</sub>O.

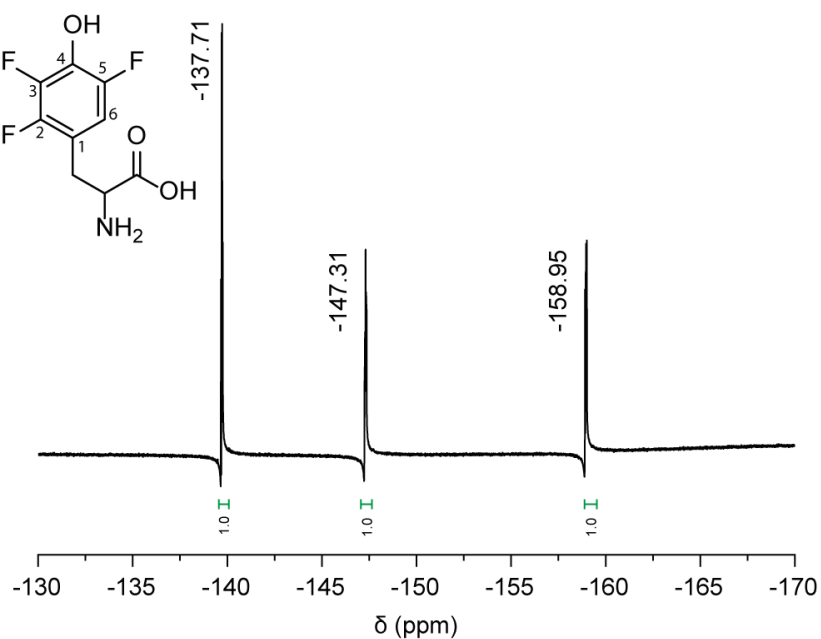


**Figure D.2:** <sup>19</sup>F-NMR of 2,3,5-F<sub>3</sub>Y. <sup>19</sup>F-NMR (377 MHz, D<sub>2</sub>O) δ (ppm) = -137.71 (1 F, C2 (CF)), -147.31 (1 F, C5 (CF)), -158.95 (1 F, C3 (CF)).

## Abbreviations

$\alpha$	Class I RNR large subunit	EPR	Electron paramagnetic resonance
Ado	Adenosyl		
Amp	Ampicillin	Eq.	Equivalents
a.u.	Arbitrary unit	ESE	Electron spin echo
azF	4-Azido-L-phenylalanine	ESR	Electron spin resonance
$\beta$	Class I RNR small subunit	<i>Et al.</i>	Et alii, Latin: and others
BNAH	1-Benzyl-1,4-dihydro-nicotinamide	FID	Free induction decay
Carb	Carbenicillin	F <sub>n</sub> Y	Fluorotyrosine ( $n = 1 - 4$ )
Cm	Chloramphenicol	FWHM	Full width at half maximum
Cryo-EM	Cryo-electron microscopy	Hfc	Hyperfine coupling
cw	Continuous wave	(His) <sub>6</sub>	Polyhistidine-tag
DEER	Double electron-electron resonance spectroscopy	IF	4-iodophenylalanine
DFT	Density functional theory	IPTG	Isopropyl-1-thio- $\beta$ -galactopyranoside
dHis	Double-histidine motif	Km	Kanamycin
DNA	Deoxyribonucleic acid	LaserIMD	Laser-induced magnetic dipolar spectroscopy
dNDP	Deoxynucleotide diphosphate	LB	Luria-Bertani broth
dNTP	Deoxynucleotide triphosphate	LiDEER	Light-induced double electron-electron resonance spectroscopy
DMB	Dimethylbenzimidazole	LITTER	Light-induced triplet-triplet electron resonance spectroscopy
DOPA	3,4-dihydroxy-phenylalanine	MTSSL	Methanethiosulfonate spin label
DOTA	Dodecane tetraacetic acid	mw	Microwave
DQC	Double quantum coherence	NA	Not available
DTT	Dithiothreitol	NADPH	$\beta$ -Nicotinamide adenine dinucleotide phosphate, reduced form
<i>E. coli</i>	<i>Escherichia coli</i>	ncAA	Non-canonical amino acid
EDTA	Ethylenediaminetetraacetic acid	N <sub>3</sub> CDP	2'-azido-2'-deoxycytidine-5'-diphosphate
ENDOR	Electron-nuclear double resonance		
EPL	Expressed protein ligation		

Appendix

N <sub>3</sub> NDP	2'-azido-2'-deoxy-nucleotide-5'-diphosphate	SEC	Size exclusion chromatography
N <sub>3</sub> UDP	2'-azido-2'-deoxyuridine-5'-diphosphate	SF	Stopped flow
NDP	Nucleotide diphosphates	S/N	Signal-to-noise ratio
NH <sub>2</sub> Y	3-aminotyrosine	S.O.C.	Super optimal broth with catabolite repression
Ni-NTA	Nickel nitriloacetic acid	spp	Shots per point
NIR	Near-infrared	srt	Shot repetition time
NMR	Nuclear magnetic resonance	TLC	Thin layer chromatography
NO <sub>2</sub> Y	3-nitrotyrosine	TPL	Tyrosine phenol lyase
NTA	Nitrilotriacetic acid	TPP	5-(4-carboxyphenyl)-10,15,20-
NTP	Nucleotide triphosphate		triphenylporphyrin
OD	Optical density		
O.D.	Outer diameter	Tris	Tris(hydroxymethyl)-aminoethane
PaNDA	Photoactivatable Nitroxide for inverse-electron-demand Diels-Alder reaction	U	Enzyme unit
PCET	Proton-coupled electron transfer	UAA	Unnatural amino acid
PDB	Protein data bank	wt	Wild-type
PELDOR	Pulsed electron-electron double resonance	WURST	Wideband, uniform rate, smooth truncation
PMSF	Phenylmethylsulfonyl fluoride	Y•	Tyrosyl radical
RF	Radiofrequency	ZFS	Zero-field splitting
RFQ	Rapid freeze-quench	2PESEEM	Two pulse electron spin echo envelope modulation
RIDME	Relaxation-Induced Dipolar Modulation Enhancement		
RMSD	Root-mean-square deviation		
RNR	Ribonucleotide reductase		
RS	tRNA synthetase		
RT	Room temperature		
SAM	S-adenosylmethionine		
SDSL	Site-directed spin labeling		
SDS-PAGE	Sodium dodecyl sulfate polyacrylamide gel electrophoresis		

## List of figures

1.1	Reaction catalyzed by ribonucleotide reductases. ....	1
1.2	Different classes of RNR based on the required metallocofactor for Cys• formation.....	2
1.3	Cofactor assembly mechanisms in different class I RNRs. ....	3
1.4	Structure of the <i>E. coli</i> class Ia RNR. ....	5
1.5	Schematic representation of allosteric regulation of <i>E. coli</i> class Ia RNR via ATP and dATP binding. ....	6
1.6	Overview of UAA usage in RNR.....	8
1.7	Proposed relative reduction potentials of unnatural amino acids substituting residues on the radical transfer pathway in <i>E. coli</i> RNR. ....	9
1.8	Distances between redox-active amino acids in <i>E. coli</i> class Ia RNR. ....	10
1.9	<i>E. coli</i> class Ia RNR reaction mechanism. ....	11
1.10	Estimated relative reduction potentials of residues involved in the radical transfer mechanism. ....	12
1.11	Current model of the radical transfer pathway in <i>E. coli</i> class Ia RNR, including redox-active amino acids Y <sub>122</sub> , Y <sub>356</sub> , Y <sub>731</sub> , Y <sub>730</sub> , and C <sub>439</sub> .....	14
1.12	Unnatural amino acid incorporation through <i>in vivo</i> nonsense codon suppression method. ....	15
1.13	Two or none radical distribution in <i>E. coli</i> class Ia RNR. ....	16
1.14	Schematic representation of the half-sites reactivity in <i>E. coli</i> RNR. ....	17
2.1	Electron Zeeman splitting of the energy levels of an electron spin with $S = 1/2$ in the absence and presence of magnetic field $B_0$ . ....	25
2.2	Dipole-dipole interactions. ....	29
2.3	Nuclear quadrupole interactions.....	30
2.4	The Hahn echo sequence, consisting of two pulses leading to the electron spin echo (ESE). ....	34
2.5	2PESEEM pulse sequence.....	35
2.6	Double electron-electron resonance spectroscopy.....	36
2.7	Electron-nuclear resonance spectroscopy. ....	38
2.8	Detected transitions in cw-EPR and ENDOR experiments. ....	39
2.9	Overview of different spin labels covered in this section. ....	40
2.10	LiDEER and LaserIMD pulse sequence.....	43
3.1	Fluorescence images of the $\beta 2$ subunit of <i>E. coli</i> class Ia RNR in living HeLa cells or in a cell-mimicking system.....	48
3.2	SDS-PAGE and cw-EPR analysis of <i>E. coli</i> in-cell samples under different treatment conditions.....	54

3.3	Multi-frequency EPR spectra of Y <sub>122</sub> • in whole <i>E. coli</i> cells. ....	55
3.4	Orientation-selective <sup>1</sup> H Davies ENDOR of Y <sub>122</sub> •. ....	58
3.5	Orientation-averaged time traces for Y <sub>122</sub> •-Y <sub>122</sub> • in <i>E. coli</i> RNR for in-cell and <i>in vitro</i> . ....	59
3.6	DEER measurements of <i>E. coli</i> cells that contain overexpressed apo wt-β2 (blue) or lack it (black) at 34 GHz and 10 K. ....	60
3.7	Analysis of 34 GHz orientation-selective DEER data of Y <sub>122</sub> •-Y <sub>122</sub> • in <i>E. coli</i> RNR <i>in vitro</i> . ....	63
3.8	34 GHz ESE spectra of Y <sub>122</sub> • and Mn <sup>II</sup> in different samples. ....	64
3.9	Refocused spin echo field sweep experiments with pump pulse on or off. ....	65
3.10	Modulation depth analysis of <i>in vitro</i> β2 samples containing different equivalents of Mn <sup>II</sup> compared to in-cell samples. ....	67
3.11	Cw-EPR spectra of in-cell samples supplemented with chloroform showing signal intensities as a function of chloroform content. ....	68
3.12	ESE spectra of Y <sub>122</sub> • in <i>E. coli</i> cells measured at 94 GHz. ....	69
3.13	SDS-PAGE analysis of the supernatant of <i>E. coli</i> cells treated with different amounts of chloroform. ....	70
3.14	Cw- and derivative pulse EPR spectra of F <sub>3</sub> Y <sub>122</sub> • measured at 9.6 and 34 GHz. ....	71
3.15	Distance determination between the F <sub>3</sub> Y <sub>122</sub> •-F <sub>3</sub> Y <sub>122</sub> • pair in <i>E. coli</i> RNR. ....	73
3.16	34 GHz ESE spectra of F <sub>3</sub> Y <sub>122</sub> •-β2 expressed under different conditions. ....	75
3.17	34 GHz DEER measurements of F <sub>3</sub> Y <sub>122</sub> • expressed in <i>E. coli</i> BL21(DE3)-Gold or TOP10 cells. ....	76
3.18	An outlook for trapping of Y <sub>356</sub> • investigated by 34 GHz ESE spectra. ....	78
4.1	Detect and pump position used for DEER experiments in this chapter. ....	84
4.2	Different parameters monitored during 20 h wt-β2 expression in <i>E. coli</i> cells. ....	85
4.3	Modulation depth analysis of in-cell samples expressing the β2-subunit of <i>E. coli</i> RNR under iron-chelated and iron-available conditions. ....	87
4.4	Iron or manganese bound in the homodimeric β2 subunit of <i>E. coli</i> RNR. ....	88
4.5	Cw-EPR spectrum before and after adding Fe <sup>II</sup> to Mn <sup>II</sup> -bound <i>E. coli</i> RNR. ....	90
4.6	Detection of a Y <sub>122</sub> •-Mn <sup>II</sup> Mn <sup>II</sup> distance in <i>E. coli</i> RNR via DEER measurements. ....	91
4.7	ESE spectra of Mn <sup>II</sup> added to Y <sub>122</sub> • in <i>E. coli</i> RNR performed at 34 GHz and 10 K depending on the microwave pulse power applied. ....	92
4.8	Power-dependent DEER experiments for Mn <sup>II</sup> -bound <i>E. coli</i> class Ia RNR, proving a Y <sub>122</sub> •-Mn <sup>II</sup> Mn <sup>II</sup> distance. ....	93
4.9	Calibration curve for <i>E. coli</i> RNR <i>in vitro</i> prepared under different metal-availabilities, mimicking cellular conditions. ....	95
4.10	Influence of Mn <sup>II</sup> on the time-dependent radical formation of Y <sub>122</sub> • in <i>E. coli</i> RNR. ....	96

4.11	Time-dependent detection of the $Y_{122}\bullet/\beta_2$ yield in the presence and absence of 1 $Mn^{II}/\beta_2$ , obtained via UV-Vis measurements. ....	97
4.12	Percentage of free $Mn^{II}$ before (0 min), directly after (1 min), and 2 h after the addition of $Fe^{II}$ to <i>E. coli</i> RNR. ....	98
4.13	The effect of further addition of $Fe^{II}$ to $Mn^{II}$ -mismetallated RNR $\beta_2$ . ....	98
4.14	5 equivalents of iron and manganese added simultaneously to apo- $\beta_2$ . ....	99
4.15	Power-dependent DEER experiments for samples in which iron and manganese were added simultaneously to apo- $\beta_2$ . ....	100
4.16	<i>E. coli</i> class Ia RNR recovers from $Mn^{II}$ mismetallation via metal release and scrambling. ....	102
4.17	Detection of oligomeric states of the $\beta_2$ subunit in <i>E. coli</i> RNR upon mismetallation. ....	103
4.18	Probing the catalytic activity of mismetallated RNR using the $N_3$ CDP assay, monitoring the $Y_{122}\bullet$ decay. ....	104
4.19	Determination of the catalytic activity of mismetallated RNR using the $N_3$ CDP assay, monitoring $N\bullet$ formation. ....	105
4.20	<i>E. coli</i> RNR complex assembly investigated by size exclusion chromatography. ....	106
4.21	SDS-PAGE of fractions obtained after size exclusion column of <i>E. coli</i> supplemented with 0 $Mn^{II}/\beta_2$ (left) and 4 $Mn^{II}/\beta_2$ (right). ....	107
4.22	Fraction of peaks detected by size exclusion chromatography. ....	108
5.1	9.6 GHz cw-EPR spectra of different amino acid radicals formed via photolysis at 100 K. ....	115
5.2	X-band studies of the photolysis product of 4-azido-L-phenylalanine. ....	116
5.3	EPR investigation of azidophenylalanine in different environments. ....	118
5.4	Analysis of generated triplet species. ....	119
5.5	Background-corrected 3-pulse DEER trace of azF <sub>122</sub> - $\beta_2$ detected at 450 mT and 34 GHz. ....	120
6.1	Exemplary <i>p,T</i> -stability diagram of SNase at pH 5.5. ....	123
6.2	Exemplarily folding funnel for $\beta$ -lactoglobulin with the five major conformations: native (N), the low-lying excited state (N'), two intermediate states (I <sub>1</sub> and I <sub>2</sub> ), and the unfolded state (U). ....	124
6.3	Pulse EPR spectra of $Y_{122}\bullet$ in the $\beta_2$ -subunit of <i>E. coli</i> RNR as a function of glycerol content in the buffer, recorded at 34 GHz and 10 K. ....	127
6.4	DEER distance measurements for <i>E. coli</i> RNR supplemented with different amounts of glycerol. ....	128
6.5	Analysis of obtained distances. ....	130
6.6	Trimers (top row) and tetramers (bottom row) of the $\beta$ -subunit of <i>E. coli</i> RNR. ....	132
6.7	Pulse EPR spectra of $Y_{122}\bullet$ in the $\beta_2$ -subunit of <i>E. coli</i> RNR under pressure, recorded at 34 GHz and 10 K. ....	133

6.8	First derivative spectra of $Y_{122}^{\bullet}$ and an unknown radical species, recorded at 34 GHz and 10 K. ....	134
6.9	Simulation of the radical species. ....	135
6.10	Tyrosine $Y_{122}$ and $Y_{78}$ in <i>E. coli</i> class Ia RNR. ....	136
6.11	DEER distance measurements of <i>E. coli</i> RNR under ambient (0 kbar, black) or 2 kbar (turquoise) pressure. ....	138
7.1	Structures of Fullerene $C_{60}$ and the coordination cage. ....	143
7.2	The one-electron photoreduction of $C_{60}$ by BNAH. ....	145
7.3	Cw-EPR control experiments of different compounds performed at X-band under aerobic conditions. ....	146
7.4	X-band EPR analysis of generated radicals. ....	147
7.5	Power saturation behavior of generated radicals. ....	149
7.6	Half-lifetime determination of $C_{60}^{\bullet-}$ . ....	150
7.7	Relative weight of $C_{60}^{\bullet-}$ (blue) and its oxygenated species (yellow) in samples produced under aerobic conditions as determined by spectral simulations. ....	151
7.8	Half-lifetimes of $C_{60}^{\bullet-}$ under different conditions. ....	152
A.1	DEER measurements of $Y_{122}^{\bullet}$ in <i>E. coli</i> RNR performed at 34 GHz and 10 K. (A) ESE-detected EPR spectrum of in-cell sample 1 recorded at 10 K. ....	167
A.2	Analysis of orientation-selective DEER data of $Y_{122}^{\bullet}$ - $Y_{122}^{\bullet}$ in <i>E. coli</i> RNR <i>in vitro</i> . ....	169
A.3	Analysis of orientation-selective DEER data of $Y_{122}^{\bullet}$ - $Y_{122}^{\bullet}$ in <i>E. coli</i> RNR inside cells. ....	170
A.4	$T_m$ measurements. ....	171
A.5	Modulation depth analysis of <i>in vitro</i> $\beta 2$ mimic and in-cell samples compared to pure <i>E. coli</i> cells. ....	172
A.6	$T_m$ measurements of samples presented in Figure A.5. ....	172
A.7	34 GHz ESE spectra of in-cell samples supplemented with chloroform. ....	173
A.8	Background correction for the in-cell $Y_{122}^{\bullet}$ EPR spectra detected via primary spin echo at W-band. ....	174
A.9	DEER measurements of $F_3Y_{122}^{\bullet}$ in <i>E. coli</i> RNR performed at 34 GHz and 10 K. ....	176
B.1	TLC plate to monitor the dephosphorylation of $N_3CTP$ . ....	177
B.2	Modulation depth analysis of in-cell samples expressing the $\beta 2$ -subunit of <i>E. coli</i> RNR under iron-chelated and iron-available conditions. ....	178
B.3	Manganese-bound <i>E. coli</i> class Ia $\beta 2$ RNR. ....	179
B.4	DEER measurements of $Y_{122}^{\bullet}$ in <i>E. coli</i> RNR with different equivalents of $Mn^{II}$ added, performed at 34 GHz and 10 K. ....	180
B.5	UV-Vis measurements of $Fe^{II}$ solutions and <i>E. coli</i> RNR $\beta 2$ in the Fe- or Mn-bound state. ....	181
B.6	DEER experiments of manganese-bound $\beta 2$ (30 $\mu M$ ) after first (5 eq. $Mn^{II}$ ) and second (10 eq. $Mn^{II}$ ) iron addition. ....	181

B.7	Apo- $\beta$ 2 (150 $\mu$ M) of <i>E. coli</i> RNR treated with iron and manganese in two different ways.....	182
B.8	Time-dependent detection of the $Y_{122}\bullet/\beta$ 2 yield as a function of added $Mn^{II}$ .	183
B.9	Reaction of <i>E. coli</i> RNR supplemented with 1 or 2 equivalents of $Mn^{II}$ per $\beta$ 2, followed by the addition of 5 equivalents $Fe^{II}$ , monitored over time.....	184
C.1	First-derivative 34 GHz pulse EPR spectra of photolyzed 2,3,5-trifluorotyrosine ( $F_3Y$ ), <i>E. coli</i> RNR $\beta$ 2- $F_3Y_{122}$ , and <i>E. coli</i> RNR $\alpha$ 2. ....	185
D.1	$^1H$ -NMR of 2,3,5- $F_3Y$ .....	186
D.2	$^{19}F$ -NMR of 2,3,5- $F_3Y$ .....	186

## List of tables

3.1	Samples used in Chapter 3. ....	52
3.2	$^1\text{H}$ Hyperfine coupling parameters used for spectral simulations of multi-frequency EPR spectra of $\text{Y}_{122}\bullet$ in whole <i>E. coli</i> cells. ....	56
3.3	$\text{Y}_{122}\bullet$ - $\text{Y}_{122}\bullet$ pair distance analysis derived from DEER experiments using PeldorFit. ....	62
3.4	Hyperfine coupling parameters used for spectral simulations of multi-frequency EPR spectra of $2,3,5\text{-F}_3\text{Y}_{122}\bullet$ in whole <i>E. coli</i> cells. ....	72
3.5	$\text{C}\beta$ -proton hyperfine couplings for $2,3,5\text{-F}_3\text{Y}_{122}\text{-}\beta 2$ IN and OUT conformers as determined by Oyala <i>et al.</i> <sup>38</sup> ....	74
4.1	$\text{Y}_{122}\bullet$ yield, $\text{Mn}^{\text{II}}$ and OD600 of <i>E. coli</i> in-cell samples expressing wt- $\beta 2$ RNR for 4 h under iron chelated and iron available conditions. ....	81
6.1	Simulation parameters. ....	137
8.1	Bacterial strains used in this work. ....	154
8.2	Plasmids used in this work. ....	155
8.3	Laboratory equipment in alphabetical order. ....	155
8.4	Commercial kits and ready-to-use mixtures in alphabetical order. ....	156
8.5	Chemicals and CAS registry numbers. ....	157
8.6	Software utilized in this work. ....	159
A.1	$\text{Y}_{122}\bullet$ - $\text{Y}_{122}\bullet$ <i>in vitro</i> pair analysis derived from DEER experiments using PeldorFit. ....	168
A.2	$\text{Y}_{122}\bullet$ - $\text{Y}_{122}\bullet$ in-cell pair analysis derived from DEER experiments using PeldorFit. ....	171
B.1	Possible distances obtained by the crystal structures in Figure B.3. ....	179

## Acknowledgments

First of all, I would like to thank my PhD supervisor *Prof. Dr. Müge Kasanmascheff*. Although I joined the group without any prior knowledge about EPR, she always believed in me and supported me. This support already started in my first month of work when she kindly allowed me to learn protein purification at MIT. Thank you so much for this extraordinary opportunity. She was the source of ideas for all projects and always had good advice at hand. I would also like to thank her for always being open to my ideas and suggestions while judging them fairly and critically. Nevertheless, she gave me the freedom to develop myself at work.

I would also like to thank my second doctoral supervisor, *Prof. Dr. Daniel Summerer* from TU Dortmund. He kindly allowed me to use his entire laboratory. Therefore, this work would never have been possible without his support. Furthermore, I would like to thank him for agreeing to the second appraisal of this work.

Furthermore, I would like to thank all of my coworkers in the Kasanmscheff lab for the great time I was allowed to spend with the group. I appreciate our relaxed atmosphere and have always found an open ear with you. I would especially like to thank *Dr. Yury Kutin*, who helped me learn EPR from the very beginning. I admire your patience and accuracy in your work, which have always been a great inspiration for me. Finally, thanks also go to *Melanie Heghmanns* and *Simon Schumann* for the many fun evenings with you.

Afterward, I thank all the members of the Summerer lab, who helped me with any question quickly and in a friendly manner. I would like to mention *Dr. Benjamin Buchmuller*, *Damian Schiller*, and *Lena Engelhard*, who were particularly helpful. In addition, special thanks go to the lab's research technicians *Simone Eppmann* and *Nadine Schmidt*. They always had to adjust to the large quantities of medium I needed and were always there to help me without ever complaining.

I would also like to thank *Prof. Dr. JoAnne Stubbe* and her group members for introducing me to the beautiful world of RNR. The month I spent there in her group laid the foundation to do any further work. Her passion for work and RNR, in particular, is boundless and serves as an example to me.

Even though *Prof. Dr. Roland Winter* and *Prof. Dr. Claus Czeslik* from TU Dortmund did not directly contribute to the development of this thesis, I would like to thank them. It

was through them that I found my passion for physical chemistry and my way into the group of Müge Kasanmascheff.

Moreover, I would like to thank *Dr. Lennart Poppe*, who kindly agreed to proofread my work. I thank *Maria Sergani* and *Andrea Jeworrek* for handling all administrative affairs. I gratefully acknowledge funding from TU Dortmund University and the cluster of excellence RESOLV.

Of course, I would also like to thank people from my private environment who mostly encouraged me mentally rather than scientifically. The most important person is my mother, *Carmen*, who supports me unconditionally as far as she can and beyond. I would also like to thank *Hendrik*, who has bravely endured many outbursts of despair. Also, I can not thank all of my friends enough. Especially *Janine* and *Jessica* were always able to give me good advice, not only as friends but also as competent colleagues.

## References

1. Stubbe, J. A. Protein radical involvement in biological catalysis? *Annual review of biochemistry* **58**, 257–285; 10.1146/annurev.bi.58.070189.001353 (1989).
2. Jordan, A. & Reichard, P. Ribonucleotide reductases. *Annual review of biochemistry* **67**, 71–98; 10.1146/annurev.biochem.67.1.71 (1998).
3. Stubbe, J. & van der Donk, W. A. Protein Radicals in Enzyme Catalysis. *Chemical reviews* **98**, 705–762; 10.1021/cr9400875 (1998).
4. Nordlund, P. & Reichard, P. Ribonucleotide reductases. *Annual review of biochemistry* **75**, 681–706; 10.1146/annurev.biochem.75.103004.142443 (2006).
5. Zimanyi, C. M., Chen, P. Y., Kang, G., Funk, M. A. & Drennan, C. L. Molecular basis for allosteric specificity regulation in class Ia ribonucleotide reductase from *Escherichia coli*. *eLife Sciences Publications, Ltd* (2016).
6. Elledge, S. J., Zhou, Z. & Allen, J. B. Ribonucleotide reductase: regulation, regulation, regulation. *Trends in biochemical sciences* **17**, 119–123; 10.1016/0968-0004(92)90249-9 (1992).
7. Greene, B. L. *et al.* Ribonucleotide Reductases: Structure, Chemistry, and Metabolism Suggest New Therapeutic Targets. *Annual review of biochemistry* **89**, 45–75; 10.1146/annurev-biochem-013118-111843 (2020).
8. Aye, Y., Li, M., Long, M. J. C. & Weiss, R. S. Ribonucleotide reductase and cancer: biological mechanisms and targeted therapies. *Oncogene* **34**, 2011–2021; 10.1038/onc.2014.155 (2015).
9. Shao, J., Zhou, B., Chu, B. & Yen, Y. Ribonucleotide reductase inhibitors and future drug design. *Current cancer drug targets* **6**, 409–431; 10.2174/15680090677723949 (2006).
10. Duan, J. *et al.* Antiviral activity of a selective ribonucleotide reductase inhibitor against acyclovir-resistant herpes simplex virus type 1 in vivo. *Antimicrobial agents and chemotherapy* **42**, 1629–1635; 10.1128/AAC.42.7.1629 (1998).
11. Dutia, B. M., Frame, M. C., Subak-Sharpe, J. H., Clark, W. N. & Marsden, H. S. Specific inhibition of herpesvirus ribonucleotide reductase by synthetic peptides. *Nature* **321**, 439–441; 10.1038/321439a0 (1986).
12. Narasimhan, J. *et al.* Ribonucleotide reductase, a novel drug target for gonorrhoea. *eLife* **11**; 10.7554/eLife.67447 (2022).

13. Ruskoski, T. B. & Boal, A. K. The periodic table of ribonucleotide reductases. *The Journal of biological chemistry* **297**, 101137; 10.1016/j.jbc.2021.101137 (2021).
14. Tomter, A. B. *et al.* Ribonucleotide reductase class I with different radical generating clusters. *Coordination Chemistry Reviews* **257**, 3–26; 10.1016/j.ccr.2012.05.021 (2013).
15. M. Kolberg, K. Strand, P. Graff & K. Andersson. Structure, function, and mechanism of ribonucleotide reductases. *undefined* (2004).
16. Atkin, C. L., Thelander, L., Reichard, P. & Lang, G. Iron and Free Radical in Ribonucleotide Reductase. *Journal of Biological Chemistry* **248**, 7464–7472; 10.1016/S0021-9258(19)43313-9 (1973).
17. Cotruvo, J. A. & Stubbe, J. An active dimanganese(III)-tyrosyl radical cofactor in Escherichia coli class Ib ribonucleotide reductase. *Biochemistry* **49**, 1297–1309; 10.1021/bi902106n (2010).
18. Cotruvo, J. A. & Stubbe, J. Escherichia coli class Ib ribonucleotide reductase contains a dimanganese(III)-tyrosyl radical cofactor in vivo. *Biochemistry* **50**, 1672–1681; 10.1021/bi101881d (2011).
19. Hammerstad, M. *et al.* The class Ib ribonucleotide reductase from Mycobacterium tuberculosis has two active R2F subunits. *J Biol Inorg Chem* **19**, 893–902; 10.1007/s00775-014-1121-x (2014).
20. Jiang, W., Bollinger, J. M. & Krebs, C. The active form of Chlamydia trachomatis ribonucleotide reductase R2 protein contains a heterodinuclear Mn(IV)/Fe(III) cluster with S = 1 ground state. *Journal of the American Chemical Society* **129**, 7504–7505; 10.1021/ja072528a (2007).
21. Kutin, Y. *et al.* Divergent assembly mechanisms of the manganese/iron cofactors in R2lox and R2c proteins. *Journal of Inorganic Biochemistry* **162**, 164–177; 10.1016/j.jinorgbio.2016.04.019 (2016).
22. Dassama, L. M. K., Krebs, C., Bollinger, J. M., Rosenzweig, A. C. & Boal, A. K. Structural basis for assembly of the Mn(IV)/Fe(III) cofactor in the class Ic ribonucleotide reductase from Chlamydia trachomatis. *Biochemistry* **52**, 6424–6436; 10.1021/bi400819x (2013).
23. Rose, H. R. *et al.* Structural Basis for Superoxide Activation of Flavobacterium johnsoniae Class I Ribonucleotide Reductase and for Radical Initiation by Its Dimanganese Cofactor. *Biochemistry* **57**, 2679–2693; 10.1021/acs.biochem.8b00247 (2018).
24. Rozman Grinberg, I. *et al.* Novel ATP-cone-driven allosteric regulation of ribonucleotide reductase via the radical-generating subunit. *eLife* **7**; 10.7554/eLife.31529 (2018).

25. Srinivas, V. *et al.* Metal-free ribonucleotide reduction powered by a DOPA radical in *Mycoplasma* pathogens. *Nature* **563**, 416–420; 10.1038/s41586-018-0653-6 (2018).
26. Blaesi, E. J. *et al.* Metal-free class Ie ribonucleotide reductase from pathogens initiates catalysis with a tyrosine-derived dihydroxyphenylalanine radical. *Proceedings of the National Academy of Sciences of the United States of America* **115**, 10022–10027; 10.1073/pnas.1811993115 (2018).
27. Reichard, P., Baldesten, A. & Rutberg, L. Formation of Deoxycytidine Phosphates from Cytidine Phosphates in Extracts from *Escherichia coli*. *Journal of Biological Chemistry* **236**, 1150–1157; 10.1016/S0021-9258(18)64258-9 (1961).
28. Eriksson, M. *et al.* Binding of allosteric effectors to ribonucleotide reductase protein R1: reduction of active-site cysteines promotes substrate binding. *Structure* **5**, 1077–1092; 10.1016/S0969-2126(97)00259-1 (1997).
29. Uhlin, U. & Eklund, H. Structure of ribonucleotide reductase protein R1. *Nature* **370**, 533–539; 10.1038/370533a0 (1994).
30. Brown, N. C. & Reichard, P. Role of effector binding in allosteric control of ribonucleoside diphosphate reductase. *Journal of Molecular Biology* **46**, 39–55; 10.1016/0022-2836(69)90056-4 (1969).
31. Ando, N. *et al.* Structural interconversions modulate activity of *Escherichia coli* ribonucleotide reductase. *Proceedings of the National Academy of Sciences of the United States of America* **108**, 21046–21051; 10.1073/pnas.1112715108 (2011).
32. Thelander, L., Gräslund, A. & Thelander, M. Continual presence of oxygen and iron required for mammalian ribonucleotide reduction: Possible regulation mechanism. *Biochemical and biophysical research communications* **110**, 859–865; 10.1016/0006-291x(83)91040-9 (1983).
33. Aye, Y. & Stubbe, J. Clofarabine 5'-di and -triphosphates inhibit human ribonucleotide reductase by altering the quaternary structure of its large subunit. *Proceedings of the National Academy of Sciences of the United States of America* **108**, 9815–9820; 10.1073/pnas.1013274108 (2011).
34. Kang, G., Taguchi, A. T., Stubbe, J. & Drennan, C. L. Structure of a trapped radical transfer pathway within a ribonucleotide reductase holocomplex. *Science (New York, N.Y.)* **368**, 424–427; 10.1126/science.aba6794 (2020).
35. Oyala, P. H. *et al.* Biophysical Characterization of Fluorotyrosine Probes Site-Specifically Incorporated into Enzymes: *E. coli* Ribonucleotide Reductase As an Example. *J. Am. Chem. Soc.* **138**, 7951–7964; 10.1021/jacs.6b03605 (2016).
36. Brown, N. C., Canellakis, Z. N., Lundin, B., Reichard, P. & Thelander, L. Ribonucleoside diphosphate reductase. Purification of the two subunits, proteins

- B1 and B2. *European journal of biochemistry* **9**, 561–573; 10.1111/j.1432-1033.1969.tb00646.x (1969).
37. Ravichandran, K., Olshansky, L., Nocera, D. G. & Stubbe, J. Subunit Interaction Dynamics of Class Ia Ribonucleotide Reductases: In Search of a Robust Assay. *Biochemistry* **59**, 1442–1453; 10.1021/acs.biochem.0c00001 (2020).
38. Minnihan, E. C. *et al.* Generation of a stable, aminotyrosyl radical-induced  $\alpha\beta\gamma$  complex of Escherichia coli class Ia ribonucleotide reductase. *Proceedings of the National Academy of Sciences of the United States of America* **110**, 3835–3840; 10.1073/pnas.1220691110 (2013).
39. Brignole, E. J., Ando, N., Zimanyi, C. M. & Drennan, C. L. The prototypic class Ia ribonucleotide reductase from Escherichia coli: still surprising after all these years. *Biochemical Society transactions* **40**, 523–530; 10.1042/BST20120081 (2012).
40. Page, C. C., Moser, C. C., Chen, X. & Dutton, P. L. Natural engineering principles of electron tunnelling in biological oxidation-reduction. *Nature* **402**, 47–52; 10.1038/46972 (1999).
41. Stubbe, J., Nocera, D. G., Yee, C. S. & Chang, M. C. Y. Radical initiation in the class I ribonucleotide reductase: long-range proton-coupled electron transfer? *Chemical reviews* **103**, 2167–2201; 10.1021/cr020421u (2003).
42. Minnihan, E. C., Nocera, D. G. & Stubbe, J. Reversible, long-range radical transfer in E. coli class Ia ribonucleotide reductase. *Accounts of Chemical Research* **46**, 2524–2535; 10.1021/ar4000407 (2013).
43. Climent, I., Sjöberg, B. M. & Huang, C. Y. Site-directed mutagenesis and deletion of the carboxyl terminus of Escherichia coli ribonucleotide reductase protein R2. Effects on catalytic activity and subunit interaction. *Biochemistry* **31**, 4801–4807; 10.1021/bi00135a009 (1992).
44. Ekberg, M., Birgander, P. & Sjöberg, B. In vivo assay for low-activity mutant forms of Escherichia coli ribonucleotide reductase. *Journal of bacteriology* **185**, 1167–1173; 10.1128/JB.185.4.1167-1173.2003 (2003).
45. Nordlund, P. & Eklund, H. Structure and function of the Escherichia coli ribonucleotide reductase protein R2. *Journal of Molecular Biology* **232**, 123–164; 10.1006/jmbi.1993.1374 (1993).
46. Ekberg, M., Sahlin, M., Eriksson, M. & Sjöberg, B. M. Two conserved tyrosine residues in protein R1 participate in an intermolecular electron transfer in ribonucleotide reductase. *Journal of Biological Chemistry* **271**, 20655–20659; 10.1074/jbc.271.34.20655 (1996).

47. Ge, J., Yu, G., Ator, M. A. & Stubbe, J. Pre-steady-state and steady-state kinetic analysis of *E. coli* class I ribonucleotide reductase. *Biochemistry* **42**, 10071–10083; 10.1021/bi034374r (2003).
48. Normanly, J., Kleina, L. G., Masson, J.-M., Abelson, J. & Miller, J. H. Construction of *Escherichia coli* amber suppressor tRNA genes. *Journal of Molecular Biology* **213**, 719–726; 10.1016/S0022-2836(05)80258-X (1990).
49. Wang, L., Brock, A., Herberich, B. & Schultz, P. G. Expanding the genetic code of *Escherichia coli*. *Science* **292**, 498–500; 10.1126/science.1060077 (2001).
50. Wang, L., Magliery, T. J., Liu, D. R. & Schultz, P. G. A New Functional Suppressor tRNA/Aminoacyl-tRNA Synthetase Pair for the in Vivo Incorporation of Unnatural Amino Acids into Proteins. *J. Am. Chem. Soc.* **122**, 5010–5011; 10.1021/ja000595y (2000).
51. Yokoyama, K., Uhlin, U. & Stubbe, J. Site-specific incorporation of 3-nitrotyrosine as a probe of pKa perturbation of redox-active tyrosines in ribonucleotide reductase. *J. Am. Chem. Soc.* **132**, 8385–8397; 10.1021/ja101097p (2010).
52. Yee, C. S., Seyedsayamdost, M. R., Chang, M. C. Y., Nocera, D. G. & Stubbe, J. Generation of the R2 subunit of ribonucleotide reductase by intein chemistry: insertion of 3-nitrotyrosine at residue 356 as a probe of the radical initiation process. *Biochemistry* **42**, 14541–14552; 10.1021/bi0352365 (2003).
53. Seyedsayamdost, M. R. & Stubbe, J. Site-specific replacement of Y356 with 3,4-dihydroxyphenylalanine in the beta2 subunit of *E. coli* ribonucleotide reductase. *J. Am. Chem. Soc.* **128**, 2522–2523; 10.1021/ja057776q (2006).
54. Minnihhan, E. C., Seyedsayamdost, M. R., Uhlin, U. & Stubbe, J. Kinetics of radical intermediate formation and deoxynucleotide production in 3-aminotyrosine-substituted *Escherichia coli* ribonucleotide reductases. *J. Am. Chem. Soc.* **133**, 9430–9440; 10.1021/ja201640n (2011).
55. Seyedsayamdost, M. R., Xie, J., Chan, C. T. Y., Schultz, P. G. & Stubbe, J. Site-specific insertion of 3-aminotyrosine into subunit alpha2 of *E. coli* ribonucleotide reductase: direct evidence for involvement of Y730 and Y731 in radical propagation. *J. Am. Chem. Soc.* **129**, 15060–15071; 10.1021/ja076043y (2007).
56. Minnihhan, E. C., Young, D. D., Schultz, P. G. & Stubbe, J. Incorporation of fluorotyrosines into ribonucleotide reductase using an evolved, polyspecific aminoacyl-tRNA synthetase. *J. Am. Chem. Soc.* **133**, 15942–15945; 10.1021/ja207719f (2011).
57. Yee, C. S., Chang, M. C. Y., Ge, J., Nocera, D. G. & Stubbe, J. 2,3-difluorotyrosine at position 356 of ribonucleotide reductase R2: a probe of long-range proton-coupled electron transfer. *J. Am. Chem. Soc.* **125**, 10506–10507; 10.1021/ja036242r (2003).

58. Yokoyama, K., Smith, A. A., Corzilius, B., Griffin, R. G. & Stubbe, J. Equilibration of tyrosyl radicals (Y356•, Y731•, Y730•) in the radical propagation pathway of the Escherichia coli class Ia ribonucleotide reductase. *J. Am. Chem. Soc.* **133**, 18420–18432; 10.1021/ja207455k (2011).
59. Seyedsayamdost, M. R., Yee, C. S., Reece, S. Y., Nocera, D. G. & Stubbe, J. pH Rate profiles of FnY356-R2s (n = 2, 3, 4) in Escherichia coli ribonucleotide reductase: evidence that Y356 is a redox-active amino acid along the radical propagation pathway. *J. Am. Chem. Soc.* **128**, 1562–1568; 10.1021/ja055927j (2006).
60. Seyedsayamdost, M. R., Reece, S. Y., Nocera, D. G. & Stubbe, J. Mono-, di-, tri-, and tetra-substituted fluorotyrosines: new probes for enzymes that use tyrosyl radicals in catalysis. *J. Am. Chem. Soc.* **128**, 1569–1579; 10.1021/ja055926r (2006).
61. DeFelippis, M. R. *et al.* Electrochemical properties of tyrosine phenoxy and tryptophan indolyl radicals in peptides and amino acid analogs. *J. Phys. Chem.* **95**, 3416–3419; 10.1021/j100161a081 (1991).
62. Minnihan, E. C., Seyedsayamdost, M. R. & Stubbe, J. Use of 3-aminotyrosine to examine the pathway dependence of radical propagation in Escherichia coli ribonucleotide reductase. *Biochemistry* **48**, 12125–12132; 10.1021/bi901439w (2009).
63. Lee, W. *et al.* Properties of Site-Specifically Incorporated 3-Aminotyrosine in Proteins To Study Redox-Active Tyrosines: Escherichia coli Ribonucleotide Reductase as a Paradigm. *Biochemistry* **57**, 3402–3415; 10.1021/acs.biochem.8b00160 (2018).
64. Bennati, M. *et al.* Pulsed ELDOR spectroscopy measures the distance between the two tyrosyl radicals in the R2 subunit of the E. coli ribonucleotide reductase. *J. Am. Chem. Soc.* **125**, 14988–14989; 10.1021/ja0362095 (2003).
65. Seyedsayamdost, M. R., Chan, C. T. Y., Mugnaini, V., Stubbe, J. & Bennati, M. PELDOR spectroscopy with DOPA-beta2 and NH2Y-alpha2s: distance measurements between residues involved in the radical propagation pathway of E. coli ribonucleotide reductase. *J. Am. Chem. Soc.* **129**, 15748–15749; 10.1021/ja076459b (2007).
66. Sjöberg, B. M., Gräslund, A. & Eckstein, F. A substrate radical intermediate in the reaction between ribonucleotide reductase from Escherichia coli and 2'-azido-2'-deoxynucleoside diphosphates. *Journal of Biological Chemistry* **258**, 8060–8067 (1983).
67. van der Donk, W. A., Stubbe, J., Gerfen, G. J., Bellew, B. F. & Griffin, R. G. EPR Investigations of the Inactivation of E. coli Ribonucleotide Reductase with 2'-Azido-2'-deoxyuridine 5'-Diphosphate: Evidence for the Involvement of the Thiyl Radical of C225-R1. *J. Am. Chem. Soc.* **117**, 8908–8916; 10.1021/ja00140a003 (1995).

68. Bennati, M. *et al.* EPR distance measurements support a model for long-range radical initiation in E. coli ribonucleotide reductase. *J. Am. Chem. Soc.* **127**, 15014–15015; 10.1021/ja054991y (2005).
69. Fritscher, J. *et al.* Structure of the nitrogen-centered radical formed during inactivation of E. coli ribonucleotide reductase by 2'-azido-2'-deoxyuridine-5'-diphosphate: trapping of the 3'-ketonucleotide. *J. Am. Chem. Soc.* **127**, 7729–7738; 10.1021/ja043111x (2005).
70. Nick, T. U., Ravichandran, K. R., Stubbe, J., Kasanmascheff, M. & Bennati, M. Spectroscopic Evidence for a H Bond Network at Y356 Located at the Subunit Interface of Active E. coli Ribonucleotide Reductase. *Biochemistry* **56**, 3647–3656; 10.1021/acs.biochem.7b00462 (2017).
71. Tkach, I. *et al.* 1H high field electron-nuclear double resonance spectroscopy at 263 GHz/9.4 T. *Journal of magnetic resonance (San Diego, Calif. : 1997)* **303**, 17–27; 10.1016/j.jmr.2019.04.001 (2019).
72. Hecker, F., Stubbe, J. & Bennati, M. Detection of Water Molecules on the Radical Transfer Pathway of Ribonucleotide Reductase by 17O Electron-Nuclear Double Resonance Spectroscopy. *J. Am. Chem. Soc.* **143**, 7237–7241; 10.1021/jacs.1c01359 (2021).
73. Kasanmascheff, M., Lee, W., Nick, T. U., Stubbe, J. & Bennati, M. Radical transfer in E. coli ribonucleotide reductase: a NH2Y731/R411A- $\alpha$  mutant unmasks a new conformation of the pathway residue 731. *Chem. Sci.* **7**, 2170–2178; 10.1039/C5SC03460D (2016).
74. Meyer, A. *et al.* 19F Electron-Nuclear Double Resonance Reveals Interaction between Redox-Active Tyrosines across the  $\alpha/\beta$  Interface of E. coli Ribonucleotide Reductase. *J. Am. Chem. Soc.*; 10.1021/jacs.2c02906 (2022).
75. Gfeller, D., Michielin, O. & Zoete, V. SwissSidechain: a molecular and structural database of non-natural sidechains. *Nucleic acids research* **41**, D327-32; 10.1093/nar/gks991 (2013).
76. Dougherty, D. A. & van Arnam, E. B. In vivo incorporation of non-canonical amino acids by using the chemical aminoacylation strategy: a broadly applicable mechanistic tool. *Chembiochem : a European journal of chemical biology* **15**, 1710–1720; 10.1002/cbic.201402080 (2014).
77. Arnold, U. Incorporation of non-natural modules into proteins: structural features beyond the genetic code. *Biotechnol Lett* **31**, 1129–1139; 10.1007/s10529-009-0002-9 (2009).

78. Muir, T. W., Sondhi, D. & Cole, P. A. Expressed protein ligation: a general method for protein engineering. *Proceedings of the National Academy of Sciences* **95**, 6705–6710; 10.1073/pnas.95.12.6705 (1998).
79. Anderson, J. C. *et al.* An expanded genetic code with a functional quadruplet codon. *Proceedings of the National Academy of Sciences* **101**, 7566–7571; 10.1073/pnas.0401517101 (2004).
80. Xie, J. & Schultz, P. G. Adding amino acids to the genetic repertoire. *Current Opinion in Chemical Biology* **9**, 548–554; 10.1016/j.cbpa.2005.10.011 (2005).
81. Wang, L. & Schultz, P. G. A general approach for the generation of orthogonal tRNAs. *Chemistry & Biology* **8**, 883–890; 10.1016/S1074-5521(01)00063-1 (2001).
82. Ravichandran, K. R., Minnihan, E. C., Wei, Y., Nocera, D. G. & Stubbe, J. Reverse Electron Transfer Completes the Catalytic Cycle in a 2,3,5-Trifluorotyrosine-Substituted Ribonucleotide Reductase. *J. Am. Chem. Soc.* **137**, 14387–14395; 10.1021/jacs.5b09189 (2015).
83. Mao, S. S. *et al.* A model for the role of multiple cysteine residues involved in ribonucleotide reduction: amazing and still confusing. *Biochemistry* **31**, 9733–9743; 10.1021/bi00155a029 (1992).
84. Erickson, H. K. Formation of the cystine between cysteine 225 and cysteine 462 from ribonucleoside diphosphate reductase is kinetically competent. *Biochemistry* **39**, 9241–9250; 10.1021/bi992820y (2000).
85. Ortigosa, A. D. *et al.* Determination of the in vivo stoichiometry of tyrosyl radical per betabeta' in *Saccharomyces cerevisiae* ribonucleotide reductase. *Biochemistry* **45**, 12282–12294; 10.1021/bi0610404 (2006).
86. Bollinger, J. M. *et al.* Mechanism of assembly of the tyrosyl radical-dinuclear iron cluster cofactor of ribonucleotide reductase. *Science* **253**, 292–298; 10.1126/science.1650033 (1991).
87. Bollinger, J. M. *et al.* [20] Use of rapid kinetics methods to study the assembly of the diferric-tyrosyl radical cofactor of *E. coli* ribonucleotide reductase. In *Methods in Enzymology : Redox-active amino acids in biology* (Academic Press 1995), Vol. 258, pp. 278–303.
88. Bollinger, J. M. *et al.* Mechanism of Assembly of the Tyrosyl Radical-Diiron(III) Cofactor of *E. coli* Ribonucleotide Reductase. 2. Kinetics of The Excess Fe<sup>2+</sup> Reaction by Optical, EPR, and Moessbauer Spectroscopies. *J. Am. Chem. Soc.* **116**, 8015–8023; 10.1021/ja00097a008 (1994).
89. Voegtli, W. C. *et al.* Variable coordination geometries at the diiron(II) active site of ribonucleotide reductase R2. *J. Am. Chem. Soc.* **125**, 15822–15830; 10.1021/ja0370387 (2003).

90. Tong, W. H. *et al.* Mechanism of Assembly of the Diferric Cluster–Tyrosyl Radical Cofactor of Escherichia coli Ribonucleotide Reductase from the Diferrous Form of the R2 Subunit. *J. Am. Chem. Soc.* **118**, 2107–2108; 10.1021/ja952764y (1996).
91. Moënne-Loccoz, P., Baldwin, J., Ley, B. A., Loehr, T. M. & Bollinger, J. M. O<sub>2</sub> activation by non-heme diiron proteins: identification of a symmetric  $\mu$ -1,2-peroxide in a mutant of ribonucleotide reductase. *Biochemistry* **37**, 14659–14663; 10.1021/bi981838q (1998).
92. Dassama, L. M. K. *et al.* A 2.8 Å Fe-Fe separation in the Fe<sub>2</sub>(III/IV) intermediate, X, from Escherichia coli ribonucleotide reductase. *J. Am. Chem. Soc.* **135**, 16758–16761; 10.1021/ja407438p (2013).
93. Han, W.-G., Liu, T., Lovell, T. & Noodleman, L. Seven clues to the origin and structure of class-I ribonucleotide reductase intermediate X. *Journal of Inorganic Biochemistry* **100**, 771–779; 10.1016/j.jinorgbio.2006.01.032 (2006).
94. Mitić, N., Clay, M. D., Saleh, L., Bollinger, J. M. & Solomon, E. I. Spectroscopic and electronic structure studies of intermediate X in ribonucleotide reductase R2 and two variants: a description of the FeIV-oxo bond in the FeIII-O-FeIV dimer. *J. Am. Chem. Soc.* **129**, 9049–9065; 10.1021/ja070909i (2007).
95. Wu, C.-H., Jiang, W., Krebs, C. & Stubbe, J. YfaE, a ferredoxin involved in diferric-tyrosyl radical maintenance in Escherichia coli ribonucleotide reductase. *Biochemistry* **46**, 11577–11588; 10.1021/bi7012454 (2007).
96. Yang, Y.-S., Baldwin, J., Ley, B. A., Bollinger, J. M. & Solomon, E. I. Spectroscopic and Electronic Structure Description of the Reduced Binuclear Non-Heme Iron Active Site in Ribonucleotide Reductase from E.coli : Comparison to Reduced  $\Delta$  9 Desaturase and Electronic Structure Contributions to Differences in O<sub>2</sub> Reactivity. *J. Am. Chem. Soc.* **122**, 8495–8510; 10.1021/ja994406r (2000).
97. Bollinger, J. M. *et al.* Differential Iron(II) Affinity of the Sites of the Diiron Cluster in Protein R2 of Escherichia coli Ribonucleotide Reductase: Tracking the Individual Sites through the O<sub>2</sub> Activation Sequence. *J. Am. Chem. Soc.* **119**, 5976–5977; 10.1021/ja970319s (1997).
98. Bencini, A. & Gatteschi, D. *EPR of Exchange Coupled Systems* (Dover Publications, Newburyport, 2012).
99. Atta, M., Nordlund, P., Aberg, A., Eklund, H. & Fontecave, M. Substitution of manganese for iron in ribonucleotide reductase from Escherichia coli. Spectroscopic and crystallographic characterization. *Journal of Biological Chemistry* **267**, 20682–20688 (1992).
100. Pierce, B. S., Elgren, T. E. & Hendrich, M. P. Mechanistic implications for the formation of the diiron cluster in ribonucleotide reductase provided by

- quantitative EPR spectroscopy. *J. Am. Chem. Soc.* **125**, 8748–8759; 10.1021/ja021290h (2003).
101. Hristova, D., Wu, C.-H., Jiang, W., Krebs, C. & Stubbe, J. Importance of the maintenance pathway in the regulation of the activity of Escherichia coli ribonucleotide reductase. *Biochemistry* **47**, 3989–3999; 10.1021/bi702408k (2008).
  102. Sjöberg, B. M. & Reichard, P. Nature of the free radical in ribonucleotide reductase from Escherichia coli. *Journal of Biological Chemistry* **252**, 536–541; 10.1016/S0021-9258(17)32750-3 (1977).
  103. Sjöberg, B. M., Reichard, P., Gräslund, A. & Ehrenberg, A. The tyrosine free radical in ribonucleotide reductase from Escherichia coli. *Journal of Biological Chemistry* **253**, 6863–6865; 10.1016/S0021-9258(17)37999-1 (1978).
  104. Perlstein, D. L. *et al.* The active form of the Saccharomyces cerevisiae ribonucleotide reductase small subunit is a heterodimer in vitro and in vivo. *Biochemistry* **44**, 15366–15377; 10.1021/bi051616 (2005).
  105. Chabes, A. *et al.* Yeast ribonucleotide reductase has a heterodimeric iron-radical-containing subunit. *Proceedings of the National Academy of Sciences* **97**, 2474–2479; 10.1073/pnas.97.6.2474 (2000).
  106. Huang, M. & Elledge, S. J. Identification of RNR4, encoding a second essential small subunit of ribonucleotide reductase in Saccharomyces cerevisiae. *Molecular and cellular biology* **17**, 6105–6113; 10.1128/MCB.17.10.6105 (1997).
  107. Atherton, N. M. *Principles of Electron Spin Resonance* (Ellis Horwood, 1993).
  108. Junk, M. J. N. *Assessing the Functional Structure of Molecular Transporters by EPR Spectroscopy* (Springer Berlin Heidelberg, Berlin, Heidelberg, 2012).
  109. Reijerse, E. J. High-Frequency EPR Instrumentation. *Appl Magn Reson* **37**, 795–818; 10.1007/s00723-009-0070-y (2010).
  110. Abragam, A. & Pryce, M. H. L. Theory of the nuclear hyperfine structure of paramagnetic resonance spectra in crystals. *Proc. R. Soc. Lond. A* **205**, 135–153; 10.1098/rspa.1951.0022 (1951).
  111. Mostafanejad, M. Basics of the spin Hamiltonian formalism. *Int. J. Quantum Chem.* **114**, 1495–1512; 10.1002/qua.24721 (2014).
  112. Pribitzer, S., Mannikko, D. & Stoll, S. Determining electron-nucleus distances and Fermi contact couplings from ENDOR spectra. *Phys. Chem. Chem. Phys.* **23**, 8326–8335; 10.1039/D1CP00229E (2021).
  113. Schweiger, A. & Jeschke, G. *Principles of pulse electron paramagnetic resonance* (Oxford University Press, Oxford, UK, New York, 2001).

114. Weil, J. A. & Bolton, J. R. *Electron paramagnetic resonance. Elementary theory and practical applications*. 2nd ed. (Wiley; John Wiley [distributor], Hoboken, N.J., Chichester, 2007).
115. Jeschke, G. Electron Paramagnetic Resonance Spectroscopy. *Ullmann's Encyclopedia of Industrial Chemistry*; 10.1002/14356007.q09\_q01 (2013).
116. Goldfarb, D. & Stoll, S. (eds.). *EPR spectroscopy. Fundamentals and methods* (Wiley, Chichester, West Sussex, 2018).
117. R. E. Coffman & G. Buettner. General magnetic dipolar interaction of spin-spin coupled molecular dimers. Application to an EPR spectrum of xanthine oxidase. *undefined* (1979).
118. Slichter, C. P. *Principles of Magnetic Resonance* (Springer International Publishing, Cham, 2013).
119. Schiemann, O. & Prisner, T. F. Long-range distance determinations in biomacromolecules by EPR spectroscopy. *Quarterly reviews of biophysics* **40**, 1–53; 10.1017/S003358350700460X (2007).
120. Abdullin, D. & Schiemann, O. Pulsed Dipolar EPR Spectroscopy and Metal Ions: Methodology and Biological Applications. *ChemPlusChem* **85**, 353–372; 10.1002/cplu.201900705 (2020).
121. Berliner, L. J., Eaton, G. R. & Eaton, S. S. (eds.). *Distance Measurements in Biological Systems by EPR* (Springer, New York, NY, 2006).
122. Borbat, P. P. & Freed, J. H. Pulse Dipolar Electron Spin Resonance: Distance Measurements. In *Structural Information from Spin-Labels and Intrinsic Paramagnetic Centres in the Biosciences*, edited by C. R. Timmel & J. R. Harmer (Springer Berlin Heidelberg, Berlin, Heidelberg, 2013), Vol. 152, pp. 1–82.
123. Colligiani, A. Nuclear quadrupole resonance data ( $I=1$ ) from endor experiments. *Journal of Molecular Structure* **58**, 53–61; 10.1016/0022-2860(80)85007-1 (1980).
124. Bertrand, P. *Electron Paramagnetic Resonance Spectroscopy. Fundamentals* (Springer International Publishing, Cham, 2020).
125. Hyde, J. S., Strangeway, R. A., Camenisch, T. G., Ratke, J. J. & Froncisz, W. W-band frequency-swept EPR. *Journal of magnetic resonance (San Diego, Calif. : 1997)* **205**, 93–101; 10.1016/j.jmr.2010.04.005 (2010).
126. Eaton, G. R. *Quantitative EPR* (Springer Wien, Vienna, 2010).
127. Bowman, M. K., Chen, H. & Maryasov, A. G. Pulsed EPR Signals from Triplets. *Zeitschrift für Physikalische Chemie* **231**, 637–652; 10.1515/zpch-2016-0869 (2017).
128. Hahn, E. L. Spin Echoes. *Phys. Rev.* **80**, 580–594; 10.1103/PhysRev.80.580 (1950).

129. Eaton, S. S. & Eaton, G. R. Saturation Recovery EPR. In *Biomedical EPR, Part B: Methodology, Instrumentation, and Dynamics*, edited by S. R. Eaton, G. R. Eaton & L. J. Berliner (Springer US, Boston, MA, 2005), pp. 3–18.
130. Kevan, L. (ed.). *Time domain electron spin resonance* (Wiley, New York, 1979).
131. Casto, J., Mandato, A. & Saxena, S. dHis-troying Barriers: Deuteration Provides a Pathway to Increase Sensitivity and Accessible Distances for Cu<sup>2+</sup> Labels. *The journal of physical chemistry letters* **12**, 4681–4685; 10.1021/acs.jpcclett.1c01002 (2021).
132. Bode, B. E. *et al.* Counting the monomers in nanometer-sized oligomers by pulsed electron-electron double resonance. *Journal of the American Chemical Society* **129**, 6736–6745; 10.1021/ja065787t (2007).
133. Ward, R. & Schiemann, O. Interspin Distance Determination by EPR. In *Encyclopedia of Biophysics*, edited by G. C. K. Roberts (Springer Berlin Heidelberg, Berlin, Heidelberg, 2013), pp. 1116–1123.
134. Schiemann, O. *et al.* Benchmark Test and Guidelines for DEER/PELDOR Experiments on Nitroxide-Labeled Biomolecules. *J. Am. Chem. Soc.* **143**, 17875–17890; 10.1021/jacs.1c07371 (2021).
135. Mims, W. B. Pulsed endor experiments. *Proc. R. Soc. Lond. A* **283**, 452–457; 10.1098/rspa.1965.0034 (1965).
136. Davies, E. R. A new pulse endor technique. *Physics Letters A* **47**, 1–2; 10.1016/0375-9601(74)90078-4 (1974).
137. Kulik, L. & Lubitz, W. Electron-nuclear double resonance. *Photosynthesis Research* **102**, 391–401; 10.1007/s11120-009-9401-y (2009).
138. Tyryshkin, A. M., Morton, J. J. L., Ardavan, A. & Lyon, S. A. Davies electron-nuclear double resonance revisited: enhanced sensitivity and nuclear spin relaxation. *The Journal of Chemical Physics* **124**, 234508; 10.1063/1.2204915 (2006).
139. Cutsail, G. E., Telser, J. & Hoffman, B. M. Advanced paramagnetic resonance spectroscopies of iron-sulfur proteins: Electron nuclear double resonance (ENDOR) and electron spin echo envelope modulation (ESEEM). *Biochimica et biophysica acta* **1853**, 1370–1394; 10.1016/j.bbamcr.2015.01.025 (2015).
140. Sahu, I. D. & Lorigan, G. A. Site-Directed Spin Labeling EPR for Studying Membrane Proteins. *BioMed Research International* **2018**, 3248289; 10.1155/2018/3248289 (2018).
141. Altenbach, C., Flitsch, S. L., Khorana, H. G. & Hubbell, W. L. Structural studies on transmembrane proteins. 2. Spin labeling of bacteriorhodopsin mutants at unique cysteines. *Biochemistry* **28**, 7806–7812; 10.1021/bi00445a042 (1989).

142. Altenbach, C., Froncisz, W., Hyde, J. S. & Hubbell, W. L. Conformation of spin-labeled melittin at membrane surfaces investigated by pulse saturation recovery and continuous wave power saturation electron paramagnetic resonance. *Biophysical journal* **56**, 1183–1191; 10.1016/S0006-3495(89)82765-1 (1989).
143. Hubbell, W. L., López, C. J., Altenbach, C. & Yang, Z. Technological advances in site-directed spin labeling of proteins. *Current Opinion in Structural Biology* **23**, 725–733; 10.1016/j.sbi.2013.06.008 (2013).
144. Cornish, V. W. *et al.* Site-specific incorporation of biophysical probes into proteins. *Proceedings of the National Academy of Sciences of the United States of America* **91**, 2910–2914; 10.1073/pnas.91.8.2910 (1994).
145. Torricella, F., Pierro, A., Mileo, E., Belle, V. & Bonucci, A. Nitroxide spin labels and EPR spectroscopy: A powerful association for protein dynamics studies. *Biochimica et biophysica acta. Proteins and proteomics* **1869**, 140653; 10.1016/j.bbapap.2021.140653 (2021).
146. Steinhoff, H.-J. A simple method for determination of rotational correlation times and separation of rotational and polarity effects from EPR spectra of spin-labeled biomolecules in a wide correlation time range. *Journal of Biochemical and Biophysical Methods* **17**, 237–247; 10.1016/0165-022X(88)90047-4 (1988).
147. White, G. F. *et al.* Analysis of nitroxide spin label motion in a protein-protein complex using multiple frequency EPR spectroscopy. *Journal of Magnetic Resonance* **185**, 191–203; 10.1016/j.jmr.2006.12.009 (2007).
148. Sale, K., Song, L., Liu, Y.-S., Perozo, E. & Fajer, P. Explicit treatment of spin labels in modeling of distance constraints from dipolar EPR and DEER. *Journal of the American Chemical Society* **127**, 9334–9335; 10.1021/ja051652w (2005).
149. Griffith, O. H. & McConnell, H. M. A nitroxide-maleimide spin label. *Proceedings of the National Academy of Sciences of the United States of America* **55**, 8–11; 10.1073/pnas.55.1.8 (1966).
150. Widder, P., Berner, F., Summerer, D. & Drescher, M. Double Nitroxide Labeling by Copper-Catalyzed Azide-Alkyne Cycloadditions with Noncanonical Amino Acids for Electron Paramagnetic Resonance Spectroscopy. *ACS Chemical Biology* **14**, 839–844; 10.1021/acschembio.8b01111 (2019).
151. Widder, P., Schuck, J., Summerer, D. & Drescher, M. Combining site-directed spin labeling in vivo and in-cell EPR distance determination. *Phys. Chem. Chem. Phys.* **22**, 4875–4879; 10.1039/C9CP05584C (2020).
152. Kugele, A. *et al.* Site-directed spin labelling of proteins by Suzuki-Miyaura coupling via a genetically encoded aryl iodide amino acid. *Chem. Commun.* **55**, 1923–1926; 10.1039/C8CC09325C (2019).

153. Fleissner, M. R. *et al.* Site-directed spin labeling of a genetically encoded unnatural amino acid. *Proceedings of the National Academy of Sciences* **106**, 21637–21642; 10.1073/pnas.0912009106 (2009).
154. Azarkh, M., Okle, O., Eyring, P., Dietrich, D. R. & Drescher, M. Evaluation of spin labels for in-cell EPR by analysis of nitroxide reduction in cell extract of *Xenopus laevis* oocytes. *Journal of magnetic resonance (San Diego, Calif. : 1997)* **212**, 450–454; 10.1016/j.jmr.2011.07.014 (2011).
155. Couet, W. R., Brasch, R. C., Sosnovsky, G. & Tozer, T. N. Factors affecting nitroxide reduction in ascorbate solution and tissue homogenates. *Magnetic Resonance Imaging* **3**, 83–88; 10.1016/0730-725X(85)90012-8 (1985).
156. Paletta, J. T., Pink, M., Foley, B., Rajca, S. & Rajca, A. Synthesis and reduction kinetics of sterically shielded pyrrolidine nitroxides. *Organic letters* **14**, 5322–5325; 10.1021/ol302506f (2012).
157. Bleicken, S. *et al.* gem-Diethyl Pyrroline Nitroxide Spin Labels: Synthesis, EPR Characterization, Rotamer Libraries and Biocompatibility. *ChemistryOpen* **8**, 1057–1065; 10.1002/open.201900119 (2019).
158. Braun, T. S. *et al.* Isoindoline-Based Nitroxides as Bioresistant Spin Labels for Protein Labeling through Cysteines and Alkyne-Bearing Noncanonical Amino Acids. *ChemBioChem* **21**, 958–962; 10.1002/cbic.201900537 (2020).
159. Karthikeyan, G. *et al.* A Bioresistant Nitroxide Spin Label for In-Cell EPR Spectroscopy: In Vitro and In Oocytes Protein Structural Dynamics Studies. *Angew. Chem. Int. Ed.* **57**, 1366–1370; 10.1002/anie.201710184 (2018).
160. Pierro, A. *et al.* Probing the Structural Dynamics of a Bacterial Chaperone in Its Native Environment by Nitroxide-Based EPR Spectroscopy. *Chemistry – A European Journal*, e202202249; 10.1002/chem.202202249 (2022).
161. Cattani, J., Subramaniam, V. & Drescher, M. Room-temperature in-cell EPR spectroscopy: alpha-Synuclein disease variants remain intrinsically disordered in the cell. *Phys. Chem. Chem. Phys.* **19**, 18147–18151; 10.1039/C7CP03432F (2017).
162. Torricella, F., Bonucci, A., Polykretis, P., Cencetti, F. & Banci, L. Rapid protein delivery to living cells for biomolecular investigation. *Biochemical and biophysical research communications* **570**, 82–88; 10.1016/j.bbrc.2021.07.006 (2021).
163. Singewald, K., Lawless, M. J. & Saxena, S. Increasing nitroxide lifetime in cells to enable in-cell protein structure and dynamics measurements by electron spin resonance spectroscopy. *Journal of magnetic resonance (San Diego, Calif. : 1997)* **299**, 21–27; 10.1016/j.jmr.2018.12.005 (2019).

164. Potapov, A. *et al.* Nanometer-scale distance measurements in proteins using Gd<sup>3+</sup> spin labeling. *Journal of the American Chemical Society* **132**, 9040–9048; 10.1021/ja1015662 (2010).
165. Qi, M., Gross, A., Jeschke, G., Godt, A. & Drescher, M. Gd(III)-PyMTA label is suitable for in-cell EPR. *Journal of the American Chemical Society* **136**, 15366–15378; 10.1021/ja508274d (2014).
166. Martorana, A. *et al.* Probing protein conformation in cells by EPR distance measurements using Gd<sup>3+</sup> spin labeling. *Journal of the American Chemical Society* **136**, 13458–13465; 10.1021/ja5079392 (2014).
167. Theillet, F.-X. *et al.* Structural disorder of monomeric  $\alpha$ -synuclein persists in mammalian cells. *Nature* **530**, 45–50; 10.1038/nature16531 (2016).
168. Kucher, S., Elsner, C., Safonova, M., Maffini, S. & Bordignon, E. In-Cell Double Electron-Electron Resonance at Nanomolar Protein Concentrations. *The journal of physical chemistry letters* **12**, 3679–3684; 10.1021/acs.jpcllett.1c00048 (2021).
169. Yang, Y. *et al.* High Sensitivity In-Cell EPR Distance Measurements on Proteins using an Optimized Gd(III) Spin Label. *The journal of physical chemistry letters* **9**, 6119–6123; 10.1021/acs.jpcllett.8b02663 (2018).
170. Ketter, S. *et al.* In situ distance measurements in a membrane transporter using maleimide functionalized orthogonal spin labels and 5-pulse electron-electron double resonance spectroscopy. *Journal of Magnetic Resonance Open* **10-11**, 100041; 10.1016/j.jmro.2022.100041 (2022).
171. Kucher, S., Korneev, S., Klare, J. P., Klose, D. & Steinhoff, H.-J. In cell Gd<sup>3+</sup>-based site-directed spin labeling and EPR spectroscopy of eGFP. *Phys. Chem. Chem. Phys.* **22**, 13358–13362; 10.1039/d0cp01930e (2020).
172. Cunningham, T. F., Putterman, M. R., Desai, A., Horne, W. S. & Saxena, S. The double-histidine Cu<sup>2+</sup>-binding motif: a highly rigid, site-specific spin probe for electron spin resonance distance measurements. *Angewandte Chemie (International ed. in English)* **54**, 6330–6334; 10.1002/anie.201501968 (2015).
173. Gamble Jarvi, A., Ranguelova, K., Ghosh, S., Weber, R. T. & Saxena, S. On the Use of Q-Band Double Electron-Electron Resonance To Resolve the Relative Orientations of Two Double Histidine-Bound Cu<sup>2+</sup> Ions in a Protein. *The journal of physical chemistry. B* **122**, 10669–10677; 10.1021/acs.jpccb.8b07727 (2018).
174. Gamble Jarvi, A., Bogetti, X., Singewald, K., Ghosh, S. & Saxena, S. Going the dHis-tance: Site-Directed Cu<sup>2+</sup> Labeling of Proteins and Nucleic Acids. *Accounts of Chemical Research* **54**, 1481–1491; 10.1021/acs.accounts.0c00761 (2021).

175. Shenberger, Y., Gevorkyan-Airapetov, L., Hirsch, M., Hofmann, L. & Ruthstein, S. *An in cell site-specific labeling methodology reveals conformational changes of proteins in bacteria* (2022).
176. Jassoy, J. J. *et al.* Versatile Trityl Spin Labels for Nanometer Distance Measurements on Biomolecules In Vitro and within Cells. *Angewandte Chemie International Edition* **56**, 177–181; 10.1002/anie.201609085 (2017).
177. Fleck, N. *et al.* SLIM: A Short-Linked, Highly Redox-Stable Trityl Label for High-Sensitivity In-Cell EPR Distance Measurements. *Angewandte Chemie (International ed. in English)* **59**, 9767–9772; 10.1002/anie.202004452 (2020).
178. Fleck, N. *et al.* Ox-SLIM: Synthesis of and Site-Specific Labelling with a Highly Hydrophilic Trityl Spin Label. *Chemistry – A European Journal* **27**, 5292–5297; 10.1002/chem.202100013 (2021).
179. Yang, Y. *et al.* In-Cell Trityl-Trityl Distance Measurements on Proteins. *The journal of physical chemistry letters* **11**, 1141–1147; 10.1021/acs.jpcllett.9b03208 (2020).
180. Hasanbasri, Z., Singewald, K., Gluth, T. D., Driesschaert, B. & Saxena, S. Cleavage-Resistant Protein Labeling With Hydrophilic Trityl Enables Distance Measurements In-Cell. *The journal of physical chemistry. B* **125**, 5265–5274; 10.1021/acs.jpccb.1c02371 (2021).
181. Roser, P., Schmidt, M. J., Drescher, M. & Summerer, D. Site-directed spin labeling of proteins for distance measurements in vitro and in cells. *Org. Biomol. Chem.* **14**, 5468–5476; 10.1039/C6OB00473C (2016).
182. Kugele, A., Silkenath, B., Langer, J., Wittmann, V. & Drescher, M. Protein Spin Labeling with a Photocaged Nitroxide Using Diels-Alder Chemistry. *ChemBioChem* **20**, 2479–2484; 10.1002/cbic.201900318 (2019).
183. Kugele, A. *et al.* In situ EPR spectroscopy of a bacterial membrane transporter using an expanded genetic code. *Chem. Commun.* **57**, 12980–12983; 10.1039/D1CC04612H (2021).
184. Kay, C., Di Valentin, M. & Möbius, K. A time-resolved Electron Nuclear Double Resonance (ENDOR) study of the photoexcited triplet state of free-base tetraphenylporphyrin. *Solar Energy Materials and Solar Cells* **38**, 111–118; 10.1016/0927-0248(94)00219-3 (1995).
185. Lubitz, W., Lendzian, F. & Bittl, R. Radicals, radical pairs and triplet states in photosynthesis. *Accounts of Chemical Research* **35**, 313–320; 10.1021/ar000084g (2002).
186. Bieber, A., Bucker, D. & Drescher, M. Light-induced dipolar spectroscopy - A quantitative comparison between LiDEER and LaserIMD. *Journal of magnetic resonance (San Diego, Calif. : 1997)* **296**, 29–35; 10.1016/j.jmr.2018.08.006 (2018).

187. Bowen, A. M. *et al.* Orientation-Selective and Frequency-Correlated Light-Induced Pulsed Dipolar Spectroscopy. *The journal of physical chemistry letters* **12**, 3819–3826; 10.1021/acs.jpcllett.1c00595 (2021).
188. Di Valentin, M., Albertini, M., Zurlo, E., Gobbo, M. & Carbonera, D. Porphyrin triplet state as a potential spin label for nanometer distance measurements by PELDOR spectroscopy. *Journal of the American Chemical Society* **136**, 6582–6585; 10.1021/ja502615n (2014).
189. Di Valentin, M. *et al.* Light-Induced Porphyrin-Based Spectroscopic Ruler for Nanometer Distance Measurements. *Chemistry – A European Journal* **22**, 17204–17214; 10.1002/chem.201603666 (2016).
190. Hintze, C., Bücker, D., Domingo Köhler, S., Jeschke, G. & Drescher, M. Laser-Induced Magnetic Dipole Spectroscopy. *The journal of physical chemistry letters* **7**, 2204–2209; 10.1021/acs.jpcllett.6b00765 (2016).
191. Bertran, A. *et al.* Light-Induced Triplet-Triplet Electron Resonance Spectroscopy. *The journal of physical chemistry letters* **12**, 80–85; 10.1021/acs.jpcllett.0c02884 (2021).
192. Meichsner, S. L., Kutin, Y. & Kasanmascheff, M. In-Cell Characterization of the Stable Tyrosyl Radical in E. coli Ribonucleotide Reductase Using Advanced EPR Spectroscopy. *Angewandte Chemie (International ed. in English)* **60**, 19155–19161; 10.1002/anie.202102914 (2021).
193. Sellers, V. M., Dailey, T. A. & Dailey, H. A. Examination of Ferrochelatase Mutations That Cause Erythropoietic Protoporphyrria. *Blood* **91**, 3980–3985; 10.1182/blood.V91.10.3980 (1998).
194. Commoner, B., Heise, J. J. & Townsend, J. LIGHT-INDUCED PARAMAGNETISM IN CHLOROPLASTS. *Proceedings of the National Academy of Sciences* **42**, 710–718; 10.1073/pnas.42.10.710 (1956).
195. Yewdall, N. A., André, A. A., Lu, T. & Spruijt, E. Coacervates as models of membraneless organelles. *Current Opinion in Colloid & Interface Science* **52**, 101416; 10.1016/j.cocis.2020.101416 (2021).
196. Yewdall, N. A. *et al.* Physicochemical Characterization of Polymer-Stabilized Coacervate Protocells. *ChemBioChem* **20**, 2643–2652; 10.1002/cbic.201900195 (2019).
197. Kalantari N. & Ghaffari S. Evaluation of Toxicity of Heavy Metals for Escherichia Coli Growth. *Journal of Environmental Health Science & Engineering* **5**, 173–178 (2008).
198. Svistunenko, D. A. & Jones, G. A. Tyrosyl radicals in proteins: a comparison of empirical and density functional calculated EPR parameters. *Physical chemistry chemical physics : PCCP* **11**, 6600–6613; 10.1039/B905522C (2009).

199. Un, S., Atta, M., Fontecave, M. & Rutherford, A. W. g-Values as a Probe of the Local Protein Environment: High-Field EPR of Tyrosyl Radicals in Ribonucleotide Reductase and Photosystem II. *J. Am. Chem. Soc.* **117**, 10713–10719; 10.1021/ja00148a013 (1995).
200. Un, S., Gerez, C., Elleingand, E. & Fontecave, M. Sensitivity of tyrosyl radical g-values to changes in protein structure: a high-field EPR study of mutants of ribonucleotide reductase. *J. Am. Chem. Soc.* **123**, 3048–3054; 10.1021/ja003650b (2001).
201. Retegan, M., Cox, N., Lubitz, W., Neese, F. & Pantazis, D. A. The first tyrosyl radical intermediate formed in the S2-S3 transition of photosystem II. *Phys. Chem. Chem. Phys.* **16**, 11901–11910; 10.1039/C4CP00696H (2014).
202. Engström, M. *et al.* Hydrogen Bonding to Tyrosyl Radical Analyzed by Ab Initio g-Tensor Calculations. *J. Phys. Chem. A* **104**, 5149–5153; 10.1021/jp0006633 (2000).
203. Liu, A., Barra, A.-L., Rubin, H., Lu, G. & Gräslund, A. Heterogeneity of the Local Electrostatic Environment of the Tyrosyl Radical in Mycobacterium tuberculosis Ribonucleotide Reductase Observed by High-Field Electron Paramagnetic Resonance. *J. Am. Chem. Soc.* **122**, 1974–1978; 10.1021/ja990123n (2000).
204. Liu, A. *et al.* The tyrosyl free radical of recombinant ribonucleotide reductase from Mycobacterium tuberculosis is located in a rigid hydrophobic pocket. *Biochemistry* **37**, 16369–16377; 10.1021/bi981471p (1998).
205. Bennati, M., Lendzian, F., Schmittel, M. & Zipse, H. Spectroscopic and theoretical approaches for studying radical reactions in class I ribonucleotide reductase. *Biological chemistry* **386**, 1007–1022; 10.1515/BC.2005.117 (2005).
206. Lendzian, F. Structure and interactions of amino acid radicals in class I ribonucleotide reductase studied by ENDOR and high-field EPR spectroscopy. *Biochimica et biophysica acta* **1707**, 67–90; 10.1016/j.bbabi.2004.02.011 (2005).
207. McConnell, H. M. & Chesnut, D. B. Theory of Isotropic Hyperfine Interactions in  $\pi$ -Electron Radicals. *The Journal of Chemical Physics* **28**, 107–117; 10.1063/1.1744052 (1958).
208. Wang, L., Zhou, Y. J., Ji, D. & Zhao, Z. K. An accurate method for estimation of the intracellular aqueous volume of Escherichia coli cells. *Journal of microbiological methods* **93**, 73–76; 10.1016/j.mimet.2013.02.006 (2013).
209. Tabares, L. C. & Un, S. In situ determination of manganese(II) speciation in Deinococcus radiodurans by high magnetic field EPR: detection of high levels of Mn(II) bound to proteins. *The Journal of biological chemistry* **288**, 5050–5055; 10.1074/jbc.C112.444992 (2013).

210. Keller, K. *et al.* EPR characterization of Mn(ii) complexes for distance determination with pulsed dipolar spectroscopy. *Phys. Chem. Chem. Phys.* **18**, 25120–25135; 10.1039/C6CP04884F (2016).
211. Martin, J. E., Waters, L. S., Storz, G. & Imlay, J. A. The Escherichia coli small protein MntS and exporter MntP optimize the intracellular concentration of manganese. *PLoS Genetics* **11**, e1004977; 10.1371/journal.pgen.1004977 (2015).
212. Yang, Y., Yang, F., Li, X.-Y., Su, X.-C. & Goldfarb, D. In-Cell EPR Distance Measurements on Ubiquitin Labeled with a Rigid PyMTA-Gd(III) Tag. *The journal of physical chemistry. B* **123**, 1050–1059; 10.1021/acs.jpcc.8b11442 (2019).
213. Denysenkov, V. P., Prisner, T. F., Stubbe, J. & Bennati, M. High-field pulsed electron-electron double resonance spectroscopy to determine the orientation of the tyrosyl radicals in ribonucleotide reductase. *Proceedings of the National Academy of Sciences* **103**, 13386–13390; 10.1073/pnas.0605851103 (2006).
214. Fasanella, E. L. & Gordy, W. Electron spin resonance of an irradiated single crystal of L-tyrosine-HC. *Proceedings of the National Academy of Sciences* **62**, 299–304; 10.1073/pnas.62.2.299 (1969).
215. Högbom, M. *et al.* Displacement of the tyrosyl radical cofactor in ribonucleotide reductase obtained by single-crystal high-field EPR and 1.4-Å x-ray data. *Proceedings of the National Academy of Sciences* **100**, 3209–3214; 10.1073/pnas.0536684100 (2003).
216. Wuebben, C. *et al.* Site-Directed Spin Labeling of RNA with a Gem-Diethylisoindoline Spin Label: PELDOR, Relaxation, and Reduction Stability. *Molecules* **24**, 4482; 10.3390/molecules24244482 (2019).
217. Abdullin, D. *et al.* Pulsed EPR Dipolar Spectroscopy on Spin Pairs with one Highly Anisotropic Spin Center: The Low-Spin FeIII Case. *Chemistry – A European Journal* **25**, 14388–14398; 10.1002/chem.201902908 (2019).
218. Kerzhner, M. *et al.* Post-synthetic Spin-Labeling of RNA through Click Chemistry for PELDOR Measurements. *Chemistry – A European Journal* **22**, 12113–12121; 10.1002/chem.201601897 (2016).
219. Abdullin, D., Florin, N., Hagelueken, G. & Schiemann, O. EPR-based approach for the localization of paramagnetic metal ions in biomolecules. *Angew. Chem. Int. Ed.* **54**, 1827–1831; 10.1002/anie.201410396 (2015).
220. Stratmann, L. M., Kutin, Y., Kasanmascheff, M. & Clever, G. H. Precise Distance Measurements in DNA G-Quadruplex Dimers and Sandwich Complexes by Pulsed Dipolar EPR Spectroscopy. *Angew. Chem. Int. Ed.* **60**, 4939–4947; 10.1002/anie.202008618 (2021).

221. Abragam, A. & Bleaney, B. *Electron Paramagnetic Resonance of Transition Ions* (OUP Oxford, Oxford, 2012).
222. Duboc, C., Collomb, M.-N. & Neese, F. Understanding the Zero-Field Splitting of Mononuclear Manganese(II) Complexes from Combined EPR Spectroscopy and Quantum Chemistry. *Appl Magn Reson* **37**, 229–245; 10.1007/s00723-009-0085-4 (2010).
223. Šimėnas, M. *et al.* EPR of Structural Phase Transition in Manganese- and Copper-Doped Formate Framework of  $[\text{NH}_3(\text{CH}_2)_4\text{NH}_3][\text{Zn}(\text{HCOO})_3]$  2. *J. Phys. Chem. C* **120**, 19751–19758; 10.1021/acs.jpcc.6b07389 (2016).
224. Stich, T. A. *et al.* Multifrequency Pulsed EPR Studies of Biologically Relevant Manganese(II) Complexes. *Appl Magn Reson* **31**, 321–341; 10.1007/BF03166263 (2007).
225. Kaminker, I. *et al.* Spectroscopic selection of distance measurements in a protein dimer with mixed nitroxide and Gd<sup>3+</sup> spin labels. *Phys. Chem. Chem. Phys.* **14**, 4355–4358; 10.1039/C2CP40219J (2012).
226. Garbuio, L. *et al.* Orthogonal spin labeling and Gd(III)-nitroxide distance measurements on bacteriophage T4-lysozyme. *The journal of physical chemistry. B* **117**, 3145–3153; 10.1021/jp401806g (2013).
227. Yulikov, M., Lueders, P., Warsi, M. F., Chechik, V. & Jeschke, G. Distance measurements in Au nanoparticles functionalized with nitroxide radicals and Gd(3+)-DTPA chelate complexes. *Phys. Chem. Chem. Phys.* **14**, 10732–10746; 10.1039/C2CP40282C (2012).
228. Jeschke, G., Koch, A., Jonas, U. & Godt, A. Direct conversion of EPR dipolar time evolution data to distance distributions. *Journal of Magnetic Resonance* **155**, 72–82; 10.1006/jmre.2001.2498 (2002).
229. Crouse, B. R., Sellers, V. M., Finnegan, M. G., Dailey, H. A. & Johnson, M. K. Site-directed mutagenesis and spectroscopic characterization of human ferrochelatase: identification of residues coordinating the 2Fe-2S cluster. *Biochemistry* **35**, 16222–16229; 10.1021/bi9620114 (1996).
230. Zaccaro Scelza, M. F., Lima Oliveira, L. R., Carvalho, F. B. & Côte-Real Faria, S. In vitro evaluation of macrophage viability after incubation in orange oil, eucalyptol, and chloroform. *Oral surgery, oral medicine, oral pathology, oral radiology, and endodontics* **102**, e24-7; 10.1016/j.tripleo.2006.02.030 (2006).
231. Reigada, R. Atomistic study of lipid membranes containing chloroform: looking for a lipid-mediated mechanism of anesthesia. *PLoS ONE* **8**, e52631; 10.1371/journal.pone.0052631 (2013).

232. Miller, K. W. & Pang, K. Y. General anaesthetics can selectively perturb lipid bilayer membranes. *Nature* **263**, 253–255; 10.1038/263253a0 (1976).
233. Nick, T. U. Hydrogen Bonds and Electrostatic Environment of Radical Intermediates in Ribonucleotide Reductase Ia. Niedersächsische Staats- und Universitätsbibliothek Göttingen.
234. Jeschke, G. DEER distance measurements on proteins. *Annual review of physical chemistry* **63**, 419–446; 10.1146/annurev-physchem-032511-143716 (2012).
235. Jeschke, G. *et al.* DeerAnalysis2006—a comprehensive software package for analyzing pulsed ELDOR data. *Appl Magn Reson* **30**, 473–498; 10.1007/BF03166213 (2006).
236. O' Malley, P. J., MacFarlane, A. J., Rigby, S. E. & Nugent, J. H. The geometry and spin density distribution of the tyrosyl radical: a molecular orbital study. *Biochimica et Biophysica Acta (BBA) - Bioenergetics* **1232**, 175–179; 10.1016/0005-2728(95)00102-6 (1995).
237. Pujols-Ayala, I. & Barry, B. A. Tyrosyl radicals in photosystem II. *Biochimica et biophysica acta* **1655**, 205–216; 10.1016/j.bbabi.2003.07.010 (2004).
238. Blomberg, M. R. A. Mechanism of Oxygen Reduction in Cytochrome c Oxidase and the Role of the Active Site Tyrosine. *Biochemistry* **55**, 489–500; 10.1021/acs.biochem.5b01205 (2016).
239. Kneuttinger, A. C., Heil, K., Kashiwazaki, G. & Carell, T. The radical SAM enzyme spore photoproduct lyase employs a tyrosyl radical for DNA repair. *Chem. Commun.* **49**, 722–724; 10.1039/C2CC37735G (2013).
240. Irving, H. & Williams, R. J. P. 637. The stability of transition-metal complexes. *J. Chem. Soc.*, 3192; 10.1039/jr9530003192 (1953).
241. James A. Imlay. The Mismetallation of Enzymes during Oxidative Stress\*. *J Biol Chem* **289**, 28121–28128; 10.1074/jbc.R114.588814 (2014).
242. Cotruvo, J. A. & Stubbe, J. Metallation and mismetallation of iron and manganese proteins in vitro and in vivo: the class I ribonucleotide reductases as a case study. *Metallomics : integrated biometal science* **4**, 1020–1036; 10.1039/c2mt20142a (2012).
243. Robinson, N. J. & Glasfeld, A. Metalation: nature's challenge in bioinorganic chemistry. *J Biol Inorg Chem* **25**, 543–545; 10.1007/s00775-020-01790-3 (2020).
244. Lovyagina, E. R. & Semin, B. K. Competitive interaction of Mn(II) and Fe(II) cations with the high-affinity Mn-binding site of the photosystem II: evolutionary aspect. *Orig Life Evol Biosph*, 1–16; 10.1007/s11084-022-09625-8 (2022).
245. Persson, A. L. *et al.* A new mechanism-based radical intermediate in a mutant R1 protein affecting the catalytically essential Glu441 in Escherichia coli

- ribonucleotide reductase. *J Biol Chem* **272**, 31533–31541; 10.1074/jbc.272.50.31533 (1997).
246. Outten, C. E. & O'Halloran, T. V. Femtomolar sensitivity of metalloregulatory proteins controlling zinc homeostasis. *Science* **292**, 2488–2492; 10.1126/science.1060331 (2001).
247. Kisseleva, N., Kraut, S., Jäschke, A. & Schiemann, O. Characterizing multiple metal ion binding sites within a ribozyme by cadmium-induced EPR silencing. *HFSP Journal* **1**, 127–136; 10.2976/1.2756332 (2007).
248. Peana, M. *et al.* Manganese and cobalt binding in a multi-histidinic fragment. *Dalton Trans.* **42**, 16293–16301; 10.1039/C3DT51091C (2013).
249. Young, H. E., Donohue, M. P., Smirnova, T. I., Smirnov, A. I. & Zhou, P. The UDP-diacetylglucosamine pyrophosphohydrolase LpxH in lipid A biosynthesis utilizes Mn<sup>2+</sup> cluster for catalysis. *Journal of Biological Chemistry* **288**, 26987–27001; 10.1074/jbc.M113.497636 (2013).
250. Igdaloff, D., Santi, D. V., Eckert, T. S. & Bruice, T. C. Effects of 1,7- and 1,10-phenanthroline dione on tissue culture cells. *Biochemical Pharmacology* **32**, 172–174; 10.1016/0006-2952(83)90674-3 (1983).
251. Howard, T., Telser, J. & DeRose, V. J. An electron paramagnetic resonance study of Mn<sub>2</sub>(H<sub>2</sub>O)(OAc)<sub>4</sub>(tmeda)<sub>2</sub> (tmeda = N,N,N',N'-tetramethylethylenediamine): a model for dinuclear manganese enzyme active sites. *Inorganic Chemistry* **39**, 3379–3385; 10.1021/ic0000247 (2000).
252. Conlan, B. *et al.* Photo-catalytic oxidation of a di-nuclear manganese centre in an engineered bacterioferritin 'reaction centre'. *Biochimica et biophysica acta* **1787**, 1112–1121; 10.1016/j.bbabi.2009.04.011 (2009).
253. Golombek, A. P. & Hendrich, M. P. Quantitative analysis of dinuclear manganese(II) EPR spectra. *Journal of Magnetic Resonance* **165**, 33–48; 10.1016/j.jmr.2003.07.001 (2003).
254. Antanaitis, B. C. *et al.* Electron paramagnetic resonance and magnetic susceptibility studies of dimanganese concanavalin A. Evidence for antiferromagnetic exchange coupling. *Biochemistry* **26**, 7932–7937; 10.1021/bi00398a058 (1987).
255. Khangulov, S. V., Barynin, V. V., Voevodskaya, N. V. & Grebenko, A. I. ESR spectroscopy of the binuclear cluster of manganese ions in the active center of Mn-catalase from *Thermus thermophilus*. *Biochimica et Biophysica Acta (BBA) - Bioenergetics* **1020**, 305–310; 10.1016/0005-2728(90)90161-V (1990).
256. Pierce, B. S. & Hendrich, M. P. Local and global effects of metal binding within the small subunit of ribonucleotide reductase. *J. Am. Chem. Soc.* **127**, 3613–3623; 10.1021/ja0491937 (2005).

257. Xu, Y., Feng, L., Jeffrey, P. D., Shi, Y. & Morel, F. M. M. Structure and metal exchange in the cadmium carbonic anhydrase of marine diatoms. *Nature* **452**, 56–61; 10.1038/nature06636 (2008).
258. Lin, Q. *et al.* Glutamate 52- $\beta$  at the  $\alpha/\beta$  subunit interface of Escherichia coli class Ia ribonucleotide reductase is essential for conformational gating of radical transfer. *J Biol Chem* **292**, 9229–9239; 10.1074/jbc.M117.783092 (2017).
259. Salowe, S. P., Ator, M. A. & Stubbe, J. Products of the inactivation of ribonucleoside diphosphate reductase from Escherichia coli with 2'-azido-2'-deoxyuridine 5'-diphosphate. *Biochemistry* **26**, 3408–3416; 10.1021/bi00386a024 (1987).
260. Wang, J., Lohman, G. J. S. & Stubbe, J. Enhanced subunit interactions with gemcitabine-5'-diphosphate inhibit ribonucleotide reductases. *Proceedings of the National Academy of Sciences* **104**, 14324–14329; 10.1073/pnas.0706803104 (2007).
261. Reichard, P. Ribonucleotide reductase and deoxyribonucleotide pools. *Basic life sciences* **31**, 33–45; 10.1007/978-1-4613-2449-2\_3 (1985).
262. Li, Z. *et al.* Cofactor Editing by the G-protein Metallochaperone Domain Regulates the Radical B12 Enzyme IcmF. *Journal of Biological Chemistry* **292**, 3977–3987; 10.1074/jbc.M117.775957 (2017).
263. Igarashi, R. *et al.* Distance determination in proteins inside Xenopus laevis oocytes by double electron-electron resonance experiments. *J. Am. Chem. Soc.* **132**, 8228–8229; 10.1021/ja906104e (2010).
264. Dunkel, S., Pulagam, L. P., Steinhoff, H.-J. & Klare, J. P. In vivo EPR on spin labeled colicin A reveals an oligomeric assembly of the pore-forming domain in E. coli membranes. *Phys. Chem. Chem. Phys.* **17**, 4875–4878; 10.1039/c4cp05638h (2015).
265. Joseph, B. *et al.* Distance Measurement on an Endogenous Membrane Transporter in E. coli Cells and Native Membranes Using EPR Spectroscopy. *Angew. Chem. Int. Ed.* **54**, 6196–6199; 10.1002/anie.201501086 (2015).
266. Joseph, B., Sikora, A. & Cafiso, D. S. Ligand Induced Conformational Changes of a Membrane Transporter in E. coli Cells Observed with DEER/PELDOR. *J. Am. Chem. Soc.* **138**, 1844–1847; 10.1021/jacs.5b13382 (2016).
267. Gopinath, A. & Joseph, B. Conformational Flexibility of the Protein Insertase BamA in the Native Asymmetric Bilayer Elucidated by ESR Spectroscopy. *Angew. Chem. Int. Ed.* **61**, e202113448; 10.1002/anie.202113448 (2022).
268. Giannoulis, A. *et al.* DEER distance measurements on trityl/trityl and Gd(iii)/trityl labelled proteins. *Phys. Chem. Chem. Phys.* **21**, 10217–10227; 10.1039/C8CP07249C (2019).

269. Spicher, S., Abdullin, D., Grimme, S. & Schiemann, O. Modeling of spin-spin distance distributions for nitroxide labeled biomacromolecules. *Phys. Chem. Chem. Phys.* **22**, 24282–24290; 10.1039/D0CP04920D (2020).
270. Hagelueken, G., Ward, R., Naismith, J. H. & Schiemann, O. MtsslWizard: In Silico Spin-Labeling and Generation of Distance Distributions in PyMOL. *Appl Magn Reson* **42**, 377–391; 10.1007/s00723-012-0314-0 (2012).
271. Islam, S. M. & Roux, B. Simulating the distance distribution between spin-labels attached to proteins. *The journal of physical chemistry. B* **119**, 3901–3911; 10.1021/jp510745d (2015).
272. Polyhach, Y., Bordignon, E. & Jeschke, G. Rotamer libraries of spin labelled cysteines for protein studies. *Phys. Chem. Chem. Phys.* **13**, 2356–2366; 10.1039/C0CP01865A (2011).
273. Alexander, N. S. *et al.* RosettaEPR: rotamer library for spin label structure and dynamics. *PLoS ONE* **8**, e72851; 10.1371/journal.pone.0072851 (2013).
274. Jeschke, G. Conformational dynamics and distribution of nitroxide spin labels. *Progress in Nuclear Magnetic Resonance Spectroscopy* **72**, 42–60; 10.1016/j.pnmrs.2013.03.001 (2013).
275. Matalon, E. *et al.* Gadolinium(III) Spin Labels for High-Sensitivity Distance Measurements in Transmembrane Helices. *Angew. Chem.* **125**, 12047–12050; 10.1002/ange.201305574 (2013).
276. Izmailov, S. A. *et al.* Structural and dynamic origins of ESR lineshapes in spin-labeled GB1 domain: the insights from spin dynamics simulations based on long MD trajectories. *Sci Rep* **10**, 957; 10.1038/s41598-019-56750-y (2020).
277. Schmidt, M. J. *et al.* EPR Distance Measurements in Native Proteins with Genetically Encoded Spin Labels. *ACS Chemical Biology* **10**, 2764–2771; 10.1021/acscchembio.5b00512 (2015).
278. Anjos, V. A., Da Silva, F. M. R. & Souza, M. M. Cell damage induced by copper: an explant model to study anemone cells. *Toxicology in vitro : an international journal published in association with BIBRA* **28**, 365–372; 10.1016/j.tiv.2013.11.013 (2014).
279. Bower, D. V., Richter, J. K., Tengg-Kobligk, H. von, Heverhagen, J. T. & Runge, V. M. Gadolinium-Based MRI Contrast Agents Induce Mitochondrial Toxicity and Cell Death in Human Neurons, and Toxicity Increases With Reduced Kinetic Stability of the Agent. *Investigative radiology* **54**, 453–463; 10.1097/RLI.0000000000000567 (2019).
280. Grey, B. & Steck, T. R. Concentrations of copper thought to be toxic to *Escherichia coli* can induce the viable but nonculturable condition. *Applied and Environmental Microbiology* **67**, 5325–5327; 10.1128/AEM.67.11.5325-5327.2001 (2001).

281. Baker, A. S. & Deiters, A. Optical control of protein function through unnatural amino acid mutagenesis and other optogenetic approaches. *ACS Chemical Biology* **9**, 1398–1407; 10.1021/cb500176x (2014).
282. Wu, N., Deiters, A., Cropp, T. A., King, D. & Schultz, P. G. A genetically encoded photocaged amino acid. *J. Am. Chem. Soc.* **126**, 14306–14307; 10.1021/ja040175z (2004).
283. Liu, J., Hemphill, J., Samanta, S., Tsang, M. & Deiters, A. Genetic Code Expansion in Zebrafish Embryos and Its Application to Optical Control of Cell Signaling. *J. Am. Chem. Soc.* **139**, 9100–9103; 10.1021/jacs.7b02145 (2017).
284. Wolffgramm, J. *et al.* Light-Activation of DNA-Methyltransferases. *Angew. Chem. Int. Ed.* **60**, 13507–13512; 10.1002/anie.202103945 (2021).
285. Palei, S. *et al.* Light-Activatable TET-Dioxygenases Reveal Dynamics of 5-Methylcytosine Oxidation and Transcriptome Reorganization. *J. Am. Chem. Soc.* **142**, 7289–7294; 10.1021/jacs.0c01193 (2020).
286. Lemke, E. A., Summerer, D., Geierstanger, B. H., Brittain, S. M. & Schultz, P. G. Control of protein phosphorylation with a genetically encoded photocaged amino acid. *Nat Chem Biol* **3**, 769–772; 10.1038/nchembio.2007.44 (2007).
287. Nguyen, D. P. *et al.* Genetic encoding of photocaged cysteine allows photoactivation of TEV protease in live mammalian cells. *J. Am. Chem. Soc.* **136**, 2240–2243; 10.1021/ja412191m (2014).
288. Gautier, A., Deiters, A. & Chin, J. W. Light-activated kinases enable temporal dissection of signaling networks in living cells. *J. Am. Chem. Soc.* **133**, 2124–2127; 10.1021/ja1109979 (2011).
289. Gautier, A. *et al.* Genetically encoded photocontrol of protein localization in mammalian cells. *J. Am. Chem. Soc.* **132**, 4086–4088; 10.1021/ja910688s (2010).
290. Yuan, X. *et al.* Effect of Laser Irradiation on Cell Function and Its Implications in Raman Spectroscopy. *Applied and Environmental Microbiology* **84**; 10.1128/AEM.02508-17 (2018).
291. Sousa, N. T. A. de *et al.* Blue Laser Inhibits Bacterial Growth of *Staphylococcus aureus*, *Escherichia coli*, and *Pseudomonas aeruginosa*. *Photomedicine and Laser Surgery* **33**, 278–282; 10.1089/pho.2014.3854 (2015).
292. Minnihan, E. C. Mechanistic studies of proton-coupled electron transfer in aminotyrosine- and fluorotyrosine- substituted class Ia Ribonucleotide reductase. Mechanistic studies of proton-coupled electron transfer in aminotyrosine- and fluorotyrosine- substituted class Ia Ribonucleotide reductase. Massachusetts Institute of Technology.

293. Barry, B. A., el-Deeb, M. K., Sandusky, P. O. & Babcock, G. T. Tyrosine radicals in photosystem II and related model compounds. Characterization by isotopic labeling and EPR spectroscopy. *Journal of Biological Chemistry* **265**, 20139–20143 (1990).
294. Pagba, C. V. *et al.* A tyrosine-tryptophan dyad and radical-based charge transfer in a ribonucleotide reductase-inspired maquette. *Nat Commun* **6**, 10010; 10.1038/ncomms10010 (2015).
295. McCaslin, T. G. *et al.* Structure and Function of Tryptophan-Tyrosine Dyads in Biomimetic  $\beta$  Hairpins. *The journal of physical chemistry. B* **123**, 2780–2791; 10.1021/acs.jpcc.8b12452 (2019).
296. Crippa, P. R., Loh, E. & Isotani, S. Electron paramagnetic resonance of x-irradiated tyrosine, thyronine and their iodine-derivatives. *Radiation Effects* **25**, 13–15; 10.1080/00337577508242048 (1975).
297. Stoll, S. *et al.* Hydrogen bonding of tryptophan radicals revealed by EPR at 700 GHz. *J. Am. Chem. Soc.* **133**, 18098–18101; 10.1021/ja208462t (2011).
298. Stauffer, E., Dolan, J. A. & Newman, R. *Fire debris analysis* (Academic Press, Amsterdam, Boston, 2008).
299. Moore, B. N. & Julian, R. R. Dissociation energies of X-H bonds in amino acids. *Phys. Chem. Chem. Phys.* **14**, 3148–3154; 10.1039/C2CP23443B (2012).
300. Ly, T. *et al.* Rapid, quantitative, and site specific synthesis of biomolecular radicals from a simple photocaged precursor. *Chem. Commun.* **47**, 2835–2837; 10.1039/C0CC03363D (2011).
301. Huisgen, R. 1,3-Dipolar Cycloadditions. Past and Future. *Angew. Chem. Int. Ed.* **2**, 565–598; 10.1002/anie.196305651 (1963).
302. Kanakarajan, K., Goodrich, R., Young, M. J. T., Soundararajan, S. & Platz, M. S. EPR spectroscopy of triplet aryl nitrenes covalently bound to .alpha.-chymotrypsin. Application of low-temperature methods to photoaffinity labeling. *J. Am. Chem. Soc.* **110**, 6536–6541; 10.1021/ja00227a039 (1988).
303. Kuzaj, M., Lüerssen, H. & Wentrup, C. ESR Observation of Thermally Produced Triplet Nitrenes and Photochemically Produced Triplet Cycloheptatrienylidenes. *Angew. Chem. Int. Ed.* **25**, 480–482; 10.1002/anie.198604801 (1986).
304. Morris, J. L. *et al.* Aryl azide photochemistry in defined protein environments. *Organic letters* **15**, 728–731; 10.1021/ol3028779 (2013).
305. Peng, H. *et al.* An unexpected copper catalyzed 'reduction' of an arylazide to amine through the formation of a nitrene intermediate. *Tetrahedron* **69**, 5079–5085; 10.1016/j.tet.2013.04.091 (2013).

306. Kutin, Y. *et al.* Characterization of a Triplet Vinylidene. *J. Am. Chem. Soc.* **143**, 21410–21415; 10.1021/jacs.1c11062 (2021).
307. Sander, W., Grote, D., Kossmann, S. & Neese, F. 2,3,5,6-Tetrafluorophenylnitren-4-yl: electron paramagnetic resonance spectroscopic characterization of a quartet-ground-state nitreno radical. *J. Am. Chem. Soc.* **130**, 4396–4403; 10.1021/ja078171s (2008).
308. Hall, J. H., Fargher, J. M. & Gisler, M. R. Substituent effects on spin delocalization in triplet phenylnitrenes. 1. Para-substituted phenylnitrenes. *J. Am. Chem. Soc.* **100**, 2029–2034; 10.1021/ja00475a010 (1978).
309. Chapyshev, S. V., Korchagin, D. V., Costa, P. & Sander, W. The powder X-band electron paramagnetic resonance spectroscopy of septet pyridyl-2,4,6-trinitrene. *Magn. Reson. Chem.* **60**, 829–835; 10.1002/mrc.5269 (2022).
310. Akimov, A. *et al.* W-band EPR studies of high-spin nitrenes with large spin-orbit contribution to zero-field splitting. *The Journal of Chemical Physics* **143**, 84313; 10.1063/1.4929589 (2015).
311. Lovett, J. E., Lovett, B. W. & Harmer, J. DEER-Stitch: combining three- and four-pulse DEER measurements for high sensitivity, deadtime free data. *Journal of magnetic resonance (San Diego, Calif. : 1997)* **223**, 98–106; 10.1016/j.jmr.2012.08.011 (2012).
312. Milov, A. D., Ponomarev, A. B. & Tsvetkov, Y. Electron-electron double resonance in electron spin echo: Model biradical systems and the sensitized photolysis of decalin. *Chemical Physics Letters* **110**, 67–72; 10.1016/0009-2614(84)80148-7 (1984).
313. Spindler, P. E., Schöps, P., Kallies, W., Glaser, S. J. & Prisner, T. F. Perspectives of shaped pulses for EPR spectroscopy. *Journal of magnetic resonance (San Diego, Calif. : 1997)* **280**, 30–45; 10.1016/j.jmr.2017.02.023 (2017).
314. Singh, P. N. D. *et al.* Selective formation of triplet alkyl nitrenes from photolysis of beta-azido-propiofenone and their reactivity. *J. Am. Chem. Soc.* **129**, 16263–16272; 10.1021/ja077523s (2007).
315. Upul Ranaweera, R. R. A., Rajam, S. & Gudmundsdottir, A. D. Phenylethanol derivatives as triplet sensitizers for 1-azidoadamantane. *J. Phys. Org. Chem.* **24**, 902–908; 10.1002/poc.1922 (2011).
316. Nödling, A. R., Spear, L. A., Williams, T. L., Luk, L. Y. P. & Tsai, Y.-H. Using genetically incorporated unnatural amino acids to control protein functions in mammalian cells. *Essays Biochem* **63**, 237–266; 10.1042/EBC20180042 (2019).
317. Mozhaev, V. V., Heremans, K., Frank, J., Masson, P. & Balny, C. High pressure effects on protein structure and function. *Proteins* **24**, 81–91; 10.1002/(SICI)1097-0134(199601)24:1<81::AID-PROT6>3.0.CO;2-R (1996).

318. Gross, M. & Jaenicke, R. Proteins under pressure. The influence of high hydrostatic pressure on structure, function and assembly of proteins and protein complexes. *European journal of biochemistry* **221**, 617–630; 10.1111/j.1432-1033.1994.tb18774.x (1994).
319. Morild, E. The Theory of Pressure Effects on Enzymes. In *Advances in Protein Chemistry*, edited by C. B. Anfinsen, J. T. Edsall & F. M. Richards (Academic Press 1981), Vol. 34, pp. 93–166.
320. Heremans, K. High pressure effects on proteins and other biomolecules. *Annual review of biophysics and bioengineering* **11**, 1–21; 10.1146/annurev.bb.11.060182.000245 (1982).
321. Silva, J. L. & Weber, G. Pressure stability of proteins. *Annual review of physical chemistry* **44**, 89–113; 10.1146/annurev.pc.44.100193.000513 (1993).
322. Lüdemann, H.-D. Influence of pressure on protein conformation. *Makromolekulare Chemie. Macromolecular Symposia* **17**, 29–38; 10.1002/masy.19880170105 (1988).
323. Winter, R., Lopes, D., Grudzielanek, S. & Vogtt, K. Towards an Understanding of the Temperature/ Pressure Configurational and Free-Energy Landscape of Biomolecules. *Journal of Non-Equilibrium Thermodynamics* **32**, 41–97; 10.1515/JNETDY.2007.003 (2007).
324. Roche, J. & Royer, C. A. Lessons from pressure denaturation of proteins. *Journal of the Royal Society, Interface* **15**; 10.1098/rsif.2018.0244 (2018).
325. Lerch, M. T., Yang, Z., Brooks, E. K. & Hubbell, W. L. Mapping protein conformational heterogeneity under pressure with site-directed spin labeling and double electron-electron resonance. *Proceedings of the National Academy of Sciences* **111**, E1201-10; 10.1073/pnas.1403179111 (2014).
326. Xu, X., Gagné, D., Aramini, J. M. & Gardner, K. H. Volume and compressibility differences between protein conformations revealed by high-pressure NMR. *Biophysical journal* **120**, 924–935; 10.1016/j.bpj.2020.12.034 (2021).
327. Kitahara, R. *et al.* High pressure NMR reveals active-site hinge motion of folate-bound *Escherichia coli* dihydrofolate reductase. *Biochemistry* **39**, 12789–12795; 10.1021/bi0009993 (2000).
328. Librizzi, F., Carrotta, R., Peters, J. & Cupane, A. The effects of pressure on the energy landscape of proteins. *Sci Rep* **8**, 2037; 10.1038/s41598-018-20417-x (2018).
329. Akasaka, K. Exploring the entire conformational space of proteins by high-pressure NMR. *Pure and Applied Chemistry* **75**, 927–936; 10.1351/pac200375070927 (2003).

330. Ma, B., Kumar, S., Tsai, C. J. & Nussinov, R. Folding funnels and binding mechanisms. *Protein engineering* **12**, 713–720; 10.1093/protein/12.9.713 (1999).
331. Lerch, M. T., Yang, Z., Altenbach, C. & Hubbell, W. L. Chapter Two - High-Pressure EPR and Site-Directed Spin Labeling for Mapping Molecular Flexibility in Proteins. In *Methods in Enzymology*, Vol. 564, pp. 29–57.
332. Casteleijn, G., Bosch, J. J. ten & Smidt, J. Error Analysis of the Determination of Spin Concentration with the Electron Spin Resonance Method. *Journal of Applied Physics* **39**, 4375–4380; 10.1063/1.1656979 (1968).
333. Jeschke, G. EPR techniques for studying radical enzymes. *Biochimica et biophysica acta* **1707**, 91–102; 10.1016/j.bbabi.2004.02.012 (2005).
334. Ramm, I. *et al.* The Impact of Glycerol on an Affibody Conformation and Its Correlation to Chemical Degradation. *Pharmaceutics* **13**; 10.3390/pharmaceutics13111853 (2021).
335. Hirai, M. *et al.* Direct Evidence for the Effect of Glycerol on Protein Hydration and Thermal Structural Transition. *Biophysical journal* **115**, 313–327; 10.1016/j.bpj.2018.06.005 (2018).
336. Vagenende, V., Yap, M. G. S. & Trout, B. L. Mechanisms of protein stabilization and prevention of protein aggregation by glycerol. *Biochemistry* **48**, 11084–11096; 10.1021/bi900649t (2009).
337. Mendes, M. A., Souza, B. M. de, dos Santos, L. D., Santos, K. S. & Palma, M. S. Analyzing glycerol-mediated protein oligomerization by electrospray ionization mass spectrometry. *Rapid communications in mass spectrometry : RCM* **19**, 2636–2642; 10.1002/rcm.2113 (2005).
338. Grinberg, I. R. *et al.* Novel ATP-cone-driven allosteric regulation of ribonucleotide reductase via the radical-generating subunit. *eLife Sciences Publications, Ltd* (2018).
339. Hasan, M., Banerjee, I., Rozman Grinberg, I., Sjöberg, B. & Logan, D. T. Solution Structure of the dATP-Inactivated Class I Ribonucleotide Reductase From *Leeuwenhoekia blandensis* by SAXS and Cryo-Electron Microscopy. *Front. Mol. Biosci.* **8**, 713608; 10.3389/fmolb.2021.713608 (2021).
340. Rozman Grinberg, I. *et al.* A glutaredoxin domain fused to the radical-generating subunit of ribonucleotide reductase (RNR) functions as an efficient RNR reductant. *The Journal of biological chemistry* **293**, 15889–15900; 10.1074/jbc.RA118.004991 (2018).
341. Desta, I. T., Porter, K. A., Xia, B., Kozakov, D. & Vajda, S. Performance and Its Limits in Rigid Body Protein-Protein Docking. *Structure* **28**, 1071-1081.e3; 10.1016/j.str.2020.06.006 (2020).

342. Vajda, S. *et al.* New additions to the ClusPro server motivated by CAPRI. *Proteins* **85**, 435–444; 10.1002/prot.25219 (2017).
343. Kozakov, D. *et al.* How good is automated protein docking? *Proteins* **81**, 2159–2166; 10.1002/prot.24403 (2013).
344. Kozakov, D. *et al.* The ClusPro web server for protein-protein docking. *Nature protocols* **12**, 255–278; 10.1038/nprot.2016.169 (2017).
345. Mendes, M. A., Souza, B. M., Marques, M. R. & Palma, M. S. The effect of glycerol on signal suppression during electrospray ionization analysis of proteins. *Spectroscopy* **18**, 339–345; 10.1155/2004/732938 (2004).
346. Mendes, M. A., Chies, J. M., Oliveira Dias, A. C. de, Filho, S. A. & Palma, M. S. The shielding effect of glycerol against protein ionization in electrospray mass spectrometry. *Rapid communications in mass spectrometry : RCM* **17**, 672–677; 10.1002/rcm.958 (2003).
347. Jeffries, C. M., Graewert, M. A., Svergun, D. I. & Blanchet, C. E. Limiting radiation damage for high-brilliance biological solution scattering: practical experience at the EMBL P12 beamline PETRAIII. *J Synchrotron Rad* **22**, 273–279; 10.1107/S1600577515000375 (2015).
348. Lendzian, F. *et al.* Electronic Structure of Neutral Tryptophan Radicals in Ribonucleotide Reductase Studied by EPR and ENDOR Spectroscopy. *J. Am. Chem. Soc.* **118**, 8111–8120; 10.1021/ja960917r (1996).
349. Bleifuss, G. *et al.* Tryptophan and tyrosine radicals in ribonucleotide reductase: a comparative high-field EPR study at 94 GHz. *Biochemistry* **40**, 15362–15368; 10.1021/bi010707d (2001).
350. Pogni, R., Teutloff, C., Lendzian, F. & Basosi, R. Tryptophan radicals as reaction intermediates in versatile peroxidases: Multifrequency EPR, ENDOR and density functional theory studies. *Appl Magn Reson* **31**, 509–526; 10.1007/BF03166599 (2007).
351. Svistunenko, D. A. & Cooper, C. E. A new method of identifying the site of tyrosyl radicals in proteins. *Biophysical journal* **87**, 582–595; 10.1529/biophysj.104.041046 (2004).
352. Fessenden, R. W. & Schuler, R. H. Electron Spin Resonance Studies of Transient Alkyl Radicals. *The Journal of Chemical Physics* **39**, 2147–2195; 10.1063/1.1701415 (1963).
353. Svistunenko, D. A., Wilson, M. T. & Cooper, C. E. Tryptophan or tyrosine? On the nature of the amino acid radical formed following hydrogen peroxide treatment of cytochrome c oxidase. *Biochimica et biophysica acta* **1655**, 372–380; 10.1016/j.bbabbio.2003.06.006 (2004).

354. Bradley, J. M. *et al.* Three Aromatic Residues are Required for Electron Transfer during Iron Mineralization in Bacterioferritin. *Angew. Chem. Int. Ed.* **54**, 14763–14767; 10.1002/anie.201507486 (2015).
355. Un, S., Gerez, C., Elleingand, E. & Fontecave, M. Sensitivity of tyrosyl radical g-values to changes in protein structure: a high-field EPR study of mutants of ribonucleotide reductase. *J. Am. Chem. Soc.* **123**, 3048–3054; 10.1021/ja003650b (2001).
356. Valente-Mesquita, V. L., Botelho, M. M. & Ferreira, S. T. Pressure-Induced Subunit Dissociation and Unfolding of Dimeric  $\beta$ -Lactoglobulin. *Biophysical journal* **75**, 471–476; 10.1016/S0006-3495(98)77535-6 (1998).
357. Silva, J. L., Villas-Boas, M., Bonafe, C. F. S. & Meirelles, N. C. Anomalous Pressure Dissociation of Large Protein Aggregates. *Journal of Biological Chemistry* **264**, 15863–15868; 10.1016/S0021-9258(18)71557-3 (1989).
358. Paladini, A. A. & Weber, G. Pressure-induced reversible dissociation of enolase. *Biochemistry* **20**, 2587–2593; 10.1021/bi00512a034 (1981).
359. Balny, C. High Pressure and Protein Oligomeric Dissociation. *High Pressure Research* **22**, 737–741; 10.1080/08957950212447 (2002).
360. Sahlin, M. *et al.* Tryptophan radicals formed by iron/oxygen reaction with Escherichia coli ribonucleotide reductase protein R2 mutant Y122F. *Journal of Biological Chemistry* **269**, 11699–11702; 10.1016/S0021-9258(17)32628-5 (1994).
361. Sahlin, M., Lassmann, G., Pötsch, S., Sjöberg, B. M. & Gräslund, A. Transient free radicals in iron/oxygen reconstitution of mutant protein R2 Y122F. Possible participants in electron transfer chains in ribonucleotide reductase. *Journal of Biological Chemistry* **270**, 12361–12372; 10.1074/jbc.270.21.12361 (1995).
362. Hulsebosch, R. J. *et al.* Electronic Structure of the Neutral Tyrosine Radical in Frozen Solution. Selective 2 H-, 13 C-, and 17 O-Isotope Labeling and EPR Spectroscopy at 9 and 35 GHz. *J. Am. Chem. Soc.* **119**, 8685–8694; 10.1021/ja9707872 (1997).
363. Arns, L., Schuabb, V., Meichsner, S., Berghaus, M. & Winter, R. The Effect of Natural Osmolyte Mixtures on the Temperature-Pressure Stability of the Protein RNase A. *Zeitschrift für Physikalische Chemie* **232**, 615–634; 10.1515/zpch-2017-1039 (2018).
364. Silva, J. L. *et al.* High-pressure chemical biology and biotechnology. *Chemical reviews* **114**, 7239–7267; 10.1021/cr400204z (2014).
365. Hasegawa, S. *et al.* Long-Lived C60 Radical Anion Stabilized Inside an Electron-Deficient Coordination Cage. *J. Am. Chem. Soc.* **143**, 9718–9723; 10.1021/jacs.1c02860 (2021).

366. Kroto, H. W. *C60. Some Inside Stories* (Pan Stanford Publishing, 2015).
367. Kroto, H. W., Heath, J. R., O'Brien, S. C., Curl, R. F. & Smalley, R. E. C60: Buckminsterfullerene. *Nature* **318**, 162–163; 10.1038/318162a0 (1985).
368. Kroto, H. Symmetry, Space, Stars, and C60(Nobel Lecture). *Angew. Chem. Int. Ed.* **36**, 1578–1593; 10.1002/anie.199715781 (1997).
369. Smalley, R. E. Discovering the Fullerenes(Nobel Lecture). *Angew. Chem. Int. Ed.* **36**, 1594–1601; 10.1002/anie.199715941 (1997).
370. Curl, R. F. Dawn of Fullerenes: Conjecture and Experiment(Nobel Lecture). *Angew. Chem. Int. Ed.* **36**, 1566–1576; 10.1002/anie.199715661 (1997).
371. Filippone, S. & Martín, N. Exohedral Fullerenes. In *Encyclopedia of Polymeric Nanomaterials*, edited by S. Kobayashi & K. Müllen (Springer Berlin Heidelberg; Imprint: Springer, Berlin, Heidelberg, 2020), pp. 1–16.
372. Bhakta, P. & Barthunia, B. Fullerene and its applications: A review. *J Indian Acad Oral Med Radiol* **32**, 159; 10.4103/jiaomr.jiaomr\_191\_19 (2020).
373. Colbert, D. Fullerene nanobutes for molecular electronics. *Trends in Biotechnology* **17**, 46–50; 10.1016/S0167-7799(98)01256-6 (1999).
374. Collavini, S. & Delgado, J. L. Fullerenes: the stars of photovoltaics. *Sustainable Energy Fuels* **2**, 2480–2493; 10.1039/C8SE00254A (2018).
375. Jiang, Z., Zhao, Y., Lu, X. & Xie, J. Fullerenes for rechargeable battery applications: Recent developments and future perspectives. *Journal of Energy Chemistry* **55**, 70–79; 10.1016/j.jechem.2020.06.065 (2021).
376. Rašović, I. Water-soluble fullerenes for medical applications. *Materials Science and Technology* **33**, 777–794; 10.1080/02670836.2016.1198114 (2017).
377. Chai, Y. *et al.* Fullerenes with metals inside. *J. Phys. Chem.* **95**, 7564–7568; 10.1021/j100173a002 (1991).
378. Krachmalnicoff, A., Levitt, M. H. & Whitby, R. J. An optimised scalable synthesis of H<sub>2</sub>O@C<sub>60</sub> and a new synthesis of H<sub>2</sub>@C<sub>60</sub>. *Chem. Commun.* **50**, 13037–13040; 10.1039/C4CC06198E (2014).
379. Brenner, W., Ronson, T. K. & Nitschke, J. R. Separation and Selective Formation of Fullerene Adducts within an M(II)(8)L(6) Cage. *J. Am. Chem. Soc.* **139**, 75–78; 10.1021/jacs.6b11523 (2017).
380. García-Simón, C., Costas, M. & Ribas, X. Metallosupramolecular receptors for fullerene binding and release. *Chem. Soc. Rev.* **45**, 40–62; 10.1039/C5CS00315F (2016).

381. Han, W.-K. *et al.* Tetrahedral metal-organic cages with cube-like cavities for selective encapsulation of fullerene guests and their spin-crossover properties. *Chem. Commun.* **54**, 12646–12649; 10.1039/C8CC06652C (2018).
382. Kishi, N., Li, Z., Yoza, K., Akita, M. & Yoshizawa, M. An M2L4 molecular capsule with an anthracene shell: encapsulation of large guests up to 1 nm. *J. Am. Chem. Soc.* **133**, 11438–11441; 10.1021/ja2037029 (2011).
383. Kishi, N., Akita, M. & Yoshizawa, M. Selective host-guest interactions of a transformable coordination capsule/tube with fullerenes. *Angew. Chem. Int. Ed.* **53**, 3604–3607; 10.1002/anie.201311251 (2014).
384. Clever, G. H. & Punt, P. Cation-Anion Arrangement Patterns in Self-Assembled Pd2L4 and Pd4L8 Coordination Cages. *Accounts of Chemical Research* **50**, 2233–2243; 10.1021/acs.accounts.7b00231 (2017).
385. Jansze, S. M., Wise, M. D., Vologzhanina, A. V., Scopelliti, R. & Severin, K. PdII2L4-type coordination cages up to three nanometers in size. *Chem. Sci.* **8**, 1901–1908; 10.1039/C6SC04732G (2017).
386. Chen, B., Horiuchi, S., Holstein, J. J., Tessarolo, J. & Clever, G. H. Tunable Fullerene Affinity of Cages, Bowls and Rings Assembled by PdII Coordination Sphere Engineering. *Chemistry – A European Journal* **25**, 14921–14927; 10.1002/chem.201903317 (2019).
387. Chen, B., Holstein, J. J., Horiuchi, S., Hiller, W. G. & Clever, G. H. Pd(II) Coordination Sphere Engineering: Pyridine Cages, Quinoline Bowls, and Heteroleptic Pills Binding One or Two Fullerenes. *J. Am. Chem. Soc.* **141**, 8907–8913; 10.1021/jacs.9b02207 (2019).
388. Fukuzumi, S. *et al.* Selective One-Electron and Two-Electron Reduction of C 60 with NADH and NAD Dimer Analogues via Photoinduced Electron Transfer. *J. Am. Chem. Soc.* **120**, 8060–8068; 10.1021/ja9813459 (1998).
389. Pivrikas, A., Sariciftci, N. S., Juška, G. & Österbacka, R. A review of charge transport and recombination in polymer/fullerene organic solar cells. *Prog. Photovolt: Res. Appl.* **15**, 677–696; 10.1002/pip.791 (2007).
390. Pansare, V., Hejazi, S., Faenza, W. & Prud'homme, R. K. Review of Long-Wavelength Optical and NIR Imaging Materials: Contrast Agents, Fluorophores and Multifunctional Nano Carriers. *Chemistry of Materials* **24**, 812–827; 10.1021/cm2028367 (2012).
391. Fabian, J., Nakazumi, H. & Matsuoka, M. Near-infrared absorbing dyes. *Chem. Rev.* **92**, 1197–1226; 10.1021/cr00014a003 (1992).
392. Staško, A. *et al.* Anion radicals of [60]fullerenes. An EPR study. *Res. Chem. Intermed.* **23**, 453–478; 10.1163/156856797X00187 (1997).

393. Araki, Y. & Osamu, I. Factors controlling lifetimes of photoinduced charge-separated states of fullerene-donor molecular systems. *Journal of Photochemistry and Photobiology C: Photochemistry Reviews* **9**, 93–110; 10.1016/j.jphotochemrev.2008.04.004 (2008).
394. Futagoishi, T. *et al.* A Stable, Soluble, and Crystalline Supramolecular System with a Triplet Ground State. *Angew. Chem. Int. Ed.* **56**, 4261–4265; 10.1002/anie.201701212 (2017).
395. Hasegawa, S., Hashikawa, Y., Kato, T. & Murata, Y. Construction of a Metal-Free Electron Spin System by Encapsulation of an NO Molecule Inside an Open-Cage Fullerene C<sub>60</sub> Derivative. *Angew. Chem. Int. Ed.* **57**, 12804–12808; 10.1002/anie.201807823 (2018).
396. Kato, T. *et al.* Electronic absorption spectra of the radical anions and cations of fullerenes: C<sub>60</sub> and C<sub>70</sub>. *Chemical Physics Letters* **180**, 446–450; 10.1016/0009-2614(91)85147-O (1991).
397. Gasyana, Z., Andrews, L. & Schatz, P. N. Near-infrared absorption spectra of fullerene (C<sub>60</sub>) radical cations and anions prepared simultaneously in solid argon. *J. Phys. Chem.* **96**, 1525–1527; 10.1021/j100183a005 (1992).
398. Lobach, A. S., Goldshleger, N. F., Kaplunov, M. G. & Kulikov, A. V. Near-IR and ESR studies of the radical anions of C<sub>60</sub> and C<sub>70</sub> in the system fullerene-primary amine. *Chemical Physics Letters* **243**, 22–28; 10.1016/0009-2614(95)00811-H (1995).
399. Paul, P., Kim, K.-C., Sun, D., Boyd, P. D. W. & Reed, C. A. Artifacts in the electron paramagnetic resonance spectra of C<sub>60</sub> fullerene ions: inevitable C<sub>120</sub>O impurity. *J. Am. Chem. Soc.* **124**, 4394–4401; 10.1021/ja011832f (2002).
400. Pace, M. D., Christidis, T. C., Yin, J. J. & Milliken, J. EPR of a free radical in fullerene, C<sub>60</sub>: effect of molecular oxygen. *J. Phys. Chem.* **96**, 6855–6858; 10.1021/j100196a001 (1992).
401. Niklas, J., Mardis, K. L. & Poluektov, O. G. Spin Signature of the C<sub>60</sub> Fullerene Anion: A Combined X- and D-Band EPR and DFT Study. *The journal of physical chemistry letters* **9**, 3915–3921; 10.1021/acs.jpcclett.8b01613 (2018).
402. Allemand, P. M. *et al.* The unusual electron spin resonance of fullerene C<sub>60</sub> anion radical. *J. Am. Chem. Soc.* **113**, 2780–2781; 10.1021/ja00007a078 (1991).
403. Stankowski, J., Byszewski, P., Kempniński, W., Trybuła, Z. & Żuk, T. Electron Paramagnetic Resonance in MexC<sub>60</sub> Fullerenes for Me = K and Rb. *phys. stat. sol. (b)* **178**, 221–231; 10.1002/pssb.2221780122 (1993).
404. Stankowski, J., Piekara-Sady, L. & Kempniński, W. EPR of a fullerene-molecule-derived paramagnetic center as a mesoscopic conducting object. *Appl Magn Reson* **19**, 539–546; 10.1007/BF03162398 (2000).

405. Norman, R. O. C. *Structures of Organic Radicals* (1970).
406. Schell-Sorokin, A. J. *et al.* Electron spin relaxation times of C-60 in solution. *Chemical Physics Letters* **195**, 225–232; 10.1016/0009-2614(92)86140-D (1992).
407. Paul, P., Bolskar, R. D., Clark, A. M. & Reed, C. A. The origin of the ‘spike’ in the EPR spectrum of C60-. *Chem. Commun.*, 1229–1230; 10.1039/B003428M (2000).
408. Hase, H. & Miyatake, Y. Comparative ESR study of C60 and C70 radical anions produced in  $\gamma$ -irradiated organic solid solutions at 77 K. *Chemical Physics Letters* **245**, 95–101; 10.1016/0009-2614(95)00974-9 (1995).
409. Stergiou, A. *et al.* A Long-Lived Azafullerenyl Radical Stabilized by Supramolecular Shielding with a 10Cycloparaphenylene. *Angew. Chem. Int. Ed.* **58**, 17745–17750; 10.1002/anie.201909126 (2019).
410. Krumkacheva, O. A. *et al.* Triplet Fullerenes as Prospective Spin Labels for Nanoscale Distance Measurements by Pulsed Dipolar EPR Spectroscopy. *Angew. Chem. Int. Ed.* **58**, 13271–13275; 10.1002/anie.201904152 (2019).
411. Timofeev, I. O. *et al.* Fullerene-based triplet spin labels: methodology aspects for pulsed dipolar EPR spectroscopy. *Phys. Chem. Chem. Phys.* **24**, 4475–4484; 10.1039/D1CP05545C (2022).
412. Stoll, S. & Schweiger, A. EasySpin, a comprehensive software package for spectral simulation and analysis in EPR. *Journal of Magnetic Resonance* **178**, 42–55; 10.1016/j.jmr.2005.08.013 (2006).
413. Abdullin, D., Hagelueken, G., Hunter, R. I., Smith, G. M. & Schiemann, O. Geometric model-based fitting algorithm for orientation-selective PELDOR data. *Molecular Physics* **113**, 544–560; 10.1080/00268976.2014.960494 (2015).
414. Ravichandran, K. Mechanistic investigations of the radical transport pathway in fluorotyrosine-substituted class Ia ribonucleotide reductases. Mechanistic investigations of the radical transport pathway in fluorotyrosine-substituted class Ia ribonucleotide reductases. Massachusetts Institute of Technology; Massachusetts Institute of Technology.
415. Salowe, S. P. & Stubbe, J. Cloning, overproduction, and purification of the B2 subunit of ribonucleoside-diphosphate reductase. *Journal of bacteriology* **165**, 363–366; 10.1128/jb.165.2.363-366.1986 (1986).
416. Chen, H., Gollnick, P. & Phillips, R. S. Site-Directed Mutagenesis of His343Ala in *Citrobacter freundii* Tyrosine Phenol-Lyase. Effects on the Kinetic Mechanism and Rate-Determining Step. *European journal of biochemistry* **229**, 540–549; 10.1111/j.1432-1033.1995.0540k.x (1995).

417. Kim, K. & Cole, P. A. Kinetic Analysis of a Protein Tyrosine Kinase Reaction Transition State in the Forward and Reverse Directions. *J. Am. Chem. Soc.* **120**, 6851–6858; 10.1021/ja9808393 (1998).
418. Seyedsayamdost, M. R., Yee, C. S. & Stubbe, J. Site-specific incorporation of fluorotyrosines into the R2 subunit of E. coli ribonucleotide reductase by expressed protein ligation. *Nat Protoc* **2**, 1225–1235; 10.1038/nprot.2007.159 (2007).

## Eidesstattliche Versicherung (Affidavit)

\_\_\_\_\_  
Name, Vorname  
(Surname, first name)

\_\_\_\_\_  
Matrikel-Nr.  
(Enrolment number)

**Belehrung:**

Wer vorsätzlich gegen eine die Täuschung über Prüfungsleistungen betreffende Regelung einer Hochschulprüfungsordnung verstößt, handelt ordnungswidrig. Die Ordnungswidrigkeit kann mit einer Geldbuße von bis zu 50.000,00 € geahndet werden. Zuständige Verwaltungsbehörde für die Verfolgung und Ahndung von Ordnungswidrigkeiten ist der Kanzler/die Kanzlerin der Technischen Universität Dortmund. Im Falle eines mehrfachen oder sonstigen schwerwiegenden Täuschungsversuches kann der Prüfling zudem exmatrikuliert werden, § 63 Abs. 5 Hochschulgesetz NRW.

Die Abgabe einer falschen Versicherung an Eides statt ist strafbar.

Wer vorsätzlich eine falsche Versicherung an Eides statt abgibt, kann mit einer Freiheitsstrafe bis zu drei Jahren oder mit Geldstrafe bestraft werden, § 156 StGB. Die fahrlässige Abgabe einer falschen Versicherung an Eides statt kann mit einer Freiheitsstrafe bis zu einem Jahr oder Geldstrafe bestraft werden, § 161 StGB.

Die oben stehende Belehrung habe ich zur Kenntnis genommen:

**Official notification:**

Any person who intentionally breaches any regulation of university examination regulations relating to deception in examination performance is acting improperly. This offence can be punished with a fine of up to EUR 50,000.00. The competent administrative authority for the pursuit and prosecution of offences of this type is the chancellor of the TU Dortmund University. In the case of multiple or other serious attempts at deception, the candidate can also be unenrolled, Section 63, paragraph 5 of the Universities Act of North Rhine-Westphalia.

The submission of a false affidavit is punishable.

Any person who intentionally submits a false affidavit can be punished with a prison sentence of up to three years or a fine, Section 156 of the Criminal Code. The negligent submission of a false affidavit can be punished with a prison sentence of up to one year or a fine, Section 161 of the Criminal Code.

I have taken note of the above official notification.

\_\_\_\_\_  
Ort, Datum  
(Place, date)

\_\_\_\_\_  
Unterschrift  
(Signature)

\_\_\_\_\_  
Titel der Dissertation:  
(Title of the thesis):

\_\_\_\_\_

\_\_\_\_\_

\_\_\_\_\_

Ich versichere hiermit an Eides statt, dass ich die vorliegende Dissertation mit dem Titel selbstständig und ohne unzulässige fremde Hilfe angefertigt habe. Ich habe keine anderen als die angegebenen Quellen und Hilfsmittel benutzt sowie wörtliche und sinngemäße Zitate kenntlich gemacht.

Die Arbeit hat in gegenwärtiger oder in einer anderen Fassung weder der TU Dortmund noch einer anderen Hochschule im Zusammenhang mit einer staatlichen oder akademischen Prüfung vorgelegen.

I hereby swear that I have completed the present dissertation independently and without inadmissible external support. I have not used any sources or tools other than those indicated and have identified literal and analogous quotations.

The thesis in its current version or another version has not been presented to the TU Dortmund University or another university in connection with a state or academic examination.\*

**\*Please be aware that solely the German version of the affidavit ("Eidesstattliche Versicherung") for the PhD thesis is the official and legally binding version.**

\_\_\_\_\_  
Ort, Datum  
(Place, date)

\_\_\_\_\_  
Unterschrift  
(Signature)